

Editorial corner – a personal view

Inorganic/organic hybrids, ceramic precursor polymers, composites: specialty materials of the future?

Gy. Bánhegyi*

Department of Advanced Materials and Processes, Bay Zoltán Nonprofit Ltd. for Applied Research, Fehérvári út 130., H-1116 Budapest, Hungary

Inorganic and organic solids have significant, but mostly mutually exclusive advantages over each other, therefore one usually selects inorganic or organic solid for certain applications depending on the requirements. Traditional mineral filled polymers meant the simplest combination of organic polymers with inorganic materials, followed later by organic-inorganic hybrids, ceramic precursor polymers and other organic/inorganic nanostructures. Even the classical filler technology was tuned up e.g. by using low melting point metal alloys (DOI: [10.1081/PPT-100101407](https://doi.org/10.1081/PPT-100101407)) or phosphate glasses (DOI: [10.1002/pc.10070](https://doi.org/10.1002/pc.10070)) which behave as liquids (melts) during the melt processing of polymers. This results not only in completely new morphologies, but in new behavior. Micro-phase separation of inorganic moieties appears not only in ionomers, but also in sol-gel derived polymeric composites. Sol-gel derived structures can also be fired to remove all organic components, resulting in glassy, crystalline or nano-structured bulk, coating or fibrous structures. Nano-wire and nano-fiber formation by electrospinning of inorganic filled or ceramic precursor polymers became very fashionable and successful research direction, among others in the development of energy-harvesting. Ceramic precursor polymers are becoming more and more sophisticated and the up-to-date structural investigation methods allow a more precise understanding of their decomposition and transformation process. The extensive use of electrochemical technologies to develop new conducting polymer/inorganic, conducting polymers/

nanotube and/or graphene and/or nanoplatelet structures allow the development of new, ordered nanostructures with special properties. Not only periodical superlattices (DOI: [10.1186/1556-276X-7-71](https://doi.org/10.1186/1556-276X-7-71)), but also quantum dot nanocomposites can be developed using conducting polymers (DOI: [10.1021/bk-2010-1034.ch010](https://doi.org/10.1021/bk-2010-1034.ch010)). Organic-inorganic copolymers are used as precursors (DOI: [10.1002/adfm.200400462](https://doi.org/10.1002/adfm.200400462)) or as electrolytes (DOI: [10.1021/ma301404q](https://doi.org/10.1021/ma301404q)). Nanostructured, metal containing polymer precursors are used for high temperature, non-oxide ceramic synthesis (DOI: [10.1016/S0955-2219\(02\)00119-X](https://doi.org/10.1016/S0955-2219(02)00119-X)). Biopolymer based hybrids (see e.g. DOI: [10.1039/B505640N](https://doi.org/10.1039/B505640N)) include not only immobilized enzymes but also polysaccharide based hybrids, including cyclodextrin moieties attached to inorganic particles or media, capable of selective adsorption. Even this cursory glance at the recent development of inorganic/organic hybrid technologies, including ceramic precursor systems shows that several new technical solutions can be expected from this lively research field.



Dr. György Bánhegyi
Member of Executive Editorial Board

*Corresponding author, e-mail: gyorgy.banhegyi@bayzoltan.hu
© BME-PT

Unexpected differences between thermal and photoinitiated cationic curing of a diglycidyl ether of bisphenol A modified with a multiarm star poly(styrene)-*b*-poly(ϵ -caprolactone) polymer

J. M. Morancho^{1*}, A. Cadenato¹, X. Ramis¹, M. Morell², X. Fernández-Francos², J. M. Salla¹, A. Serra²

¹Thermodynamics Laboratory, Heat Engines Department, ETSEIB, Universitat Politècnica de Catalunya, Av. Diagonal 647, 08028 Barcelona, Spain

²Department of Analytical and Organic Chemistry, Universitat Rovira i Virgili, C/ Marcel·lí Domingo s/n, 43007 Tarragona, Spain

Received 4 January 2013; accepted in revised form 18 March 2013

Abstract. The effect of adding a multiarm star poly(styrene)-*b*-poly(ϵ -caprolactone) polymer on the cationic thermal and photoinitiated curing of diglycidyl ether of bisphenol A was studied. This star-polymer decelerated the thermal curing of diglycidyl ether of bisphenol A and modified the final structure of the epoxy matrix. The photocuring was influenced significantly by the addition of the multiarm star. When the proportion of this modifier added was 5%, much more time was necessary for complete photocuring (160 min at 40°C). In the presence of 10% of modifier, the degree of photocuring reached was very low (0.196 at 120°C). A subsequent thermal post-curing was necessary to cure completely the system. During photocuring in presence of poly(styrene)-*b*-poly(ϵ -caprolactone), the formation of dormant species, which are reactivated when the temperature increases, takes place. The kinetics of the thermal curing and the photocuring was analyzed using an isoconversional method due to the complexity of the reactive process. Applying this method, it has been confirmed the dependence of activation energy on the degree of conversion. The fracture morphology analyzed by scanning electron microscopy exhibited a second phase originated during photocuring by the presence of the modifier.

Keywords: thermosetting resins, multiarm star polymer, thermal curing, photocuring, kinetics

1. Introduction

Epoxy resins are used in a wide range of applications, such as adhesives, coatings, castings, electrical and electronic materials, encapsulation of semiconductor devices, matrix material for composites, structural components [1–9] and cryogenic engineering [10–12]. Epoxy resins have good mechanical and chemical properties, adhesion, thermal stability and electrical characteristics. However, they are inherently brittle due to their relatively rigid

molecular structure, which limits their use. In coatings, the curing shrinkage can cause serious problems due to the generation of microvoids and microcracks, deformation and loss of adhesion. Then the protection capability and durability of the coating are reduced, which allows corrosion of the substrate as a result of the penetration of moisture [13]. In order to increase the toughness of the epoxy resins different modifiers can be added to them, like rubber and thermoplastic, but they always limit the processability of the resin systems [14–19].

*Corresponding author, e-mail: morancho@mmt.upc.edu
© BME-PT

Hyperbranched polymers (HBP) are a new family of polymeric modifiers that can be added to epoxy resins to increase their toughness without compromising the processability due to their highly branched dendritic structure [20]. The main advantages of HBPs are their low viscosity compared with their linear counterparts, the possibility of tailoring their core and branches structure and the functionalization of the end groups so that they can be compatible with the surrounding matrix [21]. HBPs can also reduce the shrinkage of the resin during the curing process [22] and the internal stresses [6]. The glass transition of the epoxy resin can be reduced by HBPs [21] or left unaltered [6], depending on different factors, such as the formation of a second phase during curing, the glass transition temperature of HBP and the interactions between modifier and epoxy matrix. In previous works, the influence of some HBPs in the thermal curing and the photocuring cationically initiated of a diglycidyl ether of bisphenol A (DGEBA) has been studied [23–25].

In addition to HBPs, multiarm star polymers can also be considered as a new class of reactive modifiers for epoxy resins. In this paper, the influence of a multiarm star polymer based on hyperbranched poly(styrene)-*b*-poly(ϵ -caprolactone) on the cationic thermal curing and on the cationic photocuring of an epoxy resin is reported. This polymer was previously synthesized and used as a modifier in the thermal anionic curing of DGEBA [26]. Hyperbranched poly(styrene)-*b*-poly(ϵ -caprolactone) showed a slightly decelerative effect on the curing, a homogeneous nanograined morphology and good processability when was used as reactive modifier of epoxy thermosets cured in the presence of tertiary amine. In another previous work, the influence of two multiarm star polymers, based on hyperbranched poly(glycidol)-*b*-poly(ϵ -caprolactone) on the cationic thermal curing and the cationic photocuring of the same epoxy resin was studied [27]. These polymers decelerated the thermal curing and the photocuring, but to a lesser extent than the poly(styrene)-*b*-poly(ϵ -caprolactone) polymer, studied in this work.

In addition to the kinetics of thermal and UV-induced curing and thermal properties of poly(styrene)-*b*-poly(ϵ -caprolactone)/DGEBA mixtures, the potential capacity of the star-like topology to enhance epoxy toughness is also discussed.

2. Experimental

2.1. Materials

DGEBA with an epoxy equivalent of 187 g/ee (EPIKOTE 828, Hexion Specialty Chemicals B.V., Hoogvliet, Netherlands) was dried in vacuum before use. A multiarm star poly(styrene)-*b*-poly(ϵ -caprolactone) (from now on PS-10) with 60 arms per molecule, a degree of polymerization of the poly(ϵ -caprolactone) arms of 10 and an average molecular weight in number of 76,200 g/mol was synthesized by us following a reported procedure [26]. Figure 1 shows the idealized chemical structure of this polymer. Ytterbium triflate (Yb(OTf)₃) (Aldrich, St. Louis, Missouri, USA) has been used as thermal cationic initiator. The photoinitiator used is CYRACURE UVI-6976 (triarylsulfonium hexafluoroantimonate, 50 wt% in propylene carbonate) and was received from Dow Chemical Company (Midland, Michigan, USA).

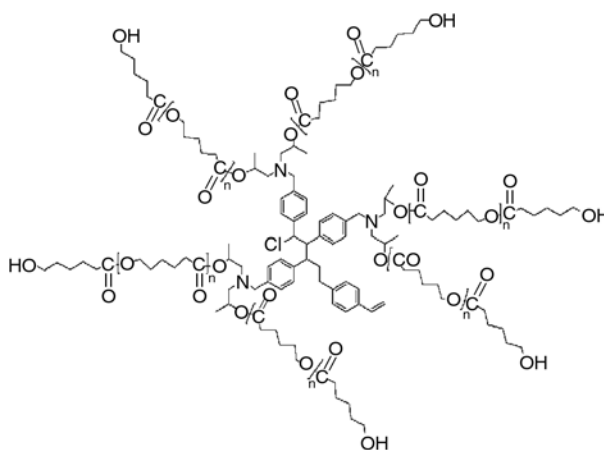


Figure 1. Idealized chemical structure of the multi arm star poly(styrene)-*b*-poly(ϵ -caprolactone)

2.2. Preparation of curing formulations

The mixtures of liquid DGEBA and solid star polymer were prepared by mixing and heating the desired quantities of these substances using a hot air blower and vigorous stirring. In the thermally curable samples, 1 phr (parts of initiator per 100 parts of resin) of the thermal initiator was added to the mixtures at room temperature and they were stirred and kept at -18°C to prevent polymerization. In the photocurable samples of neat DGEBA, 2 phr of CYRACURE UVI-6976 was added (because the concentration of photoinitiator was 50% in weight in the CYRACURE UVI-6976 solution, 2 phr of this solution was needed for a concentration of 1 phr of photoinitiator in the

reactive mixture) and they were stirred and kept in the dark at -18°C . In the photocurable samples of DGEBA with different proportions of PS-10, 4 phr of CYRACURE UVI-6976 was added (the concentration of the photoinitiator in the reactive mixture was 2 phr).

2.3. Thermal curing

The thermally curable samples were cured at different heating rates (2.5, 5, 7.5, 10 and $15^{\circ}\text{C}/\text{min}$) in a Mettler 822e calorimeter (Mettler-Toledo, Schwerzenbach, Switzerland) under a nitrogen atmosphere. The dynamic scans were performed from 0 to 250°C when the system was neat DGEBA. But when a proportion of 5 or 10% of PS-10 was added to DGEBA the dynamic scans were performed from 0 to 330°C at $15^{\circ}\text{C}/\text{min}$ and from 0 to 300°C at the other heating rates. The ultimate glass transition temperature of the cured materials ($T_{g\infty}$) was determined on the basis of a second dynamic run from -100 to 250°C at $10^{\circ}\text{C}/\text{min}$, as the temperature of the half-way point of the jump in the heat capacity when the material changed from glassy to the rubbery state under N_2 atmosphere and the error is estimated to be approximately $\pm 1^{\circ}\text{C}$.

2.4. Photocuring

The photocurable samples were photocured at different temperatures, in a Mettler DSC-821e (Mettler-Toledo, Schwerzenbach, Switzerland) calorimeter appropriately modified with a Hamamatsu Lightningcure LC5 (Hg-Xe lamp) (Hamamatsu Photonics K.K., Hamamatsu City, Japan) with two beams, one for the sample side and the other for the reference side. Samples of ca. 5 mg were cured in open aluminium pans in a nitrogen atmosphere. Two scans were performed on each sample to subtract the thermal effect of UV irradiation from the photocuring experiment, each one consisting of four minutes of temperature conditioning, a period of time of irradiation and finally four minutes more without UV light. The light intensity used was calculated by irradiation of graphite-filled plans on only the sample side. The period of time of irradiation depended on the analyzed system. For the neat DGEBA, it was 30 min. For the DGEBA modified with 5% of PS-10 this period of time depended on temperature. This period changed between 80 min (at 120°C) and 160 min (at 40°C). These different periods of time were necessary to ensure a complete

photocuring process. Dynamic postcuring experiments were carried out in the same DSC, without irradiation, from 30 to 250°C at $10^{\circ}\text{C}/\text{min}$ to determine the residual heat. After this, a second dynamic run was carried out to determine $T_{g\infty}$.

When DGEBA was modified with 10% of PS-10 the system was photocured at 120°C for 30 min, and after that, it was thermally postcured at different heating rates from 30 to 300°C , with the exception of the heating rate of $15^{\circ}\text{C}/\text{min}$, where the final temperature was 330°C .

2.5. SEM (Scanning Electron Microscopy)

Some samples were photocured isothermally in a polypropylene mould ($2.35 \times 1.2 \times 0.3 \text{ cm}^3$, with a thickness of 0.5 mm) at room temperature. Each side of the sample was irradiated for 15 min with a monochromatic UV lamp of 365 nm wavelength and $4 \text{ mW}/\text{cm}^2$ of intensity. They were subsequently postcured at 180°C for two hours, cooled in liquid nitrogen and fractured. The fracture surface of these samples was coated with a conductive gold layer and then examined with a JEOL JSM-6400 SEM (JEOL Ltd., Tokyo, Japan), with a magnification of 20,000.

3. Theory

In the thermal curing processes the degree of conversion (α) was calculated according to Equation (1):

$$\alpha = \frac{\Delta h_T}{\Delta h_{\text{dyn}}} \quad (1)$$

where Δh_T is the heat released up to a temperature T , obtained by integration of the calorimetric signal up to that temperature and Δh_{dyn} is the total reaction heat of the experiment, associated with complete conversion of all reactive groups. Cure completion was confirmed by FTIR of the samples after dynamic curing.

The rate of conversion ($d\alpha/dt$) is proportional to a function of the degree of conversion ($f(\alpha)$) which depends on the mechanism governing the reactive process, as shown by Equation (2):

$$\frac{d\alpha}{dt} = kf(\alpha) \quad (2)$$

where k is the kinetic constant. If this constant is replaced by the Arrhenius equation, Equation (3) is obtained:

$$\frac{d\alpha}{dt} = k_0 \exp\left(-\frac{E}{RT}\right) f(\alpha) \quad (3)$$

where k_0 is the preexponential factor, E activation energy, R universal gas constant and T temperature. By reordering the so-called temperature integral can be written as in Equation (4):

$$g(\alpha) = \int_0^\alpha \frac{d\alpha}{f(\alpha)} = \frac{k_0}{\beta} \int_0^T \exp\left(-\frac{E}{RT}\right) dT \quad (4)$$

where β is the heating rate (dT/dt) and $g(\alpha)$ an integral function of the degree of conversion. Equation (4) may be integrated employing Doyle's approach [28] and rewritten in logarithm form as shown by Equation (5):

$$\ln\beta = \ln\left[\frac{k_0 E}{g(\alpha) R}\right] - 5.330 - \frac{1.0516E}{RT} \quad (5)$$

This equation enables to determine E and the kinetic parameter $\ln[k_0 E/(g(\alpha) R)]$ (Ozawa method [29]) for each degree of conversion. To determine the values of the preexponential factor for each degree of conversion the R_3 model (contracting volume mechanism) is applied. This kinetic model can be represented by its differential expression $f(\alpha) = 3(1 - \alpha)^{2/3}$ and its integral expression $g(\alpha) = 1 - (1 - \alpha)^{1/3}$. This model has been previously determined for the resin/initiator system used in this work [30]. In this work it has been confirmed that the curing of PS-10/DGEBA formulations is also described by R_3 model.

In isothermal photocuring experiments the degree of conversion was calculated by Equation (6):

$$\alpha = \frac{\Delta h_t}{\Delta h_{ave}} \quad (6)$$

where Δh_t is the heat released up to a time t and Δh_{ave} is the average reaction heat obtained in the non-isothermal thermal curing (see Table 1). Equation (3) can also be used in the isothermal photocuring process and integrating this equation in isothermal conditions, Equation (7) is obtained [31]:

$$\ln t = \ln\left[\frac{g(\alpha)}{k_0}\right] + \frac{E}{RT} \quad (7)$$

which allows finding the activation energy for each degree of conversion from the slope of the linear relationship $\ln t$ vs. $1/T$.

Table 1. Hydroxyl equivalents per epoxy equivalent (eq OH/ee) of DGEBA modified with different proportions of PS-10. Average total reaction heat (Δh_{ave}), kinetic constant at 160°C at a degree of conversion of 0.5 ($k_{160^\circ\text{C}}$) and experimental maximum glass transition temperature (T_{g^∞}) of the thermal curing of DGEBA modified with different proportions of PS-10. Experimental maximum glass transition temperature (T_{g^∞}) of the photocuring of DGEBA modified with different proportions of PS-10

% PS-10	eqOH/ee	Thermal curing			Photocuring
		Δh_{ave} [kJ/ee]	$k_{160^\circ\text{C}}$ [s ⁻¹]	T_{g^∞} [°C]	T_{g^∞} [°C]
0	0.0545	99.6	$6.46 \cdot 10^{-4}$	134	162
5	0.0619	97.8	$3.74 \cdot 10^{-4}$	101	135
10	0.0692	99.1	$2.07 \cdot 10^{-4}$	98	119

In DGEBA modified with 10% of PS-10, as it has been commented in the experimental part, a dynamic post-curing (dark reaction) at different heating rates after photocuring the sample at 120°C has been made. The dynamic post-curing has also been studied by an isoconversional procedure using Equation (5) to find the activation energy and the preexponential factor, but these magnitudes have been found at different relative conversion degrees (α'), see Equation (8):

$$\alpha' = \frac{\Delta h_T}{\Delta h_{dyn}} \quad (8)$$

where in this case Δh_T is the heat released up to a temperature T during the dynamic post-curing and Δh_{dyn} the total reaction heat released during the dynamic post-curing part of the experiment.

4. Results and discussion

4.1. Thermal curing

Figure 2 shows the heat flow and the degree of conversion calculated using Equation (1) (see the inset in the figure) versus the temperature of neat DGEBA and DGEBA modified with 5 and 10% of PS-10, at a heating rate of 2.5°C/min. First of all, it must be noted that the curing process is complex, as detected by the presence of more than one peak in the thermograms and the changing slope in the conversion curves (see inset). On increasing the proportion of PS-10, the process broadens and extends to higher temperatures. However, the temperature of the first peak is hardly modified, while the second one moves towards higher temperatures on increasing

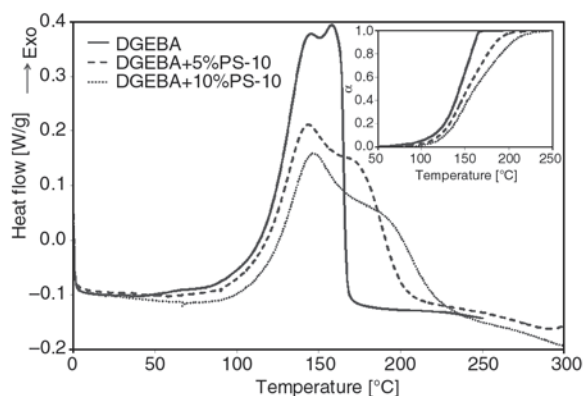


Figure 2. Heat flow and degree of conversion (as an inset) of the thermal curing at 2.5°C/min of neat DGEBA and DGEBA modified with different proportions of PS-10

the proportion of PS-10 and it becomes a shoulder. This is also observed in the conversion curves as a progressive retardation as the degree of conversion increases. The presence of two peaks can be rationalized in terms of the competition between two different propagation mechanisms, the activated chain-end (ACE) and the activated monomer (AM), which are described for cationic ring-opening polymerization. It is reported that the AM mechanism produces a proton-transfer reaction between a hydroxyl group and an activated epoxy group, which prevents subsequent chain growth and generates a new active species and growing chain, so a lower degree of crosslinking can be expected. In the absence of hydroxyl groups, the cationic epoxy curing only takes place via the ACE mechanism. In the ACE mechanism, propagation takes place through the reaction of epoxy groups with the active oxonium ion at the chain end [32]. In our case, the first peak can be related to AM mechanism and the second one with the ACE mechanism, since the first exotherm has a higher relative intensity than the second exotherm when hydroxyl content increases (see Table 1). Upon addition of a hydroxylic compound to the system, such as methanol, the first peak increases and this confirms that AM mechanism is the main process during this peak. As seen in Table 1, the number of hydroxyl groups increases with PS-10 proportion, then one would expect that the addition of PS-10 accelerated the thermal curing but the opposite effect is observed. The second curing exotherm, associated with the ACE propagation mechanism, is retarded due to the presence of PS-10, which suggests that PS-10 may participate in

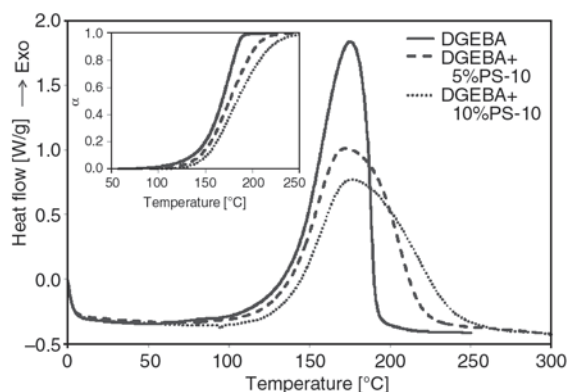


Figure 3. Heat flow and degree of conversion (as an inset) of the thermal curing at 10°C/min of neat DGEBA and DGEBA modified with different proportions of PS-10

the curing process leading to either less mobile or less active propagating species.

At the other heating rates analyzed, the thermogram of the neat DGEBA only presents one peak (see Figure 3, corresponding to a heating rate of 10°C/min) and the thermograms of the modified systems present only a shoulder. Although two maxima cannot be observed, it is expected that both mechanisms, AM and ACE, compete in a similar way as observed at low heating rates. This can be clearly appreciated in the inset of Figure 3, where it is observed the same behaviour as at the lower heating rates.

Table 1 shows that the reaction heat of all formulations (in kJee⁻¹), obtained as the average of the reaction heat at different heating rates, is almost the same and close to the reference value of 100 kJee⁻¹ for epoxy formulations [33]. This suggests that complete curing is reached for all formulations and that the presence of the multi-arm star polymer does not have any effect on the completion of the thermal cure.

Table 2 shows the results of the isoconversional analysis of the thermal curing of the different formulations, using Equation (5). In the neat DGEBA and the DGEBA modified with 5% of PS-10 the activation energy increases with degree of conversion until $\alpha = 0.9$, after which it remains fairly constant. When DGEBA is modified with 10% of PS-10 the activation energy always increases with the degree of conversion. Until $\alpha = 0.4$ the values of the activation energy for the different systems are very similar, but after this degree of conversion, the increase of activation energy with PS-10 proportion

Table 2. Activation energy and pre-exponential factor of the thermal curing of DGEBA modified with different proportions of PS-10 at different degrees of conversion

% PS-10		$\alpha = 0.05$	$\alpha = 0.1$	$\alpha = 0.2$	$\alpha = 0.3$	$\alpha = 0.4$	$\alpha = 0.5$	$\alpha = 0.6$	$\alpha = 0.7$	$\alpha = 0.8$	$\alpha = 0.9$	$\alpha = 0.95$
0	E [kJ/mol]	74.8	79.7	83.7	85.5	86.9	88.4	91.0	94.5	97.8	99.6	98.6
	k_0 [s ⁻¹]	$7.59 \cdot 10^5$	$2.70 \cdot 10^6$	$7.90 \cdot 10^6$	$1.33 \cdot 10^7$	$1.94 \cdot 10^7$	$2.99 \cdot 10^7$	$5.96 \cdot 10^7$	$1.48 \cdot 10^8$	$3.50 \cdot 10^8$	$5.50 \cdot 10^8$	$4.38 \cdot 10^8$
5	E [kJ/mol]	79.4	81.8	85.4	87.9	91.1	96.7	104.9	114.6	123.6	130.0	129.7
	k_0 [s ⁻¹]	$1.47 \cdot 10^6$	$3.11 \cdot 10^6$	$8.95 \cdot 10^6$	$1.81 \cdot 10^7$	$4.19 \cdot 10^7$	$1.70 \cdot 10^8$	$1.30 \cdot 10^9$	$1.33 \cdot 10^{10}$	$1.02 \cdot 10^{11}$	$3.52 \cdot 10^{11}$	$2.32 \cdot 10^{11}$
10	E [kJ/mol]	76.5	81.6	86.2	89.0	93.3	101.6	115.1	132.9	152.4	170.4	182.7
	k_0 [s ⁻¹]	$3.86 \cdot 10^5$	$1.94 \cdot 10^6$	$7.68 \cdot 10^6$	$1.64 \cdot 10^7$	$4.82 \cdot 10^7$	$3.74 \cdot 10^8$	$9.50 \cdot 10^9$	$6.26 \cdot 10^{11}$	$5.16 \cdot 10^{13}$	$1.96 \cdot 10^{15}$	$1.85 \cdot 10^{16}$

is considerable. Activation energy is higher at higher star polymer content, in agreement with the decelerative effect of the modifier on the kinetics of thermal curing. The observed increase in activation energy during curing, which is more pronounced in formulations with 10% of PS-10, should be attributed to either a change in the curing mechanism by the participation of PS-10, leading to less active propagating species, or mobility restrictions occurring as a consequence of the participation of PS-10, rather than simply a change in the balance between the AM and ACE mechanisms due to the different hydroxyl content of the formulations.

In Table 2 the values of the preexponential factor using the R_3 model has also been reported. From the values of the activation energy and the preexponential factor the kinetic constant at 160°C and $\alpha = 0.5$ has been calculated using the Arrhenius equation and these values are collected in Table 1. In agreement with the results presented in Figures 2 and 3, the kinetic constant decreases significantly on increasing the content in star polymer. These values are smaller than those found when a multiarm star poly(glycidol)-b-poly(ϵ -caprolactone) polymer was used as modifier [27]. It is hypothesized that the higher rigidity of the poly(styrene) core in comparison with the poly(glycidol) core can justify the observed differences between both modifiers, leading to more mobility restrictions caused by the participation of PS-10 in the curing process. However, on the basis of the results so far, in which PS-10 participates in a different way, the formation of a less active species should not be discarded.

In Table 1 the ultimate glass transition temperatures of the different systems are reported. The ultimate glass transition temperature is lower than the predicted by the Fox equation [34] and other common mixing rules. This indicates a strong modification of the structure of the epoxy matrix on samples thermally cured containing PS-10. Before curing, the star polymer has a compact structure due to the large

number of intermolecular H-bonds and intramolecular H-bond interactions. These types of interactions decrease when the terminal hydroxyl groups react with the epoxy groups. The PS-10 molecules incorporated into the network increase the free volume and reduce considerably the crosslinking density and consequently the T_g of the cured materials, even below the T_g calculated with Fox equation and other common mixing rules. The difference between $T_{g\infty}$ and the calculated T_g is much lower in the case of DGEBA modified with 10% of PS-10. Probably, this behaviour can be related to the fact that in some extent a part of OH groups in PS-10, in formulations containing a 10% of PS-10, are not completely covalently bonded to the epoxy matrix.

4.2. Photocuring

Figure 4 shows the heat flow and the degree of conversion (see inset) versus the photocuring time of DGEBA and DGEBA modified with different proportions of PS-10 at 120°C. Although the modified systems have a higher proportion of photoinitiator, PS-10 produces a strong deceleration of the photocuring process. In the case of neat DGEBA, vitri-

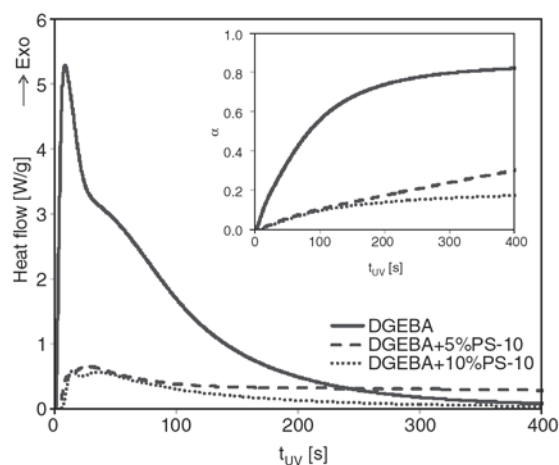


Figure 4. Heat flow and degree of conversion (as an inset) of the photocuring process of neat DGEBA and DGEBA modified with different proportions of PS-10 at 120°C

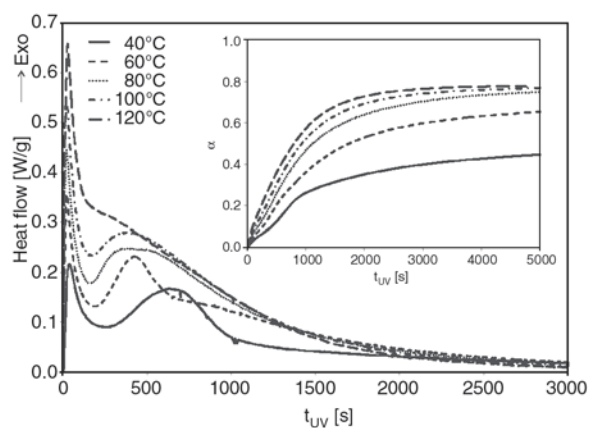
Table 3. Values of Δh_{iso} in kJ/ee for the photocuring of DGEBA modified with different proportions of PS-10 and temperatures

% PS-10	40°C	60°C	80°C	100°C	120°C
0	55.3	67.3	75.5	80.8	85.3
5	46.3	66.0	74.2	75.3	75.9
10					19.4

Table 4. Values of α_{iso} for the photocuring of DGEBA modified with different proportions of PS-10 and temperatures

% PS-10	40°C	60°C	80°C	100°C	120°C
0	0.555	0.676	0.758	0.811	0.856
5	0.473	0.674	0.759	0.770	0.776
10					0.196

fication was achieved at the end of the 30 min of irradiation time. However, in the case of DGEBA with 5% of PS-10, the photocuring process needed to be extended to longer irradiation times (see Figure 4), as described in the experimental section, in order to reach vitrification. As can be seen in Tables 3 and 4, the values of Δh_{iso} (isothermal curing heat) and α_{iso} (degree of conversion after the photocuring experiment) are only slightly lower than the attained ones when the formulation is the neat DGEBA. The photocuring process practically ends at the same time in the case of neat formulation and DGEBA modified with 10% of PS-10, as it can be appreciated from the inset of Figure 4. But, as observed in Tables 3 and 4, the values of Δh_{iso} and α_{iso} for the modified system at 120°C are much smaller than the corresponding to neat DGEBA. The heat of reaction is very low for temperatures below 120°C for DGEBA modified with 10% of PS-10 which indicates that the formulations with 10% of PS-10 hardly react even at high temperatures, whereas photocuring of neat DGEBA is near complete and only restricted by vitrification. For all these reasons the photocuring process of DGEBA modified with 5% of PS-10 has been analyzed as in the case of neat DGEBA. On the other hand, in the case of DGEBA with 10% of PS-10 the kinetics of the photocuring process has not been studied due to the low value of the heat involved in the photocur-

**Figure 5.** Heat flow and degree of conversion (as an inset) of the photocuring process of DGEBA modified with 5% of PS-10 at different temperatures

ing and only the kinetics of a subsequent thermal post-curing has been analyzed instead.

Figure 5 shows the heat flow and the degree of conversion (see inset) versus the photocuring time of DGEBA with 5% of PS-10 at different temperatures. As usually reported for other photocuring systems [35], at the beginning of the process the heat flow and the degree of conversion increase with temperature. At the lower temperatures two peaks appear, probably related to the existence of two propagation mechanisms, AM and ACE. The time corresponding to the second peak decreases on increasing the temperature. At 120°C this second peak disappears and it becomes a shoulder of the main peak.

The kinetics of the photocuring process for neat DGEBA and DGEBA with 5% of PS-10 between 80 and 120°C has been analyzed using the isoconversional methodology explained above. Using Equation (7), the activation energy for every degree of conversion has been found. The results are collected in Table 5. While for neat DGEBA formulation the activation energy increases with the degree of conversion, when a 5% of PS-10 is added the activation energy fluctuates, reaching slightly different values than the neat formulation. The different behaviour in the curing of both formulations can be explained by the complex influence of the time-dependent irradiation and subsequent photoinitia-

Table 5. Activation energy of the photocuring of DGEBA and DGEBA modified with 5% of PS-10 at different degrees of conversion

% PS-10	$\alpha = 0.05$	$\alpha = 0.1$	$\alpha = 0.2$	$\alpha = 0.3$	$\alpha = 0.4$	$\alpha = 0.5$	$\alpha = 0.6$
0	8.3	8.1	10.3	14.0	15.9	16.8	17.3
5	12.4	18.5	13.9	10.9	9.5	9.7	11.7

tion in the photocuring process, which is not, in consequence, only a temperature-dependent process [36]. It can also be hypothesized that the presence of PS-10 may interfere with the curing process, resulting in the formation of different active species, as discussed below. The competition between AM and ACE mechanism and the different protogenic nature of the reaction medium can also help to explain the observed differences [37].

Figures 6 and 7 show the heat flow of the dynamic postcuring experiment of neat DGEBA and the formulation with 5% of PS-10, respectively, made after the photocuring experiences at the temperatures indicated. In the case of neat DGEBA (Figure 6), it can be observed that the post-curing process begins at temperatures above the temperature of isothermal photocuring and shows two maxima that appear at the lower temperatures (40, 60 and 80°C). The height of the first one decreases on increasing the curing temperature. At 100°C this first peak becomes a shoulder and at 120°C this shoulder completely disappears. The height of the

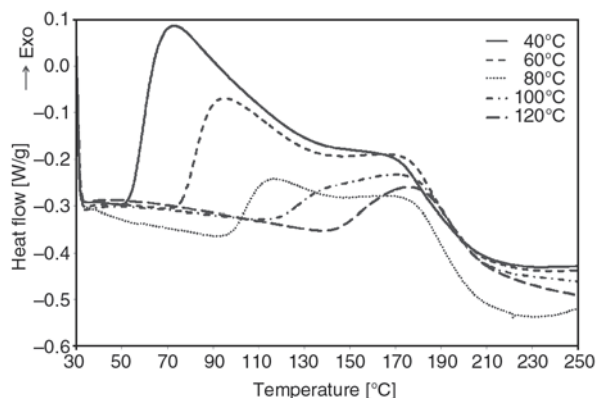


Figure 6. Dynamic postcuring of neat DGEBA after photocuring process at different temperatures

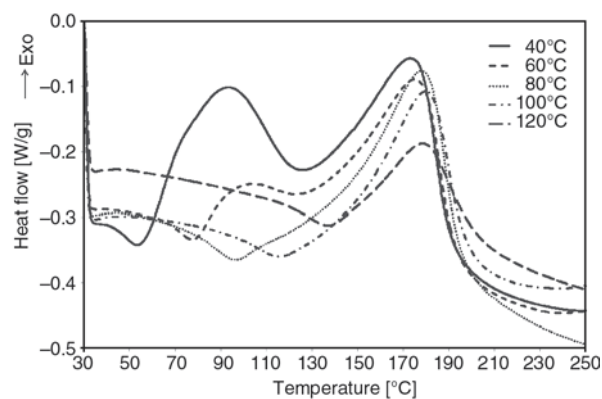


Figure 7. Dynamic postcuring of DGEBA modified with 5% of PS-10 after photocuring process at different temperatures

second peak hardly varies, because its temperature is higher than that of the photocuring process. The first exotherm, which starts at a temperature close to the photocuring temperature [38], can be associated with the propagation of active species formed during photocuring and entrapped in the vitrified material, and the second one with the propagation of less mobile species after structural relaxation of the network [39] or reactivation of dormant tertiary oxonium cations by increasing the temperature [32]. When DGEBA is modified with 5% of PS-10, a glass transition is clearly observed before the onset of the first exothermic peak, which is displaced towards higher temperatures when photocuring temperature increases (Figure 7). At the lower temperatures (40 and 60°C) two peaks appear. The first one becomes a shoulder at 80°C and at higher temperatures it disappears. The height of the second peak decreases on increasing the temperature. With the exception of the curve registered after a photocuring at 40°C, the size of the second peak is always larger than that of the first peak. However, in the case of neat DGEBA, the size of the first peak is higher than the second peak at the lower temperatures (see Figure 6). Although the nature of two peaks in 5% of PS-10 formulation is expected to be the same as in the neat formulation, the high intensity of the second peak for all photocuring temperatures suggests the formation of a dormant species during photocuring, which can be reactivated when the temperature increases (during second peak). It was previously described that the presence of nitrogen in the chemical structure of the epoxy monomers prevents photopolymerization or photocrosslinking reaction to occur. The degree of retardation depends both on the amount and basicity of the amine concerned [40]. Thus, the presence of nitrogen in the structure of stars could be the reason for the inactivation of the photocuring process, because nitrogen atoms in the form of tertiary amine can interact with the protons generated by the irradiation on the photocuring initiator, producing ammonium salts, because of their basic character. However, it should be commented that the study was done with monomers containing nitrogen in the structure, which leads to a high proportion of this heteroatom in the mixtures and no reactivation by heating of the sample was tested. Endo and Sanda [41] reported that benzyl ammonium salts can act as latent thermal initiators. Thus, it seems reasonable that the inacti-

vation of the photocuring process by the presence of benzylic amine moieties in the multiarm star structure can be followed by the reactivation at high temperature by the breakage of the benzylic ammonium salt. This breakage produces benzylic cations capable of initiating the thermal cationic polymerization of epoxides. The low nucleophilicity of the anion, hexafluoroantimonate, helps to increase the reactivity of these species.

The *in situ* generation of a thermal initiator by a photoirradiation process by addition of the PS-10 stars to the epoxy formulation opens the way to a new dual curing system, related to another previously described [42]. In that case, the responsible of the dual behaviour was the presence of a hyperbranched modifier in the formulation with thioether as repeating unit, which can be transformed into alkyl sulfonium species upon photolysis of the photoinitiator. Sulfonium cations can also act as cationic thermal latent initiators. However, the structure of the hyperbranched modifier with a huge proportion of thioether groups in the modifier structure led to a higher functionality as macroinitiator, which is not the case of the star structures, having an only benzylamine group per arm.

Figure 8 shows the heat flow and the relative conversion degree (as an inset) of the postcuring scan at different heating rates, made after photocuring samples of DGEBA with 10% of PS-10 at 120°C

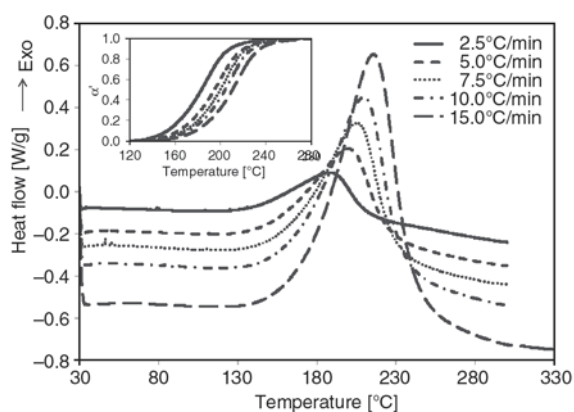


Figure 8. Dynamic postcuring (after UV irradiation) at different heating rates and relative conversion degree (as an inset) of DGEBA modified with 10% of PS-10

Table 6. Activation energy and pre-exponential factor of the thermal curing of DGEBA modified with 10% of PS-10 after photocuring at 120°C at different relative conversion degrees

	$\alpha' = 0.05$	$\alpha' = 0.1$	$\alpha' = 0.2$	$\alpha' = 0.3$	$\alpha' = 0.4$	$\alpha' = 0.5$	$\alpha' = 0.6$	$\alpha' = 0.7$	$\alpha' = 0.8$	$\alpha' = 0.9$	$\alpha' = 0.95$
E [kJ/mol]	119.4	114.8	112.9	114.3	117.0	120.0	123.2	126.4	130.5	139.1	148.1
k_0 [s ⁻¹]	$1.45 \cdot 10^{10}$	$4.07 \cdot 10^9$	$2.25 \cdot 10^9$	$2.91 \cdot 10^9$	$5.32 \cdot 10^9$	$1.06 \cdot 10^{10}$	$2.15 \cdot 10^{10}$	$4.32 \cdot 10^{10}$	$1.00 \cdot 10^{11}$	$5.44 \cdot 10^{11}$	$2.61 \cdot 10^{12}$

for 30 min. It can be observed that only one strong peak appears at high temperature. When the same formulation was thermally cured without previous UV-irradiation, the thermogram did not show any exotherm. These results suggest, as it had been hypothesized, that in presence of PS-10, UV irradiation promotes the formation of a thermal macroinitiator (dormant species), by reaction between the amine groups of PS-10 and the proton resulting from the photolysis of the photoinitiator upon irradiation, which can be subsequently activated by heating. However, this curing system shows a small latency since the slope of the stimulation-activity curve is small (see inset in Figure 8) [41].

Table 6 shows the results of the isoconversional analysis based on DSC thermograms of Figure 8. Using Equation (5), the activation energy has been found for some values of relative conversion degrees. This magnitude first decreases, but after $\alpha' = 0.2$ it increases. The high activation energy values obtained in comparison with those obtained during photocuring (Table 5) suggests again the formation of dormant species during UV irradiation which can act as thermal initiator upon heating. In the same table the values of the preexponential factor using R_3 model are also collected.

Table 1 shows the $T_{g\infty}$ of DGEBA with 5% of PS-10. These values are lower than those calculated using common mixing rules, indicating a modification of the structure of the epoxy matrix. However, the difference between $T_{g\infty}$ and the calculated T_g is smaller than in the case of the thermal curing. As it has been stated, the number of intermolecular and intramolecular H-bond interactions and the degree of chemical incorporation of PS-10 to the epoxy matrix, can justify the differences between the experimental and calculated $T_{g\infty}$. The value of the $T_{g\infty}$ of DGEBA with 10% of PS-10 is also smaller than the calculated ones, indicating a structural modification of the epoxy matrix. In fact, the breakage of the star structure by formation of benzylic cations should lead to the separation of the arms from the hyperbranched core. This process can occur to some extent, but should produce a plasticization of the matrix that counteracts the effect of the multifunc-

tional character of the benzylic hyperbranched initiator formed. Although the reason of this behaviour can be rationalized in a similar way to 5% PS-10 formulation, the fact that some part of PS-10 phase separates during curing, (as it will be seen later by scanning electron microscopy) can probably have an influence on the $T_{g\infty}$ value. The values of $T_{g\infty}$ found after photocuring are higher than those found after thermal curing (Table 1), because ytterbium triflates are able to induce reorganization, cyclization and/or degradation reactions when the curing reaches too high temperatures, which results in a network structure with a lower degree of crosslinking and consequently with a lower $T_{g\infty}$ [43, 44].

4.3. Fracture morphology by SEM

The topography of photocured and postcured samples of neat DGEBA and DGEBA with 10% of PS-10 have been investigated by SEM. The microphotographs of the fracture surface are collected in Figure 9 and 10, respectively. The existence of an only homogeneous phase in the neat DGEBA and the presence of two phases in DGEBA with 10% of PS-10 can be observed. This material shows a rougher appearance than the neat formulation, based on rod-like particles with a size of ca 50–500 nm homogeneously dispersed. It is worth to state that thermally cured samples do not show evidences of a second phase. So, it is expected that PS-10 modifier can improve the fracture properties of DGEBA by a phase-separation mechanism, only when the material is previously UV irradiated.



Figure 9. Surface morphology obtained by SEM of neat DGEBA

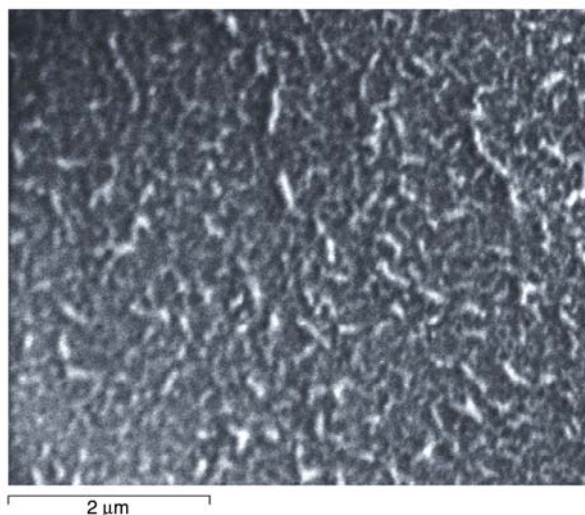


Figure 10. Surface morphology obtained by SEM of DGEBA modified with 10% of PS-10

5. Conclusions

PS-10 decelerates the thermal curing of DGEBA, modifying significantly the structure of the epoxy matrix in terms of ultimate glass transition temperature. PS-10 also decelerates the photocuring process of DGEBA but in a different way. With a 5% of PS-10, the process is significantly delayed but can proceed to vitrification, as in modified DGEBA. With a 10% of PS-10 the photocuring is strongly limited and it is necessary a subsequent thermal curing to reticulate the sample. The decelerating effect on the photocuring process is explained in terms of the formation of dormant species by protonation of the amine groups in the multiarm star molecule. The benzylic ammonium salts formed are reactivated upon heating, thus acting as a thermal initiator. Thus the addition of PS-10 to the epoxy formulation leads to a new dual photo-thermal curing system. Upon irradiation a benzylic cationic multifunctional initiator is formed, which can act a thermal curing system. In the photocuring process the addition of PS-10 also modifies the structure of the epoxy matrix, but in a lower extent than in the thermal curing.

Depending on the initiation conditions, thermal or UV induced, and on the amount of PS-10 it is possible to obtain tailor-made thermosets with different thermal and mechanical properties and morphology. The resulting morphology of DGEBA/PS-10 formulations UV-cured is that of nanosize ‘rod-like’ of homogeneously dispersed particles in the epoxy matrix, with a potential capacity of increasing toughness of UV-cured DGEBA thermosets.

Acknowledgements

The authors would like to thank MICINN (Ministerio de Ciencia e Innovación) and FEDER (Fondo Europeo de Desarrollo Regional) (MAT2011-27039-C03-01 and MAT2011-27039-C03-02) and to the Comissionat per a Universitats i Recerca del DIUE de la Generalitat de Catalunya (2009-SGR-1512). M.M. acknowledges the grant FI-DGR (2009) from the Catalanian Government. X.F.F. acknowledges the grant JCI-2010-06187 from the Spanish Government.

References

- [1] May C. A.: Introduction to epoxy resins. in 'Epoxy resins. Chemistry and technology' (ed.: May C. A.) Marcel Dekker, New York 1–8 (1988).
- [2] Petrie E. M.: Epoxy adhesive formulations. McGraw-Hill, New York (2006).
- [3] Pascault J. P., Williams R. J. J.: Epoxy polymers: New materials and innovations. Wiley-VCH, Weinheim (2010).
- [4] Kinloch A. J., Shaw S. J., Tod D. A., Hunston D. L.: Deformation and fracture behaviour of a rubber-toughened epoxy: 1. Microstructure and fracture studies. *Polymer*, **24**, 1341–1354 (1983).
DOI: [10.1016/0032-3861\(83\)90070-8](https://doi.org/10.1016/0032-3861(83)90070-8)
- [5] Ho T-H., Wang C-S.: Toughening of epoxy resins by modification with dispersed acrylate rubber for electronic packaging. *Journal of Applied Polymer Science*, **50**, 477–483 (1993).
DOI: [10.1002/app.1993.070500311](https://doi.org/10.1002/app.1993.070500311)
- [6] Mezzenga R., Boogh L., Månson J-A. E.: A review of dendritic hyperbranched polymer as modifiers in epoxy composites. *Composites Science and Technology*, **61**, 787–795 (2001).
DOI: [10.1016/S0266-3538\(01\)00022-7](https://doi.org/10.1016/S0266-3538(01)00022-7)
- [7] Guo Q., Habrard A., Park Y., Halley P. J., Simon G. P.: Phase separation, porous structure, and cure kinetics in aliphatic epoxy resin containing hyperbranched polyester. *Journal of Polymer Science Part B: Polymer Physics*, **44**, 889–899 (2006).
DOI: [10.1002/polb.20757](https://doi.org/10.1002/polb.20757)
- [8] Ratna D., Varley R., Simon G. P.: Toughening of tri-functional epoxy using an epoxy-functionalized hyperbranched polymer. *Journal of Applied Polymer Science*, **89**, 2339–2345 (2003).
DOI: [10.1002/app.12059](https://doi.org/10.1002/app.12059)
- [9] He S., Shi K., Bai J., Zhang Z., Li L., Du Z., Zhang B.: Studies on the properties of epoxy resins modified with chain-extended ureas. *Polymer*, **42**, 9641–9647 (2001).
DOI: [10.1016/S0032-3861\(01\)00450-5](https://doi.org/10.1016/S0032-3861(01)00450-5)
- [10] Evans D., Canfer S. J.: Radiation stable, low viscosity impregnating resin systems for cryogenic applications. *Advances in Cryogenic Engineering Materials*, **46**, 361–368 (2000).
DOI: [10.1007/978-1-4615-4293-3_46](https://doi.org/10.1007/978-1-4615-4293-3_46)
- [11] Ueki T., Nishijima S., Izumi Y.: Designing of epoxy resin systems for cryogenic use. *Cryogenics*, **45**, 141–148 (2005).
DOI: [10.1016/j.cryogenics.2004.07.002](https://doi.org/10.1016/j.cryogenics.2004.07.002)
- [12] Nishijima S., Honda Y., Okada T.: Application of the positron annihilation method for evaluation of organic materials for cryogenic use. *Cryogenics*, **35**, 779–781 (1995).
DOI: [10.1016/0011-2275\(95\)90913-Z](https://doi.org/10.1016/0011-2275(95)90913-Z)
- [13] Morell M., Ramis X., Ferrando F., Serra A.: Effect of polymer topology on the curing process and mechanical characteristics of epoxy thermosets modified with linear or multiarm star poly(ϵ -caprolactone). *Polymer*, **52**, 4694–4702 (2011).
DOI: [10.1016/j.polymer.2011.07.040](https://doi.org/10.1016/j.polymer.2011.07.040)
- [14] Riew C. K., Siebert A. R., Smith R. W., Fernando M., Kinloch A. J.: Toughened epoxy resins: Preformed particles as tougheners for adhesives and matrices. in: 'Toughened plastics II' (eds.: Riew C. K., Kinloch A. J.) American Chemical Society, Washington, *Advances in Chemical Series Vol 252*, 33–44 (1996).
DOI: [10.1021/ba-1996-0252.ch003](https://doi.org/10.1021/ba-1996-0252.ch003)
- [15] Wu S.: Phase structure and adhesion in polymer blends: A criterion for rubber toughening. *Polymer*, **26**, 1855–1863 (1985).
DOI: [10.1016/0032-3861\(85\)90015-1](https://doi.org/10.1016/0032-3861(85)90015-1)
- [16] Pearson R. A., Yee A. F.: Toughening mechanisms in thermoplastic-modified epoxies: 1. Modification using poly(phenylene oxide). *Polymer*, **34**, 3658–3670 (1993).
DOI: [10.1016/0032-3861\(93\)90051-B](https://doi.org/10.1016/0032-3861(93)90051-B)
- [17] Hedrick J. L., Yilgor I., Jurek M., Hedrick J. C., Wilkes G. L., McGrath J. E.: Chemical modification of matrix resin networks with engineering thermoplastics: 1. Synthesis, morphology, physical behaviour and toughening mechanisms of poly(arylene ether sulphone) modified epoxy networks. *Polymer*, **32**, 2020–2032 (1991).
DOI: [10.1016/0032-3861\(91\)90168-I](https://doi.org/10.1016/0032-3861(91)90168-I)
- [18] Wilkinson S. P., Ward T. C., McGrath J. E.: Effect of thermoplastic modifier variables on toughening a bis-maleimide matrix resin for high-performance composite materials. *Polymer*, **34**, 870–884 (1993).
DOI: [10.1016/0032-3861\(93\)90376-L](https://doi.org/10.1016/0032-3861(93)90376-L)
- [19] Kunz S. C., Sayre J. A., Assink R. A.: Morphology and toughness characterization of epoxy resins modified with amine and carboxyl terminated rubbers. *Polymer*, **23**, 1897–1906 (1982).
DOI: [10.1016/0032-3861\(82\)90215-4](https://doi.org/10.1016/0032-3861(82)90215-4)
- [20] Voit B.: New developments in hyperbranched polymers. *Journal of Polymer Science Part A: Polymer Chemistry*, **38**, 2505–2525 (2000).
DOI: [10.1002/1099-0518\(20000715\)38:14<2505::AID-POLA10>3.0.CO;2-8](https://doi.org/10.1002/1099-0518(20000715)38:14<2505::AID-POLA10>3.0.CO;2-8)
- [21] Sörensen K., Pettersson B. O., Boogh L., Månson J-A. E.: Dendritic polyester macromolecule in thermosetting resin matrix. PCT Patent SE94/04440, Sweden (1994).
- [22] Zhang Y., Zhang D., Qin C., Xu J.: Physical and mechanical properties of dental nanocomposites composed of aliphatic epoxy resin and epoxidized aromatic hyperbranched polymers. *Polymer Composites*, **30**, 176–181 (2009).
DOI: [10.1002/pc.20549](https://doi.org/10.1002/pc.20549)

- [23] Fernández-Francos X., Salla J. M., Cadenato A., Morancho J. M., Serra A., Mantecón A., Ramis X.: A new strategy for controlling shrinkage of DGEBA resins cured by cationic copolymerization with hydroxyl-terminated hyperbranched polymers and ytterbium triflate as an initiator. *Journal of Applied Polymer Science*, **111**, 2822–2829 (2009). DOI: [10.1002/app.29317](https://doi.org/10.1002/app.29317)
- [24] Morancho J. M., Cadenato A., Ramis X., Fernández-Francos X., Salla J. M.: Thermal curing and photocuring of an epoxy resin modified with a hyperbranched polymer. *Thermochimica Acta*, **510**, 1–8 (2010). DOI: [10.1016/j.tca.2010.05.008](https://doi.org/10.1016/j.tca.2010.05.008)
- [25] Morancho J. M., Cadenato A., Ramis X., Fernández-Francos X., Flores M., Salla J. M.: Effect of a hyperbranched polymer over the thermal curing and the photocuring of an epoxy resin. *Journal of Thermal Analysis and Calorimetry*, **105**, 479–488 (2011). DOI: [10.1007/s10973-010-1277-8](https://doi.org/10.1007/s10973-010-1277-8)
- [26] Morell M., Foix D., Lederer A., Ramis X., Voit B., Serra A.: Synthesis of a new multiarm star polymer based on hyperbranched poly(styrene) core and poly(ϵ -caprolactone) arms and its use as reactive modifier of epoxy thermosets. *Journal of Polymer Science Part A: Polymer Chemistry*, **49**, 4639–4649 (2011). DOI: [10.1002/pola.24908](https://doi.org/10.1002/pola.24908)
- [27] Morancho J. M., Cadenato A., Ramis X., Morell M., Fernández-Francos X., Salla J. M., Serra A.: Thermal curing and photocuring of a DGEBA modified with multiarm star poly(glycidol)-*b*-poly(ϵ -caprolactone) polymers of different arm lengths. *Journal of Thermal Analysis and Calorimetry*, in press (2013). DOI: [10.1007/s10973-012-2919-9](https://doi.org/10.1007/s10973-012-2919-9)
- [28] Doyle C. D.: Series approximations to the equation of thermogravimetric data. *Nature*, **207**, 290–291 (1965). DOI: [10.1038/207290a0](https://doi.org/10.1038/207290a0)
- [29] Ozawa T.: A new method of analyzing thermogravimetric data. *Bulletin of the Chemical Society of Japan*, **38**, 1881–1886 (1965). DOI: [10.1246/bcsj.38.1881](https://doi.org/10.1246/bcsj.38.1881)
- [30] González S., Fernández-Francos X., Salla J. M., Serra A., Mantecón A., Ramis X.: New thermosets obtained by cationic copolymerization of DGEBA with γ -caprolactone with improvement in the shrinkage. II. Time-temperature-transformation (TTT) cure diagram. *Journal of Applied Polymer Science*, **104**, 3406–3416 (2007). DOI: [10.1002/app.26021](https://doi.org/10.1002/app.26021)
- [31] Morancho J. M., Cadenato A., Fernández-Francos X., Salla J. M., Ramis X.: Isothermal kinetics of photopolymerization and thermal polymerization of bis-GMA/TEGDMA resins. *Journal of Thermal Analysis and Calorimetry*, **92**, 513–522 (2008). DOI: [10.1007/s10973-007-8432-x](https://doi.org/10.1007/s10973-007-8432-x)
- [32] Matějka L., Chabanne P., Tighzert L., Pascault J. P.: Cationic polymerization of diglycidyl ether of bisphenol A. *Journal of Polymer Science Part A: Polymer Chemistry*, **32**, 1447–1458 (1994). DOI: [10.1002/pola.1994.080320806](https://doi.org/10.1002/pola.1994.080320806)
- [33] Leonard J.: Heats and entropies of polymerization, ceiling temperatures, equilibrium monomer concentrations, and polymerizability of heterocyclic compounds. in 'Polymer handbook' (eds.: Brandrup J., Immermut E. H., Grulke E. A.), Wiley-Interscience, New York, Vol 1, II/363–II/414 (1999).
- [34] Wood L. A.: Glass transition temperatures of copolymers. *Journal of Polymer Science*, **28**, 319–330 (1958). DOI: [10.1002/pol.1958.1202811707](https://doi.org/10.1002/pol.1958.1202811707)
- [35] Fernández-Francos X., Salla J. M., Cadenato A., Morancho J. M., Mantecón A., Serra A., Ramis X.: Influence of the initiating mechanism on the cationic photopolymerization of a cycloaliphatic epoxy resin with arylsulfonium salts. *Journal of Polymer Science Part A: Polymer Chemistry*, **45**, 16–25 (2007). DOI: [10.1002/pola.21811](https://doi.org/10.1002/pola.21811)
- [36] Tryson G. R., Shultz A. R.: A calorimetric study of acrylate photopolymerization. *Journal of Polymer Science: Polymer Physics Edition*, **17**, 2059–2075 (1979). DOI: [10.1002/pol.1979.180171202](https://doi.org/10.1002/pol.1979.180171202)
- [37] Crivello J. V., Bulut U.: Dual photo- and thermally initiated cationic polymerization of epoxy monomers. *Journal of Polymer Science Part A: Polymer Chemistry*, **44**, 6750–6764 (2006). DOI: [10.1002/pola.21791](https://doi.org/10.1002/pola.21791)
- [38] Scott T. F., Cook W. D., Forsythe J. S.: Photo-DSC cure kinetics of vinyl ester resins. I. Influence of temperature. *Polymer*, **43**, 5839–5845 (2002). DOI: [10.1016/S0032-3861\(02\)00490-1](https://doi.org/10.1016/S0032-3861(02)00490-1)
- [39] Chen Z., Webster D. C.: Study of the effect of hyperbranched polyols on cationic UV curable coating properties. *Polymer International*, **56**, 754–763 (2007). DOI: [10.1002/pi.2202](https://doi.org/10.1002/pi.2202)
- [40] Rath S. K., Diby A., Seghier Z., Boey F. Y. C., Abadie M. J. M.: The effect of amines on the UV-curing of epoxy resins. *Iranian Polymer Journal*, **15**, 855–862 (2006).
- [41] Endo T., Sanda F.: Design of latent catalysts and their application to polymer synthesis. *Macromolecular Symposia*, **107**, 237–242 (1996). DOI: [10.1002/masy.19961070123](https://doi.org/10.1002/masy.19961070123)
- [42] Foix D., Ramis X., Serra A., Sangermano M.: UV generation of a multifunctional hyperbranched thermal crosslinker to cure epoxy resins. *Polymer*, **52**, 3269–3276 (2011). DOI: [10.1016/j.polymer.2011.05.029](https://doi.org/10.1016/j.polymer.2011.05.029)
- [43] Fernández-Francos X., Salla J. M., Pérez G., Mantecón A., Serra A., Ramis X.: New thermosets obtained by thermal and UV-induced cationic copolymerization of DGEBA with 4-phenyl- γ -butyrolactone. *Macromolecular Chemistry and Physics*, **210**, 1450–1460 (2009). DOI: [10.1002/macp.200900118](https://doi.org/10.1002/macp.200900118)
- [44] Aspinall H. C., Dwyer J. L. M., Greeves N., McIver E. G., Woolley J. C.: Solubilized lanthanide triflates: Lewis acid catalysis by polyether and poly(ethylene glycol) complexes of Ln(OTf)₃. *Organometallics*, **17**, 1884–1888 (1998). DOI: [10.1021/om9709087](https://doi.org/10.1021/om9709087)

The preparation and physical properties of polysulfide-based elastomers through one-pot thiol-ene click reaction

G. Z. Zhang, Z. K. Fan, Y. W. Quan*, Q. M. Chen

Department of Polymer Science and Engineering, School of Chemistry and Chemical Engineering, State Key-Laboratory of Coordination Chemistry, Nanjing University, 210093 Nanjing, P. R. China

Received 24 January 2013; accepted in revised form 18 March 2013

Abstract. In this paper, polysulfide-based elastomers were successfully prepared through a simple one-pot thiol-ene click reaction of the liquid polysulfide oligomer with bisphenol-A diacrylate resin. Real-time Fourier transform infrared spectroscopy (FTIR) analysis showed that the molecular weight of the liquid polysulfide oligomer had no effect on mercaptan functional group conversion. The obtained elastomers continued to keep low temperature flexibility of polysulfide except Elastomer-LP3, which was due to higher content of bisphenol-A structure. All the samples had a tensile strength of over 0.7 MPa, which was comparable to that of polysulfide polymer cured by metal oxide. Moreover, the samples exhibited higher thermal stability than metal oxide cured polysulfide. This vulcanization methodology will provide a fast, efficient, and environmentally friendly approach (without metal oxides and plasticizers) for preparing polysulfide elastomers.

Keywords: mechanical properties, liquid polysulfide, elastomer, click reaction

1. Introduction

During the last few years, thiol-ene coupling reaction has become a subject of intense study in various areas of science and engineering [1–4]. This reaction, whether proceeding by a free-radical reaction or Michael addition, carries many of the attributes of click reactions as follows: (a) high yields with minimal byproducts, (b) insensitive to ambient oxygen or water, (c) region or stereospecificity, (d) proceeds under mild, solventless reaction conditions. Up to now, thiol-ene chemistry has been effectively applied in a wide range of disciplines, ranging from surface modification [5–6], polymer functionalization [7–9], photolithography and microdevice fabrication [10], high-energy absorbing materials [11–12], applications in biomaterials [13], organic functionalization [14–15], and so on.

Usually, there are four low-molecular-weight thiols typically encountered in literatures, including thio-

phenols [16–17], thiol propionates [5, 7, 10–12], alkyl thiols [7–8] and thiol glycolates [7, 14]. In recent years, some new oligomeric thiols have been synthesized and incorporated into thiol-ene networks, which opens up new applications or provides improved properties. For example, the synthesis of dithiol polyester and its incorporation into thio-ene networks brings a new opportunity for creating semicrystalline networks [18–19]. The use of oligomeric thiols has the distinct advantage of low shrinkage and a reduction in stress during the photopolymerization process [20] or lower glass transition temperatures and more uniform networks [21]. In other work, thiocarbamate oligomers are synthesized to prepare photocured/thermal cured films with high glass transition temperature, excellent hardness and impact values [22].

The present investigation also extends thiol-ene click reaction to a long chain liquid polysulfide (PSF)

*Corresponding author, e-mail: quanyiwu@nju.edu.cn
© BME-PT

oligomer containing terminal thiol groups. Traditionally, the main curing agents for PSF oligomers are metal oxides and other metal oxy-salts, which make use of the reducing properties of the thiol group to cause cross-linking [23]. These cross-linked elastomers derived from PSF oligomers have high resistance to UV radiation and the environment, exhibit good low-temperature properties, low water-vapour transmission, and resist solvents and chemicals. Our earlier works have also studied metal oxide or isocyanate cured polysulfide polymer [24–26] and explore kinetic analysis of polysulfide-acrylate click reaction by dielectric analyzer and dynamic mechanical analyzer [27]. Here, we successfully prepared polysulfide-based elastomers by reacting PSF oligomers with bisphenol-A diacrylate resin through one-pot thiol-Michael addition reaction, in which tris(dimethylaminomethyl)-phenol (DMP-30) was used as a catalyst. The effect of molecular weight and cross-linking agent of PSF oligomers on mechanical and thermal properties of obtained elastomers was discussed in detail.

2. Experimental

2.1. Materials and synthesis

PSF oligomers were supplied by Thiokol Co. Japan (The main properties of the PSF oligomers are listed in Table 1). Bisphenol-A diacrylate resin (VR77, $M_n = 510\text{--}600$) was supplied by Shanghai Showa Highpolymer Co, Shanghai, China. Tris(dimethylamino-methyl)phenol (DMP-30) was commercially available material. All materials were used as received without further purification.

The polysulfide-based elastomers were prepared at the stoichiometric ratio of mercaptan/acrylate. PSF oligomers and bisphenol-A diacrylate resin were completely mixed with 2 wt% DMP-30 by a mechanical stirrer at room temperature and degassed by a Siemens DAC 150FV high-speed mixer by 3000/min (Produced by Hauschild, Wuppertal-Cronenberg, Germany). Then the bubble-free mixture was poured onto the mold of PTFE, and cured at $23\pm 2^\circ\text{C}$ for 5 days.

2.2. Instrumentation and characterization

The ^1H NMR spectra of the samples were obtained on an AVANCE DPX-500 MHz spectrometer (Bruker, Fällanden, Switzerland) in CDCl_3 . Curing behavior of the PSF oligomer and bisphenol-A diacrylate resin was obtained using real-time infrared (RTIR) spectroscopy, which was recorded on a Vector 70 spectrometer (Bruker, Ettlingen, Germany). The samples were coated on a KBr disk at 25°C , and then, the RTIR spectra were collected at a resolution of 2 from $400\text{--}4000\text{ cm}^{-1}$ every 5 min (for LP3 system, the RTIR spectra was collected every 2 min in first 30 minutes) until no further change was observed in the spectra, and the peak at 2570 or 810 cm^{-1} , was used to monitor $\text{C}=\text{C}-\text{H}$ bending or $-\text{SH}$ conversion respectively.

The extraction and swelling tests (HG/T 3870-2008 China) were performed on $20\text{ mm}\times 20\text{ mm}\times 2\text{ mm}$ cut specimen by the immersion method in toluene at 25°C . Thereafter, the test specimen was taken out, blotted with a piece of filter paper, and weighed. After immersion, the samples were dried at 100°C in the vacuum oven for 24 h. The mass of the specimen was measured by electronic digital balance with an accuracy of 0.001 g. Each result was obtained by repeating the test with three specimens. The swelling ratio is defined as: $Q\% = (M_t - M_0)\cdot 100/M_0$, where M_0 and M_t are the mass of the test piece before swelling and after immersion respectively. The gel fraction is defined as: $Ti\% = (M_w/M_0)\cdot 100$, where M_0 is the mass of the test piece before immersion, and M_w is the mass of the dry sample after immersion.

Thermal stability of the polysulfide was characterized by Thermogravimetric Analysis (TG, STA 449 C, NETZSCH, Selb, Germany), at heating rate of $20^\circ\text{C}/\text{min}$ from 25 to 650°C under nitrogen. Dynamic thermal mechanical properties of the samples (tension model) were measured using a DMA-450 (Produced by 01 dB- Metravib Co., Limonest, France) with a frequency of 1 Hz, and heating rate of $3^\circ\text{C}/\text{min}$ from -70 to $+150^\circ\text{C}$. The dimensions of the samples were $10\text{ mm}\times 15\text{ mm}\times 2\text{ mm}$. The tensile

Table 1. The main properties of liquid polysulfide oligomers

Liquid polysulfide oligomers	LP-3	LP-23	LP-980	LP-2	LP-32	LP-55
Average molecular weight	1000	2500	2500	4000	4000	4000
Cross-linking agent*	2%	2%	0.5%	2%	0.5%	0.05%
Mercaptan fraction ($-\text{SH}$)	5.9–7.7%	2.5–3.5%	2.5–3.5%	1.5–2.0%	1.5–2.0%	1.5–2.0%

*In the synthesis of liquid polysulfide oligomers, bis-2-chloroethyl formal is the usually used monomer and 0.05–4% 1,2,3-trichloropropane is added as a cross-linking agent.

properties of samples were measured on an Instron 4466 Universal Materials Testing Machine (produced by Instron Co., Norwood, MA, USA) with a speed of 200 mm/min at 23°C. The cured film in 2 mm thickness was cut into dumb-bell-shaped specimens. Each result was obtained by the test repetition with three specimens.

3. Results and discussion

3.1. Synthesis and characterization

The procedure for the preparation of polysulfide-based elastomers is outlined in Figure 1. This reaction was effectively catalyzed by a tertiary amine DMP-30. The dosage of catalyst was fixed to be 2 wt% of monomers. With more catalyst used, the operating time would be shortened extremely. Usually, this step-growth polymerization (polyaddition) gives linear polymer. However, the cross-linked elastomers are finally obtained due to the branching of PSF oligomers. The reason is that, in the synthe-

sis of PSF oligomers, bis-2-chloroethyl formal is the usually used monomer and 0.05–4% 1,2,3-trichloropropane is added as a cross-linking agent, which produces some branched chains in PSF oligomers. Figure 2 shows ^1H NMR spectra of the mixture of the PSF oligomer LP-55 and bisphenol-A diacrylate resin before and after Michael addition reaction (Here, in order to get soluble product for ^1H NMR analysis, the PSF oligomer with the lowest content of cross-linking agent, LP55 resin, was chosen. Furthermore, the reaction was carried out in the solution of CDCl_3 , and ^1H NMR spectra was investigated before the deposition appeared). In Figure 2, the peaks at 6.18 ppm (multiplet), 5.90 ppm (doublet) and 6.47 ppm (doublet) can be assigned to protons of $\text{CH}_2 = \text{CHCOO-R}$. After the thiol-Michael addition reaction, these characteristic peaks almost disappear in the spectrum (the residual double bond protons calculated from integration are about 5%). Meanwhile, the new peaks around 3.0 ppm attrib-

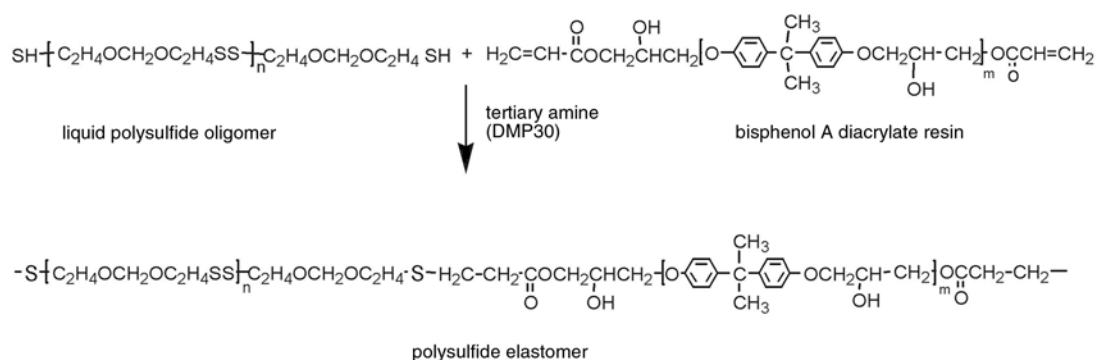


Figure 1. The thiol-Michael addition reaction between the liquid polysulfide oligomer and bisphenol-A diacrylate resin

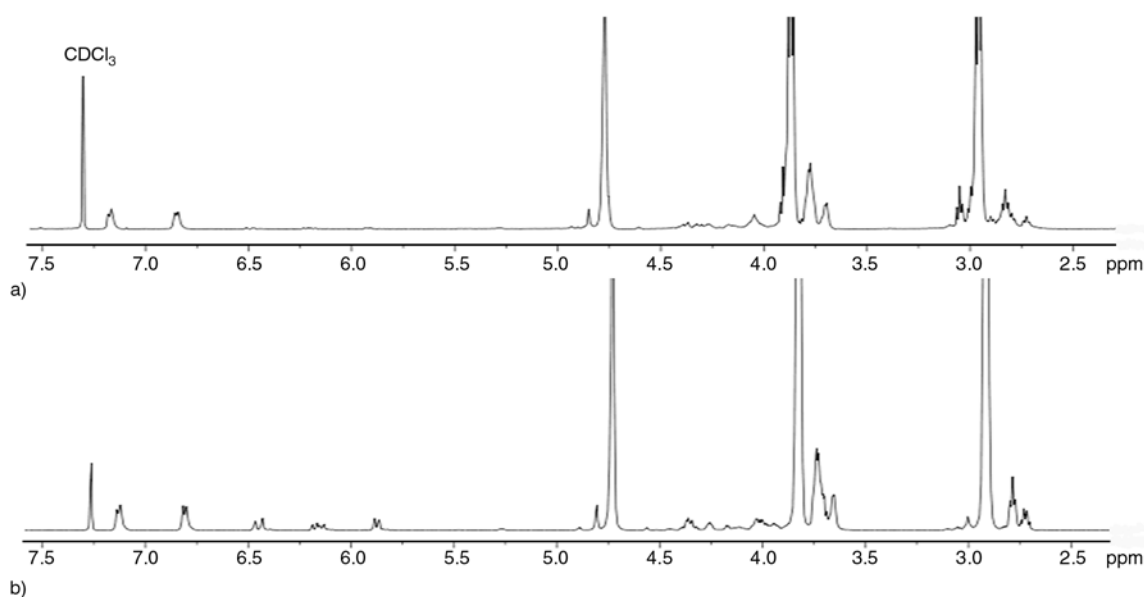


Figure 2. ^1H NMR spectra of the mixture of the liquid polysulfide oligomer and bisphenol-A diacrylate resin before (b) and after (a) Michael addition

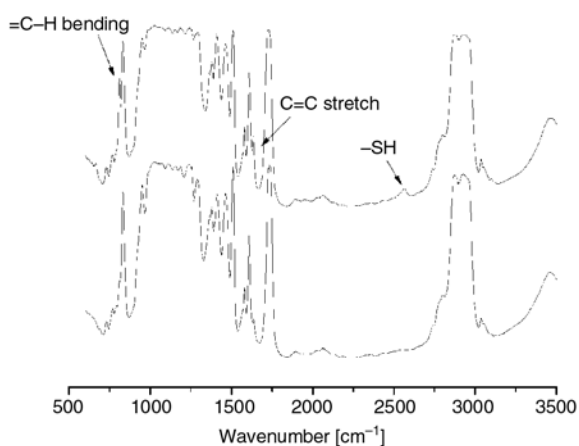


Figure 3. FTIR spectra of the mixture of the liquid polysulfide oligomer and bisphenol-A diacrylate resin before and after Michael addition reaction

uted to the protons of $\text{SCH}_2\text{--CH}_2\text{COO--R}$ appear. Furthermore, the IR spectra of the typical monomer mixture and the resulting elastomer are compared in Figure 3. The monomer mixture has absorption peaks at 1630 and 810 cm^{-1} , attributed to C=C stretching and =C–H bending respectively, which is lacking in the obtained elastomer. The complete loss of thiol (2570 cm^{-1}) in polysulfide resin also can be detected in IR spectra. All these results demonstrate that the essentially quantitative thiol-Michael addition reaction proceeded between the long chain PSF oligomer and bisphenol-A diacrylate resin.

In order to investigate the effect of molecular weight of PSF oligomers on the thiol-ene addition reaction, real-time infrared spectroscopy was used to monitor curing behavior of PSF oligomers and bisphenol-A diacrylate resin. Baseline correction and normalization were carried out by the OPUS software to eliminate the influence of transparency change during the curing process. Figure 4 illustrates the functional group conversions that were calculated according to the intensity change of the peaks (2570 cm^{-1}) as described in the literature [28]. It shows that this

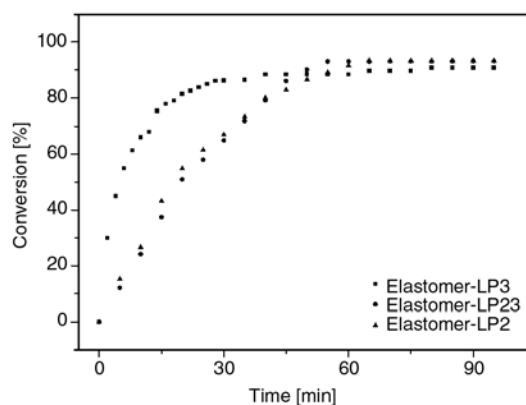


Figure 4. RTIR-based plot (% conversion vs. time) of bisphenol-A diacrylate and liquid polysulfide oligomers with different molecular weight. Peak loss was measured at 2570 cm^{-1} for thiol conversion.

thiol-ene Michael addition was efficient with conversions of about 91% after 1 hour despite of different chain length of PSF oligomers, and the final conversion of all samples reached to 98% after reacting for 24 h. However, the initial reaction rate changed with different molecular weight, it took only 5 min for Elastomer-LP3 to reach fifty percent conversion of SH group, but the difference of reaction rate between Elastomer-LP23 and Elastomer-LP2 was relatively slight, which could be directly attributed to higher mercaptan fraction and lower viscosity of the PSF oligomer LP3.

Swelling tests on cured polysulfide-based elastomers were performed by the immersion method in toluene at 25°C. The equilibrium of solvent absorption was established in 120 h, with more immersion time, the weight did not increase any more for all specimens. The swelling percentage and gel fraction of elastomers after 120 h are outlined in Table 2. All of the samples used in this study had gel fractions around 90 wt% except for Elastomer-LP55, which was due to relatively lower cross-linking agent. This also indicated a nearly complete reaction of

Table 2. Gel fractions, swelling ratio, glass transition temperature and mechanical properties of Polysulfide-based elastomers

Sample	Weight composition of PSF/VR77	Containing of polysulfide blocks [%]*	Gel fraction Ti [%]	Swelling ratio Q [%]	T _g [°C]	Tensile strength [MPa]	Ultimate elongation [%]	Hardness [Shore A]
Elastomer-LP3	1.8:1	64.2	92.3	35.6	-19.0	0.91	207	39
Elastomer-LP23	4.5:1	81.3	90.7	54.4	-36.3	0.88	175	38
Elastomer-LP980	4.5:1	80.8	89.7	60.5	-34.3	0.84	334	29
Elastomer-LP2	7.2:1	87.8	92.0	63.0	-39.5	0.74	126	35
Elastomer-LP32	7.2:1	88.2	90.2	71.3	-39.4	0.76	261	30
Elastomer-LP55	7.2:1	87.4	87.4	74.8	-38.3	0.76	412	22

*calculated from the S-elemental analysis of the obtained elastomers.

vinyl groups with thiols. From Table 2, it can be concluded that the gel fraction increased with cross-linking agent increased, and the chain length of PSF oligomers had little effect on gel fractions of corresponding elastomers. As controlled, the gel fractions of the polysulfide elastomers cured by MnO_2 (one of widely-used metal oxide curing agents for PSF oligomers) were also investigated under the same experiment conditions. The results reveal that, as for the same type of PSF oligomer, the elastomers cured by MnO_2 had somewhat lower gel fraction and higher swelling ratio than those cured by bisphenol-A diacrylate resin. The reason is that some plasticizers have to be employed with metal oxides to make up curing agents, which would be extracted by solvents.

3.2. Mechanical and thermal properties

The stress-strain curves of polysulfide-based elastomers are shown in Figure 5, and the results are summarized in Table 2. Usually, the tensile strength of polysulfide polymer without reinforce is relatively poor due to lower molecular interaction [23]. From Figure 5a, comparison of elastomers prepared from PSF oligomers with the same cross-linking agent, Elastomer-LP3, Elastomer-LP23, Elastomer-LP2, shows a simultaneously higher tensile strength and ultimate elongation for lower molecular weight PSF based elastomer (Elastomer-LP3), and comparing the tensile tests of Elastomer-LP980 and Elastomer-LP32 gives similar results. The results reveal that incorporation of the bisphenol-A structure imparted improved elongation and tensile strength for elastomers, for bisphenol-A unit acts as physical cross-linking point. This effect also has been found in high-energy-absorbing thio-ene and thiol-ene-acrylate mixture [11]. On the other hand, with the same molecular weight of PSF oligomers, the ultimate elongation increases significantly from Elastomer-LP2, Elastomer-LP32 to Elastomer-LP55 (Figure 5b) as well as from Elastomer-LP23 to Elastomer-LP980, but the tensile strength does not have obvious change due to the same dosage of bisphenol-A diacrylate employed. This effect of branching on physical properties of polysulfide elastomer is similar as that of metal oxide cured polysulfide polymer.

Thermal stability of the polysulfide-based elastomers was characterized by thermogravimetric analysis (shown in Figure 6). Usually, the thermal stability of polysulfide polymers depends on the composition of the material backbone as well as the curing agent employed to vulcanize the PSF oligomer. As observed from in Figure 6, all of the obtained polysulfide elastomers are thermally stable with 5% weight loss at temperatures around 290°C despite of different dosage of bisphenol-A diacrylate resin used, indicating higher thermal stability of bisphenol-A diacrylate structure than polysulfide units. These results can be explained by the presence of the C–O bond, more stable at high temperature than an S–S or C–S bond as indicated by the enthalpy of dissociation [29]. However, as a comparison, polysulfide elastomer cured by MnO_2 displayed 5% weight loss at temperature of 216°C. The results verify that, apart from an acid-catalyzed hydrolytic attack on the formal group in polysulfide

thermally stable with 5% weight loss at temperatures around 290°C despite of different dosage of bisphenol-A diacrylate resin used, indicating higher thermal stability of bisphenol-A diacrylate structure than polysulfide units. These results can be explained by the presence of the C–O bond, more stable at high temperature than an S–S or C–S bond as indicated by the enthalpy of dissociation [29]. However, as a comparison, polysulfide elastomer cured by MnO_2 displayed 5% weight loss at temperature of 216°C. The results verify that, apart from an acid-catalyzed hydrolytic attack on the formal group in polysulfide

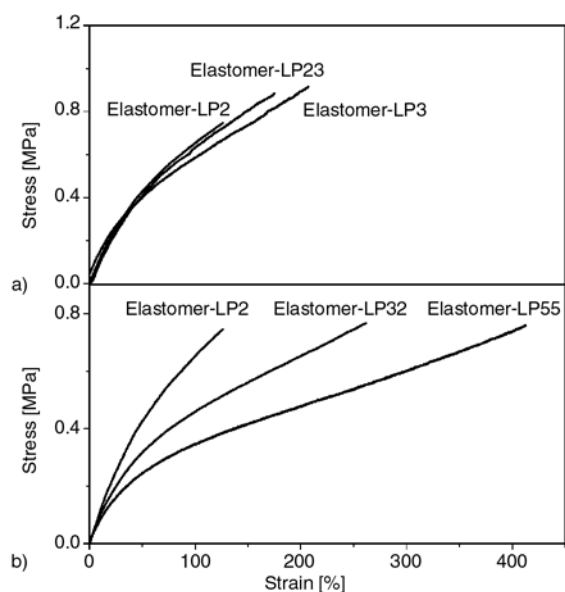


Figure 5. Strain-stress curves of polysulfide-based elastomers: Elastomer-LP3, LP23, LP2 (a) and LP55, LP32, LP2 (b)

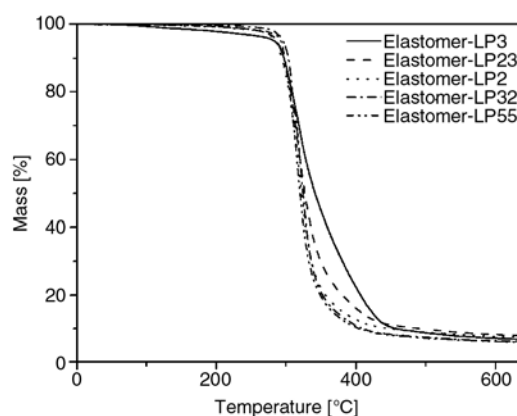


Figure 6. TGA curves of polysulfide-based elastomers

backbone, another source of thermal instability arises due to metal incorporation in polysulfide from the reaction of mercaptan with metal oxides [23, 30].

Figure 7 and Figure 8 show dynamic mechanical properties of elastomers synthesized from different liquid polysulfide oligomers as a function of molecular weight and cross-linking agent respectively, and the data of the glass transition temperatures (T_g) are outlined in Table 2. It can be seen from Figure 7 and Figure 8, all of the $\tan\delta$ versus temperature plots exhibited one single sharp peak, which indicated the formation of a homogeneous polymer

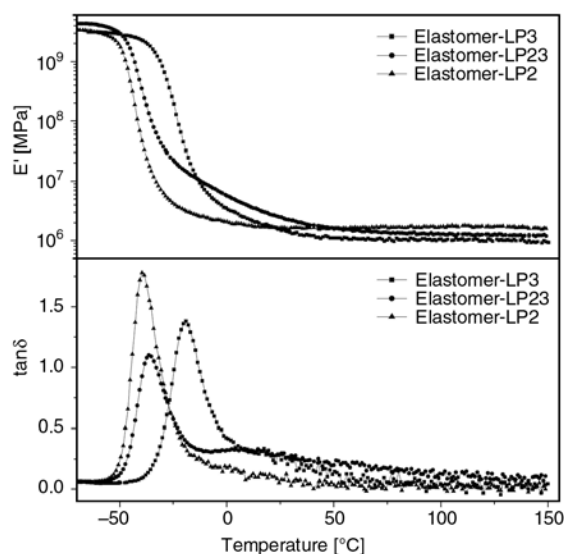


Figure 7. Dynamic mechanical properties of elastomers synthesized from different liquid polysulfide oligomers as a function of molecular weight

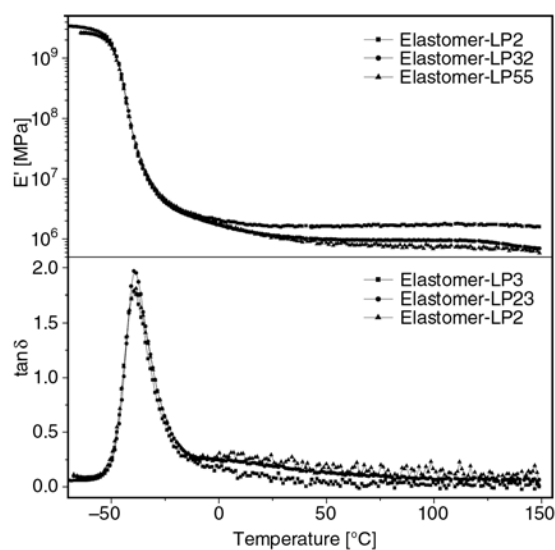


Figure 8. Dynamic mechanical properties of elastomers synthesized from different liquid polysulfide oligomers as a function of cross-linking agent

work. The T_g of the samples was around -34 – 39°C except for Elastomer-LP3, which had a higher T_g of -19°C . This was due to the characteristic step-growth process of thio-ene addition reaction, as well as the good compatibility of polysulfide and bisphenol-A structure. Bisphenol-A units gave a large number of domains dispersing in the soft-segment matrix (polysulfide), which resulted in higher T_g . However, the cross-linking agent of PSF monomers also had little effect on T_g of corresponding elastomers [23]. Another point to note is that all elastomers showed good high-temperature properties, the storage modulus (E') almost held the line between 50 – 150°C , and the greater the cross linking agent, the higher is E' .

4. Conclusions

Polysulfide-based elastomers were successfully prepared through a simple one-pot thiol-Michael addition of the liquid polysulfide oligomers with bisphenol-A diacrylate resin. High mercaptan functional group conversion was achieved despite of different molecular weight of the liquid polysulfide oligomers. After avoiding mercaptide from the reaction of mercaptan with metal oxide, the obtained elastomers having $-\text{C}-\text{C}-$ cross-linkage exhibited higher thermal stability than metal oxide cured polysulfide polymer. At the same time, the elastomers continued to keep low temperature flexibility of polysulfide polymer except Elastomer-LP3, which was due to higher content of bisphenol-A structure. All the tensile strength of the samples was comparable to that of polysulfide polymer cured by metal oxide. Moreover, the elongation of the samples could be expediently controlled by adjusting the cross-linking agent or mercaptan fraction of liquid polysulfide oligomer employed. This simplicity and efficiency of the reported procedure provides a fast and green approach (without metal oxides and plasticizers) for preparing polysulfide elastomers, and tailing their physical properties to meet a potential wide range of application.

References

- [1] Hoyle C. E., Bowman C. N.: Thiol-ene click chemistry. *Angewandte Chemie International Edition*, **49**, 1540–1573 (2010). DOI: [10.1002/anie.200903924](https://doi.org/10.1002/anie.200903924)
- [2] Kade M. J., Burke D. J., Hawker C. J.: The power of thiol-ene chemistry. *Journal of Polymer Science Part A: Polymer Chemistry*, **48**, 743–750 (2010). DOI: [10.1002/pola.23824](https://doi.org/10.1002/pola.23824)

- [3] Dondoni A.: The emergence of thiol-ene coupling as a click process for materials and bioorganic chemistry. *Angewandte Chemie International Edition*, **47**, 8995–8997 (2008).
DOI: [10.1002/anie.200802516](https://doi.org/10.1002/anie.200802516)
- [4] Kempe K., Krieg A., Becer C. R., Schubert U. S.: ‘Clicking’ on/with polymers: A rapidly expanding field for the straightforward preparation of novel macromolecular architectures. *Chemical Society Reviews*, **42**, 176–191 (2012).
DOI: [10.1039/c1cs15107j](https://doi.org/10.1039/c1cs15107j)
- [5] Khire V. S., Yi Y., Clark N. A., Bowman C. N.: Formation and surface modification of nanopatterned thiol-ene substrates using step and flash imprint lithography. *Advanced Materials*, **20**, 3308–3313 (2008).
DOI: [10.1002/adma.200800672](https://doi.org/10.1002/adma.200800672)
- [6] Khire V. S., Kloxin A. M., Couch C. L., Anseth K. S., Bowman C. N.: Synthesis, characterization and cleavage of linear polymers attached to silica nanoparticles formed using thiol-acrylate conjugate addition reactions. *Journal of Polymer Science Part A: Polymer Chemistry*, **46**, 6896–6906 (2008).
DOI: [10.1002/pola.22999](https://doi.org/10.1002/pola.22999)
- [7] Gress A., Völkel A., Schlaad H.: Thio-click modification of poly[2-(3-butenyl)-2-oxazoline]. *Macromolecules*, **40**, 7928–7933 (2007).
DOI: [10.1021/ma071357r](https://doi.org/10.1021/ma071357r)
- [8] Sengupta S. S., Parent J. S., McLean J. K.: Radical-mediated modification of polypropylene: Selective grafting via polyallyl coagents. *Journal of Polymer Science Part A: Polymer Chemistry*, **43**, 4882–4893 (2005).
DOI: [10.1002/pola.20952](https://doi.org/10.1002/pola.20952)
- [9] Keleş E., Hazer B., Cömert F. B.: Synthesis of antibacterial amphiphilic elastomer based on polystyrene-block-polyisoprene-block-polystyrene via thiol-ene addition. *Materials Science and Engineering C*, **33**, 1061–1066 (2013).
DOI: [10.1016/j.msec.2012.11.029](https://doi.org/10.1016/j.msec.2012.11.029)
- [10] Campos L. M., Meinel I., Guino R. G., Schierhorn M., Gupta N., Stucky G. D., Hawker C. J.: Highly versatile and robust materials for soft imprint lithography based on thiol-ene click chemistry. *Advanced Materials*, **20**, 3728–3733 (2008).
DOI: [10.1002/adma.200800330](https://doi.org/10.1002/adma.200800330)
- [11] Senyurt A. F., Wei H., Hoyle C. E., Piland S. G., Gould T. E.: Ternary thiol-ene/acrylate photopolymers: Effect of acrylate structure on mechanical properties. *Macromolecules*, **40**, 4901–4909 (2007).
DOI: [10.1021/ma062534b](https://doi.org/10.1021/ma062534b)
- [12] Wei H., Senyurt A. F., Jönsson S., Hoyle C. E.: Photopolymerization of ternary thiol-ene/acrylate systems: Film and network properties. *Journal of Polymer Science Part A: Polymer Chemistry*, **45**, 822–829 (2007).
DOI: [10.1002/pola.21844](https://doi.org/10.1002/pola.21844)
- [13] Niu G., Zhang H., Song L., Cui X., Cao H., Zheng Y., Zhu S., Yang Z., Yang H.: Thiol/acrylate-modified PEO-PPO-PEO triblocks used as reactive and thermosensitive copolymers. *Biomacromolecules*, **9**, 2621–2628 (2008).
DOI: [10.1021/bm800573e](https://doi.org/10.1021/bm800573e)
- [14] Zheng H., Li Y., Zhou C., Li Y., Yang W., Zhou W., Zuo Z., Liu H.: Synthesis of a [2]rotaxane incorporating a ‘magic sulfur ring’ by the thiol-ene click reaction. *Chemistry A: European Journal*, **17**, 2160–2167 (2011).
DOI: [10.1002/chem.201002964](https://doi.org/10.1002/chem.201002964)
- [15] Fairbanks B. D., Schwartz M. P., Halevi A. E., Nuttelman C. R., Bowman C. N., Anseth K. S.: A versatile synthetic extracellular matrix mimic via thiol-norbornene photopolymerization. *Advanced Materials*, **21**, 5005–5010 (2009).
DOI: [10.1002/adma.200901808](https://doi.org/10.1002/adma.200901808)
- [16] Flores J. D., Treat N. J., York A. W., McCormick C. L.: Facile, modular transformations of RAFT block copolymers via sequential isocyanate and thiol-ene reactions. *Polymer Chemistry*, **2**, 1976–1985 (2011).
DOI: [10.1039/c1py00182e](https://doi.org/10.1039/c1py00182e)
- [17] Pounder R. J., Stanford M. J., Brooks P., Richards S. P., Dove A. P.: Metal free thiol-maleimide ‘Click’ reaction as a mild functionalisation strategy for degradable polymers. *Chemical Communications*, **2008**, 5158–5160 (2008).
DOI: [10.1039/b809167f](https://doi.org/10.1039/b809167f)
- [18] Simpson N., Takwa M., Hult K., Johansson M., Martinelle M., Malmström E.: Thiol-functionalized poly(ω -pentadecalactone) telechelics for semicrystalline polymer networks. *Macromolecules*, **41**, 3613–3619 (2008).
DOI: [10.1021/ma702419m](https://doi.org/10.1021/ma702419m)
- [19] Takwa M., Hult K., Martinelle M.: Single-step, solvent-free enzymatic route to α,ω -functionalized poly-pentadecalactone macromonomers. *Macromolecules*, **41**, 5230–5236 (2008).
DOI: [10.1021/ma800074a](https://doi.org/10.1021/ma800074a)
- [20] Carioscia J. A., Lu H., Stanbury J. W., Bowman C. N.: Thiol-ene oligomers as dental restorative materials. *Dental Materials*, **21**, 1137–1143 (2005).
DOI: [10.1016/j.dental.2005.04.002](https://doi.org/10.1016/j.dental.2005.04.002)
- [21] Clark T., Kwisnek L., Hoyle C. E., Nazarenko S.: Photopolymerization of thiol-ene systems based on oligomeric thiols. *Journal of Polymer Science Part A: Polymer Chemistry*, **47**, 14–24 (2009).
DOI: [10.1002/pola.23089](https://doi.org/10.1002/pola.23089)
- [22] Li Q., Zhou H., Wicks D. A., Hoyle C. E.: Thiourethane-based thiol-ene high T_g networks: Preparation, thermal, mechanical, and physical properties. *Journal of Polymer Science Part A: Polymer Chemistry*, **45**, 5103–5111 (2007).
DOI: [10.1002/pola.22252](https://doi.org/10.1002/pola.22252)
- [23] Usmani A. M.: Chemistry and technology of polysulfide sealants. *Polymer-Plastics Technology and Engineering*, **19**, 165–199 (1982).
DOI: [10.1080/03602558208067730](https://doi.org/10.1080/03602558208067730)

- [24] Dong W., Quan Y., Zhang J., Chen Q.: The structural and mechanical properties of polysulfide-based polyurea. *Polymer International*, **52**, 1925–1929 (2003). DOI: [10.1002/pi.1301](https://doi.org/10.1002/pi.1301)
- [25] Quan Y., He P., Zhou B., Chen Q.: Modification of polysulfide sealant with polysulfide polythio-urethane-urea. *Journal of Applied Polymer Science*, **106**, 2599–2604 (2007). DOI: [10.1002/app.26792](https://doi.org/10.1002/app.26792)
- [26] Zhang J., Wang Z., Ding G., Quan Y., Chen Q.: The effect of epoxy resin to reduce the compression set of polysulfide sealant. *Journal of Applied Polymer Science*, **125**, 390–395 (2012). DOI: [10.1002/app.35651](https://doi.org/10.1002/app.35651)
- [27] Zhou B., Shen M., Wang Q., Chen Q.: Kinetic study of polysulfide-acrylate click reaction by DEA and DMA. *Polymers for Advanced Technologies*, **21**, 1–8 (2011). DOI: [10.1002/pat.1773](https://doi.org/10.1002/pat.1773)
- [28] Hoyle C. E., Lee T. Y., Roper T.: Thiol–enes: Chemistry of the past with promise for the future. *Journal of Polymer Science Part A: Polymer Chemistry*, **42**, 5301–5338 (2004). DOI: [10.1002/pola.20366](https://doi.org/10.1002/pola.20366)
- [29] Soeriyadi A. H., Li G-Z., Slavin S., Jones M. W., Amos C. M., Becer C. R., Whittaker M. R., Haddleton D. M., Boyer C., Davis T. P.: Synthesis and modification of thermoresponsive poly(oligo(ethylene glycol) methacrylate) *via* catalytic chain transfer polymerization and thiol-ene Michael addition. *Polymer Chemistry*, **2**, 815–822 (2011). DOI: [10.1039/c0py00372g](https://doi.org/10.1039/c0py00372g)
- [30] Radharkrishnan T. S., Rao M. R.: Characterization of cured polysulfide polymers by thermal degradation: Pyrolysis-GC and thermogravimetric studies. *Journal of Applied Polymer Science*, **34**, 1985–1996 (1987). DOI: [10.1002/app.1987.070340517](https://doi.org/10.1002/app.1987.070340517)

Improving the thermal conductivity of epoxy resin by the addition of a mixture of graphite nanoplatelets and silicon carbide microparticles

T. Zhou^{1*}, X. Wang², P. Cheng³, T. Wang¹, D. Xiong¹, X. Wang⁴

¹School of Materials Science and Engineering, Nanjing University of Science and Technology, 210094 Nanjing, China

²Key Laboratory for Soft Chemistry and Functional Materials of Ministry Education, Nanjing University of Science and Technology, 210094 Nanjing, China

³National Key Laboratory of Science and Technology on Micro/Nano Fabrication, Key Laboratory for Thin Film and Microfabrication of the Ministry of Education, Research Institute of Micro/Nano Science and Technology, Shanghai Jiao Tong University, 200240 Shanghai, China

⁴Department of Chemistry and Materials Science, Chaohu University, 238000 Chaohu, China

Received 6 January 2013; accepted in revised form 24 March 2013

Abstract. In this work, an alternative type of carbon-based nanofiller, graphite nanoplatelets (GNPs) with comparable properties, easier and lower-cost production, were used to improve the thermal conductivity of an epoxy. By adding 12 wt% GNPs or 71.7 wt% silicon carbide microparticles (micro-SiCs) to epoxy, the thermal conductivity reached maxima that were respectively 6.3 and 20.7 times that of the epoxy alone. To further improve the thermal conductivity a mixture of the two fillers was utilized. The utilized GNPs are characterized by two-dimensional (2-D) structure with high aspect ratio (~447), which enables GNPs effectively act as heat conductive bridges among 3-D micro-SiCs, thus contributes considerably to the formation of a more efficient 3-D percolating network for heat flow, resulting in higher thermal conductivity with relatively lower filler contents which is important for decreasing the density, viscosity and improving the processability of composites. A thermal conductivity, 26.1 times that of epoxy, was obtained with 7 wt% GNPs + 53 wt% micro-SiCs, thus not only break the bottleneck of further improving the thermal conductivity of epoxy composites but also broaden the applications of GNPs.

Keywords: polymer composites, nanocomposites, thermal conductivity, graphite nanoplatelets, silicon carbide microparticles

1. Introduction

Graphene nanosheet (GNS), a single layer of hexagonally arrayed sp²-bonded carbon, has attracted increasing attention recently due to its excellent thermal, electrical and mechanical properties. However, manufacturing GNS-filled composites has been very challenging due to the difficulties in large-scale production of GNSs and their dispersion in matrices. GNSs tend to form irreversible agglomerates or even restack to form graphite through van der Waals interactions during the processing of bulk-quantity

GNSs, especially in the drying process [1]. Carbon nanotube (CNT), another type of widely studied and applied high-performance carbon-based nanofiller, also has great challenges in composite applications especially due to its expensive production cost. Instead of trying to discover easier large-scale processes for GNSs or lower cost processes for CNTs, an alternative type of carbon-based nanofiller with comparable properties, which can be produced more easily and cost-effectively in large quantities, has also recently been emphasized. This type of nano-

*Corresponding author, e-mail: ztltianle999@hotmail.com

filler is herein referred to as graphite nanoplatelet (GNP), which is a stack of platelet-shaped GNSs but is still in the nanoscale in the thickness direction [2]. Increasing energy dissipation, due to the increasing speed and functionality of integrated circuits, calls for methods to increase the thermal conductivity of materials such as epoxy resins which are widely used in electronic industries. Recently, experimental studies have been stimulated to address the heat transport in the GNP/epoxy composites [3–26], and theoretical analysis, e.g. based on effective medium model [2, 11] and normal modes [27], was also conducted to analyze the effective thermal conductivity of the GNP/epoxy composites. Owing to the high thermal conductivity (250 W/(m·K) in basal plane and 80 W/(m·K) across basal plane at room temperature [3]), two-dimensional (2-D) structure and high aspect ratio of GNP, GNPs were found to be more efficient than carbon black (CB) nanoparticles [3–5], single-walled CNTs (SWCNTs) [4–6] and multi-walled CNTs (MWCNTs) [7, 17] in improving the thermal conductivity of epoxy. So far the reported maximum thermal conductivity of GNP/epoxy composites is 6.6 W/(m·K) obtained using a 40 wt% loading of GNPs [4].

The synergetic effect of GNPs and other nanofillers in improving the thermal conductivity of epoxy was also observed in the case of low total nanofiller loadings, i.e. 18 wt% total loading of GNPs and CB nanoparticles [14], 1 wt% total loading of GNPs and MWCNTs [13], 2 wt% total loading of GNPs and MWCNTs [25] and ≤ 40 wt% total loading of GNPs and SWCNTs [4].

The addition of 0-D CB nanoparticles helped to increase the thermal conductivity of GNP/epoxy composites by improving the dispersion of GNPs, preventing the settling of GNPs and bridging the gaps among 2-D GNPs [14]. Long and tortuous 1-D CNTs were used to bridge adjacent 2-D GNPs as well as inhibit the aggregation of GNPs, resulting in a high contact area between GNP/CNT structures and epoxy matrix and thus a more efficient percolating nanofiller network with significantly reduced thermal interface resistances, consequently the thermal conductivity of epoxy filled with a mixture of GNPs and CNTs surpassed that of epoxy filled with pure GNPs or CNTs [4, 13, 25]. However, a further increase of thermal conductivity of epoxy by increasing the total nanofiller loading is hard to realize due

to the increased filler aggregation and interfacial thermal resistance as well as dramatically increased viscosity. Recently, epoxy composites with high nanocarbon (GNPs, MWCNTs, GNPs + MWCNTs) loading up to 50 vol% were got by a well-designed fabrication method, however, the method need a special mixer in which the mixture was stirred with a rotation speed and a revolution speed [26]. Therefore, so far, by the routine fabrication method, the reported maximum thermal conductivity of epoxy filled with GNPs and other nanofillers is 4.7 W/(m·K) (obtained with 30 wt% GNPs + 10 wt% SWCNTs [4]), failing to exceed the aforementioned maximum thermal conductivity of GNP/epoxy composites.

Silicon carbide microparticle (micro-SiC) is an attractive 3-D microfiller candidate for high temperature and high power applications in electronic industries due to its high thermal conductivity (~ 390 W/(m·K) at room temperature), low thermal expansion coefficient (~ 4.0 ppm/K, a value close to that of Si chip, ~ 3.5 ppm/K; 300–673 K), etc [28]. However, improving the thermal conductivity of epoxy by combining 2-D GNPs and 3-D micro-SiCs has not been considered yet. In this work, epoxy filled with a mixture of GNPs and micro-SiCs were prepared, aiming at further improving the thermal conductivity of epoxy, thus not only breaking the bottleneck of further improving the thermal conductivity of epoxy composites but also broadening the applications of GNPs. This paper is part of a large project on the development of heat conductive composites reinforced with micro and nanoscale fillers for more demanding applications, such as in nano-electronics applications, etc.

2. Experimental

2.1. Materials

Epoxy resin used in this work was diglycidyl ether of bisphenol-A (DGEBA) supplied by Shanghai Resin Co. Ltd., China. Curing agent, 2-ethyl-4-methylimidazole (EMI-2,4), was supplied by Beijing Chemical Reagent Co. Ltd., China. Amino silane coupling agent, γ -aminopropyl-triethoxysilane (A1100), was obtained from Shanghai Chemical Reagent Co. Ltd., China. Other agents utilized were analytically pure grade and supplied by Sinopharm Chemical Reagent Co. Ltd., China.

β -SiC particles with average particle size of 0.75 μm and irregularly polyhedral shape were obtained

from Karl Co. Ltd., China. Micrographs of the micro-SiCs and the micro-SiC/epoxy composite can be seen in our earlier works [29, 30], respectively. Carboxyl-functionalized MWCNTs (COOH-MWCNTs) were provided by Chengdu Organic Chemicals Co. Ltd., Chinese Academy of Sciences, and used as-received. According to the supplier's specification, COOH-MWCNTs were synthesized by catalytic chemical vapor deposition with 50–80 nm diameter, 10–20 μm length and 125–400 aspect ratio. The purity and the specific surface area were greater than 95% and 40 m^2/g , respectively. Before stored in desiccators, COOH-MWCNTs were dried at 110°C for 24 h in vacuum to eliminate the agglomeration caused by hygroscopic absorption, as well as removing planar water, which would hinder the interaction between coupling agent and COOH-MWCNTs. Micrographs of the rod-shaped COOH-MWCNTs and the COOH-MWCNT/epoxy composite can be seen in our previous work [31]. The starting material for GNPs was graphite intercalation compound (GIC) particles (500 μm), i.e. sulfuric acid-intercalated graphite, provided by Xinfangyuan Co. Ltd., China. According to the supplier's specification, the content of intercalants was about 15 wt% and the carbon content was higher than 99%. GNPs were prepared according to the method reported in the literature [32]. Briefly, (a) as-received GIC particles were subjected to a thermal shock on rapid exposure to 1000°C for 20 s in a muffle furnace, causing the GIC particles underwent a significant expansion (~ 440 times) along the

thickness direction since the entrapped intercalants within GIC layers decomposed or vaporized instantly, (b) the obtained expanded structures were then dipped in absolute ethanol and then broken down to GNPs using a 30 min high speed shear mixing (2400 rpm) followed by a 12 h ultrasonic irradiation (100 W, 80 kHz), (c) the GNP-absolute ethanol dispersion was filtered and the obtained GNPs were dried at 110°C to remove residue solvents. The as-prepared GNPs were then kept in a dry desiccator for testing and further use.

Field emission scanning electron microscope (FESEM) micrographs in Figure 1 show that the as-prepared GNPs have flat and smooth morphology besides sharp corners. Image analysis calculation results based on 100 GNPs showed that the as-prepared GNPs have average diameter of 21 μm with the range of 3–30 μm and average thickness of 47 nm with the range of 20–80 nm. Then the aspect ratio can be calculated to be ~ 447 .

Fourier-transform infrared (FTIR) spectrum of as-prepared GNPs, shown in Figure 2, illustrates that there are a lot of hydroxyl groups ($-\text{OH}$, intense band at 3650–3050 cm^{-1}) and carboxyl functional groups ($\text{C}=\text{O}$, band at 1600–1200 cm^{-1}) confirmed to exist on the surface of as-prepared GNPs, indicating that the treatment of natural graphite with sulfuric acid and thermal shock of GICs resulted in some carbon double bonds oxidized, leading to the presence of oxygen-containing functional groups on the GNPs, which will facilitate their interactions with coupling agent or micro-SiCs.

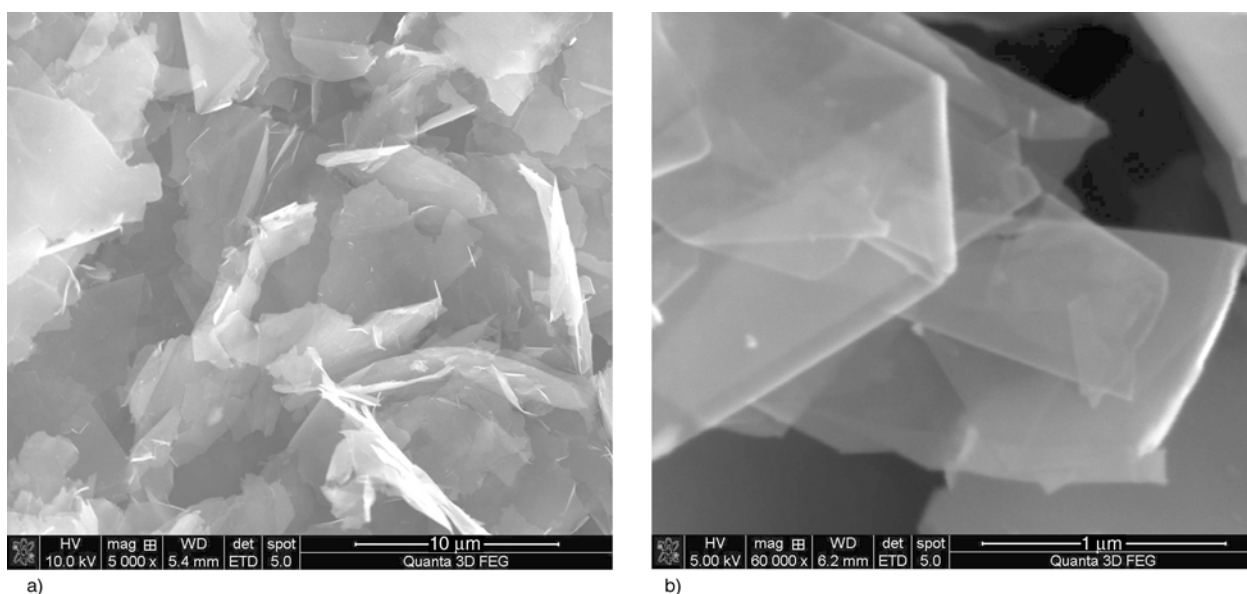


Figure 1. FESEM micrographs of GNPs, 5k \times (a) and 60k \times (b)

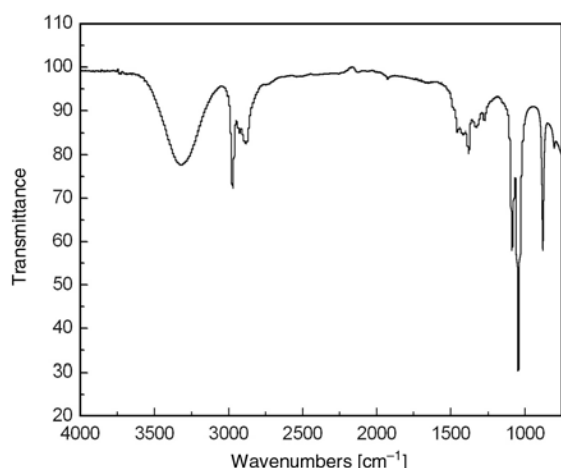


Figure 2. FTIR spectrum of GNPs

2.2. Surface modification of fillers

Oxidation of micro-SiCs involved (a) dipping micro-SiCs in a 10 vol% hydrofluoric acid solution for 20 min, (b) rinsing with acetone by filtration to remove the passivating thin native oxide film on the surface of micro-SiCs, (c) oxidizing micro-SiCs at 900°C for 20 h in a preheated furnace. The oxidized micro-SiCs were left in the furnace, cooling to room temperature, and then stored in desiccators.

Silane treatment of fillers using A1100 involved (a) making a silane-absolute ethanol solution at 0.001 g/mL concentration, and the amounts of A1100 used were 3% by weight of the micro-SiCs and 10% by weight of the nanofillers i.e. GNPs or COOH-MWCNTs, (b) adding filler particles to the solution and stirring with a high speed magnetic stirrer (1500 rpm) at 60°C for 30 min, in addition, dispersing the solution added with nanofiller particles by high intensity ultrasonication for 1 h, (c) rinsing with absolute ethanol by filtration, and drying at 110°C for 1 h in vacuum. Then the silane treated fillers were stored in desiccators.

2.3. Composite preparation

The composites were prepared by solution blending and casting method, which involved (a) stirring DGEBA-absolute ethanol solution at 80°C with a high speed magnetic stirrer for 20 min, (b) adding appropriate amount of as-prepared or pretreated filler particles to the solution and continuing stir for 30 min, in addition, ultrasonication the solution added with nanofiller particles for 2 h to ensure good homogeneity, (c) cooling to 60°C, (d) adding EMI-2,4, which is 4% by weight of DGEBA, to the mixture and continuing stir for 10 min, (e) casting

the mixture in mould and repeatedly degassing the mixture in vacuum drying oven at 60°C until no air bubble appears on the surface of mixture, (f) curing the mixture at 65°C for 1 h, 120°C for 1.5 h, and 160°C for 1.5 h, (g) cooling to room temperature, then demoulding.

2.4. Characterization

In this paper, morphological studies of GNPs and the fracture surfaces of composites were carried out using FESEM (Quanta 3D FEG, FEI Co., USA; LEO1550, LEO Electron Microscopy Ltd., UK). GNPs were pre-coated with a thin platinum layer. The aspect ratio of GNPs was calculated based on the measured dimensions of 100 GNPs from several FESEM images. Composites were fractured in liquid nitrogen and then the fracture surfaces were coated with a thin platinum layer before FESEM study.

FTIR spectrum was recorded on a Thermo Nicolet IS-10 Smart ITR spectrophotometer (Thermo Fisher Scientific Co., Ltd., USA) with the smart iTR™ ATR (Attenuated Total Reflectance) accessory.

Thermal diffusivity (δ , mm²/s) at room temperature was measured on disk samples (12.7 mm diameter, 2 mm thickness) by laser flash method (nanoflash LFA 447 system, NETZSCH Instruments Co., Ltd., UK), specific heat (C , J/gK) at room temperature was measured on disk samples (6 mm diameter, 1 mm thickness) by DSC (DSC-7 system, Perkin-Elmer Co., Ltd., UK), and bulk density (ρ , g/cm³) of specimen was measured by water displacement. For each measurement, three samples were tested three times. After that, thermal conductivity (λ , W/(m·K)) was calculated by Equation (1):

$$\lambda = \delta \cdot C \cdot \rho \quad (1)$$

The viscosity of epoxy resin and epoxy composites at room temperature was measured using a stress rheometer (ARES9A, TA Instruments, USA) in a steady flow mode. A cone-and-plate geometry was used. A freshly prepared liquid uncured sample was dispensed on the plate before the run and the experiments were conducted under stepped shear rate from 0.01 to 100 s⁻¹.

3. Results and discussion

Figure 3 presents the filler content dependence of thermal conductivity of the oxidized and silane

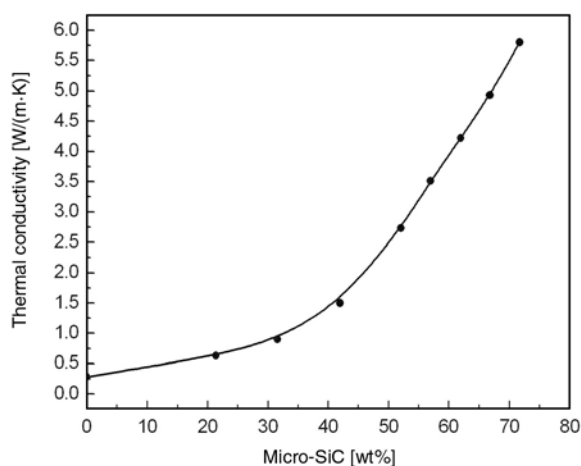


Figure 3. Thermal conductivity at room temperature of oxidized and silane treated micro-SiC/epoxy composites. Lines are given only for showing the tendency

treated micro-SiC/epoxy composites. In this work, micro-SiCs were oxidized followed by silane treatment since it was demonstrated that the ability in improving the thermal conductivity of epoxy follows the sequence: oxidized and silane treated micro-SiC > silane treated micro-SiC > untreated micro-SiC [28]. It can be seen that below the percolation threshold (~ 52.1 wt%), the thermal conductivity of oxidized and silane treated micro-SiC/epoxy composites rises slowly with the increasing micro-SiC content because of a lack of continuous micro-SiC heat conductive chains, but above the percolation threshold, the thermal conductivity increases rapidly, and when 71.7 wt% oxidized and silane treated micro-SiCs were added, the thermal conductivity reached the maximum, ~ 20.7 times that of epoxy.

Figure 4 illustrates the nanofiller content dependence of thermal conductivity of the epoxy composites containing GNPs or COOH-MWCNTs. The thermal conductivity approximately increases linearly with the increasing nanofiller content for all the investigated composites. More importantly, at identically low nanofiller contents (< 6 wt%), silane treated GNPs produced epoxy composites with higher thermal conductivities than silane treated MWCNTs despite the inherently lower thermal conductivity of individual GNP (250 W/(m·K) in basal plane and 80 W/(m·K) across basal plane at room temperature [3]) as compared with individual MWCNT (3000 W/(m·K) at room temperature [33]). There are probably two reasons behind this observation: i) the flat surface of 2-D GNPs dramatically

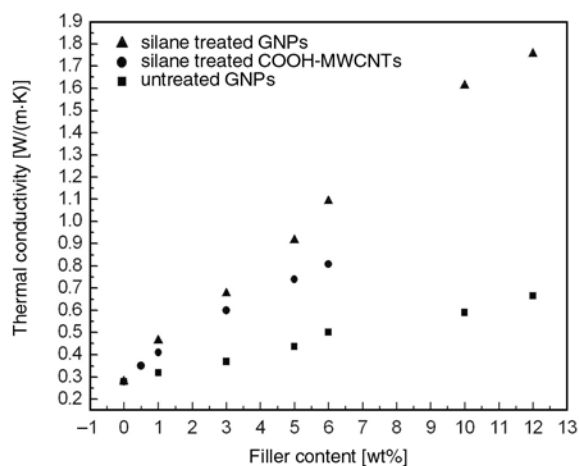


Figure 4. Thermal conductivity at room temperature of GNP/epoxy composites and COOH-MWCNT/epoxy composites

enhances the GNP/epoxy or GNP/GNP contact area, moreover, the rigidity of 2-D GNPs allows for better preservation of their high aspect ratio in comparison with the more flexible 1-D MWCNTs [4], thus 2-D GNPs are more efficient in forming heat conductive networks in epoxy matrix as compared with 1-D MWCNTs, and ii) in sharp contrast to 1-D MWCNTs, the flat surface of 2-D GNPs minimizes the geometric contribution to the thermal interface resistance since the contribution of phonon acoustic mismatch to the interface contact resistance increases with the decreasing radius of nanoparticles [5]. Furthermore, as shown in Figures 3–4, in comparison with 3-D micro-SiCs, GNPs also provided stronger improvement of the thermal conductivity of epoxy at identically low filler contents (< 12 wt%) despite the inherently lower thermal conductivity of individual GNP than micro-SiC (~ 390 W/(m·K) at room temperature [28]). The reason can be attributed to the special morphology of GNPs as well since it is easier for GNPs characterized by 2-D structure to form heat conductive networks in the epoxy matrix, and besides, the high aspect ratio (~ 447) of GNPs allows a efficient conduction of phonons over a long distance without transitions from particle to particle, whereas the poor contact of micro-SiCs due to their irregularly polyhedral shape along with a low aspect ratio of nearly unity makes it relatively difficult for them to form heat conductive networks.

As seen in Figure 4, a further increase of MWCNT content (> 6 wt%) is hard to realize, whereas GNP content can be further increased. It is known that there is only one dimension, i.e. thickness, of 2-D GNP falling within the nanoscale range, which will

induce less dramatically increased viscosity of uncured composites besides less filler aggregation. Therefore 2-D GNP is more desirable for easier composite fabrication as compared with 1-D MWCNT which has two nanoscale dimensions. In this work the maximum content of GNPs can further increase to 12 wt% and accordingly the maximum thermal conductivity of silane treated GNP/epoxy composites can reach nearly 6.3 times that of epoxy, exceeding that of silane treated COOH-MWCNT/epoxy composites, 2.9 times that of epoxy, with 6 wt% COOH-MWCNTs.

It is known that a strong interface increases the coupling effect of fillers with matrix, damps the phonons' vibrational amplitude at interface, and thus decreases the efficiency of fillers as thermal conductors in matrix [34], moreover, a layer of coupling agent on the fillers acts as a barrier to the phonon transport between filler particles [14], thus silane treatment of GNPs might be adverse to the improvement of thermal conductivity of the GNP/epoxy composites. However, the functionalized outside layers of GNPs by silane treatment can promote better dispersion of GNPs in epoxy matrix and facilitate the transport of phonons from GNPs to matrix. Relatively homogeneous-dispersed GNPs are easier to form heat conductive paths than aggregated GNPs, moreover, different from aggregated GNPs, the thermal conductivity in basal plane ($250 \text{ W}/(\text{m}\cdot\text{K})$ [3]) of well-dispersed individual GNPs will play a more important role than the thermal conductivity across basal plane ($80 \text{ W}/(\text{m}\cdot\text{K})$ [3]) in determining the final thermal conductivity of composites, so silane treatment of GNPs might also be beneficial to the improvement of thermal conductivity of the GNP/epoxy composites. However, the final overall effect of silane treatment of GNPs on the thermal conductivity of epoxy arises from the antagonistic competition of the two effects discussed above. Micrographs of 3 wt% untreated GNP or silane treated GNP filled epoxy composites are shown in Figure 5. It can be seen that silane treated GNPs were better dispersed in the matrix, which is believed to contribute to the higher thermal conductivity of GNP/epoxy composites, whereas the dispersion of untreated GNPs was not so good and more agglomeration of GNPs occurred. However, though the distribution of silane treated GNPs was relatively homogeneous, in Figure 5c–5d naked GNPs are observed on the fracture surface and a number of

GNPs were pulled out of the surface instead of being embedded and tightly held to the matrix, indicating that the interfacial bonding between GNPs and matrix is not so strong, thus it is believed that the efficiency of GNPs as thermal conductors in matrix did not decrease to a considerable extent. As a result, as shown in Figure 4, compared with untreated GNP/epoxy composites, higher thermal conductivity was observed for the epoxy composites filled with silane treated GNPs.

However, the obtained highest thermal conductivity of GNP/epoxy composites is far from being expected. A further increase of thermal conductivity by increasing nanofiller content is hard to realize due to the dramatically increased viscosity and the markedly increased filler aggregation. Methods including ultrasonication, high shear mixing and surface treatment have also already been tried. On the other hand, in order to achieve the percolation threshold and obtain high thermal conductivity, very high microfiller loadings must be used, e.g. 71.7 wt% micro-SiCs, to form as more as possible continuous heat conductive chains in the matrix, but high microfiller loadings result in high density and poor mechanical properties. Thus, issues are emerging, i.e. how to further utilize nanofillers, i.e. GNPs, to improve the thermal conductivity of epoxy composites and how to further improve the microcomposites' thermal conductivity without sacrificing their general properties.

It is noticed that the use of inorganic nanofillers has proven to be effective in reducing the filler content required for relatively high thermal conductivity and thereby minimizing the problems associated with density and mechanical properties, and in this work silane treated GNPs did efficiently improve the thermal conductivity of epoxy with low loadings and thus were considered attractively good nanofiller candidates. To combine the high performance of composite at its low nanofiller content and composite at its high microfiller content (> percolation threshold), it is reasonable to partially replace microfiller with nanofiller and expect higher thermal conductivity of composites resulting from the synergistic effect contributed from nano- and microfillers. In this paper, partial replacement method, which partially replaces micro-SiCs with GNPs, was utilized to break the bottleneck of further improving the thermal conductivity of epoxy as well as broadening the applications of GNPs. As

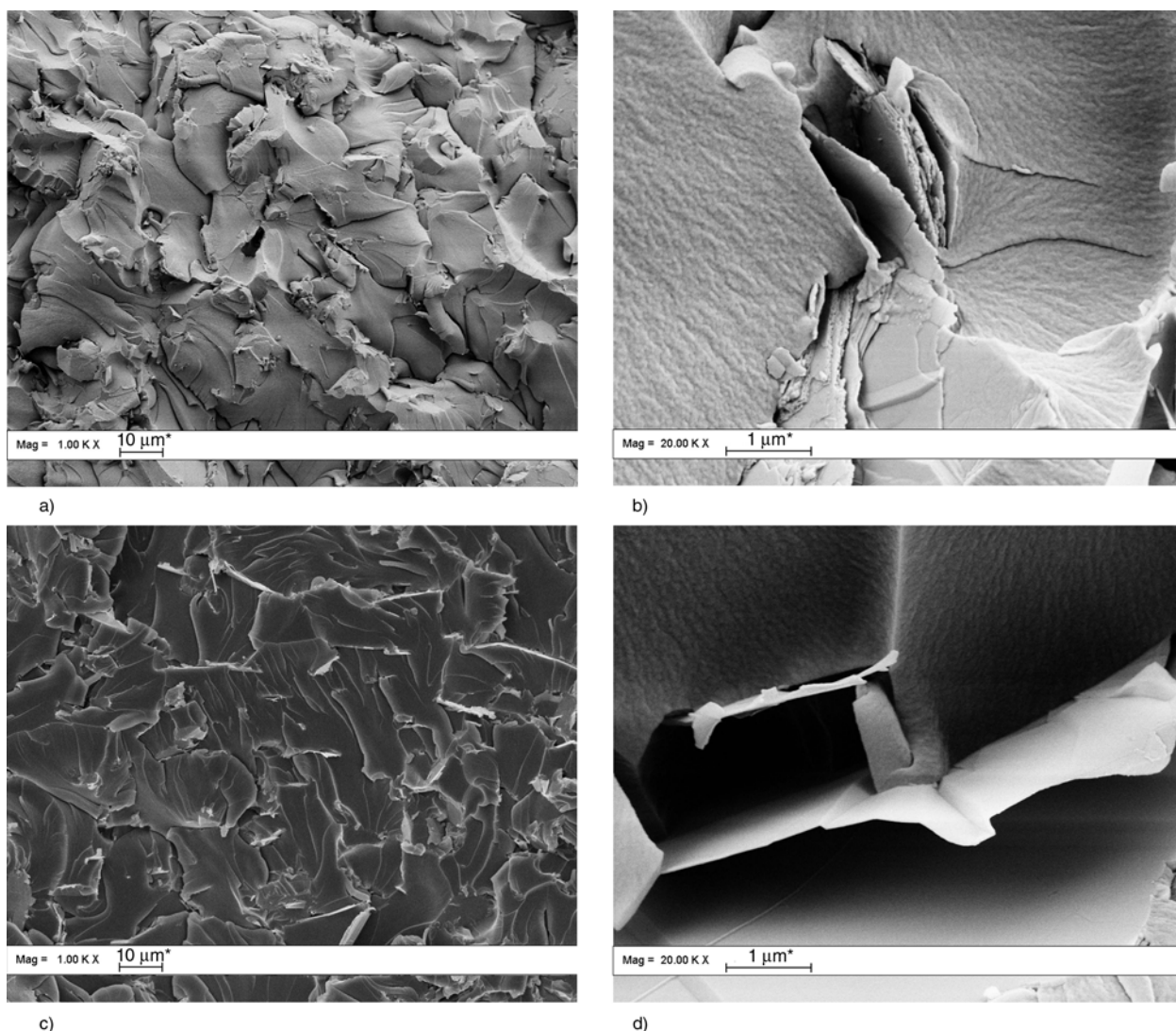


Figure 5. FESEM micrographs of 3 wt% untreated GNP/epoxy composite, 1k× (a) and 20k× (b), FESEM micrographs of 3 wt% silane treated GNP/epoxy composite, 1k× (c) and 20k× (d)

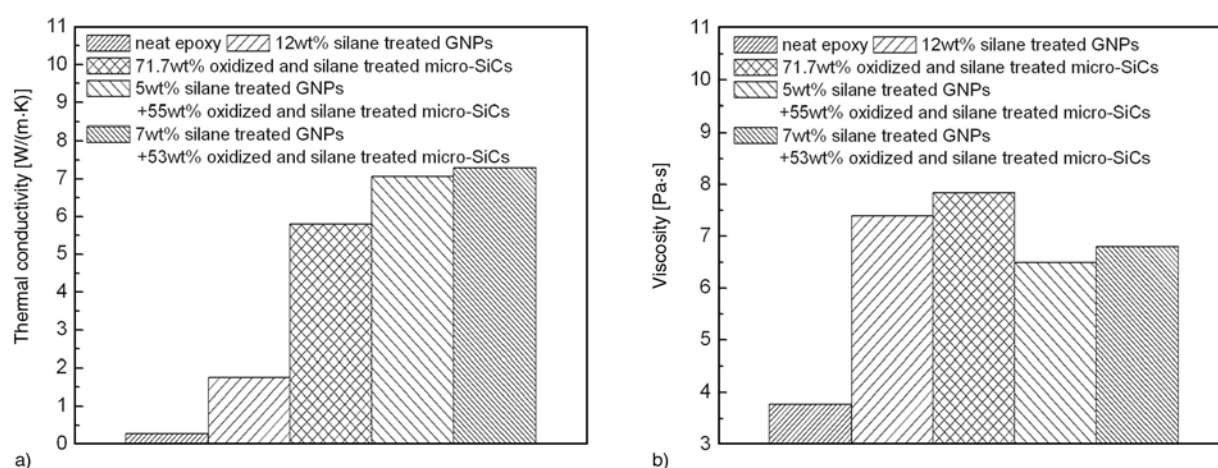


Figure 6. Thermal conductivity at room temperature of epoxy resin and epoxy composites (a), viscosity at room temperature of each uncured systems at 1 s^{-1} shear rate (b)

shown in Figure 6a, by adding 5 wt% GNPs + 55 wt% micro-SiCs, the thermal conductivity of epoxy composite reached 7.06 W/(m·K) (~25.2 times

that of epoxy), exceeding that of 71.7 wt% micro-SiC/epoxy composites and also surpassing the previously reported value (24.3 times that of epoxy

[28]) of epoxy filled with 5 wt% COOH-MWCNTs + 55 wt% micro-SiCs.

Furthermore, as shown in Figure 6b, the viscosity of epoxy filled with 5 wt% GNPs + 55 wt% micro-SiCs is 6.5 Pa·s, far lower than that of 71.7 wt% micro-SiC/epoxy composites or the previously reported value (7 Pa·s [28]) of epoxy filled with 5 wt% COOH-MWCNTs + 55 wt% micro-SiCs. Moreover, the viscosity of epoxy filled with 12 wt% GNPs is 7.4 Pa·s, even a little lower than that of epoxy filled with 6 wt% COOH-MWCNTs (7.6 Pa·s [28]), therefore GNPs was demonstrated to have advantage in inducing less increased viscosity of uncured composites as compared with MWCNTs, which is more desirable for easier composite fabrication and can be attributed to the aforementioned fact that only one dimension of GNPs, i.e. thickness, falls within nanoscale range. Then, another further increased thermal conductivity, 7.3 W/(m·K) (~26.1 times that of epoxy), was obtained with 7 wt% GNPs + 53 wt% micro-SiCs (further improved total filler content, i.e. >60 wt%, was avoided in consideration of the general properties, such as density, processability, etc).

FESEM micrograph of epoxy composite containing 7 wt% GNPs + 53 wt% micro-SiCs is shown in Figure 7a. GNPs are shown to be surrounded by quite smaller micro-SiCs. Some naked GNPs are also observed on the fracture surface, indicating that the interfacial bonding of GNP/epoxy or GNP/micro-SiC is not so strong. The thermal conductivity of all composites will be determined mainly by the heat transport of the highly heat conductive filler particles, therefore, the formation of heat conductive 3-D

percolating network in matrix is the key parameter, which influences the value of thermal conductivity of the composites. In this paper, the utilized GNPs are characterized by 2-D structure with high aspect ratio (~447), which enables GNPs effectively act as heat conductive bridges among 3-D micro-SiCs, as illustrated in Figure 7b. This kind of morphology of GNPs contributes considerably to the formation of a more efficient 3-D percolating network for heat flow, resulting in higher thermal conductivity with relatively lower filler contents. As is known, lower filler content is important for decreasing the density, viscosity and improving the processability of composites. Thus, with only a small fraction of GNPs, a mixture filler of 7 wt% GNPs + 53 wt% micro-SiCs provided higher thermal conductivity of epoxy composites in comparison with 71.7 wt% micro-SiCs.

4. Conclusions

In this study, 2D-GNPs with high aspect ratio (~447) were used to improve the thermal conductivity of epoxy. By adding 12 wt% GNPs or 71.7 wt% micro-SiCs to an epoxy resin the thermal conductivities of the composites reached maxima that were respectively 6.3 and 20.7 times that of the epoxy alone. To further improve the thermal conductivity a composite designing way, i.e. partial replacement method that partially replaces micro-SiCs with GNPs, was utilized to unite the respective advantage of microfiller and nanofiller in improving the thermal conductivity of epoxy. Epoxy composites with a mixture of GNPs and micro-SiCs were prepared, and a thermal conductivity, 26.1 times that of the

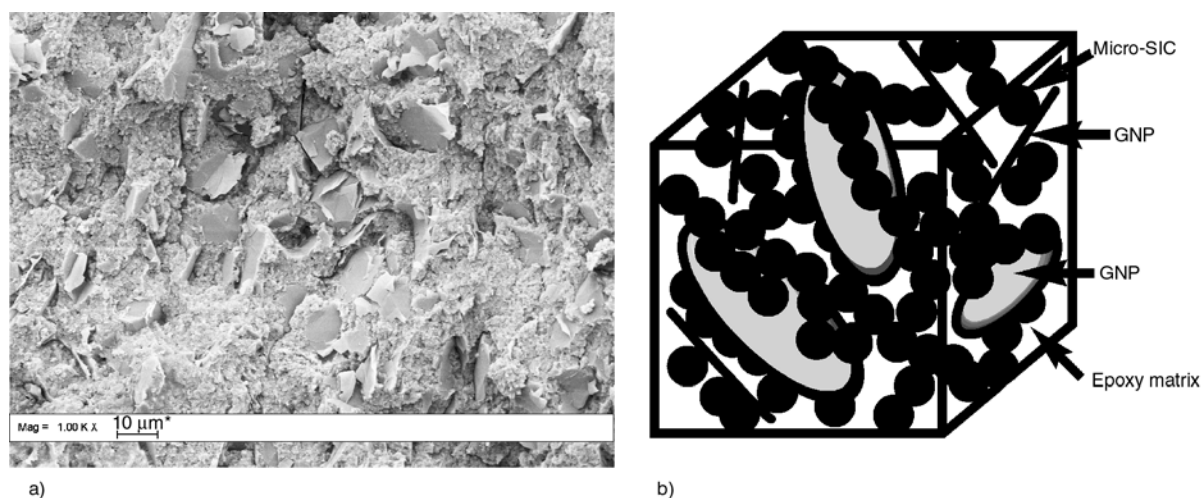


Figure 7. FESEM micrograph of epoxy composite containing 7 wt% GNPs + 53 wt% micro-SiCs (a) and schematic of heat conductive network in epoxy matrix containing a mixture of GNPs and micro-SiCs (b)

epoxy, was obtained with 7 wt% GNPs + 53 wt% micro-SiCs, thus not only break the bottleneck of further improving the thermal conductivity of epoxy composites but also broaden the applications of GNPs.

Acknowledgements

The authors are grateful for the financial support of National Natural Science Foundation of China (No.51002077, No.51203074), Fundamental Research Funds for the Central Universities (No. NUST 2011YBXM163), Jiangsu Overseas Research & Training Program for University Prominent Young & Middle-aged Teachers and Presidents, and Special Foundation for ‘first-grade Zijin’s Star’ of ‘Excellence initiative’ Project of Nanjing University of Science and Technology (No.AB41339).

References

- [1] Yan J., Wei T., Shao B., Ma F., Fan Z., Zhang M., Zheng C., Shang Y., Qian W., Wei F.: Electrochemical properties of graphene nanosheet/carbon black composites as electrodes for supercapacitors. *Carbon*, **48**, 1731–1737 (2010).
DOI: [10.1016/j.carbon.2010.01.014](https://doi.org/10.1016/j.carbon.2010.01.014)
- [2] Lin W., Zhang R., Wong C. P.: Modeling of thermal conductivity of graphite nanosheet composites. *Journal of Electronic Materials*, **39**, 268–272 (2010).
DOI: [10.1007/s11664-009-1062-2](https://doi.org/10.1007/s11664-009-1062-2)
- [3] Li J., Sham M. L., Kim J-K., Marom G.: Morphology and properties of UV/ozone treated graphite nanoplatelet/epoxy nanocomposites. *Composites Science and Technology*, **67**, 296–305 (2007).
DOI: [10.1016/j.compscitech.2006.08.009](https://doi.org/10.1016/j.compscitech.2006.08.009)
- [4] Yu A., Ramesh P., Sun X., Bekyarova E., Itkis M. E., Haddon R. C.: Enhanced thermal conductivity in a hybrid graphite nanoplatelet – Carbon nanotube filler for epoxy composites. *Advanced Materials*, **20**, 4740–4744 (2008).
DOI: [10.1002/adma.200800401](https://doi.org/10.1002/adma.200800401)
- [5] Yu A., Ramesh P., Itkis M. E., Bekyarova E., Haddon R. C.: Graphite nanoplatelet–epoxy composite thermal interface materials. *The Journal of Physical Chemistry C*, **111**, 7565–7569 (2007).
DOI: [10.1021/jp071761s](https://doi.org/10.1021/jp071761s)
- [6] Wang S., Tambraparni M., Qiu J., Tipton J., Dean D.: Thermal expansion of graphene composites. *Macromolecules*, **42**, 5251–5255 (2009).
DOI: [10.1021/ma900631c](https://doi.org/10.1021/ma900631c)
- [7] Lazarenko A., Vovchenko L., Matsui D., Prylutskyy Y., Matzuy L., Ritter U., Scharff P.: Electrical and thermal conductivity of polymer-nanocarbon composites. *Molecular Crystals and Liquid Crystals*, **497**, 65397–75407 (2008).
DOI: [10.1080/15421400802458522](https://doi.org/10.1080/15421400802458522)
- [8] Ganguli S., Roy A. K., Anderson D. P.: Improved thermal conductivity for chemically functionalized exfoliated graphite/epoxy composites. *Carbon*, **46**, 806–817 (2008).
DOI: [10.1016/j.carbon.2008.02.008](https://doi.org/10.1016/j.carbon.2008.02.008)
- [9] Hung M-T., Choi O., Ju Y. S., Hahn H. T.: Heat conduction in graphite-nanoplatelet-reinforced polymer nanocomposites. *Applied Physics Letters*, **89**, 023117/1–023117/3 (2006).
DOI: [10.1063/1.2221874](https://doi.org/10.1063/1.2221874)
- [10] Debelak B., Lafdi K.: Use of exfoliated graphite filler to enhance polymer physical properties. *Carbon*, **45**, 1727–1734 (2007).
DOI: [10.1016/j.carbon.2007.05.010](https://doi.org/10.1016/j.carbon.2007.05.010)
- [11] Veca M. L., Meziani M. J., Wang W., Wang X., Lu F., Zhang P., Lin Y., Fee R., Connell J. W., Sun Y-P.: Carbon nanosheets for polymeric nanocomposites with high thermal conductivity. *Advanced Materials*, **21**, 2088–2092 (2009).
DOI: [10.1002/adma.200802317](https://doi.org/10.1002/adma.200802317)
- [12] Sun X., Ramesh P., Itkis M. E., Bekyarova E., Haddon R. C.: Dependence of the thermal conductivity of two-dimensional graphite nanoplatelet-based composites on the nanoparticle size distribution. *Journal of Physics: Condensed Matter*, **22**, 334216/1–334216/9 (2010).
DOI: [10.1088/0953-8984/22/33/334216](https://doi.org/10.1088/0953-8984/22/33/334216)
- [13] Yang S-Y., Lin W-N., Huang Y-L., Tien H-W., Wang J-Y., Ma C-C. M., Li S-M., Wang Y-S.: Synergetic effects of graphene platelets and carbon nanotubes on the mechanical and thermal properties of epoxy composites. *Carbon*, **49**, 793–803 (2011).
DOI: [10.1016/j.carbon.2010.10.014](https://doi.org/10.1016/j.carbon.2010.10.014)
- [14] Raza M. A., Westwood A., Stirling C.: Carbon black/graphite nanoplatelet/rubbery epoxy hybrid composites for thermal interface applications. *Journal of Materials Science*, **47**, 1059–1070 (2012).
DOI: [10.1007/s10853-011-5895-8](https://doi.org/10.1007/s10853-011-5895-8)
- [15] Saw S. W. P., Mariatti M.: Properties of synthetic diamond and graphene nanoplatelet-filled epoxy thin film composites for electronic applications. *Journal of Materials Science: Materials in Electronics*, **23**, 817–824 (2011).
DOI: [10.1007/s10854-011-0499-2](https://doi.org/10.1007/s10854-011-0499-2)
- [16] Sun X., Yu A., Ramesh P., Bekyarova E., Itkis M. E., Haddon R. C.: Oxidized graphite nanoplatelets as an improved filler for thermally conducting epoxy-matrix composites. *Journal of Electronic Packaging*, **133**, 020905/1–020905/6 (2011).
DOI: [10.1115/1.4003988](https://doi.org/10.1115/1.4003988)
- [17] Teng C-C., Ma C-C. M., Lu C-H., Yang S-Y., Lee S-H., Hsiao M-C., Yen M-Y., Chiou K-C., Lee T-M.: Thermal conductivity and structure of non-covalent functionalized graphene/epoxy composites. *Carbon*, **49**, 5107–5116 (2011).
DOI: [10.1016/j.carbon.2011.06.095](https://doi.org/10.1016/j.carbon.2011.06.095)

- [18] Seo J., Cha J., Kim S.: Enhancement of the thermal conductivity of adhesives for wood flooring using xGnP. *Energy and Buildings*, **51**, 153–156 (2012). DOI: [10.1016/j.enbuild.2012.05.003](https://doi.org/10.1016/j.enbuild.2012.05.003)
- [19] Raza M. A., Westwood A. V. K., Stirling C.: Effect of processing technique on the transport and mechanical properties of graphite nanoplatelet/rubbery epoxy composites for thermal interface applications. *Materials Chemistry and Physics*, **132**, 63–73 (2012). DOI: [10.1016/j.matchemphys.2011.10.052](https://doi.org/10.1016/j.matchemphys.2011.10.052)
- [20] Min C., Yu D., Cao J., Wang G., Feng L.: A graphite nanoplatelet/epoxy composite with high dielectric constant and high thermal conductivity. *Carbon*, **55**, 116–125 (2013). DOI: [10.1016/j.carbon.2012.12.017](https://doi.org/10.1016/j.carbon.2012.12.017)
- [21] Kim J., Im H., Kim J-M., Kim J.: Thermal and electrical conductivity of Al(OH)₃ covered graphene oxide nanosheet/epoxy composites. *Journal of Materials Science*, **47**, 1418–1426 (2012). DOI: [10.1007/s10853-011-5922-9](https://doi.org/10.1007/s10853-011-5922-9)
- [22] Kim J., Yim B-S., Kim J-M., Kim J.: The effects of functionalized graphene nanosheets on the thermal and mechanical properties of epoxy composites for anisotropic conductive adhesives (ACAs). *Microelectronics Reliability*, **52**, 595–602 (2012). DOI: [10.1016/j.microrel.2011.11.002](https://doi.org/10.1016/j.microrel.2011.11.002)
- [23] Chatterjee S., Wang J. W., Kuo W. S., Tai N. H., Salzmann C., Li W. L., Hollertz R., Nüesch F. A., Chu B. T. T.: Mechanical reinforcement and thermal conductivity in expanded graphene nanoplatelets reinforced epoxy composites. *Chemical Physics Letters*, **531**, 6–10 (2012). DOI: [10.1016/j.cplett.2012.02.006](https://doi.org/10.1016/j.cplett.2012.02.006)
- [24] Chatterjee S., Nafezarefi F., Tai N. H., Schlagenhauf L., Nüesch F. A., Chu B. T. T.: Size and synergy effects of nanofiller hybrids including graphene nanoplatelets and carbon nanotubes in mechanical properties of epoxy composites. *Carbon*, **50**, 5380–5386 (2012). DOI: [10.1016/j.carbon.2012.07.021](https://doi.org/10.1016/j.carbon.2012.07.021)
- [25] He Z., Zhang X., Chen M., Li M., Gu Y., Zhang Z., Li Q.: Effect of the filler structure of carbon nanomaterials on the electrical, thermal, and rheological properties of epoxy composites. *Journal of Applied Polymer Science*, in press (2013). DOI: [10.1002/app.39096](https://doi.org/10.1002/app.39096)
- [26] Huang X., Zhi C., Jiang P.: Toward effective synergistic effects from graphene nanoplatelets and carbon nanotubes on thermal conductivity of ultrahigh volume fraction nanocarbon epoxy composites. *Journal of Physical Chemistry C*, **116**, 23812–23820 (2012). DOI: [10.1021/jp308556r](https://doi.org/10.1021/jp308556r)
- [27] Moussa A. A., Mullen K.: Using normal modes to calculate and optimize thermal conductivity in functionalized macromolecules. *Physical Review E*, **83**, 056708/1–056708/8 (2011). DOI: [10.1103/PhysRevE.83.056708](https://doi.org/10.1103/PhysRevE.83.056708)
- [28] Zhou T., Wang X., Liu X., Xiong D.: Improved thermal conductivity of epoxy composites using a hybrid multi-walled carbon nanotube/micro-SiC filler. *Carbon*, **48**, 1171–1176 (2010). DOI: [10.1016/j.carbon.2009.11.040](https://doi.org/10.1016/j.carbon.2009.11.040)
- [29] Zhou T., Wang X., Mingyuan G. U., Liu X.: Study of the thermal conduction mechanism of nano-SiC/DGEBA/EMI-2,4 composites. *Polymer*, **49**, 4666–4672 (2008). DOI: [10.1016/j.polymer.2008.08.023](https://doi.org/10.1016/j.polymer.2008.08.023)
- [30] Zhou T., Wang X., Gu M., Xiong D.: Study on mechanical, thermal and electrical characterizations of nano-SiC/epoxy composites. *Polymer Journal*, **41**, 51–57 (2009). DOI: [10.1295/polymj.PJ2008173](https://doi.org/10.1295/polymj.PJ2008173)
- [31] Zhou T., Wang X., Liu X. H., Lai J. Z.: Effect of silane treatment of carboxylic-functionalized multi-walled carbon nanotubes on the thermal properties of epoxy nanocomposites. *Express Polymer Letters*, **4**, 217–226 (2010). DOI: [10.3144/expresspolymlett.2010.28](https://doi.org/10.3144/expresspolymlett.2010.28)
- [32] Chen G., Weng W., Wu D., Wu C., Lu J., Wang P., Chen X.: Preparation and characterization of graphite nanosheets from ultrasonic powdering technique. *Carbon*, **42**, 753–759 (2004). DOI: [10.1016/j.carbon.2003.12.074](https://doi.org/10.1016/j.carbon.2003.12.074)
- [33] Yang D. J., Zhang Q., Chen G., Yoon S. F., Ahn J., Wang S. G., Zhou Q., Wang Q., Li J. Q.: Thermal conductivity of multiwalled carbon nanotubes. *Physical Review B*, **66**, 165440/1–165440/6 (2002). DOI: [10.1103/PhysRevB.66.165440](https://doi.org/10.1103/PhysRevB.66.165440)
- [34] Gojny F. H., Wichmann M. H. G., Fiedler B., Kinloch I. A., Bauhofer W., Windle A. H., Schulte K.: Evaluation and identification of electrical and thermal conduction mechanisms in carbon nanotube/epoxy composites. *Polymer*, **47**, 2036–2045 (2006). DOI: [10.1016/j.polymer.2006.01.029](https://doi.org/10.1016/j.polymer.2006.01.029)

Influence of end groups in hyperbranched polyesters used as modifiers in the characteristics of epoxy thermosets cured by adipic dihydrazide

A. M. Tomuta¹, X. Ramis², S. de la Flor³, A. Serra^{1*}

¹Department of Analytical and Organic Chemistry, Universitat Rovira i Virgili, C/Marcel·lí Domingo s/n, 43007 Tarragona, Spain

²Laboratory of Thermodynamics, ETSEIB, Universitat Politècnica de Catalunya, Diagonal 647, 08028 Barcelona, Spain

³Department of Mechanical Engineering, Universitat Rovira i Virgili, C/ Països Catalans 26, 43007 Tarragona, Spain

Received 24 January 2013; accepted in revised form 27 March 2013

Abstract. Mixtures of diglycidylether of bisphenol A (DGEBA) resin and different ratios of aliphatic-aromatic hyperbranched polyester (HBP) were cured by a latent curing agent, adipic dihydrazide (AH). The HBPs prepared have hydroxyl groups or 10-undecenoyl or allyl groups as chain ends. The curing mixtures were investigated by differential scanning calorimetry (DSC) to study the curing process and to evaluate the kinetic parameters of the different formulations. These studies suggest that HBPs decrease the curing rate of epoxy/AH in the case of vinyl terminated HBP, whereas OH terminated HBP accelerates the first stages and delays the lasts.

The thermosets obtained showed an improvement in microhardness and impact strength without any reduction of the T_g and thermal parameters. Microparticle phase separation was observed with the undecenoyl HBP derivatives or when a 10% of allyl HBP derivative was in the formulation.

Keywords: thermosetting resins, toughness, hyperbranched polymers, latency, dihydrazides

1. Introduction

Epoxy resins are widely used in several applications: adhesives, coatings, castings, electric laminates, encapsulation of semiconductor devices, matrix materials for composites, structural components and engineering [1, 2], because of their good characteristics such as adhesion and chemical resistance. However, due to their high cross-link density they are inherently brittle, which limits their applicability. With the aim to increase their toughness different types of modifiers have been added to epoxy formulations such as rubber, thermoplastic and core-shell particles. The addition of liquid rubbers and thermoplastics was one of the first attempts to improve toughness, but usually this method has a

detrimental effect on the thermomechanical characteristics of the thermosets and the processability of the formulation [3], which is a drawback for coatings applications [4, 5]. To solve the limitations related to processability, hyperbranched polymers (HBPs) were introduced as toughness modifiers [6–8]. The advantage is that their highly branched structure prevents entanglement, reducing the viscosity of the formulation in comparison to the use of their linear analogues. Moreover, the great number of terminal groups has a significant effect on the reactivity, can increase the compatibility with the resin and helps to maintain thermomechanical characteristics [9, 10]. Based on their unique properties, HBPs have been applied not only as tougheners for ther-

*Corresponding author, e-mail: angels.serra@urv.cat
© BME-PT

mosets but also in cross-linking or adhesive agents [11], compatibilizers [12], dispersers [13], processing aids, and rheology modifiers [14, 15].

One of the most effective methods of inhibiting crack growth after impact is the addition of a second phase that induces the formation of particles that absorb the impact energy and deflect the crack [5]. Usually, the particles are generated from a homogeneous solution composed of the resin, curing agent and modifiers, which on curing causes a reaction-induced phase separation (RIPS) to take place. The phase separated morphology is highly dependent on the kinetics of curing and on the dynamics of the phase separation process.

The synthesis and characterization of aromatic-aliphatic hyperbranched polyesters modified with long and short vinylic chains and their use as modifiers of DGEBA thermosets cured with hexahydro-4-methylphthalic anhydride was reported by us [16]. The addition of these modifiers led to significantly increased rates of cure. However, the materials obtained were homogeneous and the increase in impact strength was only modest. In addition, the HBPs led to a plasticization and to a considerable decrease in the T_g .

In a previous paper we demonstrated the latent character of a series of dihydrazides in the thermal curing of DGEBA [17]. Several dihydrazides were synthesized and used as stoichiometric curing agents of epoxy resins. From the dihydrazides synthesized, AH was the one that leads to curing at the lowest temperature (maximum of the curing exotherm at 165°C) and led to materials with good characteristics. However, dihydrazides possess a high crystalline character and they are difficult to disperse or dissolve, because on melting (at 181–184°C) the curing process is extremely fast.

In the present work, the influence of the addition of aromatic-aliphatic hyperbranched polyesters modified with long and short vinylic chains (see Figure 1) to the epoxy formulation has been studied with two different aims: to increase toughness and help to disperse AH in the DGEBA resin. In addition, it was expected from the fast curing process caused by the dihydrazides at the appropriate temperature that could induce phase separated morphologies, when the HBP structure cannot be covalently incorporated to the epoxy matrix, because of its solubility and the end group characteristics.

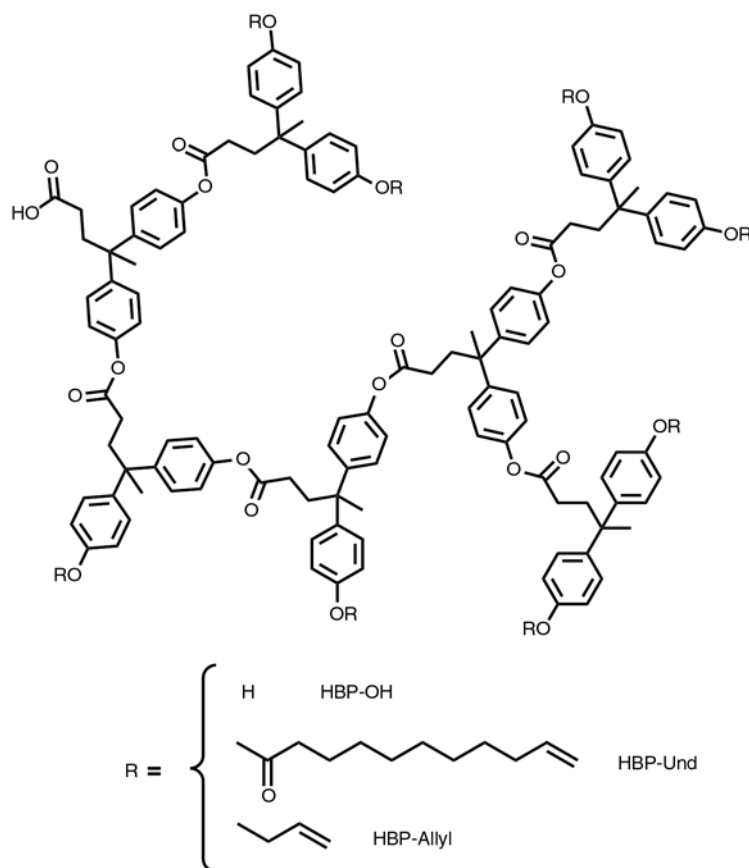


Figure 1. Structure of the HBP modifiers added to the formulations

2. Experimental

2.1. Materials

4,4-Bis(4-hydroxyphenyl) valeric acid, N,N'-dicyclohexylcarbodiimide (DCC), triethyl amine, allyl bromide, 10-undecenoyl chloride, diethyl adipate and hydrazine hydrate were purchased from Sigma Aldrich (St. Louis, MO, USA) and used without further purification. Diglycidyl ether of Bisphenol A (DGEBA) Epikote Resin 828 was provided by Momentive Speciality Chemicals Inc. (Barbastro, Spain) with an epoxy equivalent of 184 g/eq and was dried in vacuum before use. All the organic solvents were purchased from Scharlab and purified by standard procedures. 4-(N,N-dimethylamino) pyridinium p-toluenesulfonate (DPTS) was prepared as described in the literature [18].

2.2. Synthesis of adipic dihydrazide (AH)

50.5 g (0.25 mol) of the diethyl adipate were dissolved in 200 mL of absolute ethanol and 0.9 mol of hydrazine hydrate (90%) were added drop by drop. Once the addition was complete the heating was turned on and the mixture was kept 6 h at reflux. During this time a white precipitate was formed, which was filtered through a Buchner funnel and then washed twice with cold ethanol. The white powder was dried in the vacuum oven at 50°C. The obtained yield was higher than 90%. m.p. 181–4°C (recrystallized from ethanol). ¹H NMR (DMSO-d₆, δ in ppm): 8.93 s (2H, –NH–); 4.14 s (4H, –NH₂); 1.97 t (4H, –CH₂–) 1.41 m (4H, –CH₂–); ¹³C NMR (DMSO-d₆, δ in ppm): 171.49 (–CONH–); 33.27 (–CH₂–); 24.99 (–CH₂–). FTIR-ATR (cm⁻¹): 3310, 3288, 3197, 1626, 1529, 1376, 1273, 1166, 1033, 690.

2.3. Hyperbranched polyester synthesis (HBP-OH)

The HBP-OH (Figure 1) was synthesized according to a previously described procedure [19] from 4,4-bis(4-hydroxyphenyl) valeric acid as AB₂ monomer. The ¹H and ¹³C NMR data are in accordance with those published [20].

M_n: 8700 g/mol, *M_w*: 12300 g/mol. *T_g* 121°C (by DSC). The amount of hydroxyl groups was determined according to ISO 2554-1974 standards. The number of hydroxyl groups per molecule found by titration was 36 [16].

2.4. Derivatization of HBP-OH with 10-undecenoyl chain ends (HBP-Und)

The derivatization was done from HBP-OH (Figure 1) synthesized previously by reacting with 10-undecenoyl chloride in the presence of triethylamine, as previously described [16]. The product was dried in a vacuum oven at 50°C overnight and a pale brown viscous liquid was obtained. Yield: 94% *T_g* 18°C (by DSC).

¹H NMR (400 MHz, CDCl₃), δ (ppm): 1.26 m (–CH₂–); 1.41 m (–CH₃); 1.68 m (–CH₂–); 2.06 m (–CH₂–); 2.34 m (–CH₂–); 2.55 m (–CH₂–); 5.10 dd (CH₂=); 5.87 m (=CH–); 7.11 m (CH Ar).

¹³C NMR (100.6 MHz, CDCl₃), δ (ppm): 24.7 (–CH₂–); 27.6 (–CH₂–); 28.9 (–CH₂–); 33.6 (–CH₂–); 34.3 (–CH₂–) 36.2 (–CH₂–); 45.4 (=C=); 113.9 (CH₂=); 121.2 (Ar) ; 128.2 (Ar); 139.0 (=CH–); 145.6 (Ar); 148.6 (Ar); 172.3 (C=O).

2.5. Derivatization of HBP-OH with allyl chain ends (HBP-Allyl)

The derivatization was performed by nucleophilic substitution on allyl bromide by the phenolate end groups, formed by treating HBP-OH (Figure 1) with K₂CO₃ in a mixture of THF and acetone, as previously reported [16]. HBP-Allyl was obtained by precipitating the THF solution on water. The polymer was dried in a vacuum oven at 50°C overnight and a white powder was obtained. Yield: 90%. *T_g* 81°C (by DSC).

¹H NMR (400 MHz, CDCl₃), δ (ppm): 1.65 s (–CH₃–); 2.36 m (–CH₂–); 2.53 (–CH₂–); 4.53 s (–CH₂–); 5.35 dd (CH₂=); 6.07 m (=CH–); 6.8–7.2 m (CH Ar).

¹³C NMR (100.6 MHz, CDCl₃), δ (ppm): 28.0 (–CH₂–); 30.6 (–CH₂); 36.6 (–CH₂–); 45.1 (=C=); 68.9 (–CH₂–); 114.3 (Ar); 117.9 (CH₂=) ; 128.4 (Ar); 133.5 (=CH–); 141.2 (Ar); 156.9 (Ar); 172.5 (C=O).

2.6. Preparation of the curing mixtures

The neat DGEBA/AH formulation was prepared by adding the stoichiometric amounts of each reactant to a mortar and homogenizing them by mechanical mixing while heating at 90°C. For the preparation of the formulations with the HBP modifiers, first of all the corresponding proportion was dissolved in DGEBA by adding a little amount of THF. The sol-

vent was then eliminated in vacuum at 50°C overnight and then the stoichiometric amount of AH was added and homogenized by mixing in a mortar while heating at 90°C. The proportions of HBPs added were a 5 and 10% w/w in reference to DGEBA. AH was added in a molar proportion to DGEBA of 1:2.

2.7. Measurements

The 400 MHz ^1H NMR and 100.6 MHz ^{13}C NMR spectra were obtained with a Varian Gemini 400 spectrometer with Fourier Transformed (Palo Alto, California USA). ^1H NMR spectra were acquired in 1 min and 16 scans with a 1.0 s relaxation delay (D1). ^{13}C NMR spectra were obtained using a D1 of 0.5 s and an acquisition time of 0.2 s. A total of 500 accumulations were recorded. CDCl_3 was used as a solvent and tetramethylsilane (TMS) as internal standard.

Calorimetric analyses were carried out on a Mettler DSC-821e calorimeter (Greifensee, Switzerland). Samples of approximately 10 mg were cured in aluminium pans in a nitrogen atmosphere. Non-isothermal experiments were performed from 0 to 225°C at heating rates of 2, 5, 10, and 15°C/min to determine the reaction heat and the kinetic parameters. In the non-isothermal curing process, the degree of conversion at a given temperature T was calculated as the quotient between the heat released up to T and the total reaction heat associated with the complete conversion of all reactive groups. The precision of the given enthalpies is $\pm 3\%$. The T_g s of the cured materials were determined with a second scan at 20°C/min after dynamic curing by the mid-point method and the error is estimated to be approximately $\pm 1^\circ\text{C}$. The T_g s of the pure HBPs were determined by a similar procedure.

Dynamic mechanical thermal analysis (DMTA) was carried out with a TA Instruments DMTA 2980 analyzer (New Castle, USA). The samples were cured isothermally in a mould at 190°C for 1 h and then post-cured for 0.5 h at 200°C. Before the samples were prepared, they were degassed in a vacuum oven at 50°C for 3 h. Single cantilever bending at 1 Hz was performed at 3°C/min from 30 to 220°C on prismatic rectangular samples ($1.5 \times 20 \times 5 \text{ mm}^3$). Thermogravimetric analysis was carried out with a Mettler-Toledo TGA/SDTA 851e thermobalance

(Greifensee, Switzerland). Cured samples with an approximate mass of 5 mg were heated from 30 to 800°C at a heating rate of 10°C/min in a nitrogen atmosphere.

Impact tests were performed at room temperature by means of a Zwick 5110 impact tester (Altamonte Springs, USA) according to ASTM D 4508-05 using rectangular samples ($25 \times 12 \times 2.5 \text{ mm}^3$). The pendulum employed had a kinetic energy of 1 J. For each material, 9 determinations were made. The impact strength (IS) was calculated from the energy absorbed by the sample upon fracture according to Equation (1):

$$IS = \frac{E - E_0}{S} \quad (1)$$

where E and E_0 are the energy loss of the pendulum with and without sample respectively, and S is the cross-section of the samples.

The fracture area of impacted samples was metalized with gold and observed with a scanning electron microscope (SEM) Jeol JSM 6400 (Tokyo, Japan).

The kinetic triplet (pre-exponential factor, activation energy, and the kinetic model) of the curing was determined using integral isoconversional non-isothermal kinetic analysis, Kissinger-Akahira-Sunose equation, combined with the Coats-Redfern procedure. Details of the kinetic methodology are given in previous studies [21].

Microhardness was measured with a Wilson Wolpert (Micro-Knoop 401MAV) device (Massachusetts, USA) following the ASTM D1474-98 (2008) standard procedure. For each material 10 determinations were made with a confidence level of 95%. The Knoop microhardness (HKN) was calculated from Equation (2):

$$HKN = \frac{L}{A_p} = \frac{L}{l^2 C_p} \quad (2)$$

where L is the load applied to the indenter (0.025 kg), A_p is the projected area of indentation in mm^2 , l is the measured length of long diagonal of indentation in mm, and C_p is the indenter constant ($7.028 \cdot 10^{-2}$) relating l^2 to A_p . The values were obtained from 10 determinations with the calculated precision (95% of confidence level).

3. Results and discussion

3.1. Calorimetric study of the curing process and the thermosets obtained

In the preparation of epoxy thermosets, the selection of the curing agent is crucial to obtaining good thermoset properties but especially when a HBP modifier is added to the formulation, because of the role played by the chemistry of the curing agent in the possible reaction of the terminal groups in the HBP structure. A number of authors used primary amines as curing agents, which did not allow the covalent incorporation of hydroxyl terminated HBPs to the epoxy matrix and thus microphase separation in the final material could be observed [22, 23]. In the present study, the addition of a 5 or 10% in weight of HBP-OH and its derivatives with allyl and 10-undecenoyl chain ends should not react with dihydrazides and phase separation could also be expected. However, not only the chemistry of the terminal groups but also the structure of the HBP and the curing rate can influence the phase separation process.

In a previous paper, we reported the study of the curing process of DGEBA with some dihydrazides and concluded that the stoichiometric proportion is 2 mol of DGEBA per each mol of dihydrazide. The structure of the network formed was confirmed by FTIR analysis and is represented in Figure 2.

The curing could be catalyzed by acidic and basic catalysts but the latent character was reduced, and therefore some effects on the curing evolution can be expected on adding HBP modifiers.

We studied the curing process by non-isothermal scanning calorimetry. The calorimetric curves col-

lected in Figure 3 show the curing exotherms for all the formulations studied. The plot of conversion against temperature for all the studied formulations is represented in Figure 4 and the calorimetric data are collected in Table 1. In this plot, we can observe

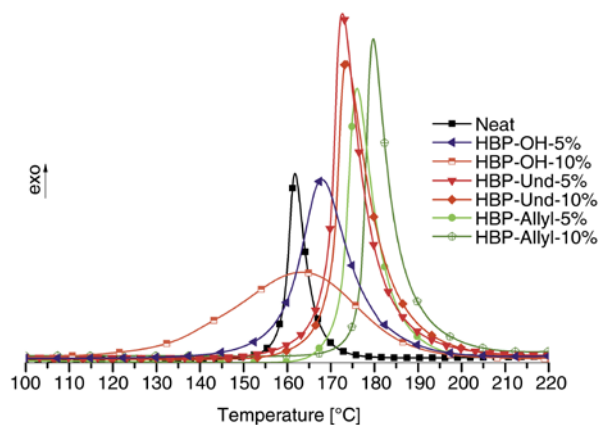


Figure 3. Calorimetric curves for the formulations studied obtained in DSC scans at 10°C/min under N₂

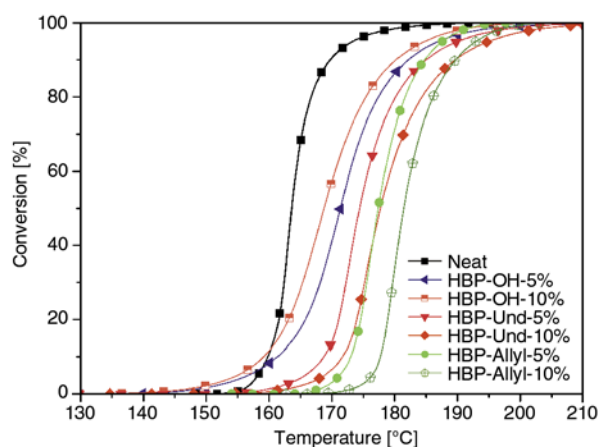


Figure 4. Conversion against temperature of the dynamic curing at 10°C/min of all the formulations studied

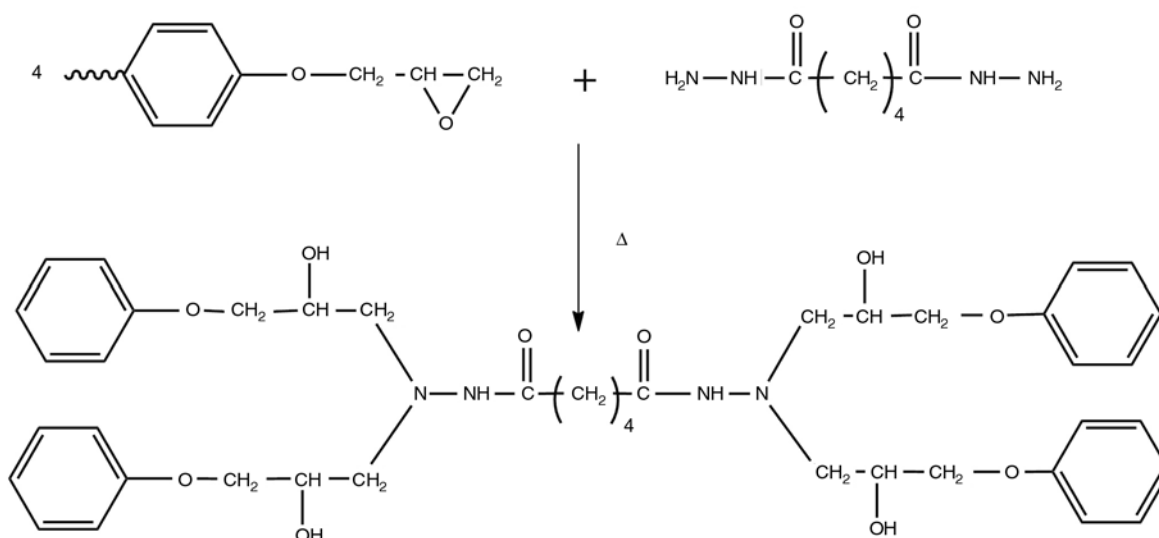


Figure 2. Structure of the network formed by reaction of the epoxy resin and the adipic dihydrazide

Table 1. Calorimetric data and kinetic parameters obtained in the curing of all the formulations

Thermoset	T_{\max}^a [°C]	Δh^b [J/g]	Δh^b [kJ/eq]	T_g^c [°C]	T_{gFox}^d [°C]	E_a^e [kJ/mol]	$\ln A^f$ [s ⁻¹]	$k_{170^\circ C}^g$ [min ⁻¹]
Neat	165	408	96	128	128	170	49.2	21.3
HBP-OH-5%	170	352	90	130	128	114	33.0	7.1
HBP-OH-10%	167	331	89	138	127	99	29.0	7.3
HBP-Und-5%	172	355	91	127	121	117	33.4	5.0
HBP-Und-10%	176	327	88	123	113	117	33.1	4.5
HBP-Allyl-5%	180	273	70	123	125	161	45.3	4.7
HBP-Allyl-10%	177	285	78	128	121	127	35.7	3.0

^aTemperature of the maximum of the curing exotherm registered at 10°C/min.

^bEnthalpy of the curing exotherm registered at 10°C/min.

^c T_g determined after curing in a dynamic scan registered at 20°C/min.

^d T_g calculated by the Fox equation.

^eValues of activation energy at 50% of conversion, evaluated by the isoconversional non-isothermal procedure.

^fPre-exponential factors calculated for autocatalytic model ($n = 2.1$, $m = 0.9$) with $g(\alpha) = [(1-\alpha)\alpha^{-1}]^{-0.9}(0.9)^{-1}$.

^gValues of rate constants at 170°C using the Arrhenius equation at 50% conversion.

that the latent character of the curing of the neat formulation is slightly reduced on adding the HBP modifiers. The effect on the latency seems to be more noticeable on adding HBP-OH, which catalyzes the first stages of the curing process. However, a delay is observed at higher conversions. The catalytic effect is increased with the proportion of HBP-OH in the formulation. This can be explained by the presence of phenolic groups, which can facilitate the nucleophilic attack of the nitrogen on the epoxy ring by the formation of hydrogen bonds, as is described for epoxy-amine formulations [24]. Since during curing of epoxy resins with active NH₂ moieties OH groups are always formed, the effect of the phenolic groups of the HBP is not as noticeable when the conversion reaches a certain extent. Moreover, the viscosity of the reactive mixture increases and can delay the curing process. The addition of HBP-Und and HBP-Allyl leads to a significant reduction of the curing rate, and higher temperatures are needed to cure these formulations. However, there is not a clear dependence of the curing rate with the amount of modifier. In a previous study in epoxy-anhydride thermosets with both modified HBPs an acceleration of the curing was observed in spite of the higher viscosities of the formulations. This acceleration was attributed to the presence of carboxylic groups in the focal point of the HBPs, which can catalyze the curing process [16]. In the present case using dihydrazides, the dilution effect on adding the modifiers and the increase in the viscosity seem to greatly influence the curing rate in comparison to the acidic catalysis produced by carboxylic groups [17].

From the values in Table 1 we can observe that the curing enthalpy of the formulations containing HBP modifiers is somewhat lower than that measured for the neat formulation, but in all cases the curing was complete, as identified by the complete disappearance of the band at 910 cm⁻¹ in the FTIR of the final thermosets. It should be stressed that the T_g measured for the modified thermosets does not decrease significantly, and even increases in the case of adding HBP-OH to the formulation. If we consider the T_g s of the different hyperbranched T_g^{HBP} and the T_g of the neat material and apply these values and the corresponding proportions (w) in the Fox equation [25] (Equation (3)) we can predict the T_g values of the homogeneously blended modified thermosets:

$$\frac{1}{T_g} = \frac{w}{T_g^{HBP}} + \frac{1-w}{T_g^{neat}} \quad (3)$$

As can be seen in Table 1, only the thermoset with a 5% of Allyl-HBP has an experimental value of T_g similar to that predicted by this equation, whereas the addition of the other vinylic modified HBPs does not significantly influence the T_g determined for the neat material. This result can be explained by a phase separation of the HBPs due to the incompatibility produced during the curing reaction, which will be further confirmed by SEM. Since the initial solution was fully compatible, the separation of the particles is originated by a reaction-induced phase separation process (RIPS), which is highly dependent on the kinetics of curing and on the dynamics of the phase separation process. It should be pointed out, that the same HBP-Allyl and HBP-Und were

used as modifiers of DGEBA/anhydride thermosets, leading to completely homogeneous materials [16]. The higher curing rate when dihydrazides are used as curing agents and the highly polar structure of the network produced with this agent could both be responsible for the phase separation process, since these HBPs cannot be chemically incorporated into the epoxy network and have non-polar characteristics, especially in case of HBP-Und, as a result of the presence of the long aliphatic chains. Thus, the addition of a 5% of HBP-Allyl to the formulation leads to a homogeneous material because of its higher compatibility, due to its shorter aliphatic structure. On adding HBP-OH to the formulation, the T_g of the final thermosets is even higher than that predicted by the Fox equation. This unexpected result in fully homogeneous materials can be rationalized by the reduction in free volume due to the hydrogen bonding established between the OH groups of HBP and the epoxy-dihydrazide network [26].

In Table 1, the kinetic parameters calculated for the curing of the different formulations are collected. The kinetics of these systems was studied by the non-isothermal isoconversional procedure, as explained in the experimental part and in a previous article [21]. Figure 5 shows the evolution of the activation energy against conversion for the formulations studied.

As is shown in the Figure 5, the activation energy remains, during curing, nearly constant for all formulations. This result suggests that the reaction mechanism is the same in the whole range of curing and only a single kinetic model is needed to describe the curing. In many reaction processes the values of

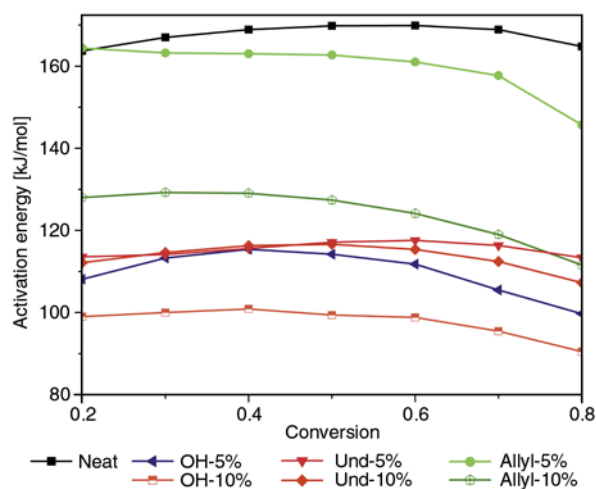


Figure 5. Apparent activation energies against conversion of all the formulations studied

activation energy, due to the compensation effect between the activation energy and the pre-exponential factor [27], do not reflect exactly the reaction rate and it is better to discuss the rate constants calculated using the Arrhenius equation and the aforementioned kinetic parameters. To calculate the frequency factors, we selected the kinetic model that best fits the experimental data, which for all formulations was the autocatalytic kinetic model with $n = 2.1$ and $m = 0.9$. This kinetic model is consistent with the accelerative effect of the hydroxyl groups generated during curing.

The calculated values of the rate constants (Table 1) illustrate the order of reactivity on curing at a conversion of 0.5 and agree with the experimental conversion-temperature curves. In this conversion, all the HBP modifiers show a delaying effect on the curing rate, as can be also observed in Figure 4. However, this effect is not produced at the beginning of curing in the case of the formulations containing HBP-OH, where hydroxyl terminal groups accelerate the curing.

3.2. Characterization of the materials by TGA and DMTA

Table 2 and Figure 6 present the thermogravimetric data and the derivatives of the TGA curves, respectively.

The thermosets obtained show a higher resistance to thermal degradation than the neat material, since the ester groups introduced are aromatic and therefore there is no β -elimination process that finally leads to the formation of little fragments that can be lost on heating. There is also no effect on the temperature of the maximum degradation rate, but the shape of the curves changes on modifying the mate-

Table 2. Thermogravimetric data for all the thermosets obtained

Thermoset	$T_{5\%}^a$ [°C]	T_{max}^b [°C]	Char yield ^c [%]
Neat	287	337–390	12.2
OH-5%	292	344–407	13.2
OH-10%	290	352–398	14.1
Und-5%	293	355–404	14.5
Und-10%	291	356–402	14.6
Allyl-5%	297	360–400	13.7
Allyl-10%	296	350–410	13.8

^aTemperature of the 5% of weight loss in N_2 atmosphere.

^bThe temperature of the peaks of the derivative on the thermogram registered in N_2 atmosphere.

^cChar yield after a dynamic scan until 600°C in N_2 atmosphere.

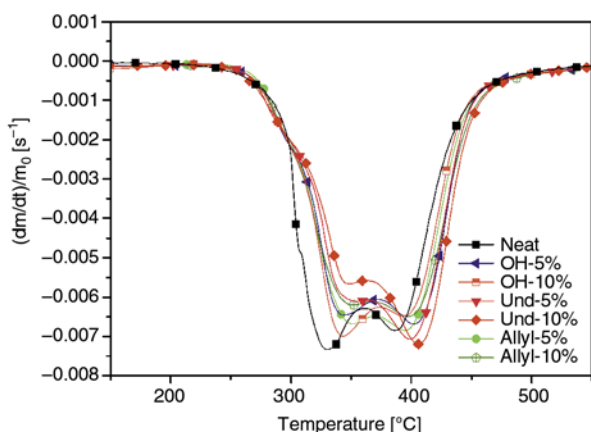


Figure 6. Derivatives of the TGA curves in N_2 atmosphere for the thermosets obtained

rials. As we can see, all the degradation curves are bimodal, indicating two different degradative processes. In case of the neat material, the peak at lower temperature is more pronounced than the one occurring at higher temperature, whereas in case of the material containing a 10% of HBP-Und the contrary trend is observed. This can be related to the lower proportion of OH groups in the latter.

Figures 7 and 8 show the curves of the storage modulus and $\tan \delta$, respectively, for all the thermosets prepared obtained by DMTA. In Figure 7 we can see that the modulus in the rubbery state is similar for the neat and HBP-OH formulations, which seems to indicate that the crosslinking density, either covalently or by hydrogen bonding, is quite similar. On the contrary, the presence of HBP-Allyl and HBP-Und leads to a reduction of the modulus. From Figure 8, it can be seen that the temperature of the maximum of the $\tan \delta$ peak is quite similar for all the thermosets studied, but the values are higher

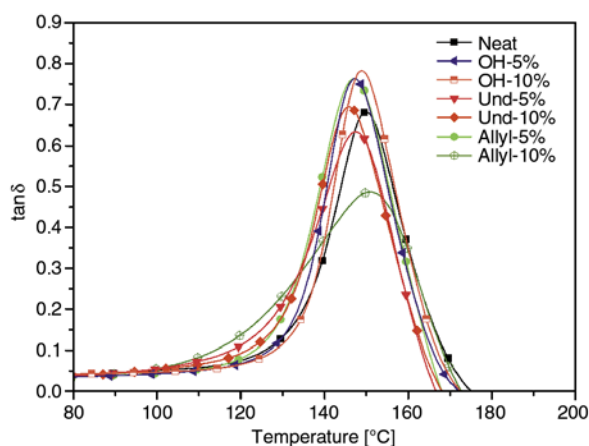


Figure 7. Evolution of storage modulus against temperature at 1 Hz for all the thermosets obtained

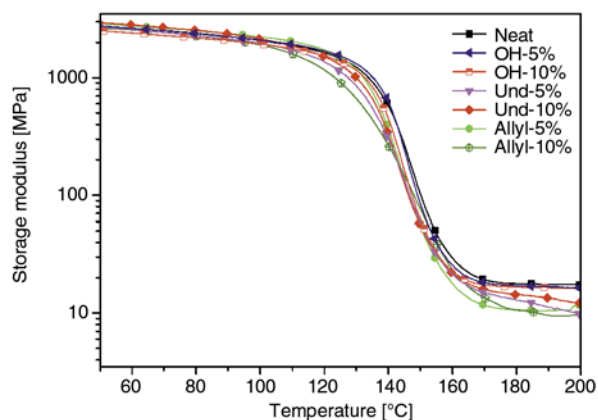


Figure 8. Evolution of $\tan \delta$ against temperature at 1 Hz for all the thermosets obtained

than those obtained by DSC, because of the differences in the frequency applied in DMTA technique. It should be noted that the materials containing a 10% of HBP-Allyl or HBP-Und show a much broader curve indicating their lower homogeneity.

3.3. Mechanical and morphological characterization

Microhardness measurements are very useful in rating coatings on rigid substrates as a measure of the resistance that one body offers against penetration by another under static loads. These measurements were carried out with a Knoop microindenter and the results are shown in Figure 9.

As can be seen, the addition of all the HBP modifiers does not reduce this parameter but even increases it, which is advantageous in the performance of the coatings. The best formulation in terms

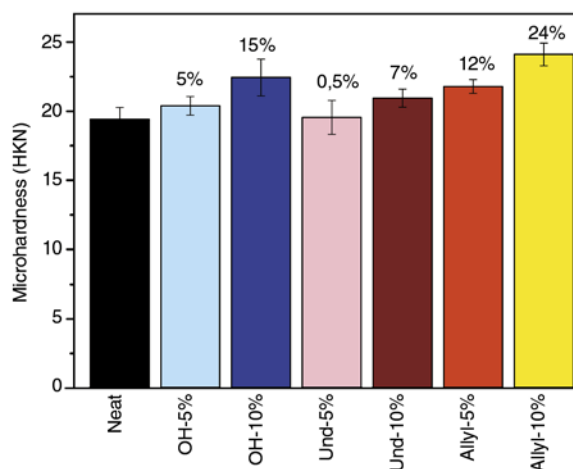


Figure 9. Microhardness values of the thermosets prepared. The increase in microhardness respect to the neat formulation is also indicated.

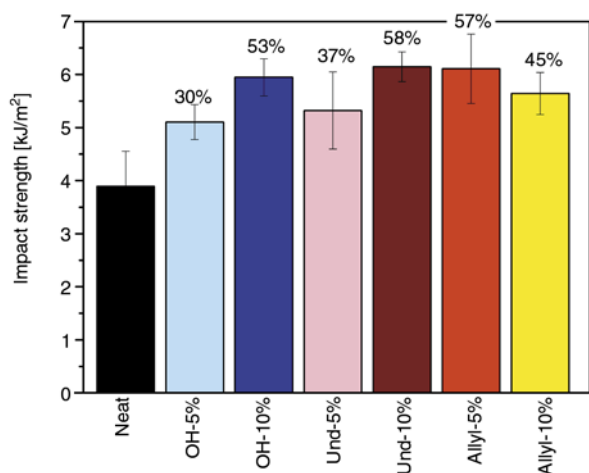


Figure 10. Impact strength values of the thermosets prepared

of microhardness enhancement is the one containing a 10% of HBP-Allyl.

The results of the impact tests are collected in Figure 10 for all the materials prepared. The values correspond to the energy absorbed by the material during crack propagation. It is possible to prove that the modification of DGEBA/AH thermosets with all the HBPs synthesized improves this value, as it was reported in previous publications on epoxy/amine or anhydride systems [28].

As we can see, all the modified thermosets present a higher value than the neat material. The highest values were obtained with a 10% of HBP-Und or a 5% of HBP-Allyl. In reference to the impact strength values, it should be pointed out that the neat system is tougher than the DGEBA/MHHPA neat material studied in a previous publication (2.4 to 3.9 kJ/m²) [16]. This illustrates the important role of the curing agent in the characteristics of the thermosets. Moreover, the addition of HBP-Und and HBP-Allyl to DGEBA/dihydrazide materials results in a greater improvement of the toughness characteristics in comparison with DGEBA/MHHPA thermosets.

The SEM micrographs of the impacted fracture surfaces are collected in Figure 11. These show a fracture surface with cracks and river-line structures in different planes in the neat material in accordance with the impact strength measured. In agreement with our earlier interpretations, on comparing the experimental T_g s which are higher than those predicted by the Fox equation, materials containing a 5% of HBP-Und or a 10% of both vinylic modifiers show a clear phase separation of the HBP from the epoxy matrix. Usually, particle phase separated

materials have enhanced toughness characteristics [5, 29]. However, the thermoset containing a 10% of HBP-OH shows a notable improvement in impact strength, quite similar to phase separated materials, but it presents a homogeneous appearance with a patterned roughness. This type of morphology was previously observed by us in materials obtained with 1-methylimidazole, which cured very fast as is also the case here [30]. The T_g measured for this thermoset does not indicate plasticization, related to ductility, that dictate its toughness characteristics [31]. However, the rougher surface appearance observed in the fractographs containing HBP-OH blends, suggests that the impact specimens experienced more plastic deformation during fracture in comparison with the unmodified epoxy network.

As we can see, materials with a 5 or a 10% in weight of HBP-Allyl show very different fracture morphologies. Whereas the first one, present a homogeneous appearance with unidirectional cracks, river-line structures and striations, the second present nanoparticles (of about 300 nm) distributed in the surface, which leads to high expanded cracks. In both materials containing HBP-Und a microphase separation is observed which stops or deflects the crack propagation. In both cases, the size of the particles has a broad distribution, and more particles with a bigger size (average about 1.5 μ m) can be observed for the material containing a larger proportion of modifier.

In Figure 12, a more detailed micrograph of the fracture surface for the material containing a 10% of HBP-Und is shown. As we can see, when the crack reaches the particle, it terminates and the energy is dissipated around the particle of HBP. This indicates that there is no interfacial adhesion between epoxy network and HBP-Und as expected as a result of the loss of hydrogen bonding by derivatization of phenolic groups. Some authors reported that the improvement in the interfacial adhesion of epoxy resin and HBP particles contributes to an improvement of the failure behaviour of epoxy resin/HBP blends [27]. According to that argument, the nano/microphase separation reached in the present study does not very effectively enhance the toughness, as was expected. HBP-OH modifiers do not separate because of the compatibility with the epoxy matrix. However, the improvement in toughness is achieved in all the materials obtained in the present work without any decrease of T_g or deterioration of the

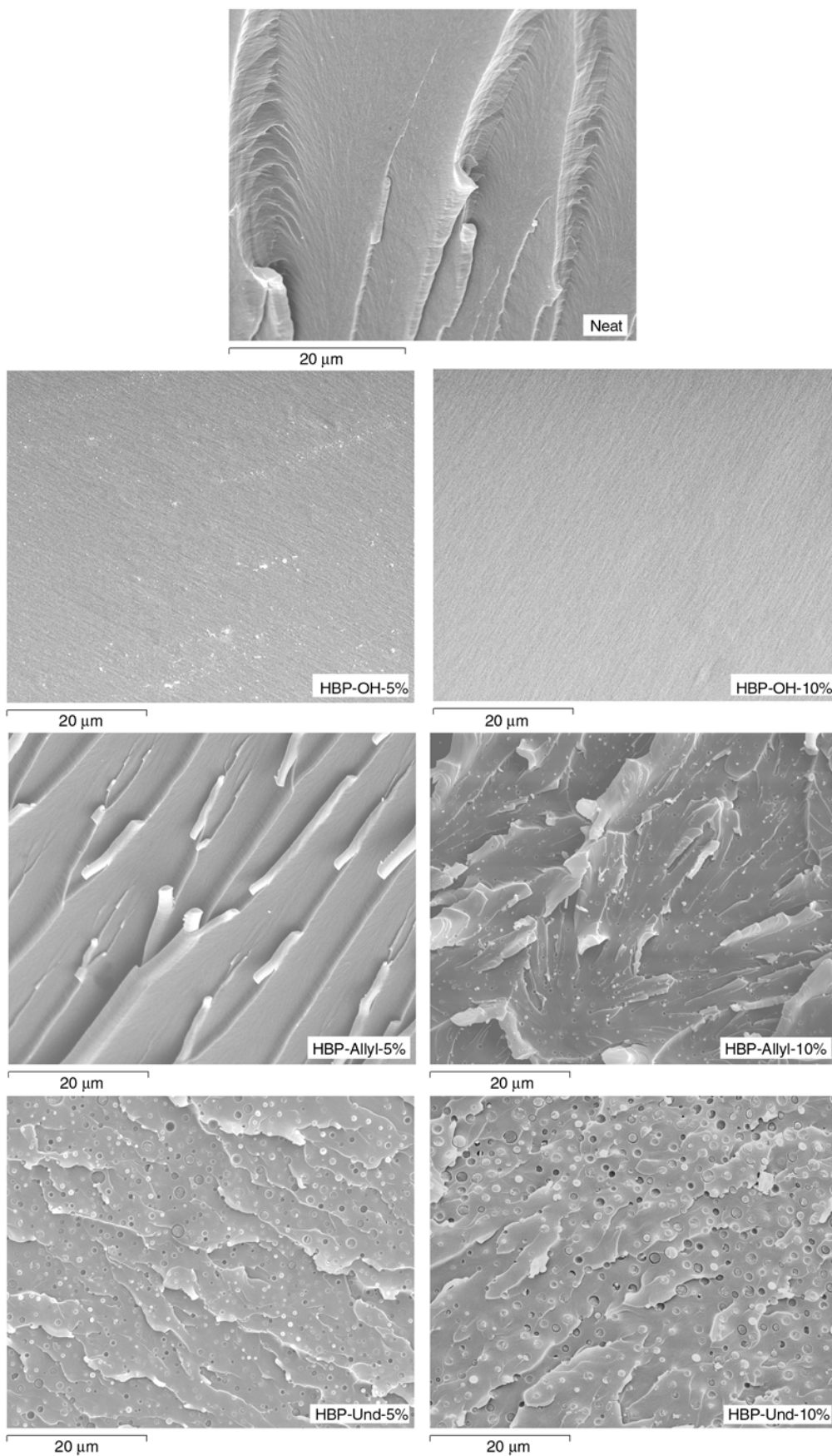


Figure 11. SEM micrographs from impacted fracture surfaces of the thermosets prepared at 2000 magnifications

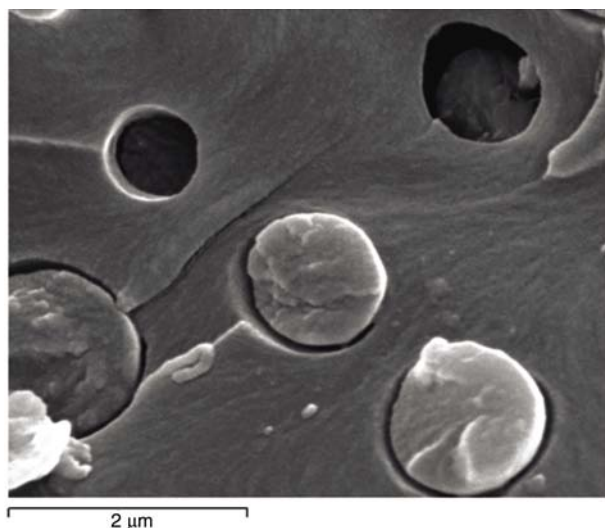


Figure 12. SEM micrograph of the impacted fracture surface for the thermoset containing a 10% of HBP-Und at 20000 magnifications

thermal characteristics and microhardness without forgetting that the addition of HBPs helps to reach a good dispersion of the dihydrazide in the formulation.

4. Conclusions

A series of HBPs with OH or vinyl groups of different length as chain ends were synthesized and used as modifiers in DGEBA/AH formulations. The addition of the HBPs helped to disperse and to compatibilize the crystalline dihydrazide in the reactive mixture.

The addition of HBP-OH to the formulation increased the curing rate at the beginning of the curing but decreased it at high conversion, and slightly reduced the latency of the adipic dihydrazide as DGEBA curing system. The addition of HBP-Allyl and HBP-Und led to a significant reduction of the curing rate and higher curing temperatures were needed to reach the complete curing of these formulations.

The T_g values of the modified thermosets were not significantly lower than that of the neat material and were even higher when HBP-OH was blended in the thermoset. This was attributed to the hydrogen bonding of the phenolic groups with the epoxy matrix. When 5 or 10% of HBP-Und or 10% of HBP-Allyl was incorporated into the material a nano or microphase separation was observed by SEM, which explains why no reduction in the T_g was observed. The materials showed a higher resistance to thermal degradation on adding the modifiers.

Microhardness and impact strength values were improved by adding all the HBP modifiers to the formulations.

Acknowledgements

The authors would like to thank MINECO (MAT2011-27039-C03-01, MAT2011-27039-C03-02) and Generalitat de Catalunya (2009-SGR-1512) for giving financial support. A.T. acknowledges the grant FI-DGR 2010 given by the Generalitat de Catalunya.

References

- [1] May C. A.: Epoxy resins. Chemistry and technology. Marcel Dekker, New York (1988).
- [2] Petrie E. M.: Epoxy adhesive formulations. McGraw-Hill, New York (2006).
- [3] Zheng S.: Nanostructured epoxies by the use of block copolymers. in 'Epoxy polymers: New materials and innovations' (eds.: Pascault J. P., Williams R. J. J.) Wiley, Weinheim, 81–108 (2010). DOI: [10.1002/9783527628704.ch5](https://doi.org/10.1002/9783527628704.ch5)
- [4] Pearson R. A., Yee A. F.: Toughening mechanisms in thermoplastic-modified epoxies: 1. Modification using poly(phenylene oxide). *Polymer*, **34**, 3658–3670 (1993). DOI: [10.1016/0032-3861\(93\)90051-B](https://doi.org/10.1016/0032-3861(93)90051-B)
- [5] Bagheri R., Marouf B. T., Pearson R. A.: Rubber-toughened epoxies: A critical review. *Journal of Macromolecular Science Part C: Polymer Review*, **49**, 201–225 (2009). DOI: [10.1080/15583720903048227](https://doi.org/10.1080/15583720903048227)
- [6] Ratna D., Varley R., Simon G. P.: Toughening of tri-functional epoxy using an epoxy-functionalized hyperbranched polymer. *Journal of Applied Polymer Science*, **89**, 2339–2345 (2003). DOI: [10.1002/app.12059](https://doi.org/10.1002/app.12059)
- [7] Boogh L., Pettersson B., Månson J-A. E.: Dendritic hyperbranched polymers as tougheners for epoxy resins. *Polymer*, **40**, 2249–2261 (1999). DOI: [10.1016/S0032-3861\(98\)00464-9](https://doi.org/10.1016/S0032-3861(98)00464-9)
- [8] Mezzenga R., Boogh L., Månson J-A. E.: A review of dendritic hyperbranched polymer as modifiers in epoxy composites. *Composites Science and Technology*, **61**, 787–795 (2001). DOI: [10.1016/S0266-3538\(01\)00022-7](https://doi.org/10.1016/S0266-3538(01)00022-7)
- [9] Morell M., Erber M., Ramis X., Ferrando F., Voit B., Serra A.: New epoxy thermosets modified with hyperbranched poly(ester-amide) of different molecular weight. *European Polymer Journal*, **46**, 1498–1509 (2010). DOI: [10.1016/j.eurpolymj.2010.04.015](https://doi.org/10.1016/j.eurpolymj.2010.04.015)
- [10] Foix D., Khalyavina A., Morell M., Voit B., Lederer A., Ramis X., Serra A.: The effect of the degree of branching in hyperbranched polyesters used as reactive modifiers in epoxy thermosets. *Macromolecular Materials and Engineering*, **297**, 85–94 (2012). DOI: [10.1002/mame.201100078](https://doi.org/10.1002/mame.201100078)

- [11] Emrick T., Chang H-T., Fréchet J. M. J., Woods J., Baccei L.: Hyperbranched aromatic epoxies in the design of adhesive materials. *Polymer Bulletin*, **45**, 1–7 (2000).
DOI: [10.1007/s002890070049](https://doi.org/10.1007/s002890070049)
- [12] Jannerfeldt G., Boogh L., Månson J-A. E.: Influence of hyperbranched polymers on the interfacial tension of polypropylene/polyamide-6 blends. *Journal of Polymer Science Part B: Polymer Physics*, **37**, 2069–2077 (1999).
DOI: [10.1002/\(SICI\)1099-0488\(19990815\)37:16<2069::AID-POLB10>3.0.CO;2-U](https://doi.org/10.1002/(SICI)1099-0488(19990815)37:16<2069::AID-POLB10>3.0.CO;2-U)
- [13] Star A., Stoddart J. F.: Dispersion and solubilization of single-walled carbon nanotubes with a hyperbranched polymer. *Macromolecules*, **35**, 7516–7520 (2002).
DOI: [10.1021/ma0204150](https://doi.org/10.1021/ma0204150)
- [14] Kim Y. H., Webster O. W.: Hyperbranched polyphenylenes. *Macromolecules*, **25**, 5561–5572 (1992).
DOI: [10.1021/ma00047a001](https://doi.org/10.1021/ma00047a001)
- [15] Hong Y., Cooper-White J. J., Mackay M. E., Hawker C. J., Malmström E., Rehnberg N.: A novel processing aid for polymer extrusion: Rheology and processing of polyethylene and hyperbranched polymer blends. *Journal of Rheology*, **43**, 781–793 (1999).
DOI: [10.1122/1.550999](https://doi.org/10.1122/1.550999)
- [16] Tomuta A. M., Ferrando F., Serra À., Ramis X.: New aromatic–aliphatic hyperbranched polyesters with vinylic end groups of different length as modifiers of epoxy/anhydride thermosets. *Reactive and Functional Polymers*, **72**, 556–563 (2012).
DOI: [10.1016/j.reactfunctpolym.2012.05.008](https://doi.org/10.1016/j.reactfunctpolym.2012.05.008)
- [17] Tomuta A. M., Ramis X., Ferrando F., Serra A.: The use of dihydrazides as latent curing agents in diglycidyl ether of bisphenol A coatings. *Progress in Organic Coatings*, **74**, 59–65 (2012).
DOI: [10.1016/j.porgcoat.2011.10.004](https://doi.org/10.1016/j.porgcoat.2011.10.004)
- [18] Moore J. S., Stupp S. I.: Room temperature polyesterification. *Macromolecules*, **23**, 65–70 (1990).
DOI: [10.1021/ma00203a013](https://doi.org/10.1021/ma00203a013)
- [19] Schallausky F., Erber M., Komber H., Lederer A.: An easy strategy for the synthesis of well-defined aliphatic-aromatic hyperbranched polyesters. *Macromolecular Chemistry and Physics*, **209**, 2331–2338 (2008).
DOI: [10.1002/macp.200800346](https://doi.org/10.1002/macp.200800346)
- [20] Schmaljohann D., Komber H., Voit B.: Conversion dependence of the structural units and the degree of branching of a hyperbranched polyester based on 4,4-bis-(4'-hydroxyphenyl)pentanoic acid determined by NMR spectroscopy. *Acta Polymerica*, **50**, 196–204 (1999).
DOI: [10.1002/\(SICI\)1521-4044\(19990501\)50:5/6<196::AID-APOL196>3.0.CO;2-J](https://doi.org/10.1002/(SICI)1521-4044(19990501)50:5/6<196::AID-APOL196>3.0.CO;2-J)
- [21] Ramis X., Salla J. M., Mas C., Mantecón A., Serra A.: Kinetic study by FTIR, TMA, and DSC of the curing of a mixture of DGEBA resin and γ -butyrolactone catalyzed by ytterbium triflate. *Journal of Applied Polymer Science*, **92**, 381–393 (2004).
DOI: [10.1002/app.20061](https://doi.org/10.1002/app.20061)
- [22] Zhang J., Guo G., Fox B.: Thermal and mechanical properties of a dendritic hydroxyl-functional hyperbranched polymer and tetrafunctional epoxy resin blends. *Journal of Polymer Science Part B: Polymer Physics*, **48**, 417–424 (2010).
DOI: [10.1002/polb.21902](https://doi.org/10.1002/polb.21902)
- [23] Cicala G., Recca A., Restuccia C.: Influence of hydroxyl functionalized hyperbranched polymers on the thermomechanical and morphological properties of epoxy resins. *Polymer Engineering and Science*, **45**, 225–237 (2005).
DOI: [10.1002/pen.20242](https://doi.org/10.1002/pen.20242)
- [24] Schechter L., Wynstra J., Kurkcy R. P.: Glycidyl ether reactions with amines. *Industrial and Engineering Chemistry*, **48**, 94–97 (1956).
DOI: [10.1021/ie50553a029](https://doi.org/10.1021/ie50553a029)
- [25] Fox T. G.: Influence of diluent and of copolymer composition on the glass temperature of a polymer system. *Bulletin of the American Physical Society*, **1**, 123–125 (1956).
- [26] Abate L., Blanco I., Cicala G., Recca G., Scamporrino A.: The influence of chain-ends on the thermal and rheological properties of some 40/60 PES/PEES copolymers. *Polymer Engineering and Science*, **49**, 1477–1483 (2009).
DOI: [10.1002/pen.21378](https://doi.org/10.1002/pen.21378)
- [27] Vyazovkin S., Wight C. A.: Kinetics in solids. *Annual Reviews in Physical Chemistry*, **48**, 125–149 (1997).
DOI: [10.1146/annurev.physchem.48.1.125](https://doi.org/10.1146/annurev.physchem.48.1.125)
- [28] Xu G., Shi W., Gong M., Yu F., Feng J.: Curing behavior and toughening performance of epoxy resins containing hyperbranched polyester. *Polymers for Advanced Technology*, **15**, 639–644 (2004).
DOI: [10.1002/pat.520](https://doi.org/10.1002/pat.520)
- [29] Brooker R. D., Kinloch A. J., Taylor A. C.: The morphology and fracture properties of thermoplastic-toughened epoxy polymers. *The Journal of Adhesion*, **86**, 726–741 (2010).
DOI: [10.1080/00218464.2010.482415](https://doi.org/10.1080/00218464.2010.482415)
- [30] Morell M., Ramis X., Ferrando F., Serra À.: New improved thermosets obtained from diglycidylether of bisphenol A and a multiarm star copolymer based on hyperbranched poly(glycidol) core and poly(methyl methacrylate) arms. *Macromolecular Chemistry and Physics*, **213**, 335–343 (2012).
DOI: [10.1002/macp.201100497](https://doi.org/10.1002/macp.201100497)
- [31] Levita G., De Petris S., Marchetti A., Lazzeri A.: Crosslink density and fracture toughness of epoxy resins. *Journal of Materials Science*, **26**, 2348–2352 (1991).
DOI: [10.1007/BF01130180](https://doi.org/10.1007/BF01130180)

Conductivity of microfibrillar polymer-polymer composites with CNT-loaded microfibrils or compatibilizer: A comparative study

S. M. Panamoottil¹, P. Pötschke², R. J. T. Lin¹, D. Bhattacharyya¹, S. Fakirov^{1*}

¹The University of Auckland, Centre for Advanced Composite Materials, Department of Mechanical Engineering, Private Bag 92019, 1142 Auckland, New Zealand

²Leibniz Institute of Polymer Research Dresden, Department of Functional Nanocomposites and Blends, Hohe Str. 6, 01069 Dresden, Germany

Received 18 January 2013; accepted in revised form 4 April 2013

Abstract. Conductive polymer composites have wide ranging applications, but when they are produced by conventional melt blending, high conductive filler loadings are normally required, hindering their processability and reducing mechanical properties. In this study, two types of polymer-polymer composites were studied: i) microfibrillar composites (MFC) of polypropylene (PP) and 5 wt% carbon nanotube (CNT) loaded poly(butylene terephthalate) (PBT) as reinforcement, and ii) maleic anhydride-grafted polypropylene (PP-g-MA) compatibilizer, loaded with 5 wt% CNTs introduced into an MFC of PP and poly(ethylene terephthalate) (PET) in concentrations of 5 and 10 wt%. For the compatibilized composite type, PP and PET were melt-blended, cold-drawn and pelletized, followed by dry-mixing with PP-g-MA/CNT, re-extrusion at 200°C, and cold-drawing. The drawn blends produced were compression moulded to produce sheets with MFC structure. Using scanning electron microscopy, CNTs coated with PP-g-MA could be observed at the interface between PP matrix and PET microfibrils in the compatibilized blends. The volume resistivities tested by four-point test method were: $2.87 \cdot 10^8$ and $9.93 \cdot 10^7 \Omega \cdot \text{cm}$ for the 66.5/28.5/5 and 63/27/10 (by wt%) PP/PET/(PP-g-MA/CNT) blends, corresponding to total CNT loadings (in the composites) of 0.07 vol% (0.24 wt%) and 0.14 vol% (0.46 wt%), respectively. For the non-compatibilized MFC types based on PP/(PBT/CNT) with higher and lower melt flow grades of PP, the resistivities of 70/(95/5) blends were $1.9 \cdot 10^6$ and $1.5 \cdot 10^7 \Omega \cdot \text{cm}$, respectively, corresponding to a total filler loading (in the composite) of 0.44 vol% (1.5 wt%) in both MFCs.

Keywords: polymer composites, electroconductivity, compatibilizer, polymer-polymer composites, carbon nanotubes

1. Introduction

An increasing amount of research over the last decade has been dedicated to studying and improving the properties of conducting polymer composites (CPCs). CPCs possess an interesting combination of properties including low weight, non-linear voltage-current behaviour, and environmental-sensitive resistivity, properties which could lead to applications in antistatic, electrostatic dissipative and electromagnetic shielding, as well as in sensors

and related devices [1–4]. Anisotropic CPCs could even have applications in the semiconductor industry [5–7].

Conductive fillers have been dispersed in polymers using a variety of techniques, including melt mixing, *in-situ* polymerization, solution mixing, and applying the latex approach [8–10]. However, as far as commercial application is concerned, melt mixing is the most attractive technique. Early attempts for producing CPCs involved mixing conductive

*Corresponding author, e-mail: ohtsf@wmail.chem.uni-sofia.bg
© BME-PT

filler with a bulk polymer, and above a certain filler loading, called *percolation threshold*, the composite begins conducting. This approach, however, depending on the aspect ratio of the conducting filler, usually requires relatively high filler content to achieve conductivity, which is undesirable as far as processability, surface finish and cost are concerned [11]. Therefore, a selective localization of conductive fillers in one component or at the interface of two-component blends is a suitable method to reduce the filler amount needed for electrical percolation. This was shown especially for blends with co-continuous structure, where the conductive filler is localized in one of the components and depending on the component composition the percolation can occur at lower than the half amount of fillers as compared with the bulk filling [12]. For carbon black as filler even the case of interfacial localization was reported [13].

The creation of fibrillar polymer-polymer composites as a special case of polymer blends offers the opportunity to load only the blend matrix or the minor reinforcing component, or even only the interface layer between the matrix and the reinforcing fibrils. The described four cases of loading a polymer or a polymer blend having the structure of a fibrillar polymer-polymer composite with conductive fillers are schematically illustrated in Figure 1. Samples corresponding to case b) of Figure 1. (matrix loading) were not prepared in this study, instead, bulk-loaded samples (Figure 1a) were used as a model system because they are free from any interaction with the reinforcing fibrils.

With reduction of filler content in mind, it should be pointed out that the choice of conductive filler by itself can make a significant difference in the percolation threshold of a filled polymer or blend. Carbon black (CB) had been the conductive filler of choice [14–19] for many years, until the recent surge in application of carbon nanotubes (CNTs) [20–24], which, due to their high aspect ratio, achieve percolation at much lower contents than CB.

With lower filler content as the aim, CPCs based on polymer blends have been observed to achieve percolation at lower filler loadings than those based on a single polymer [12, 25–27]. This can be attributed to a mechanism called double-percolation [28–35] i.e., the filler is selectively localized in one of the blend components forming a conductive network. However, in most of these cases the two polymers

have weak interfacial adhesion, resulting in poor mechanical properties of the blend. This can be improved to a certain extent by applying the concept of microfibrillar composites (MFCs) [36–39].

Microfibrillar composites are prepared from immiscible polymer blends, where the reinforcement is provided by fibrils of the minor component [37, 38]. Requirements to be met in the choice of blend components [39] include: i) both polymers should be amenable to a sufficient amount of drawing to produce microfibrils with high molecular orientation, ii) melting temperature of the minor component should be at least 40 K above that of the matrix polymer, in order to prevent melting of fibrils during consolidation, iii) both polymers should be processable at a single temperature without degrading, iv) blend composition should be selected in that way that the minor component forms a dispersed phase in the matrix. Once suitable blend partners are selected, the process sequence for MFC manufacture can be described simply as follows: i) melt-blending of the polymers above melting of higher melting component, ii) cold-drawing (for fibrillation) of the blend above the glass transition temperature of the minor reinforcing component, iii) isotropization of the blend by processing above melt temperature of matrix, but below that of the reinforcing fibrils.

The MFC concept has been applied to polypropylene (PP) melt blended with nylon-6,6 (PA66) loaded with multiwalled carbon nanotubes (MWCNTs) and cold-drawn, followed by isotropization to form MFCs [40]. Observation under the scanning electron microscope (SEM) revealed good dispersion of MWCNTs in the PA66 microfibrils. The PA66 fibrils themselves were found to reinforce the matrix, while the MWCNTs seemed to have a detrimental effect on the mechanical properties. The experience gained from this study was helpful in selecting the material ratios and processing parameters used in the current study.

A significant amount of work related to MFC-based CPCs has been carried out previously [11, 17, 41–43]. Early studies dealt with MFCs of polyethylene (PE)/poly(ethylene terephthalate) (PET) with CB as a filler. Filler loadings as high as 5.9 vol% were required to achieve percolation. These authors were later successful in finding out that the CB particles are selectively located in higher concentration near the PE/PET interface (without any special target-

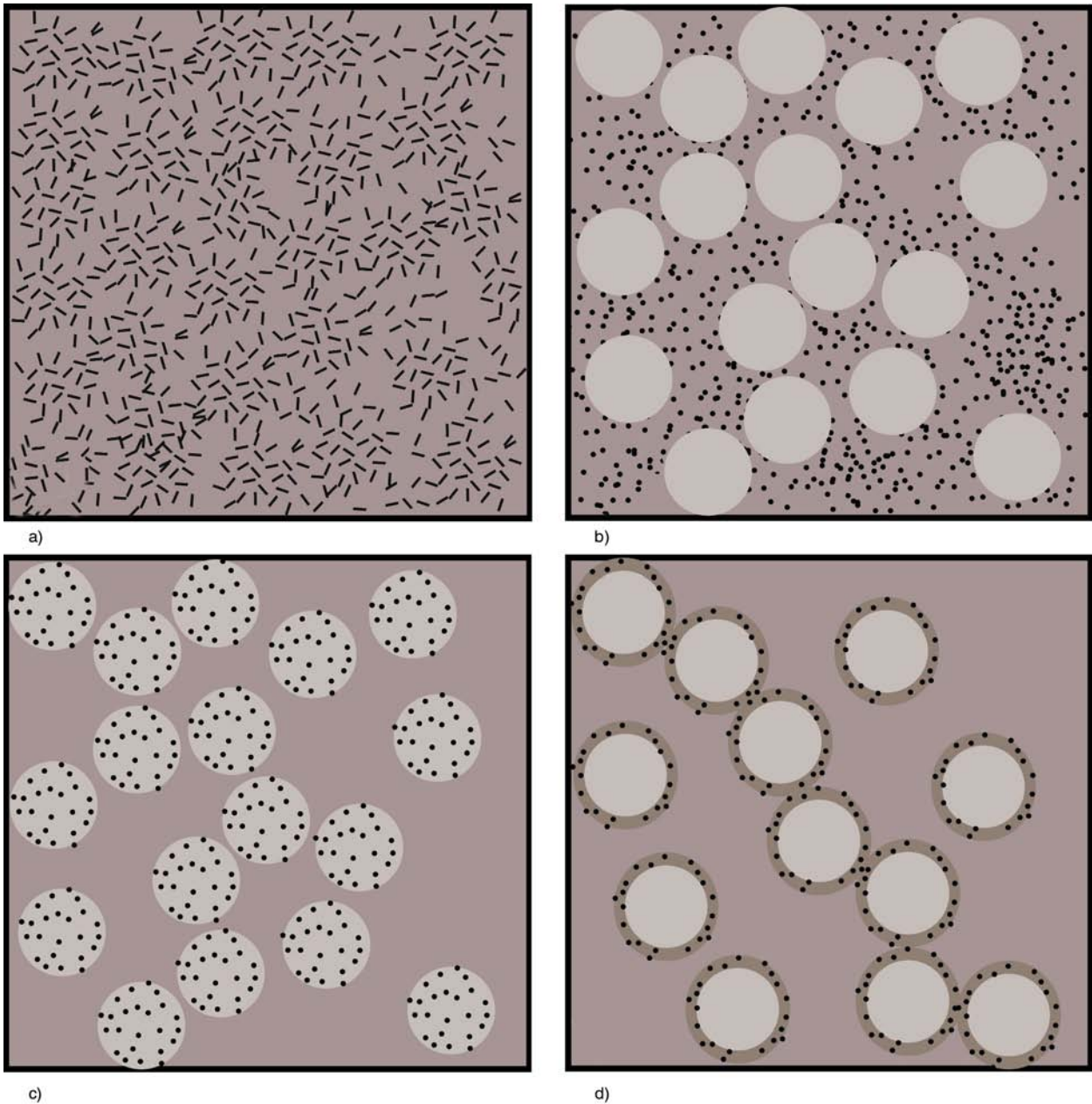


Figure 1. Schematic of different types of loading with conductive fillers: a) bulk loading, b) fibrillar polymer-polymer composite in which only the matrix is loaded (matrix loading), c) as b), but only the reinforcing fibrils are loaded (microfibrils loading), and d) as b) but only the compatibilizer is loaded (interfacial loading); the views are perpendicular to the extrusion direction

ing), which lowered the percolation threshold [19]. In this way it was demonstrated that for the blend PE/PET and conductive filler CB the threshold percolation is 11 vol% when both, the PE and PET are loaded [44], 5.2 vol% CB when only PET microfibrils are loaded [11], and only 3.5 vol% when CB particles are selectively distributed around the microfibril surface [45].

The main goal of this study is to compare the electrical conductivity for three different cases of loading with conductive filler the basic elements of a poly-

mer-polymer composite, namely the matrix only, the microfibrils only, and the compatibilizer only, i.e. to realize the three cases of bulk loading, microfibrils loading and interfacial loading (Figure 1).

It should be noted that the conducting filler in the current study are CNTs of multi walled type. Further on, in contrast to the studies of Li and coworkers [11, 44, 45], who found increased concentrations of CB on the interface, in the present study a ‘special carrier’ for delivering of CNTs to the same location, the interface between matrix and reinforc-

ing microfibrils, will be used – a suitable compatibilizer loaded with CNTs.

An additional task of the study is to find an appropriate technique for introducing the compatibilizer into the blend, thus avoiding the known negative effect of compatibilizers on the microfibrils formation.

2. Experimental

2.1. Materials

The materials used include PP, conductive grade poly(butylene terephthalate) (PBT) loaded with CNTs, PET and neat PP-g-MA and CNT-loaded PP-g-MA. The details of the materials are as follows.

Two grades of PP were used, both supplied by Lyondell Basell of Corio, Australia: HP555G grade (melt flow index (MFI) of 1.3 g/10 min, ultimate tensile strength (UTS) of 35 MPa) denoted further as high viscous PP (PPhv) and the lower viscous HP548S grade (MFI 35 g/10 min, UTS 33 MPa) denoted as PPlv.

PBT of grade SR525 loaded with 5 wt% CNTs (manufacturer tested volume resistivity of 6.61 $\Omega\cdot\text{cm}$) was supplied by Hyperion Catalysis International, Cambridge, USA. The CNTs were of type FIBRIL™ nanotubes (type MWCNT, diameter ~10 nm, density 1.66 g/cm³).

PET of grade Shinpet 5015W (density 1.4±0.1 g/cm³) was supplied by Shinkong Synthetic Fibres Corporation, Taiwan.

PP-g-MA was of grade Orevac 18732 (MFI 8 g/10 min, UTS 20 MPa). PP-g-MA was melt-mixed with 5 wt% CNTs to generate a conductive compatibilizer. The CNTs used were of grade Nanocyl™ NC7000 (type MWCNT, diameter ~10 nm, density 1.75 g/cm³ [46]), supplied by Nanocyl SA, Sambreville, Belgium.

2.2. Sample preparation

The samples had to be prepared in such a way to allow the conductivity measurements of the three basic types of loading, namely, bulk loading, fibrils loading, and interfacial loading (Figure 1). Please refer to Table 1 for a list of the samples prepared, and the designations used for them in the paper.

2.2.1. Samples with bulk loading

For this type of samples, one polymer melt mixed with CNTs was used, corresponding to Figure 1a. PBT granules containing 5 wt% of MWCNTs, as supplied by the manufacturer, were compression

moulded at 180°C and pressure of 7 MPa to produce samples with sizes of 10 mm × 80 mm × 0.3 mm suitable for measuring the electrical conductivity.

2.2.2. Samples with fibrils loading

For this purpose PP was used as matrix and PBT/CNT as reinforcing fibrils. The standard MFC protocol was used [47], namely both grades of PP and PBT were dried at 80 or 110°C, respectively, dry-mixed to a weight ratio of 70/30, followed by melt blending at 265°C in a Brabender DSE20 twin-screw extruder with 25 mm screw, and an *L/D* ratio of 40 and 5 rpm, using a 1.3 mm die. The extrudate was cooled in water bath immediately after its exit from the die. The extruded blend was then subjected to cold drawing at 80°C to ratios between 4.7 and 5, using two winders and a 2 m long heated chamber. Cold drawing was followed by isotropization of the matrix – the drawn blend was wound uniaxially on a plate, followed by compression moulding at 180°C to a sheet with a thickness of about 0.3 mm. Thus, MFC samples with microfibril reinforcement were manufactured. The next series of MFC samples using the second type of PP was prepared in the same way.

A small amount of each PP/(PBT/CNT) blend, after cold-drawing was subjected to removal of PP using hot xylene in a modified Soxhlet apparatus according to a procedure described in [48].

From the PP/(PBT/CNT) MFC sheet, specimens of 10 mm × 80 mm × 0.3 mm (length direction along direction of cold-drawing) were cut to test the electrical conductivity.

2.2.3. Samples with interfacial loading

As mentioned in the introduction, in order to guarantee a more precise localization of CNTs just on the interface boundary, a ‘special carrier’ has been used, a compatibilizer of the type PP-g-MA, which, due to its peculiar chemical composition, positions itself at interface between the matrix and the microfibrillar reinforcement only.

At the same time, as noted above, the use of compatibilizer during the MFC manufacturing is not recommendable since it has a negative effect on the microfibrils formation via preventing the coalescence of the starting spherical particles during the drawing stage [36]. For this reason it had to be checked firstly the recommendation given in ref. [36], namely, to add the compatibilizer to the blend

Table 1. Blend designations and the constitution of the composites and blends by weight

No.	Blend designation	Components	Component content in the composite/blend [wt %]
1	PBT/CNT	PBT CNT (Hyperion)	95 5
2	PP-g-MA/CNT	PP-g-MA CNT (Nanocyl)	95 5
3	PPhv/(PBT/CNT)	PP, high viscosity PBT/CNT	70 30
4	PPlv/(PBT/CNT)	PP, low viscosity PBT/CNT	70 30
5	PP/(PBT/CNT)	Refers to blends 3 and 4	
6	PPhv/PET	PP, high viscosity PET	70 30
7	PPlv/PET	PP, low viscosity PET	70 30
8	PP/PET	Refers to blends 6 and 7	
9	PPhv/PET/(PP-g-MA/CNT1)	PPhv/PET PP-g-MA/CNT	95 5
10	PPhv/PET/(PP-g-MA/CNT2)	PPhv/PET PP-g-MA/CNT	90 10

only after the drawing stage and subject the new blend to a reprocessing including re-extrusion at lower temperature and redrawing. This reprocessing requires an additional checking regarding the safe existence of the microfibrils created during the first processing. Only thereafter it is meaningful to repeat the same scenario using a compatibilizer loaded with CNTs.

For the samples with interfacial loading the best studied MFC system was used – PP as a matrix and PET as reinforcement. PP-g-MA loaded with CNTs was used as blend compatibilizer. The PP/PET/(PP-g-MA/CNT) blends were prepared in the following way:

The compatibilizer PP-g-MA loaded with 5 wt% CNTs was prepared using melt mixing in a Berstorff ZE25 co-rotating twin-screw extruder with $L = 36D$ at a throughput of 10 kg/h and a rotation speed of 500 rpm. PP granules and CNT powder were added into the hopper as premixtures and the temperatures were set to be between 200 and 180°C (from the hopper to the die). The conductivity of this composite as measured on compression moulded sheets is well in the percolated range (about 10 $\Omega \cdot \text{cm}$ [49]).

For the preparation of blends of interest, the respective components as PP, PP-g-MA/CNT and PET were dried prior to processing at 80 and 110°C (PET). The PP/PET microfibrillar drawn blend was first prepared using the same method described in section 3.2.2., and pelletized to sections of 3 mm length.

Some of the pelletized material of the drawn PP/PET blend was subjected to a second melting in the extruder at 215°C (below the melting temperature of PET). From the extrudate, a small piece was subjected to cryofracture in liquid nitrogen, and the cross-sections was cut out. A small portion of the PP/PET after the first processing was subjected to removal of PP using hot xylene [46]. These samples were inspected by SEM to confirm the preservation of the fibrils in the re-extruded PP/PET blend.

Once this was confirmed, the remaining pelletized material of PP/PET drawn blend was dry-mixed with PP-g-MA/CNT, to 95/5 and 90/10 weight ratios and re-extruded. The re-extruded blends were redrawn at 80°C to a draw ratio of around 3.5, wound uniaxially on a plate, followed by compression moulding at 180°C and a nominal pressure of 7 MPa in a hydraulic press to obtain sheets with MFC structure.

2.3. Sample characterization

Strips from the various types sample sheets with MFC structure with dimensions of 10 mm \times 50 mm \times 0.3 mm (length direction along direction of cold-drawing), were cryofractured in liquid nitrogen, and the cross sections were mounted on adhesive stubs. Specimens for the SEM were coated with colloidal platinum for 10 min prior to observation and loaded into a Philips/FEI FEG-XL30S scanning electron microscope. Micrographs were taken at different locations of each specimen at different magnifications.

Electrical conductivity was characterized using a four-point test rig (ASTM D4496). As mentioned earlier, specimens of dimensions 10 mm × 80 mm × 0.3 mm (length direction along direction of cold-drawing) were prepared. Silver paste was spread on the specimens on the lines of contact with the sharp edged contacts of the rig. The rig was connected to a constant current source (Keithley 220, Keithley, Ohio, USA) or a high resistance electrometer (Keithley 6517A, Keithley, Ohio, USA).

3. Results and discussion

3.1. Effect of matrix viscosity and the presence of compatibilizer on microfibril formation: Morphological characterization

PP was removed from both the PPhv/(PBT/CNT) and PPlv/(PBT/CNT) blends for SEM characterization. The remaining microfibrils of PBT loaded with CNT were inspected by means of SEM for getting an idea about their thickness and length. The results are shown in Figure 2. The fibrils prepared from the PPhv/(PBT/CNT) blend (Figure 2a) are rather thin (diameters between 250 and 500 nm) thus approaching the nano-range, while those from the PPlv/(PBT/CNT) blend (Figure 2b) are considerably thicker and have thicknesses between 1 and 5 μm. At the same time, the second type of fibrils seem to be smoother (Figure 2b) and possibly longer than those of the first type (using PPhv), Figure 2a. This difference can be explained by the matrix viscosity of the two PPs, whereby the higher viscous matrix generates due to higher shear stresses acting on the disperse phase smaller particles available for later coalescence. In addition, the PP with higher viscos-

ity offers better conditions for the microfibril formation during cold drawing (around T_g of PBT or PET) as compared to the lower viscous matrix PP in sense of more effective coalescence. The coalescence is the crucial process for the formation of microfibrils – without coalescence the cold drawing results in formation of elliptical particles with aspect ratio of 2–4 (Figure 4b).

It should be mentioned that the microfibrils of Figure 2 are the reinforcing component of the polymer-polymer composites of MFC type, which could be prepared from the drawn blend via compression moulding at temperatures when PP only melts.

The cryofracture surfaces of the manufactured MFCs in the direction perpendicular to the drawing direction for the two types of PP are shown in the SEM micrographs in Figure 3. Comparing the two types of composites, namely applying PPhv (Figure 3a) and PPlv (Figure 3b), a substantial difference in the structure of the cross-section surface can be observed. In the first case (Figure 3a), the fibrils are much thinner, up to ten times as compared to the second type (compare Figure 3a and 3b), which is in agreement with the results of comparison of the extracted fibrils (Figure 2). Furthermore, the cryofracture in the first case occurs with dominating pull out of fibrils from the matrix (Figure 3a), contrasting to that of the second case (Figure 3b) where break of the microfibrils is more evident. And finally, in the second case due the fibril's break one can see the carbon nanotube loading in the PBT microfibrils (Figure 3b, inset). In this way, polymer-polymer composites (PPCs) of MFC type were successfully prepared, in which only the microfibrils are loaded with CNTs

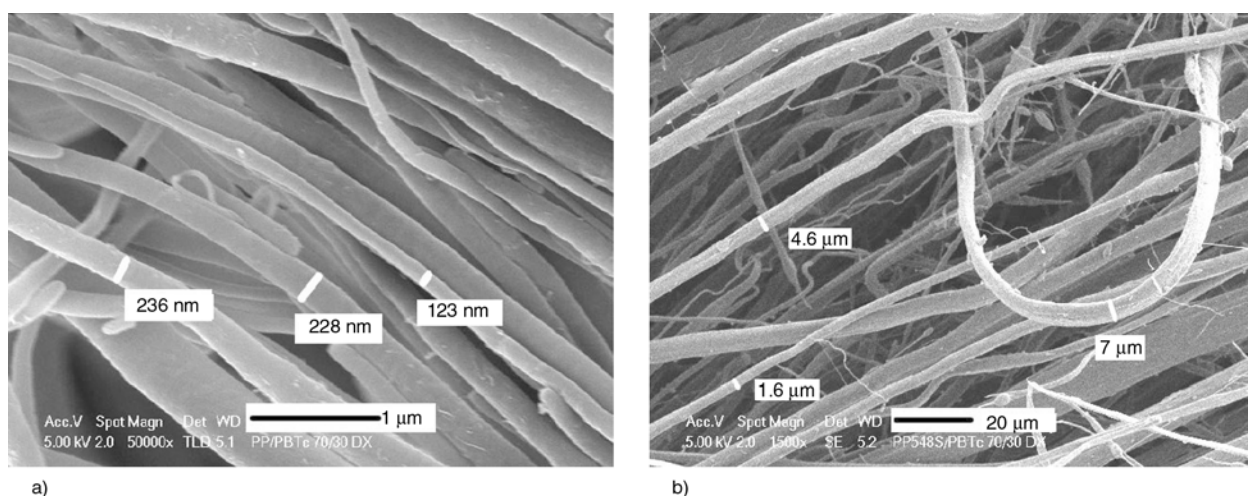


Figure 2. SEM micrographs of fibrils prepared from PP/(PBT/CNT) (70/(95/5) wt%) after extraction of PP: a) from blend containing high viscosity PPhv, and b) from blend containing low viscosity PPlv

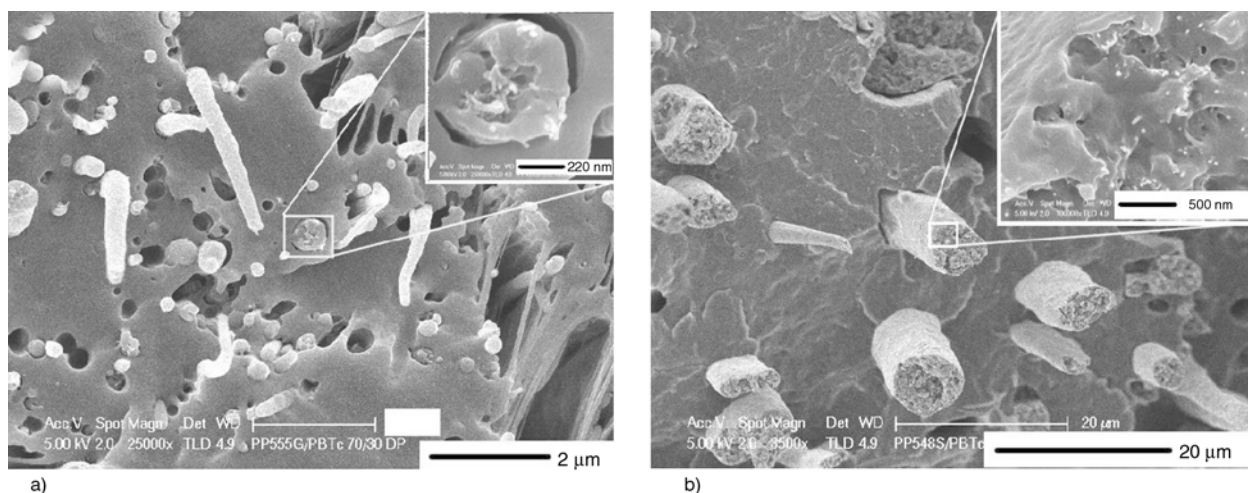


Figure 3. SEM micrographs of cryofractured cross-sections of PP/(PBT/CNT) (70/95/5) wt% drawn blend after compression moulding (isotropization step) using two types of PP: a) high viscosity PPhv and b) low viscosity PPIv, with insets at higher magnifications

(Figure 3b), following the previous experience with a blend of PP and CNT-loaded polyamide-6,6 [40]. The difference between the two studies is that the masterbatch of PBT/CNT used in the current study is of conductive type, and the previous one was not. In this way, in addition to samples with bulk loading (Figure 1a), we have the second candidate (Figure 1c) for the comparative study, and only the third type, with interfacial loading of fillers (Figure 1d) is missing.

Many researchers [11, 17, 19, 43] published results of similar studies, where they prepared polymer blends with MFC structure, loading with carbon black either the microfibril forming component (PET) or the matrix (PE) in amounts between 3 and 13 vol%. They found an accumulation of CB at the interfacial layer, so that a higher CB concentration

as compared to that of the microfibrils or the matrix was reached at the interface.

Contrasting these studies [11, 17, 19, 43], our main target was to deliver the conductive filler (CNTs) more precisely – only to the interface between reinforcement and matrix as mentioned above. Towards this target, a compatibilizer was chosen as the carrier of CNTs. Compatibilizers being in nature and action surfactants, have a molecule designed in such a way that one part is ‘friendly’ with one of the blend components, and another part with the other blend component. It can only fulfill this target by localizing at the interface. The driving force for the migration to the interface is the diphilic character of the molecule – the homogeneous one-component medium is not the final localization place. During the migration process, it is quite possible that the

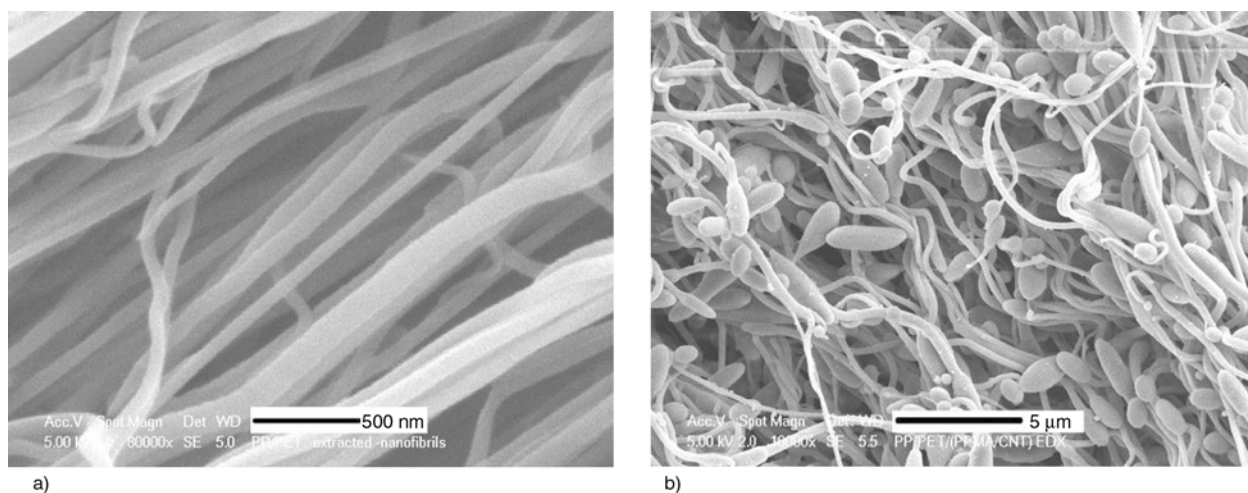


Figure 4. SEM micrographs of PET microfibrils extracted using hot xylene from drawn PPhv/PET blend: a) blend without compatibilizer, and b) blend containing PP-g-MA compatibilizer in the amount of 5 wt% referred to the total blend

compatibilizer loses part of its CNTs, particularly if the concentration gradient is very high. However, interactions between functional groups on the surface of the MWCNTs and the MA groups of the compatibilizer can fix the CNTs within the compatibilizer phase [34]. At the same time, the compatibilizer inhibits the formation of microfibrils [36] as demonstrated also by the results of the current study. In Figure 4 one can see well defined nanofibrils (Figure 4a) if the MFC material is prepared without the use of compatibilizer. In the presence of compatibilizer, mostly elliptical particles can be seen (Figure 4b) instead of smooth ‘endless’ nanofibrils. These samples were prepared to illustrate the effect of presence of compatibilizer on fibril formation, and do not contain CNTs.

Taking into account the mechanism of fibril formation – via stretching and coalescence of the starting spherical or elliptical particles [36], the result displayed in Figure 4b becomes quite clear. The inhibiting effect of the compatibilizer consists of coating the spherical particles with a thin film, which prevents their coalescence even if in contact. This situation is quite normal, if one remembers that the main task of the compatibilizers is to enhance and stabilize the dispersion of two thermodynamically immiscible liquids via prevention of coalescence of droplets. This inhibiting effect of the compatibilizer on fibril formation had to be overcome when dealing with MFCs manufacturing.

3.2. MFCs with interfacial CNT loading: Morphological characterization

The above defined problem regarding the inhibiting effect of the compatibilizer on nanofibril formation

was solved following the recommendation given in [36], namely to add the compatibilizer to the blend after fibril formation. In such a case the processing steps will be in the following order: melt blending of the two starting polymers, extrusion, cold drawing, pelletizing, mixing with the compatibilizer, drying, remelting, re-extrusion and redrawing.

Before applying this more complex processing route using a compatibilizer loaded with CNTs, the effect of the repeated treatment on the structure of the MFCs was examined. Due to the properly selected reprocessing temperature (215°C), the previously created PET fibrils were completely preserved (Figure 5). The only change observed is that they exist as twisted bundles after the reprocessing the drawn blend. Having these results, it was possible to perform the same reprocessing using the PP-g-MA compatibilizer loaded with 5 wt% CNTs.

The cryofractured surfaces of the drawn PPhv/PET/(PP-g-MA/CNT1) blend (Table 1) are shown in Figure 6. The main task of this microscopic inspection of the prepared samples was to find reliable proofs for the proper localization of the CNTs delivered by the compatibilizer – just at the interface between the matrix (PP) and the reinforcing microfibrils (PET). For this purpose, SEM micrographs are taken from various spots using increasing magnifications. The fibrils appear to be coated by the PP matrix in most cases, as in the case of the bundle shown in Figure 6a. The CNTs can be seen only on the surface of the fibrils (Figure 6b) as a random network, coated by the compatibilizer (Figures 6c–6f). This gives an idea that the CNT filler has indeed localized near the interface of PP matrix and PET reinforcement, as desired.

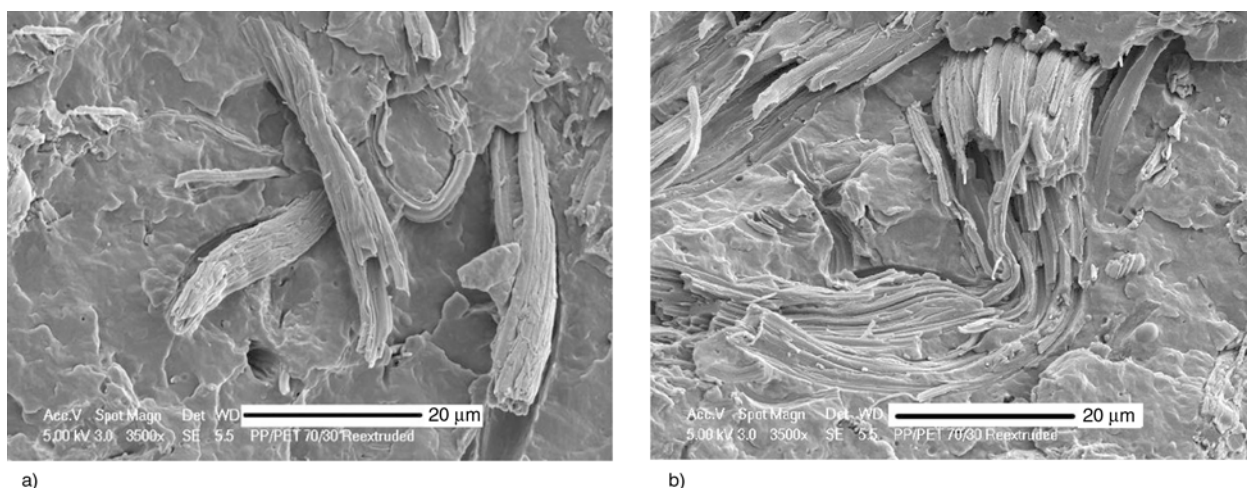


Figure 5. SEM micrographs of cryofractured cross-sections of remelted and re-extruded MFC based on PPhv/PET (70/30 by weight). a) twisted bundles of PET nanofibrils in PP matrix, b) nanofibrils forming the bundles

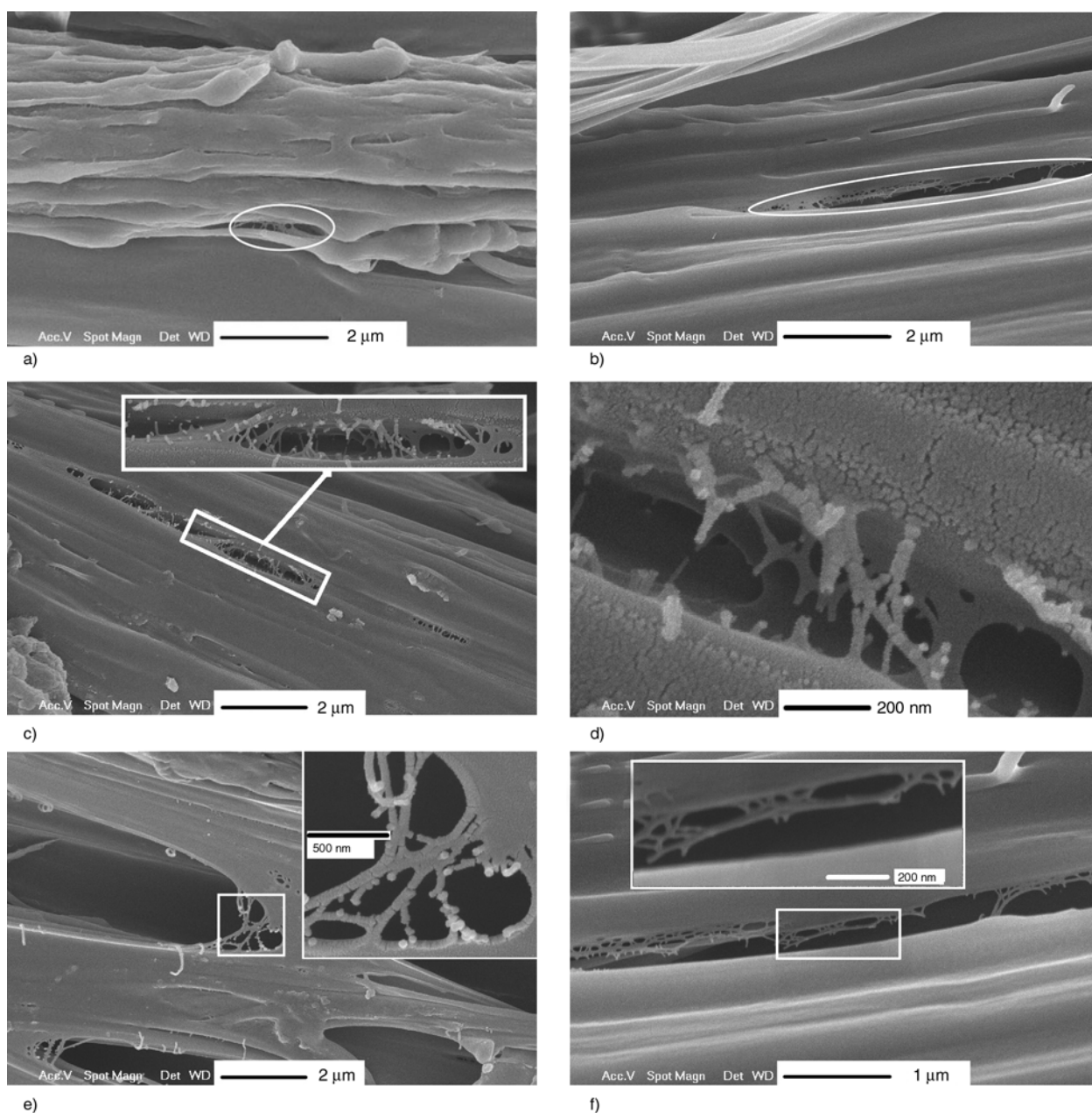


Figure 6. SEM micrographs of cryofractured longitudinal sections of drawn blend based on PPhv/PET/(PP-g-MA/CNT1). The micrographs are taken from different spots of the sample at various magnifications (see the insets)

However, the best proof for the presence of CNTs in this material will be the positive results of the electrical measurements as well as their comparison with the non-compatible polymer blend containing CNTs in the fibrils only.

3.3. Electrical properties of the blend PPhv/PET/(PP-g-MA/CNT)

The testing of the electrical properties of the prepared materials was performed on specimens from sheets manufactured by compression molding at

such a temperature as to melt PP only, thus forming a polymer-polymer composite of MFC type.

All the materials tested contained MWCNTs but dispersed in different structural elements of the MFCs, namely: i) in the microfibrils alone (microfibril loading, Figure 1c), ii) in the compatibilizer only (interfacial loading, Figure 1d), and (iii) in the matrix polymer only (bulk loading, one polymer blended with CNTs, Figure 1a), using the as supplied PBT/CNT blend. Further on, the microfibrils loaded samples were prepared using the two grades of PP

(PPhv and PPIv). These are denoted as PPhv/(PBT/CNT) and PPIv/(PBT/CNT).

Figure 7 shows the electrical resistivities of the samples produced in this study, which all were made under comparable pressing and measurement conditions. In order to judge the results, these results are plotted together with references from literature, for which the wt% were recalculated in vol% in order to compare materials with matrices of different densities. Of course, the mixing, compression molding and measurement conditions of the composites taken from literature were partially different from those in this study and this comparison has to be taken with care. Also the resistivities of the neat polymers differ. However, this comparison enables to compare the results of this study with electrical percolation results from literature.

The respective values of the volume resistivity for the microfibrils loaded case (Figure 1c) are $1.5 \cdot 10^7 \Omega \cdot \text{cm}$ (for PPhv/(PBT/CNT)) and $1.9 \cdot 10^6 \Omega \cdot \text{cm}$ (for PPIv/(PBT/CNT)). Both values are in the *electrostatic dissipative* range, i.e., between 10^4 – $10^{12} \Omega \cdot \text{cm}$ [50]. The sample comprising the lower viscosity matrix (PPIv) is characterized by a volume resistivity an order of magnitude lower than the sample with the higher viscosity matrix (PPhv). This difference could be due to the difference in microfibril diameters between the two types of MFCs which were 10–

20 times lower in the case of PPhv. Having in mind the fact that the concentration of the CNTs in the two types of fibrils is the same (5 wt%), the preparation of PBT nanofibrils using the PPhv matrix generates in the thinner fibrils higher draw ratios and thus higher orientation of both the macromolecules and CNTs as compared to PPIv. Orientation of CNTs along the fiber axis was found in melt spun fibers to increase the resistivity [51] due to the reduced number of contacts between the individual CNT particles.

What the second basic case of interest, the interfacial loading (Figure 1d) concerns, it should be noted that higher values of resistivity ($2.87 \cdot 10^8$ and $9.93 \cdot 10^7 \Omega \cdot \text{cm}$) as compared with the case of microfibrillar loading (Figure 1b) are obtained for the two samples prepared with PPhv only and denoted as PPhv/PET/(PP-g-MA/CNT1) and PPhv/PET/(PP-g-MA/CNT2), where 1 and 2 represent 5 and 10 wt% compatibilizer added to PP/PET blends, respectively.

Starting from the fact that the two values of the volume resistivity obtained for the two concentrations of compatibilizer are rather close to each other, one can conclude that the amount of compatibilizer itself does not affect the electrical properties that strongly. As the compatibilizer itself is conductive (with 5 wt% CNTs well above percolation) and pro-

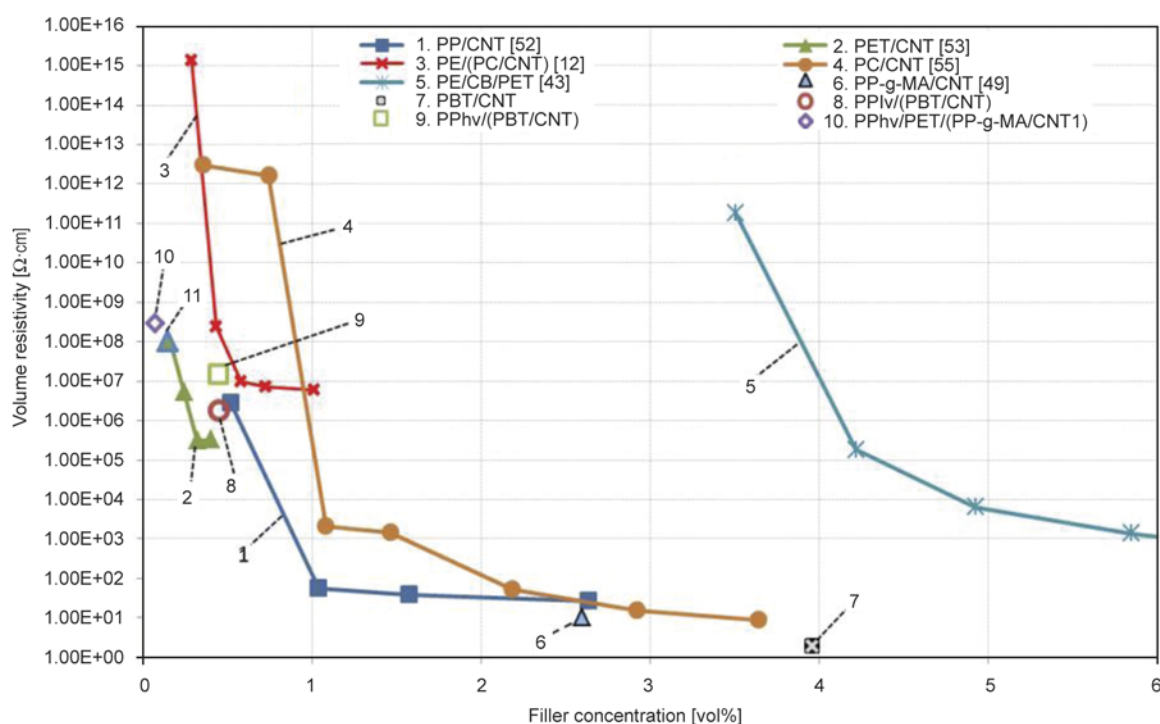


Figure 7. Dependence of volume resistivity on the filler concentration in various polymeric materials loaded with CNTs or CB

vides the conductive path through the sample, the amount of compatibilizer seems to be not so important. This finding also implies indirectly, that the compatibilizer covers the surface of the fibrils in a sufficient way to reach conductivity in the whole sample. At the same time, it is well documented that the compatibilizer, particularly in increased concentrations, has a deteriorating effect on the mechanical performance of polymer-polymer composites. This will mean that a good balance between the electrical and mechanical properties of the same material could be expected via using compatibilizers with higher CNT loading and possibly lower compatibilizer concentrations in the MFC material. An idea of how the values of volume resistivity from samples prepared in this study are related to the typical percolation thresholds of similar systems could be got from Figure 7. Samples 1–6 refer to published data [12, 43, 49, 52–55], whereas sample 6 represents the compatibilizer material used in this study, and samples 7–10 are from the present study. In the majority of cases the conductive filler is dispersed in the polymer bulk (Figure 7, samples 1, 2, 4, 6, 7), in some cases only in the reinforcing microfibrils within MFCs (Figure 7, samples 5, 8, 9) or in one phase of co-continuous blends (Figure 7, sample 3), and only in two cases (present study) in the compatibilizer within MFCs (Figure 7, samples 9 and 10).

One can see that the resistivity values of the blends with MFC structure tested in this study (Figure 7, samples 8–11) are near or lower than the values of the percolation threshold for PE/(PC/CNT) (Figure 7, sample 3), 1–3 orders of magnitude away from the threshold for PET/CNT (Figure 7, sample 2), 3–5 order of magnitude away from the threshold for PP/CNT (Figure 7, sample 1). The curves in Figure 7 demonstrate the extremely strong dependence of the volume resistivity on the concentration of the filler – a change of CNT concentration by 1 vol% can result in a decrease of the resistivity by up to 10 orders of magnitude. This bodes well for MFC blends which will be prepared in a future study, with higher CNT loadings.

Another peculiarity of the polymer conductive materials is their sensitivity to many other factors affecting their electrical conductivity, including also such a ‘secondary’ factor as pressing conditions.

For this reason a more detailed comparison of the obtained data with the reported ones is hardly justified. Nevertheless, the results obtained in the current study look quite promising because they demonstrate the possibility of obtaining reasonable values for the electrical conductivity when loading conductive filler only in the minor component of the fibrils containing blend or in the interfacial area of such microfibrillar blends. Such an approach also allows avoiding or decreasing drastically the deterioration effect of CNTs on the mechanical properties of the polymer blends. In addition, when working with polymer blends having MFC structure, one is getting considerable improvement of mechanical properties, particularly when the matrix is a polyolefin [37, 39]. In this way, applying the MFC concept to polymer blends, we observe a dual benefit, namely improvement of mechanical performance via fibrils reinforcement and avoiding the detrimental effect of CNTs using microfibrils or compatibilizer loading only for improving the functional properties of the polymer blend.

The further steps of this study will be in the direction of finding the real percolation threshold for these new types of loading via variation of the concentration of CNTs as well as using second conductive filler for improvement of contacts between individual highly oriented carbon nanotubes.

4. Conclusions

The main goal of this study was to investigate the possibility for preparation of conductive two-component polymer blends loaded with conductive filler (CNTs in the present case) only at the interface between the two immiscible polymers. As a reference, blends with MFC structure were used and as carrier for CNTs a compatibilizer was applied. The conductivity of such blends was compared with microfibril loaded MFCs and bulk loaded homopolymers. The dispersion of CNTs in the minor component or in the interface only allows us to avoid significantly the detrimental effect of CNTs on the mechanical properties of polymers and their blends. Exploring the strong dependence of conductivity on filler concentration, experiments with compatibilizer containing higher CNT loadings are in progress with the target to determine the real threshold concentration for this type of loading.

Acknowledgements

The authors would like to thank the Foundation for Research Science and Technology of New Zealand for the financial support (Grant No. UOAX 0406). S.F. acknowledges the financial support of the Alexander von Humboldt Foundation, Germany, in the frame of the program ‘Reinvitation of former AVH awardees’ making possible his stay at the Leibniz Institute of Polymer Research Dresden (IPF), where this paper was initiated. We thank Mr. Bernd Kretzschmar (IPF) for compounding the PP-g-MA/CNT compatibilizer.

References

- [1] Smith J., Connell J., Delozier D. M., Lillehei P. T., Watson K. A., Lin Y., Zhou B., Sun Y-P.: Space durable polymer/carbon nanotube films for electrostatic charge mitigation. *Polymer*, **45**, 825–836 (2004).
DOI: [10.1016/j.polymer.2003.11.024](https://doi.org/10.1016/j.polymer.2003.11.024)
- [2] Xu N. S., Wu Z. S., Deng S. Z., Chen J.: High-voltage triode flat-panel display using field-emission nanotube-based thin films. *Journal of Vacuum Science and Technology B*, **19**, 1370–1372 (2001).
DOI: [10.1116/1.1387451](https://doi.org/10.1116/1.1387451)
- [3] Wang Q. H., Setlur A. A., Lauerhaas J. M., Dai J. Y., Seelig E. W., Chang R. P. H.: A nanotube-based field-emission flat panel display. *Applied Physics Letters*, **72**, 2912–2913 (1998).
DOI: [10.1063/1.121493](https://doi.org/10.1063/1.121493)
- [4] Villmow T., Pegel S., John A., Rentenberger R., Pötschke P.: Liquid sensing: Smart polymer/CNT composites. *Materials Today*, **14**, 340–345 (2011).
DOI: [10.1016/S1369-7021\(11\)70164-X](https://doi.org/10.1016/S1369-7021(11)70164-X)
- [5] Tai X., Wu G., Tominaga Y., Asai S., Sumita M.: An approach to one-dimensional conductive polymer composites. *Journal of Polymer Science Part B: Polymer Physics*, **43**, 184–189 (2005).
DOI: [10.1002/polb.20305](https://doi.org/10.1002/polb.20305)
- [6] Yoshio M., Kagata T., Hoshino K., Mukai T., Ohno H., Kato T.: One-dimensional ion-conductive polymer films: Alignment and fixation of ionic channels formed by self-organization of polymerizable columnar liquid crystals. *Journal of the American Chemical Society*, **128**, 5570–5577 (2006).
DOI: [10.1021/ja0606935](https://doi.org/10.1021/ja0606935)
- [7] Lanticse L. J., Tanabe Y., Matsui K., Kaburagi Y., Suda K., Hoteida M., Endo M., Yasuda E.: Shear-induced preferential alignment of carbon nanotubes resulted in anisotropic electrical conductivity of polymer composites. *Carbon*, **44**, 3078–3086 (2006).
DOI: [10.1016/j.carbon.2006.05.008](https://doi.org/10.1016/j.carbon.2006.05.008)
- [8] Breuer O., Sundararaj U.: Big returns from small fibers: A review of polymer/carbon nanotube composites. *Polymer Composites*, **25**, 630–645 (2004).
DOI: [10.1002/pc.20058](https://doi.org/10.1002/pc.20058)
- [9] Grossiord N., Loos J., Regev O., Koning C. E.: Toolbox for dispersing carbon nanotubes into polymers to get conductive nanocomposites. *Chemistry of Materials*, **18**, 1089–1099 (2006).
DOI: [10.1021/cm051881h](https://doi.org/10.1021/cm051881h)
- [10] Pötschke P., Bhattacharyya A. R., Janke A., Pegel S., Leonhardt A., Täschner C., Ritschel M., Roth S., Hornbostel B., Cech J.: Melt mixing as method to disperse carbon nanotubes into thermoplastic polymers. *Fullerenes, Nanotubes and Carbon Nanostructures*, **13**, 211–224 (2005).
DOI: [10.1081/FST-200039267](https://doi.org/10.1081/FST-200039267)
- [11] Xu X-B., Li Z-M., Yang M-B., Jiang S., Huang R.: The role of the surface microstructure of the microfibrils in an electrically conductive microfibrillar carbon black/poly(ethylene terephthalate)/polyethylene composite. *Carbon*, **43**, 1479–1487 (2005).
DOI: [10.1016/j.carbon.2005.01.039](https://doi.org/10.1016/j.carbon.2005.01.039)
- [12] Pötschke P., Bhattacharyya A. R., Janke A.: Carbon nanotube-filled polycarbonate composites produced by melt mixing and their use in blends with polyethylene. *Carbon*, **42**, 965–969 (2004).
DOI: [10.1016/j.carbon.2003.12.001](https://doi.org/10.1016/j.carbon.2003.12.001)
- [13] Gubbels F., Blacher S., Vanlathem E., Jérôme R., Deltour R., Brouers F., Teyssie P.: Design of electrical composites: Determining the role of the morphology on the electrical properties of carbon black filled polymer blends. *Macromolecules*, **28**, 1559–1566 (1995).
DOI: [10.1021/ma00109a030](https://doi.org/10.1021/ma00109a030)
- [14] Balberg I.: A comprehensive picture of the electrical phenomena in carbon black–polymer composites. *Carbon*, **40**, 139–143 (2002).
DOI: [10.1016/S0008-6223\(01\)00164-6](https://doi.org/10.1016/S0008-6223(01)00164-6)
- [15] Dong X. M., Fu R. W., Zhang M. Q., Zhang B., Rong M. Z.: Electrical resistance response of carbon black filled amorphous polymer composite sensors to organic vapors at low vapor concentrations. *Carbon*, **42**, 2551–2559 (2004).
DOI: [10.1016/j.carbon.2004.05.034](https://doi.org/10.1016/j.carbon.2004.05.034)
- [16] Naficy S., Garmabi H.: Study of the effective parameters on mechanical and electrical properties of carbon black filled PP/PA6 microfibrillar composites. *Composites Science and Technology*, **67**, 3233–3241 (2007).
DOI: [10.1016/j.compscitech.2007.04.001](https://doi.org/10.1016/j.compscitech.2007.04.001)
- [17] Zhang C., Ma C-A., Wang P., Sumita M.: Temperature dependence of electrical resistivity for carbon black filled ultra-high molecular weight polyethylene composites prepared by hot compaction. *Carbon*, **43**, 2544–2553 (2005).
DOI: [10.1016/j.carbon.2005.05.006](https://doi.org/10.1016/j.carbon.2005.05.006)
- [18] Hindermann-Bischoff M., Ehrburger-Dolle F.: Electrical conductivity of carbon black–polyethylene composites: Experimental evidence of the change of cluster connectivity in the PTC effect. *Carbon*, **39**, 375–382 (2001).
DOI: [10.1016/S0008-6223\(00\)00130-5](https://doi.org/10.1016/S0008-6223(00)00130-5)

- [19] Dai K., Xu X-B., Li Z-M.: Electrically conductive carbon black (CB) filled *in situ* microfibrillar poly(ethylene terephthalate) (PET)/polyethylene (PE) composite with a selective CB distribution. *Polymer*, **48**, 849–859 (2007).
DOI: [10.1016/j.polymer.2006.12.026](https://doi.org/10.1016/j.polymer.2006.12.026)
- [20] Kim Y. J., Shin T. S., Choi H. D., Kwon J. H., Chung Y. C., Yoon H. G.: Electrical conductivity of chemically modified multiwalled carbon nanotube/epoxy composites. *Carbon*, **43**, 23–30 (2005).
DOI: [10.1016/j.carbon.2004.08.015](https://doi.org/10.1016/j.carbon.2004.08.015)
- [21] Bauhofer W., Kovacs J. Z.: A review and analysis of electrical percolation in carbon nanotube polymer composites. *Composites Science and Technology*, **69**, 1486–1498 (2009).
DOI: [10.1016/j.compscitech.2008.06.018](https://doi.org/10.1016/j.compscitech.2008.06.018)
- [22] Byrne M. T., Gun'ko Y. K.: Recent advances in research on carbon nanotube–polymer composites. *Advanced Materials*, **22**, 1672–1688 (2010).
DOI: [10.1002/adma.200901545](https://doi.org/10.1002/adma.200901545)
- [23] Spitalsky Z., Tasis D., Papagelis K., Galotis C.: Carbon nanotube–polymer composites: Chemistry, processing, mechanical and electrical properties. *Progress in Polymer Science*, **35**, 357–401 (2010).
DOI: [10.1016/j.progpolymsci.2009.09.003](https://doi.org/10.1016/j.progpolymsci.2009.09.003)
- [24] Logakis E., Pandis C., Pissis P., Pionteck J., Pötschke P.: Highly conducting poly(methyl methacrylate)/carbon nanotubes composites: Investigation on their thermal, dynamic-mechanical, electrical and dielectric properties. *Composites Science and Technology*, **71**, 854–862 (2011).
DOI: [10.1016/j.compscitech.2011.01.029](https://doi.org/10.1016/j.compscitech.2011.01.029)
- [25] Fournier J., Boiteux G., Seytre G., Marichy G.: Positive temperature coefficient effect in carbon black/epoxy polymer composites. *Journal of Materials Science Letters*, **16**, 1677–1679 (1997).
DOI: [10.1023/A:1018582216002](https://doi.org/10.1023/A:1018582216002)
- [26] Bin Y., Xu C., Zhu D., Matsuo M.: Electrical properties of polyethylene and carbon black particle blends prepared by gelation/crystallization from solution. *Carbon*, **40**, 195–199 (2002).
DOI: [10.1016/S0008-6223\(01\)00173-7](https://doi.org/10.1016/S0008-6223(01)00173-7)
- [27] Xiong C., Zhou Z., Xu W., Hu H., Zhang Y., Dong L.: Polyurethane/carbon black composites with high positive temperature coefficient and low critical transformation temperature. *Carbon*, **43**, 1778–1814 (2005).
DOI: [10.1016/j.carbon.2005.02.001](https://doi.org/10.1016/j.carbon.2005.02.001)
- [28] Thongruang W., Spontak R. J., Balik C. M.: Bridged double percolation in conductive polymer composites: An electrical conductivity, morphology and mechanical property study. *Polymer*, **43**, 3717–3725 (2002).
DOI: [10.1016/S0032-3861\(02\)00180-5](https://doi.org/10.1016/S0032-3861(02)00180-5)
- [29] Sumita M., Sakata K., Hayakawa Y., Asai S., Miyasaka K., Tanemura M.: Double percolation effect on the electrical conductivity of conductive particles filled polymer blends. *Colloid and Polymer Science*, **270**, 134–139 (1992).
DOI: [10.1007/bf00652179](https://doi.org/10.1007/bf00652179)
- [30] Zhang L., Wan C., Zhang Y.: Morphology and electrical properties of polyamide 6/polypropylene/multiwalled carbon nanotubes composites. *Composites Science and Technology*, **69**, 2212–2217 (2009).
DOI: [10.1016/j.compscitech.2009.06.005](https://doi.org/10.1016/j.compscitech.2009.06.005)
- [31] Pötschke P., Bhattacharyya A. R., Janke A.: Morphology and electrical resistivity of melt mixed blends of polyethylene and carbon nanotube filled polycarbonate. *Polymer*, **44**, 8061–8069 (2003).
DOI: [10.1016/j.polymer.2003.10.003](https://doi.org/10.1016/j.polymer.2003.10.003)
- [32] Meincke O., Kaempfer D., Weickmann H., Friedrich C., Vathauer M., Warth H.: Mechanical properties and electrical conductivity of carbon-nanotube filled polyamide-6 and its blends with acrylonitrile/butadiene/styrene. *Polymer*, **45**, 739–748 (2004).
DOI: [10.1016/j.polymer.2003.12.013](https://doi.org/10.1016/j.polymer.2003.12.013)
- [33] Gödel A., Kasaliwal G., Pötschke P.: Selective localization and migration of multiwalled carbon nanotubes in blends of polycarbonate and poly(styrene-acrylonitrile). *Macromolecular Rapid Communications*, **30**, 423–429 (2008).
DOI: [10.1002/marc.200800549](https://doi.org/10.1002/marc.200800549)
- [34] Gültner M., Gödel A., Pötschke P.: Tuning the localization of functionalized MWCNTs in SAN/PC blends by a reactive component. *Composites Science and Technology*, **72**, 41–48 (2011).
DOI: [10.1016/j.compscitech.2011.09.013](https://doi.org/10.1016/j.compscitech.2011.09.013)
- [35] Gödel A., Marmur A., Kasaliwal G. R., Pötschke P., Heinrich G.: Shape-dependent localization of carbon nanotubes and carbon black in an immiscible polymer blend during melt mixing. *Macromolecules*, **44**, 6094–6102 (2011).
DOI: [10.1021/ma200793a](https://doi.org/10.1021/ma200793a)
- [36] Fakirov S., Bhattacharyya D., Lin R. J. T., Fuchs C., Friedrich K.: Contribution of coalescence to microfibril formation in polymer blends during cold drawing. *Journal of Macromolecular Science Part B: Physics*, **46**, 183–194 (2007).
DOI: [10.1080/00222340601044375](https://doi.org/10.1080/00222340601044375)
- [37] Fakirov S., Evstatiev M.: Microfibrillar reinforced composites – New materials from polymer blends. *Advanced Materials*, **6**, 395–398 (1994).
DOI: [10.1002/adma.19940060513](https://doi.org/10.1002/adma.19940060513)
- [38] Fakirov S., Evstatiev M., Petrovich S.: Microfibrillar reinforced composites from binary and ternary blends of polyesters and nylon 6. *Macromolecules*, **26**, 5219–5226 (1993).
DOI: [10.1021/ma00071a038](https://doi.org/10.1021/ma00071a038)
- [39] Shields R. J., Bhattacharyya D., Fakirov S.: Fibrillar polymer–polymer composites: Morphology, properties and applications. *Journal of Materials Science*, **43**, 6758–6770 (2008).
DOI: [10.1007/s10853-008-2693-z](https://doi.org/10.1007/s10853-008-2693-z)
- [40] Lin R. J. T., Bhattacharyya D., Fakirov S.: Innovative manufacturing of carbon nanotube-loaded fibrillar polymer composites. *International Journal of Modern Physics B*, **24**, 2459–2465 (2010).
DOI: [10.1142/S021797921006509X](https://doi.org/10.1142/S021797921006509X)

- [41] Xu H-P., Dang Z-M., Shi D-H., Bai J-B.: Remarkable selective localization of modified nanoscaled carbon black and positive temperature coefficient effect in binary-polymer matrix composites. *Journal of Materials Chemistry*, **18**, 2685–2690 (2008). DOI: [10.1039/B717591D](https://doi.org/10.1039/B717591D)
- [42] Gao J-F., Yan D-X., Yuan B., Huang H-D., Li Z-M.: Large-scale fabrication and electrical properties of an anisotropic conductive polymer composite utilizing preferable location of carbon nanotubes in a polymer blend. *Composites Science and Technology*, **70**, 1973–1979 (2010). DOI: [10.1016/j.compscitech.2010.07.019](https://doi.org/10.1016/j.compscitech.2010.07.019)
- [43] Zhang Y-C., Dai K., Tang J-H., Ji X., Li Z-M.: Anisotropically conductive polymer composites with a selective distribution of carbon black in an *in situ* microfibrillar reinforced blend. *Materials Letters*, **64**, 1430–1432 (2010). DOI: [10.1016/j.matlet.2010.03.041](https://doi.org/10.1016/j.matlet.2010.03.041)
- [44] Li Z-M., Xu X-B., Lu A., Shen K-Z., Huang R., Yang M-B.: Carbon black/poly(ethylene terephthalate)/polyethylene composite with electrically conductive *in situ* microfiber network. *Carbon*, **42**, 428–432 (2004). DOI: [10.1016/j.carbon.2003.10.032](https://doi.org/10.1016/j.carbon.2003.10.032)
- [45] Dai K., Li Z-M., Xu X-B.: Electrically conductive *in situ* microfibrillar composite with a selective carbon black distribution: An unusual resistivity–temperature behavior upon cooling. *Polymer*, **49**, 1037–1048 (2008). DOI: [10.1016/j.polymer.2007.12.043](https://doi.org/10.1016/j.polymer.2007.12.043)
- [46] Shaffer M. S. P., Windle A. H.: Fabrication and characterization of carbon nanotube/poly(vinyl alcohol) composites. *Advanced Materials*, **11**, 937–941 (1999). DOI: [10.1002/\(sici\)1521-4095\(199908\)11:11<937::aid-adma937>3.0.co;2-9](https://doi.org/10.1002/(sici)1521-4095(199908)11:11<937::aid-adma937>3.0.co;2-9)
- [47] Evstatiev M., Fakirov S., Friedrich K.: Manufacturing and characterization of microfibrillar reinforced composites from polymer blends. in ‘Polymer composites’ (eds.: Friedrich K., Fakirov S., Zhang Z.) 149–167 (2005).
- [48] Fakirov S.: Modified Soxhlet apparatus for high-temperature extraction. *Journal of Applied Polymer Science*, **102**, 2013–2014 (2006). DOI: [10.1002/app.23397](https://doi.org/10.1002/app.23397)
- [49] Menzer K., Krause B., Boldt R., Kretzschmar B., Weidisch R., Pötschke P.: Percolation behaviour of multi-walled carbon nanotubes of altered length and primary agglomerate morphology in melt mixed isotactic polypropylene-based composites. *Composites Science and Technology*, **71**, 1936–1943 (2011). DOI: [10.1016/j.compscitech.2011.09.009](https://doi.org/10.1016/j.compscitech.2011.09.009)
- [50] ANSI/ESD S541-2008: Packaging material standards for ESD sensitive items (2008).
- [51] Pötschke P., Andres T., Villmow T., Pegel S., Brüning H., Kobashi K., Fischer D., Häussler L.: Liquid sensing properties of fibres prepared by melt spinning from poly(lactic acid) containing multi-walled carbon nanotubes. *Composites Science and Technology*, **70**, 343–349 (2010). DOI: [10.1016/j.compscitech.2009.11.005](https://doi.org/10.1016/j.compscitech.2009.11.005)
- [52] Seo M-K., Park S-J.: Electrical resistivity and rheological behaviors of carbon nanotubes-filled polypropylene composites. *Chemical Physics Letters*, **395**, 44–48 (2004). DOI: [10.1016/j.cplett.2004.07.047](https://doi.org/10.1016/j.cplett.2004.07.047)
- [53] Logakis E., Pissis P., Pospiech D., Korwitz A., Krause B., Reuter U., Pötschke P.: Low electrical percolation threshold in poly(ethylene terephthalate)/multi-walled carbon nanotube nanocomposites. *European Polymer Journal*, **46**, 928–936 (2010). DOI: [10.1016/j.eurpolymj.2010.01.023](https://doi.org/10.1016/j.eurpolymj.2010.01.023)
- [54] King J. A., Via M. D., King M. E., Miskioglu I., Bogucki G. R.: Electrical and thermal conductivity and tensile and flexural properties: Comparison of carbon black/polycarbonate and carbon nanotube/polycarbonate resins. *Journal of Applied Polymer Science*, **121**, 2273–2281 (2011). DOI: [10.1002/app.33890](https://doi.org/10.1002/app.33890)
- [55] Pötschke P., Bhattacharyya A. R., Janke A., Goering H.: Melt mixing of polycarbonate/multi-wall carbon nanotube composites. *Composite Interfaces*, **10**, 389–404 (2003). DOI: [10.1163/156855403771953650](https://doi.org/10.1163/156855403771953650)

Multiwalled carbon nanotubes incorporated into a miscible blend of poly(phenylenether)/polystyrene – Processing and characterization

S. Sathyanarayana^{1,2*}, M. Wegrzyn³, G. Olowojoba¹, A. Benedito³, E. Giménez⁴, C. Hübner¹, F. Henning^{1,2}

¹Polymer Engineering Department, Fraunhofer Institute for Chemical Technology ICT, Joseph von Fraunhofer Strasse 7, 76327 Pfinztal, Germany

²Institute of Vehicle System Technology, Chair of Lightweight Technology (FAST), Karlsruhe Institute of Technology (KIT), Rintheimer-Querallee 2, 76131 Karlsruhe, Germany

³Instituto Tecnológico del Plástico (AIMPLAS), Calle Gustave Eiffel 4, 46980 Paterna, Spain

⁴Instituto de Tecnología de Materiales. Universidad Politécnica de Valencia, Camino de Vera, 46022 Valencia, Spain

Received 8 February 2013; accepted in revised form 11 April 2013

Abstract. 4 wt% multiwalled carbon nanotubes (MWCNTs) were incorporated into a miscible blend of polyphenylenether/polystyrene (PPE/PS) on a twin-screw extruder at a screw speed of 600 rpm. The masterbatch obtained was diluted at 400 and 600 rpm to obtain lower MWCNT loadings in PPE/PS. Electron microscopy & optical microscopy images show very good MWCNT dispersion even at high filler loadings of 4 wt%, but slightly larger agglomerate size fractions are observable at higher screw speeds. While MWCNT addition enhanced the thermal stability of PPE/PS, a small change in glass transition was observed on the composites at different filler concentrations compared to PPE/PS. The specific heat capacity at glass transition decreases considerably until 2 wt% MWCNT and levels down thereafter for both processing conditions pointing to enhanced filler-matrix interaction at lower loadings. Storage modulus of the nanocomposites was enhanced significantly on MWCNT incorporation with reinforcing effect dropping considerably as a function of temperature, especially at lower filler contents. The modulus and the tensile strength of PPE/PS were only marginally enhanced in spite of excellent MWCNT dispersion in the matrix. Electrical percolation occurs at 0.4 wt% MWCNT content, and the electrical conductivity of 0.5 wt% MWCNT reinforced PPE/PS was close to 12 orders in magnitude higher compared to PPE/PS.

Keywords: nanocomposites, carbon nanotubes, twin-screw compounding, characterization and properties

1. Introduction

Carbon nanotube (CNT) reinforced polymer nanocomposites have generated significant interest due to the excellent inherent mechanical, electronic and thermal properties of CNTs as reported by Dresselhaus *et al.* [1]. Reality however indicates otherwise as it has not been possible to achieve the expected commercial success out of these materials owing to the intrinsic tendency of CNTs to agglomerate due to van der Waals forces. The intrinsic cohesive strength

of the agglomerates is quite high which makes it difficult to achieve only individually dispersed CNTs in the matrix. Although the extent of initial agglomeration have been demonstrated to be successfully reduced by suitable processing conditions [2, 3], desired results especially from the perspective of developing good mechanical properties have been difficult to obtain. The high aspect ratio of CNTs which is expected to enhance the efficiency of reinforcement at extremely lower filler loadings com-

*Corresponding author, e-mail: shyam.sathyanarayana@ict.fraunhofer.de
© BME-PT

pared to its competitors like carbon black, carbon fibers etc. is one reason why CNTs are so attractive. The degree of dispersion of CNTs and the consequent macroscopic behavior is strongly dictated by the choice of the matrix [4, 5], the type of CNT [6–9] and modification of their surface [10–13], and the processing method and associated parameters [2, 3, 14]. Low filler percolation thresholds have been achieved with CNT reinforcements in epoxy [15, 16], owing to excellent filler dispersion and better compatibility of the CNTs with the resin. Nevertheless, nanocomposites based on thermoplastic resins show more complexities especially when analyzing the effect of processing method on the final properties. Several possibilities exist for the processing of CNT/thermoplastic nanocomposites, but melt mixing is the most interesting from the viewpoint of large-scale industrial processing. CNT based thermoplastic polymer nanocomposites produced by compounding on a twin-screw extruder requires the control of a great number of process variables to tailor the quality of dispersion. Typically, melt compounding must be accompanied by a secondary processing step of either compression molding or injection molding to produce the final part. The low viscosity and minimal influence of shear during compression molding facilitates a suitable environment for the nanoscale re-agglomeration of the previously dispersed agglomerates increasing the composite conductivity [14, 17]; while decreasing composite mechanical properties. On the other hand, injection molding leads to higher composite bulk resistivity and anisotropy in mechanical characteristics due to two principal reasons: orientation of the CNTs in the direction of flow due to process shear, and the polymer rich skin-core structure due to high temperature differences between the mold wall and the composite melt [18]. Thus, there is a clear relationship between the percolation threshold and the processing methodology.

Several CNT/thermoplastic nanocomposites have been investigated for improvements in mechanical properties, electrical properties or both on single polymers [4, 14, 18] and polymer blends [19, 20]. Polymer blends offer an attractive proposition owing to their innovative properties combining the valuable characteristics of the participating polymers. The effectiveness of filler incorporation in a polymer blend is dependent on the wetting parameter and the compatibility of the blends at the molecular

level, the former assuming much significance in immiscible blends. The main interest arose in this field after the explanation of the double percolation strategy by Sumita *et al.* [21] in carbon black filled polymer blends. When the phase in which the filler is localized acts as a continuous phase, the percolation occurs at very low concentration. Double percolation strategy (or co-continuous morphology) has seemingly worked leading to low percolation thresholds especially from the point of electrical conductivity. Multiwalled carbon nanotube (MWCNT) incorporation in polyamide 6 (PA6)/polypropylene (PP) resulted in the selective localization of CNTs in the PA6 phase and a small amount was also found in the interphase between the polymers [20]. In the study reported by Bose *et al.* [22], nanocomposites based on PA6/acrylonitrile butadiene styrene (ABS) were prepared by melt mixing and a preferential localization of CNTs was observed on the PA6 phase while a few were found to be bridging the two phases. Several other blend systems filled with CNTs such as polycarbonate (PC)/polyethylene (PE) [19], poly(ϵ -caprolactone)/polylactide (PCL/PLA) [23], polyamide (PA)/ethyl acetate (EA) [24], PP/ABS [25], polyethylene terephthalate (PET)/polyvinylidene fluoride (PVDF) [26] etc. have also been investigated. However, incorporating MWCNT into miscible polymer blends is seldom reported and hence we focus our attention on this issue in this work. Polyphenylenether/high impact polystyrene (PPE/PS) is one of the very few completely miscible polymer blends commercially available. The miscibility at the molecular level is a result of the strong interaction between the phenylene ring of PPE and phenyl ring of PS [27]. Tiwari *et al.* [28] reported enhanced thermal stability and mechanical properties with the addition of nanoclay onto PPE/PS by melt mixing. In this work, we expect a good compatibility between PPE/PS and MWCNTs, principally due to the presence of phenyl groups on all components and possible hydrogen bonding. Higher PPE loading presents enhanced polarity to the blend [29], and this could be expected to contribute to the increased compatibility of the blend with the MWCNTs leading to good filler dispersion in the matrix.

We report the effect of MWCNTs on the morphology, thermal, mechanical and electrical properties of PPE/PS nanocomposites processed on a lab scale twin-screw extruder in this article.

2. Experimental

2.1. Materials

MWCNT grade NC7000 (Nanocyl S.A., Sambreville, Belgium) used in this work was produced by the chemical vapor deposition (CVD) process. It had a carbon purity of 90%, average length of 1.5 μm , average diameter of 9.5 nm and surface area of 250–300 m^2/g according to the suppliers. Noryl[®] 731, a commercial blend of PPE/PS was used as matrix and was supplied by SABIC Innovative Plastics. It had a melt flow rate (MVR) of 8 $\text{cm}^3/10$ min. The polymer was dried for 4 h at 120°C while the MWCNTs were used as-received.

2.2. Processing of the composites

PPE/PS-MWCNT nanocomposites were produced with a throughput of 1 kg/h on a twin-screw co-rotating laboratory extruder Prism Eurolab 16 (Thermo Fisher Scientific, Waltham, USA) with $D = 16$ mm and $L/D = 25$. The barrel temperatures were set to 280°C while two screw speeds of 400 and 600 rpm were employed. A screw profile with a combination of transporting, kneading and back flow elements was employed. MWCNT was fed to the extruder with a pneumatic feeder (Brabender Technologie GmbH & Co. AG, Duisburg, Germany) together with polymer pellets through the main hopper at a screw speed of 600 rpm which resulted in a masterbatch of 4.0 wt% MWCNT content. Nanocomposites with lower MWCNT loadings (0.5, 1, 1.5 and 2 wt%) were prepared by masterbatch dilution. The 4 wt% MWCNT filled masterbatch was re-processed at both screw speeds to produce reference composites. Specific mechanical energy (SME) is an important parameter in extrusion. It is a measure of the resulting energy going into the compounding per unit mass of the melt from the motor and is given by Equation (1):

$$SME \left[\frac{\text{kWh}}{\text{kg}} \right] = \frac{Q_{\text{rat}} \cdot T \cdot \frac{N_{\text{process}}}{N_{\text{max}}} \cdot \eta}{M} \quad (1)$$

where Q_{rat} – motor rating [kW], T – % of maximum permissible torque used, N_{process} – screw speed for the process [rpm], N_{max} – maximum permissible speed [rpm], η – gearbox efficiency [%] and M – process throughput [kg/h].

For measuring and characterization of PPE/PS nanocomposites, plates and bars with varying dimensions (refer section 2.3) were prepared by compres-

sion molding in a Collin 6300 press (Dr. Collin GmbH, Ebersberg, Germany) aided by ZYVAX water shield mold release agent (ZYVAX, Ellijay, USA). Processing was based on five-step program with pressures varying from 10 to 210 bars between steps at constant upper and lower plate temperatures of 290°C.

Injection molding of the extruded composites were carried out with the help of a BOY Spritzgiessautomaten 12A equipment (Dr. Boy GmbH & Co. KG, Neustadt-Fernthal, Germany) fitted with a CTM-12LH mold temperature control to produce composite bars for mechanical testing. The temperatures of the mold and melt were set at 100 and 290°C respectively, and the melt was injected into the mold at 100 mm/s. An injection speed of 10 mm/s was also employed to study variations in a few composites.

2.3. Characterization of the composites

Scanning electron microscopy (SEM) was carried out using a JEOL JSM-7001F FESEM (JEOL, Tokyo, Japan) on cryofractured compression-molded plates. The samples were coated with Platinum for 20 sec at 40 mA on a sputter coater. Optical micrographs of the composites were made on thin films of approximately 20 μm thickness.

Thermo-gravimetric analysis (TGA) was carried out on TGA Q5000 (TA Instruments, New Castle, USA). Around 15 mg of extruded granulates were heated from 50 to 900°C at a heating rate of 20°C/min under air atmosphere. The temperature at which 5 wt% of the material has been degraded is taken to be the temperature of onset of degradation (T_{onset}) and is evaluated from the temperature vs % weight loss curve.

Differential scanning calorimetry (DSC) measurements were carried out on extruded granules (8–10 mg) using a PYRIS Diamond DSC (Perkin Elmer, Waltham, USA). Samples were heated from 40 to 180°C at a heating rate of 10°C/min to remove any thermal history on the material. The sample was then cooled to 40°C at the rate of 30°C/min. Second heating regime was performed similar to the first heating and these observations were used for interpretations. The glass transition temperature (T_g) and the change in specific heat capacity (C_p) at T_g were measured.

Dynamic mechanical behavior of the PPE/PS-MWCNT nanocomposites was measured on DMA-

2980 (TA Instruments, New Castle, USA) with dual cantilever clamp at a vibration frequency of 1 Hz from 35 to 200°C and scan rate of 3°C/min. Compression-molded samples (35 mm × 10 mm × 1.95 mm) were used for the test.

Electrical volume conductivity of the nanocomposites (at least three samples) were measured on compression molded bars (60 mm × 10 mm × 2 mm) following the Van der Pauw method with four point contact configuration (ISO 3915) using a Keithley Multimeter DMM 2000 (Keithley Instruments Inc. Cleveland, USA). Silver electrodes were painted on the samples in order to minimize contact resistance. The volume conductivity of PPE/PS matrix (three samples) was measured with the help of a Keithley Electrometer 6517A combined with a Keithley 8009 resistivity test fixture on compression molded plates (110 mm × 110 mm × 2 mm) owing to the inability to measure range of conductivities using the previously mentioned set up. In addition to these, the volume conductivity of the extruded strand was measured similarly to the methodology adopted on compressed bars. The electrical percolation threshold was estimated using the scaling law which describes the statistical percolation behavior in the vicinity of percolation (Equation (2)):

$$\sigma \propto (w - w_c)^t \quad (2)$$

where σ – experimental volume conductivity for $w \geq w_c$, w – MWCNT concentration [wt%], w_c – critical/percolation MWCNT concentration [wt%], t – critical exponent governing the dimensionality of the system.

Tensile testing of the injection-molded composites was carried out on at least 5 specimens using an Instron Universal Machine 3343 (1 kN load cell) (Instron Deutschland GmbH, Pfungstadt, Germany). Dumb-bell shaped specimens (4 mm thick) were tested according to the ASTM D638 standard. The samples were drawn at a crosshead speed of 5 mm/min at room temperature. The samples were conditioned for 24 h at 23°C and 50% RH before testing.

3. Results and discussion

3.1. Effect of processing parameters on morphology

MWCNT dispersion in matrix is a complicated mechanism involving the wetting of MWCNT agglomer-

ates by the melt, matrix infiltration into the agglomerates subsequently followed by the dispersion of agglomerates by erosion, or rupture (i.e. agglomerate shattering) mechanisms determined by the fragmentation number as reported elsewhere [30]. Though wetting, infiltration and dispersion mechanisms directly contribute to the nature and type of the matrix material and CNT, the nature of processing significantly influences the final morphology of the extruded composite.

Figure 1a shows the variations in the *SME* inputs as a function of MWCNT loadings at two different processing speeds. Increasing the processing speed from 400 to 600 rpm augmented the *SME* by a factor of approximately 1.5 owing to the increase in the shear stresses applied to the melt. This is quite significant as all the other process parameters remained constant. The *SME* for the processing of a PPE/PS-4 wt% MWCNT masterbatch stood at 0.87 kWh/kg. The other nanocomposites processed by diluting or re-processing masterbatch showed lower *SME*'s as a result of initial agglomerate dispersion in the masterbatch. The increase in MWCNT loadings resulted in higher *SME* values owing to the increase in the viscosity which is a direct function of the filler concentration and its dispersive morphology in the matrix. Improvement in the quality of dispersion with the process condi-

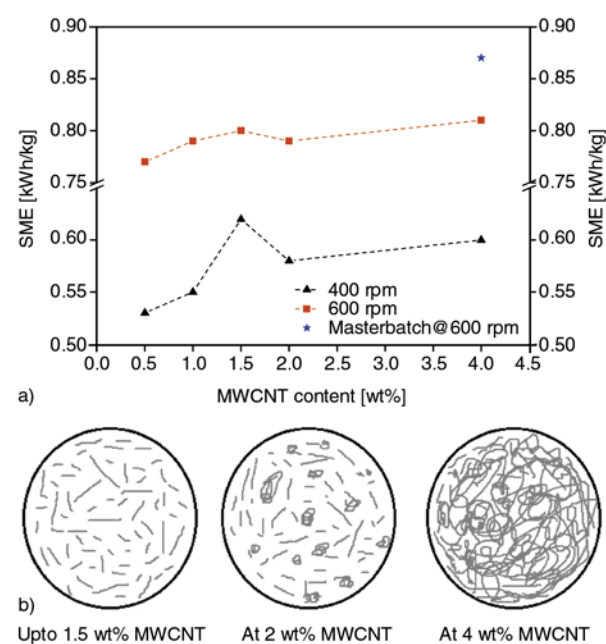


Figure 1. Variation of *SME* inputs with MWCNT loadings as a function of processing speed (a) and the sketch showing dispersive morphology at different loadings (b)

tion owing to de-agglomeration presents an increased surface area for the MWCNTs to interact with the matrix consequently enhancing the viscosity and thus the *SME* input. With further increase in MWCNT loading (at 2 wt% for both processing conditions here), the threshold for optimum filler dispersion could have been exceeded. This represents a scenario where CNT agglomerates behave like large particles which would eventually lower the viscosity than what would be achieved with a perfectly dispersed morphology. Hence, we find a decrease in the *SME* at this filler concentration. Further addition of MWCNTs would result in the increase in *SMEs* principally because of the increased density of agglomerates. This is well illustrated by the sketch in Figure 1b.

Although significant variations in the processing conditions were observed by analyzing the mixing energies, the morphologies of the nanocomposites observed by SEM in Figure 2a–2d do not show many differences in the qualities of dispersion. It

was also surprising to note the lack of visible agglomerates even at loadings of 4 wt% which is quite uncommon when dealing with CNTs. Aromatic group interactions between the matrix and the CNT, together with the polar nature of PPE/PS could have contributed to better filler-matrix compatibility and hence excellent MWCNT dispersion in the matrix.

In spite of the high resolution SEM images not showing significant variations in the degree of MWCNT dispersion, it was interesting to note that the optical micrographs of PPE/PS-0.5 wt% MWCNT composite processed at 600 rpm (*SME* = 0.77 kWh/kg) showed larger agglomerates than those observed on its 400 rpm (*SME* = 0.53 kWh/kg) counterpart (Figure 3). This could be due to the shorter residence time for the melt at higher processing speed, which inhibits the efficiency of de-agglomeration of the primary CNT agglomerates.

It is typical of CNT incorporation into an immiscible polymer blend to have a substantial influence on the size of the dispersed phase, this however was

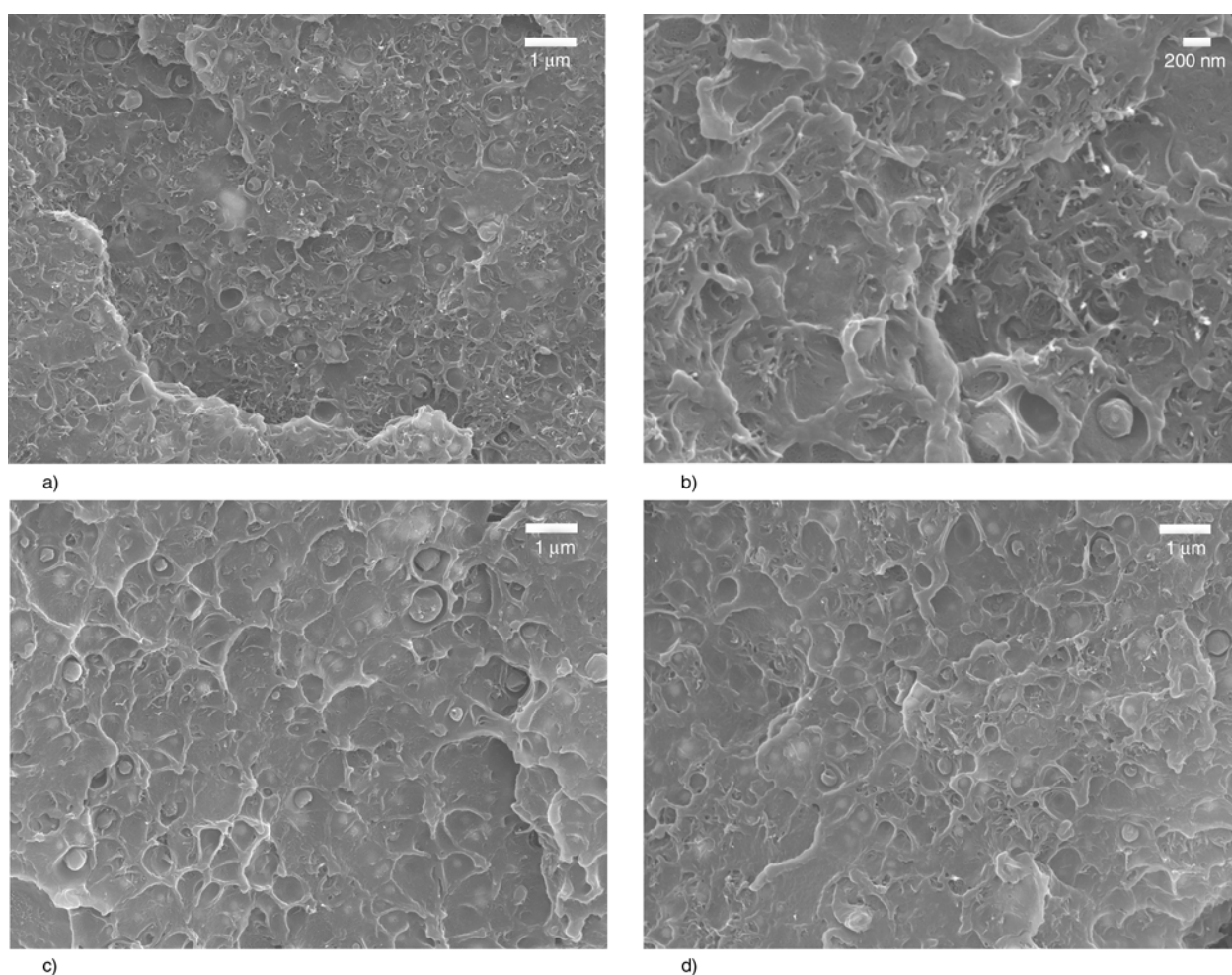


Figure 2. SEM Morphology (a) PPE/PS-4 wt% MWCNT (Masterbatch), (b) PPE/PS-4 wt% MWCNT (Masterbatch-Higher magnification), (c) PPE/PS-0.5 wt% MWCNT-600 rpm and (d) PPE/PS-1.5 wt% MWCNT-600 rpm

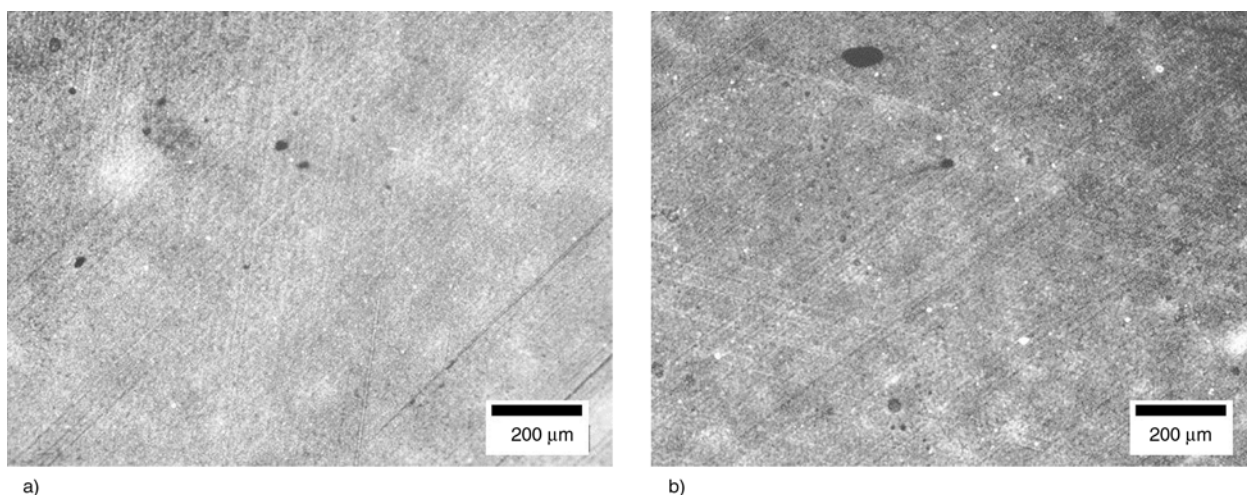


Figure 3. Representative optical micrographs of PPE/PS-0.5 wt% MWCNT composites processed at 400 rpm (a) and at 600 rpm (b)

not observable in this work as PPE/PS is miscible on a molecular level and hence the SEM images are not presented here.

3.2. Thermal stability of the nanocomposites

Figure 4 shows the onset temperature of thermal degradation of the prepared nanocomposites and the pristine matrix. The pure PPE/PS material (PPE/PS-1) and the PPE/PS-4 wt% MWCNT masterbatch showed T_{onset} at 417 and 426°C respectively. The presence of MWCNTs can lead to the stabilization of PPE/PS matrix, resulting in enhanced thermal stability (about 9°C) of the nanocomposite compared to the pristine polymer. It is well known that CNTs belonging to the C_{60} family have high electron affinities of about 2.65 eV [31] enabling them to act as efficient radical scavengers. The strong radical accepting capacities interrupt the radical propagation mechanism and hence decrease the rate of

degradation. This may be the main reason why nanocomposites exhibit better thermal stability compared to the pure polymer. The MWCNTs can effectively act as physical barriers to hinder the transport of volatile decomposed products out of PPE/PS nanocomposites during thermal decomposition.

A 4°C decrease in T_{onset} is observed when the pure PPE/PS is processed twice (PPE/PS-2) as compared to PPE/PS-1. The thermal stability of the material suffers in reprocessing as a result of polymer degradation. The same tendency could be expected with nanocomposites which have been processed by diluting the masterbatch. The thermal stability of the samples processed with 400 rpm is slightly better than those processed at 600 rpm. The quality of dispersion which was slightly better in the samples processed with 400 rpm enhanced the thermal stability owing to the creation of enhanced MWCNT surface area for interaction with the polymer. To add to this is the contribution of polymer degradation at higher processing speed.

The thermal stability of the composites increased significantly up to 1.5 wt% MWCNT loading, increasing filler addition beyond this loading does not seem to have a role in regulating the thermal stability of the composite. The filler loading and their respective quality of dispersion would have been the best at 1.5 wt% MWCNT loading, beyond which agglomeration tendencies of CNTs would have an impact on the composite properties. This correlates well with the observations and discussion on the *SME* of the composites from Figure 1.

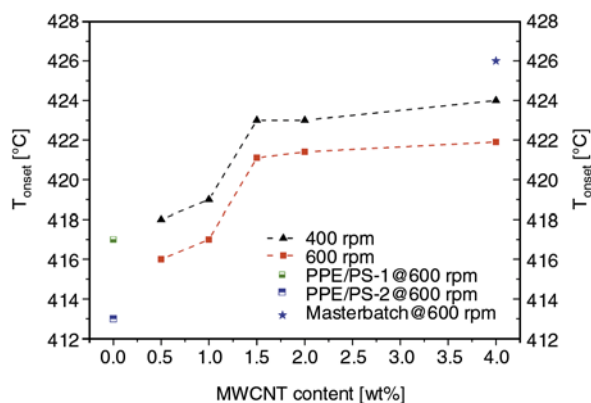


Figure 4. Temperature of onset of degradation (T_{onset}) of the matrix and the composites as a function of MWCNT content

The thermal stability of nanocomposites is determined by competitive effects. Whereas MWCNTs act as radical scavengers at low loadings [14] delaying the degradation pattern and enhancing thermal stability, it has also been reported that the enhancement in thermal conductivity on MWCNT addition to the matrix lowers the degradation temperatures [32]. The thermal stability of the nanocomposites depends to a certain extent on the interaction between the phases [33] (which can be presumed to be good here at least from the matrix perspective as PPE/PS is miscible) and the amount of residual metal catalyst in the MWCNTs which was used for their production. The quality of dispersion obtained by process conditions and the effect of polymer degradation also has to be accounted for. The fact that the masterbatch shows higher thermal stability than the diluted nanocomposites at 400 and 600 rpm conveys the combined effect of polymer degradation, dispersion quality and the reinforcing effect of MWCNTs on the thermal stability. It should however be stated that the magnitude of thermal stability increase observed with the PPE/PS-MWCNT nanocomposites compared to PPE/PS is significantly lower than those observed on PS/MWCNT nanocomposites [14] where close to 45°C variations were observed between pure PS and 2 wt% MWCNT reinforced nanocomposites depending on process conditions.

3.3. Glass transition and matrix-filler interactions

Glass transition measurements provide a qualitative measure of the interaction of the filler with the matrix. Here, glass transition values are reported from the variation of heat capacity from DSC measurements and temperature corresponding to the instance of maximum value of loss modulus (E'') and temperature at maximum $\tan \delta$ inflexion from the DMA measurements. DMA measurements are conducted at frequency range of 1 Hz compared to those of 10^{-2} – 10^{-3} Hz employed in DSC [34] and this could be the reason for the variation in the magnitude of T_g measured by the two methods.

From the DSC measurements, it can be seen that the T_g of once extruded PPE/PS-1 stood at 138°C while re-processing it (PPE/PS-2) under the same conditions resulted in a slight T_g drop (Figure 5). Polymer degradation with enhanced processing history could

be the only reason to explain this T_g drop. Though we speak of thermal degradation here, it is important to be wary of the fact that we had earlier observed a slight enhancement in thermal stability with varying MWCNT loadings into PPE/PS. On the other hand comparing PPE/PS-1 with the PPE/PS-4 wt% MWCNT masterbatch, T_g increase of 1.6°C is observed in the latter which is principally a result of the filler addition resulting in an interface between the matrix and the filler. Going along this notion, it is worthwhile to refer to the values of PPE/PS-2 for comparison with the composites. MWCNT addition increases the glass transition temperature of the matrix, but the variations are not very significant. The values are slightly higher for nanocomposites processed with 400 rpm. After a defined MWCNT loading, T_g suffers slightly.

The principal attribute in a filler-polymer system is the mechanism with which the filler and the polymer contribute to the property fluctuations both on microscopic and macroscopic scales. With CNT reinforcements in polymers three different interactions could be thought of namely polymer-CNT interaction, CNT-CNT interaction and polymer-polymer interaction. At optimum MWCNT concentrations, the two morphologies of fillers would be bridged by a polymer chain if the distance between the neighboring CNT would be less than the actual radius of gyration of the chain. When the MWCNT loading exceeds the threshold for the nanocomposite system in reference, there would be many polymer chains contributing to link the CNT.

Addition of the filler imposes a restriction on the molecular mobility of the polymer in close vicinity

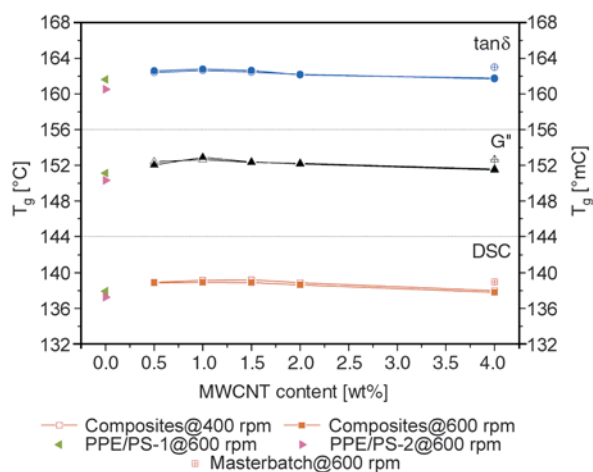


Figure 5. Observation of glass transition (T_g) by DSC and DMA measurements

to the filler contributing to the increase in glass transition. T_g of the intermediate layer is dependent upon the thickness of the layer [35, 36] and it decreases with approaching distance to the bulk polymer. When the MWCNT concentration is high, the probability for a filler-filler interaction is high resulting in decreasing size of the intermediate layer owing to their overlapping. This could potentially cause an overall reduction in the T_g because of the increase in the free volume for polymer chain mobility.

As MWCNT addition in theory could catalyze polymer degradation [37], the contribution of chain degradation with MWCNT addition and higher speeds of processing should also be taken into account while interpreting these observations. However, it is very difficult to quantify the contribution of degradation and polymer-filler interaction in affecting glass transition. Similar trends of glass transition observations have also been reported on MWCNT filled polystyrene composites [14], but the magnitude of T_g variations was very significant in those observations.

Variation of specific heat (C_p) during glass transition is a good indicator for the measurement of the level of interaction between the polymer and the filler. It is possible to estimate the fraction of polymer taking part in the glass transition [38]. The fraction of the polymer in direct contact with the filler (tethered onto the filler surface) behaves much different than the bulk and this layer has been regarded as immobile or a rigid amorphous fraction by Litvinov and Speiss [39]. The contribution of this fraction towards glass transition would be minimal as compared to the bulk polymer. With increasing filler contents it is expected of this rigid amorphous fraction to grow in stature thereby reducing the amount of polymer taking part in the glass transition and lowering the specific heat. Figure 6 shows the changes in the specific heat with MWCNT loadings at two different processing speeds. The C_p at glass transition of PPE/PS-2 was lowered from 0.252 to 0.216 and 0.213 J/(g·°C) on addition of 1 wt% MWCNT at 400 and 600 rpm respectively. Nanocomposites processed at 600 rpm always showed lower C_p values than its 400 rpm counterpart. The fact that the 4 wt% composites re-processed composites from the masterbatch showing lower C_p values may be attributed to the fact that the variation of C_p is also dependent on the morphology (quality of dispersion) in spite of polymer degrada-

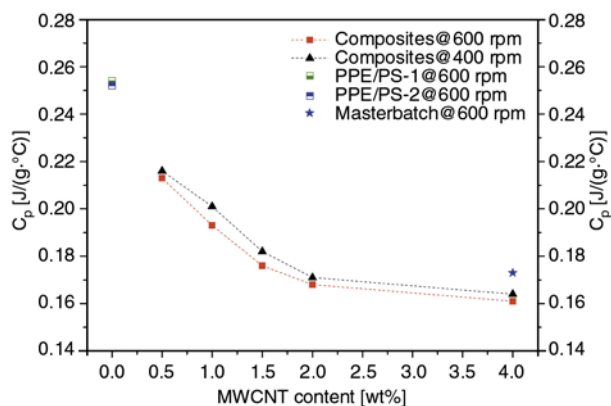


Figure 6. Variation of specific heat at glass transition of the nanocomposites with varying MWCNT loadings at two different processing speeds

tion enhanced processing history. Enhanced surface area of interaction presented by the filler for interaction with the polymer matrix would result in lower C_p values, owing to increased probability of interaction. The rate of C_p decay however slows down on greater than 2 wt% filler reinforcement which probably indicates the MWCNT threshold. It is also interesting to observe, at higher MWCNT loadings, a decrease in T_g and C_p , which is quite uncommon but has however been earlier reported [40, 41].

The area under the $\tan\delta$ curve of DMA measurement is a measure of the amount of polymer taking part in the glass transition according to Brady *et al.* [38]. Figure 7 shows that the area under the $\tan\delta$ decreases with increase in the filler concentration at the same processing parameters. It is very complicated to evaluate this area for quantitative assessments of polymer-CNT interactions (in terms of evaluating the amount of immobilized polymer etc.). It is generally accepted that the decrease in the storage modulus (E') of the composites with increase in

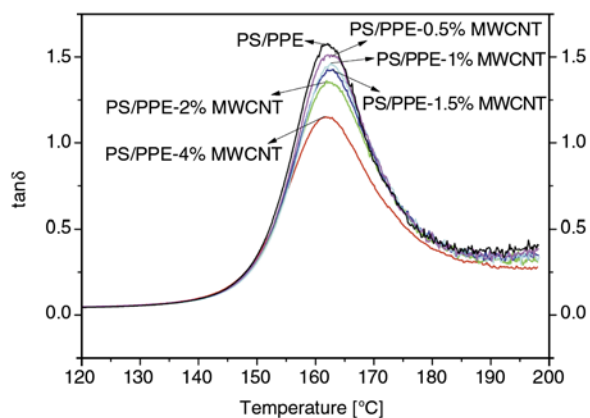


Figure 7. $\tan\delta$ observations as a function of MWCNT content at 600 rpm processing

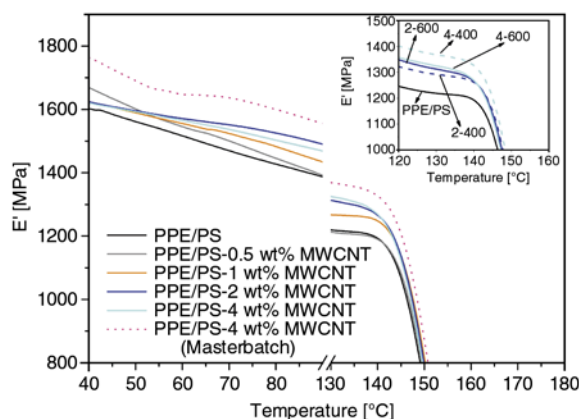


Figure 8. Variation of storage modulus as a function of MWCNT content at 600 rpm. Inset: zoomed view of the composites at 400 and 600 rpm.

temperature is a result of the co-operative motion of polymer chains leading to energy dissipation. This is among one of the significant observations with our nanocomposite system as well. E' of the nanocomposites measured by DMA is shown in Figure 8. The temperature regime has been broken in the axis to illustrate the effects of MWCNT incorporation both in low and high temperature regimes.

Considering the glassy regime, the addition of 4 wt% MWCNT to the matrix (masterbatch) has resulted in a 10% increase in the E' . The modulus of the matrix increased with MWCNT additions primarily due to the inherently higher stiffness of the filler. Increasing addition of MWCNT is generally expected to result in higher modulus, but this need not necessarily be the case always. The composite containing 0.5 wt% MWCNT exhibited a modulus of 1668 MPa at 40°C, higher than its counterpart with 4 wt% CNT loading but less than that of the masterbatch. Also interesting was the significant reduction in the modulus of the masterbatch ($E' = 1763$ MPa) when it was re-processed ($E' = 1620$ MPa). These observations point to the fact that the filler loading fraction does not alone suffice for enhancing the modulus of the composites, but the morphology of the composite and the degradation effects also make significant contributions. These observations are slightly contradictory to the extent of C_p change at different MWCNT loadings, but it must be noted that DMA measurements have been made on compression molded samples where potential re-agglomeration of the previously dispersed tubes could have changed the morphology.

When the CNT-CNT distance is less than the radius of gyration of the polymer, the polymer chains tend

to bridge the CNTs. With increase in the temperature, the chains lose their stiffness and the morphology is completely revamped and the stability of the polymer-CNT chain decreases and the system is dominated by the polymer-polymer entanglements. At lower CNT loadings this could be a potential cause for the drastic reduction of stiffness with temperature. This is clearly observed where very little difference is noticed between the matrix and the 0.5 wt% MWCNT reinforced composite. When the filler loading fraction is higher, there is an increased probability of enhanced filler-filler interaction which dominates the aforementioned drawback contributing to enhancement of the mechanical properties; however with the tradeoff of CNT agglomerates acting as elements of stress concentration. At temperatures above the glass transition, very little differences were observed between the modulus of the matrix and the composites.

E' of the composites processed with 600 rpm were always higher than their 400 rpm counterparts until 2 wt% MWCNT loadings (refer inset of Figure 8). At 4 wt% loading the sample processed with 400 rpm showed higher E' which may be attributed to degradation effect in addition to existence of larger primary agglomerates.

3.4. Mechanical properties of the nanocomposites

Figure 9 shows the mechanical properties of PPE/PS and its composites processed with a screw speed of 400 rpm and injection-molded thereafter using an injection speed of 100 mm/s. The elastic modulus of PPE/PS (2746 MPa) increases by about 2% on the incorporation of 0.5 wt% MWCNT. Increasing MWCNT additions further results in improvement in the elastic modulus with 4 wt% filler incorporation leading to an increase of modulus by 11%. It is expected of inorganic filler to improve the modulus of PPE/PS, and with significantly high aspect ratio of CNTs substantial increase was expected theoretically. A significant reduction in the aspect ratio of the as-received CNTs can be expected as a result of the compounding and the injection molding processes. Also, it might be the case that we do not find individualized CNTs in the matrix (which inherently should have higher modulus), and hence the contribution of the filler to the composite modulus primarily comes from its agglomerates. The agglomerate modulus of the CNTs may not be sig-

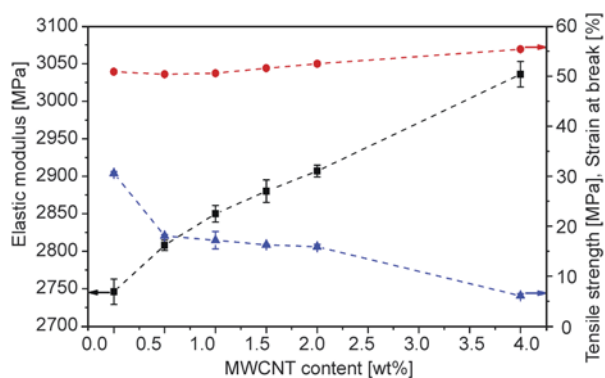


Figure 9. Mechanical properties of the composites (diluted from PPE/PS-4 wt% MWCNT masterbatch) and PPE/PS (processed twice through the extruder) at 400 rpm. All samples have identical processing history.

nificantly higher than that of the already stiff PPE/PS matrix so as to lead to the expected reinforcement. The chance for the dispersed CNTs to exist as entanglements is higher than as a long rigid rod. These reasons could have contributed to lower than expected elastic modulus of the composites in spite of excellent MWCNT dispersion in the matrix (as observed from Figures 2 and 3). Similar observations have been reported earlier in [42–44].

The tensile strength of the composites as observed in Figure 9 happens to be almost identical to the stress at yield and the stress at break. The addition of 0.5 and 1 wt% MWCNT to PPE/PS resulted in a very minimal drop in the tensile strength of PPE/PS (50.9 MPa), but further MWCNT addition resulted in improved composite tensile strength. The tensile strength of the composite containing 4 wt% MWCNT was around 9% higher than that of the matrix. The load bearing capacity of the CNTs is strongly dependent on the level of filler dispersion, matrix-filler interface, aspect ratio of the CNTs and the intrinsic strength of the CNT. In spite of the enhanced surface area available for CNT as a result of good filler dispersion that would facilitate improved polymer-filler interaction, the CNTs used in this work were not functionalized and hence the possibility of a strong interface between the PPE/PS and CNTs is less likely. The aspect ratio of the CNTs in the end composite would not be significant (compared to its as-received form) and the inherent strength of the agglomerated CNTs is obviously not sufficient to create substantial reinforcement. Such reports of very slight improvements or deterioration or tensile strength of polymer-CNT composites are not

uncommon [45–47]. It is widely accepted that the addition of CNT results in the lowering of composite ductility. The strain at break of PPE/PS is lowered by 70% on the addition of 0.5 wt% MWCNT and by about 400% on the addition of 4 wt% MWCNT. Higher CNT loading fraction together with the increasing presence of CNT agglomerates can be attributed to the dramatic lowering of the ductility of the composites.

The mechanical properties of the composites processed at 600 rpm (not presented here) are slightly lower than that of its counterparts processed at 400 rpm. The combined effect of slightly poorer quality of macro dispersion of CNT in the composites processed at higher screw speeds (Figure 3), potential polymer degradation, and increased reduction in the length of the CNTs during the compounding process may explain the aforementioned. Concerning the composites processed with a lower injection speed (10 mm/s), it was found that the modulus of the composite containing 0.5 wt% CNT was 2% lower than those observed for composites processed with an injection speed of 100 mm/s (Figure 9). Similar observations were also found on the composites with higher CNT loading. Even though the probability of CNT aspect ratio reduction would be higher at a higher injection speed, higher modulus of the composites in this case points out the fact that filler orientation (predominant at higher injection speed) plays a key role in affecting the tensile behavior of the composites.

Observation of tensile testing results indicate that it is possible to slightly enhance the mechanical properties of miscible PPE/PS blend by the addition of CNTs with a compromise in composite ductility. This would be a certain value addition to any improved electrical properties of the composite towards the development of a multifunctional composite.

It has to be mentioned here that a direct comparison of the mechanical properties of the composites observed on tensile testing (wherein tested samples were processed by injection molding) to those observed from the DMA measurements (wherein tested samples were processed by compression molding) would not be realistic. The observed properties are influenced by the distribution of CNTs and orientation of flow, anisotropy, crystallinity, etc. which arise due to the nature of the composite shaping process.

3.5. Electrical volume conductivity of the nanocomposites

The electrical conductivity of the compression molded samples and those of the extruded strands are presented in Figure 10. The electrical conductivity of pure PPE/PS was measured to be $1.1 \cdot 10^{-15}$ S/cm. Irrespective of the processing speed of the twin-screw extruder, the electrical conductivity of the compression molded PPE/PS-0.5 wt% MWCNT composite was 12 orders of magnitude higher than those observed on the pure matrix. Further additions of the filler only contributed to slight improvement in electrical properties. By fitting the measured conductivity data to Equation (2) the percolation concentration (w_c) and exponent (t) for the composite processed at 600 rpm is observed to be 0.395 wt% and 1.53 respectively with high a R^2 value of 0.998 (indicating excellent fit of the regression line to the measured data). The composites processed at 400 rpm shows ' w_c ' and ' t ' values of 0.4 wt% and 1.62 respectively, also with a very high R^2 value of 0.996. Hence, the percolation threshold is not significantly affected by employing varying screw speeds, if the secondary processing operation happens to be compression molding. The determined values of ' t ' as 1.53 and 1.62 for the composites processed with 600 and 400 rpm respectively, agrees well with typically reported ' t ' values in literature between 1.3 and 4 [48], but according to the same literature the physical interpretation of this

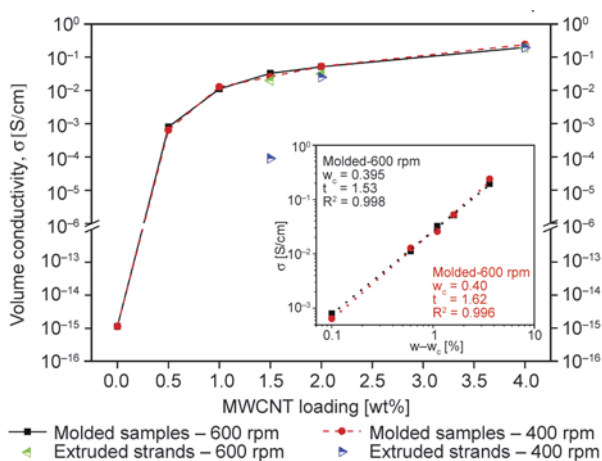


Figure 10. Electrical volume conductivity measurements on extruded strands and compression molded bars of PPE/PS with varying MWCNT loadings at 400 and 600 rpm. Inset: log-log plot of conductivity of the compression molded samples as a function of $(w - w_c)$ with exponent ' t ' and percolation concentration ' w_c ' determined from Equation (2).

critical exponent is still controversial. However, it can be interpreted that lower values of ' t ' would mean an abrupt variation in the electrical properties in the vicinity of the percolation, as the magnitude of ' $w - w_c$ ' is less than 1. According to [16, 25], the estimated ' t ' values of the PPE/PS-MWCNT composite system show that electrical percolation is principally governed by the 2-D network of MWCNTs in the matrix.

The compression molded composite samples showed similar electrical conductivity irrespective of the processing speeds at a fixed MWCNT concentration. However, it is interesting to note the variations in the conductivities of the extruded strand. A 1.5 wt% MWCNT loaded PPE/PS composite processed at 600 rpm exhibited three orders of magnitude lower resistivity than those observed on samples processed at 400 rpm. The potential re-agglomeration of the MWCNT as observed in the optical micrographs caused by enhanced *SME* at 600 rpm could be responsible for creating a conglomerative conductive pathway with comparatively large sized agglomerates and individualized nanotubes compared to processing with 400 rpm. The extent of variation decreases at higher MWCNT loadings which may be attributed to enhancement in nanotube content in a defined volume either by increased CNT-CNT contacts or reduced hopping/tunneling distance. The fact that compression molding reduces the percolation threshold owing to facilitation of nanoscale re-agglomeration at higher temperatures (low viscosity) of pre-dispersed nanotubes (created due to extrusion/melt mixing) explains why the volume resistivities in the extruded strands are higher than those observed on the compression molded bars at lower MWCNT concentrations.

4. Conclusions

PPE/PS nanocomposites with varying MWCNT contents were processed on a twin-screw lab scale extruder employing two different processing speeds. Good MWCNT dispersion morphologies were observable on different metric scales from the SEM images and optical micrographs for composites with lower CNT contents. The latter also showed that composites processed at higher screws speeds exhibited larger agglomerate size fractions than those processed at lower screw speeds.

The counter balance between the reinforcing effect of dispersed CNT and the polymer degradation at

higher processing speeds and at higher filler concentrations determined the thermal stability of the nanocomposites. DSC and dynamic mechanical measurements indicated very little changes in the T_g of the nanocomposites relative to the matrix and higher processing speeds resulted in qualitatively better interfaces. Storage modulus of the nanocomposites increased with MWCNT loading as expected with the 4 wt% masterbatch showing 10% enhancement compared to the matrix, while re-processing it diminished its reinforcing capabilities. E' was however higher for 0.5 wt% loading among all the other masterbatch diluted nanocomposites indicative of very high reinforcement capabilities, but with increase in temperature the effect lost its significance.

Tensile testing data showed that the elastic modulus and tensile strength of PPE/PS improved marginally, accompanied with reduction in ductility on MWCNT incorporation. In spite of achieving a good MWCNT dispersion morphology in PPE/PS, substantial improvements in the mechanical properties of the composites were not possible. Reduction in the aspect ratio on processing, inherently weaker mechanical characteristics of the CNT agglomerate fractions (compared to those from highly individualized CNTs with large aspect ratios) that are observed in the matrix, lack of a strong chemical interface and potential polymer degradation could all be attributed as potential reasons for the aforementioned. It was interesting to observe that the orientation effect of CNTs (more predominant at higher injection speed of 100 mm/s) led to slightly higher mechanical characteristics than its counterparts processed with a lower injection speed of 10 mm/s. Electrical volume conductivity of a 0.5 wt% MWCNT filled composite samples (compression molded) was twelve orders of magnitude higher compared to pure PPE/PS and no significant differences were observed depending on the processing speed. Electrical percolation was estimated to occur around 0.4 wt% MWCNT content on the compression molded composites. A favorable environment for the nanoscale re-agglomeration of the dispersed CNTs facilitated by longer holding times at reduced viscosity (during the compression molding process) results in higher electrical conductivity compared to

that of the extruded strands at 1.5 wt% MWCNT loading in PPE/PS. However, this difference diminished with increased MWCNT loadings.

The incorporation of MWCNTs to PPE/PS has led to a significant improvement in the electrical characteristics of the composite at very low filler loading with marginal improvements in thermal stability and mechanical characteristics. Further work on improving the mechanical attributes of the composite is needed for the development of good multi-functional composites.

Acknowledgements

The research leading to these results has received funding from the European Community's Seventh Framework Programme (FP7-PEOPLE-ITN-2008) under grant agreement number 238363.

References

- [1] Dresselhaus M. S., Dresselhaus G., Charlier J. C., Hernández E.: Electronic, thermal and mechanical properties of carbon nanotubes. *Philosophical Transactions of the Royal Society A: Mathematical, Physical and Engineering Sciences*, **362**, 2065–2098 (2004). DOI: [10.1098/rsta.2004.1430](https://doi.org/10.1098/rsta.2004.1430)
- [2] Müller M. T., Krause B., Kretzschmar B., Pötschke P.: Influence of feeding conditions in twin-screw extrusion of PP/MWCNT composites on electrical and mechanical properties. *Composites Science and Technology*, **71**, 1535–1542 (2011). DOI: [10.1016/j.compscitech.2011.06.003](https://doi.org/10.1016/j.compscitech.2011.06.003)
- [3] Krause B., Pötschke P., Häußler L.: Influence of small scale melt mixing conditions on electrical resistivity of carbon nanotube-polyamide composites. *Composites Science and Technology*, **69**, 1505–1515 (2009). DOI: [10.1016/j.compscitech.2008.07.007](https://doi.org/10.1016/j.compscitech.2008.07.007)
- [4] Socher R., Krause B., Müller M. T., Boldt R., Pötschke P.: The influence of matrix viscosity on MWCNT dispersion and electrical properties in different thermoplastic nanocomposites. *Polymer*, **53**, 495–504 (2012). DOI: [10.1016/j.polymer.2011.12.019](https://doi.org/10.1016/j.polymer.2011.12.019)
- [5] Ha H., Ha K., Kim S. L.: An empirical equation for electrical resistivity of thermoplastic polymer/multi-walled carbon nanotube composites. *Carbon*, **48**, 1939–1944 (2010). DOI: [10.1016/j.carbon.2010.01.061](https://doi.org/10.1016/j.carbon.2010.01.061)
- [6] Thostenson E. T., Chou T-W.: Aligned multi-walled carbon nanotube-reinforced composites: Processing and mechanical characterization. *Journal of Physics D: Applied Physics*, **35**, L77–L80 (2002). DOI: [10.1088/0022-3727/35/16/103](https://doi.org/10.1088/0022-3727/35/16/103)

- [7] López-Manchado M. A., Valentini L., Biagiotti J., Kenny J. M.: Thermal and mechanical properties of single-walled carbon nanotubes–polypropylene composites prepared by melt processing. *Carbon*, **43**, 1499–1505 (2005).
DOI: [10.1016/j.carbon.2005.01.031](https://doi.org/10.1016/j.carbon.2005.01.031)
- [8] Grossiord N., Miltner H. E., Loos J., Meuldijk J., Mele B. V., Koning C. E.: On the crucial role of wetting in the preparation of conductive polystyrene–carbon nanotube composites. *Chemistry of Materials*, **19**, 3787–3792 (2007).
DOI: [10.1021/cm062998o](https://doi.org/10.1021/cm062998o)
- [9] Pötschke P., Bhattacharyya A. R., Janke A.: Melt mixing of polycarbonate with multiwalled carbon nanotubes: Microscopic studies on the state of dispersion. *European Polymer Journal*, **40**, 137–148 (2004).
DOI: [10.1016/j.eurpolymj.2003.08.008](https://doi.org/10.1016/j.eurpolymj.2003.08.008)
- [10] Ramanathan T., Liu H., Brinson L. C.: Functionalized SWNT/polymer nanocomposites for dramatic property improvement. *Journal of Polymer Science Part B: Polymer Physics*, **43**, 2269–2279 (2005).
DOI: [10.1002/polb.20510](https://doi.org/10.1002/polb.20510)
- [11] Camponeschi E., Florkowski B., Vance R., Garrett G., Garmestani H., Tannenbaum R.: Uniform directional alignment of single-walled carbon nanotubes in viscous polymer flow. *Langmuir*, **22**, 1858–1862 (2006).
DOI: [10.1021/la052714z](https://doi.org/10.1021/la052714z)
- [12] Ma P. C., Tang B. Z., Kim J.-K.: Effect of CNT decoration with silver nanoparticles on electrical conductivity of CNT-polymer composite. *Carbon*, **46**, 1497–1505 (2008).
DOI: [10.1016/j.carbon.2008.06.048](https://doi.org/10.1016/j.carbon.2008.06.048)
- [13] Zou J., Liu L., Chen H., Khondaker S. I., McCullough R. D., Huo Q., Zhai L.: Dispersion of pristine carbon nanotubes using conjugated block copolymers. *Advanced Materials*, **20**, 2055–2060 (2008).
DOI: [10.1002/adma.200701995](https://doi.org/10.1002/adma.200701995)
- [14] Sathyanarayana S., Olowojoba G., Weiss P., Caglar B., Pataki B., Mikonsaari I., Hübner C., Henning F.: Compounding of MWCNTs with PS in a twin-screw extruder with varying process parameters: Morphology, interfacial behavior, thermal stability, rheology, and volume resistivity. *Macromolecular Materials and Engineering*, **298**, 89–105 (2013).
DOI: [10.1002/mame.201200018](https://doi.org/10.1002/mame.201200018)
- [15] Sandler J. K. W., Kirk J. E., Kinloch I. A., Shaffer M. S. P., Windle A. H.: Ultra-low electrical percolation threshold in carbon-nanotube-epoxy composites. *Polymer*, **44**, 5893–5899 (2003).
DOI: [10.1016/S0032-3861\(03\)00539-1](https://doi.org/10.1016/S0032-3861(03)00539-1)
- [16] Hollertz R., Chatterjee S., Gutmann H., Geiger T., Nüesch F. A., Chu B. T. T.: Improvement of toughness and electrical properties of epoxy composites with carbon nanotubes prepared by industrially relevant processes. *Nanotechnology*, **22**, 125702/1–125702/9 (2011).
DOI: [10.1088/0957-4484/22/12/125702](https://doi.org/10.1088/0957-4484/22/12/125702)
- [17] Pegel S., Pötschke P., Petzold G., Alig I., Dudkin S. M., Lellinger D.: Dispersion, agglomeration, and network formation of multiwalled carbon nanotubes in polycarbonate melts. *Polymer*, **49**, 974–984 (2008).
DOI: [10.1016/j.polymer.2007.12.024](https://doi.org/10.1016/j.polymer.2007.12.024)
- [18] Villmow T., Pegel S., Pötschke P., Wagenknecht U.: Influence of injection molding parameters on the electrical resistivity of polycarbonate filled with multiwalled carbon nanotubes. *Composites Science and Technology*, **68**, 777–789 (2008).
DOI: [10.1016/j.compscitech.2007.08.031](https://doi.org/10.1016/j.compscitech.2007.08.031)
- [19] Pötschke P., Bhattacharyya A. R., Janke A.: Morphology and electrical resistivity of melt mixed blends of polyethylene and carbon nanotube filled polycarbonate. *Polymer*, **44**, 8061–8069 (2003).
DOI: [10.1016/j.polymer.2003.10.003](https://doi.org/10.1016/j.polymer.2003.10.003)
- [20] Zhang L., Wan C., Zhang Y.: Investigation on the multiwalled carbon nanotubes reinforced polyamide 6/polypropylene composites. *Polymer Engineering and Science*, **49**, 1909–1917 (2009).
DOI: [10.1002/pen.21428](https://doi.org/10.1002/pen.21428)
- [21] Sumita M., Sakata S., Asai S., Miyasaka K., Nakagawa H.: Dispersion of fillers and the electrical conductivity of polymer blends filled with carbon black. *Polymer Bulletin*, **25**, 265–271 (1991).
DOI: [10.1007/BF00310802](https://doi.org/10.1007/BF00310802)
- [22] Bose S., Bhattacharya A. R., Bondre A. P., Kulkarni A. R., Pötschke P.: Rheology, electrical conductivity, and the phase behavior of cocontinuous PA6/ABS blends with MWNT: Correlating the aspect ratio of MWNT with the percolation threshold. *Journal of Polymer Science Part B: Polymer Physics*, **46**, 1619–1631 (2008).
DOI: [10.1002/polb.21501](https://doi.org/10.1002/polb.21501)
- [23] Wu D., Zhang Y., Zhang M., Yu W.: Selective localization of multiwalled carbon nanotubes in poly(ϵ -caprolactone)/polylactide blend. *Biomacromolecules*, **10**, 417–424 (2009).
DOI: [10.1021/bm801183f](https://doi.org/10.1021/bm801183f)
- [24] Baudouin A.-C., Devaux J., Bailly C.: Localization of carbon nanotubes at the interface in blends of polyamide and ethylene–acrylate copolymer. *Polymer*, **51**, 1341–1354 (2010).
DOI: [10.1016/j.polymer.2010.01.050](https://doi.org/10.1016/j.polymer.2010.01.050)
- [25] Khare R. A., Bhattacharyya A. R., Kulkarni A. R., Saroop M., Biswas A.: Influence of multiwall carbon nanotubes on morphology and electrical conductivity of PP/ABS blends. *Journal of Polymer Science Part B: Polymer Physics*, **46**, 2286–2295 (2008).
DOI: [10.1002/polb.21560](https://doi.org/10.1002/polb.21560)
- [26] Wu M., Shaw L. L.: On the improved properties of injection-molded, carbon nanotube-filled PET/PVDF blends. *Journal of Power Sources*, **136**, 37–44 (2004).
DOI: [10.1016/j.jpowsour.2004.04.016](https://doi.org/10.1016/j.jpowsour.2004.04.016)

- [27] Wellinghoff S. T., Koenig J. L., Baer E.: Spectroscopic examination of chain conformation and bonding in poly(phenylene oxide)–polystyrene blends. *Journal of Polymer Science: Polymer Physics Edition*, **15**, 1913–1925 (1977).
DOI: [10.1002/pol.1977.180151104](https://doi.org/10.1002/pol.1977.180151104)
- [28] Tiwari R. R., Khilar K. C., Natarajan U.: New poly(phenylene oxide)/polystyrene blend nanocomposites with clay: Intercalation, thermal and mechanical properties. *Journal of Applied Polymer Science*, **108**, 1818–1828 (2008).
DOI: [10.1002/app.27743](https://doi.org/10.1002/app.27743)
- [29] Everaert V., Groeninckx G., Pionteck J., Favis B. D., Aerts L., Moldenaers P., Mewis J.: Miscible PS/PPE compounds: An alternative for blend phase morphology studies? Influence of the PPE content on the surface tension of PS/PPE and on the interfacial tension in PP/(PS/PPE) and POM/(PS/PPE) blends. *Polymer*, **41**, 1011–1025 (2000).
DOI: [10.1016/S0032-3861\(99\)00239-6](https://doi.org/10.1016/S0032-3861(99)00239-6)
- [30] Ottino J. M., DeRoussel P., Hansen S., Khakhar D. V.: Mixing and dispersion of viscous liquids and powdered solids. in ‘Advances in chemical engineering’ (ed.: Wei J.) Academic Press, San Diego, Vol 25, 105–204 (1999).
- [31] Krusic P. J., Wassermann E., Keizer P. N., Morton J. R., Preston K. F.: Radical reactions of C₆₀. *Science*, **254**, 1183–1185 (1991).
DOI: [10.1126/science.254.5035.1183](https://doi.org/10.1126/science.254.5035.1183)
- [32] Liu Y., Yao Z., Adronov A.: Functionalization of single-walled carbon nanotubes with well-defined polymers by radical coupling. *Macromolecules*, **38**, 1172–1179 (2005).
DOI: [10.1021/ma048273s](https://doi.org/10.1021/ma048273s)
- [33] Lizymol P. P., Thomas S.: Thermal behaviour of polymer blends: A comparison of the thermal properties of miscible and immiscible systems. *Polymer Degradation and Stability*, **41**, 59–64 (1993).
DOI: [10.1016/0141-3910\(93\)90061-M](https://doi.org/10.1016/0141-3910(93)90061-M)
- [34] Vatalis A. S., Kanapitsas A., Delides C. G., Pissis P.: Relaxation phenomena and morphology in polymer blends based on polyurethanes investigated by various thermal analysis techniques. *Thermochimica Acta*, **372**, 33–38 (2001).
DOI: [10.1016/S0040-6031\(01\)00430-0](https://doi.org/10.1016/S0040-6031(01)00430-0)
- [35] Forrest J. A., Dalnoki-Veress K., Stevens J. R., Dutcher J. R.: Effect of free surfaces on the glass transition temperature of thin polymer films. *Physical Review Letters*, **56**, 2002–2005 (1996).
DOI: [10.1103/PhysRevLett.77.2002](https://doi.org/10.1103/PhysRevLett.77.2002)
- [36] Forrest J. A., Dalnoki-Veress K., Dutcher J. R.: Interface and chain confinement effects on the glass transition temperature of thin polymer films. *Physical Review E*, **56**, 5705–5716 (1997).
DOI: [10.1103/PhysRevE.56.5705](https://doi.org/10.1103/PhysRevE.56.5705)
- [37] Pötschke P., Bhattacharyya A. R., Janke A., Goering H.: Melt mixing of polycarbonate/multi-wall carbon nanotube composites. *Composite Interfaces*, **10**, 389–404 (2003).
DOI: [10.1163/156855403771953650](https://doi.org/10.1163/156855403771953650)
- [38] Grady B., Paul A., Peters J. E., Ford W.: Glass transition behavior of single-walled carbon nanotube–polystyrene composites. *Macromolecules*, **42**, 6152–6158 (2009).
DOI: [10.1021/ma900375g](https://doi.org/10.1021/ma900375g)
- [39] Litvinov V. M., Speiss H. W.: ²H NMR study of molecular motions in polydimethylsiloxane and its mixtures with aerosils. *Die Makromolekulare Chemie*, **192**, 3005–3019 (1991).
DOI: [10.1002/macp.1991.021921216](https://doi.org/10.1002/macp.1991.021921216)
- [40] Wurm A., Ismail M., Kretzschmar B., Pospiech D., Schick C.: Retarded crystallization in polyamide/layered silicates nanocomposites caused by an immobilized interphase. *Macromolecules*, **43**, 1480–1487 (2010).
DOI: [10.1021/ma902175r](https://doi.org/10.1021/ma902175r)
- [41] Castillo F. Y., Socher R., Krause B., Headrick R., Grady B. P., Prada-Silvy R., Pötschke P.: Electrical, mechanical, and glass transition behavior of polycarbonate-based nanocomposites with different multi-walled carbon nanotubes. *Polymer*, **52**, 3835–3845 (2011).
DOI: [10.1016/j.polymer.2011.06.018](https://doi.org/10.1016/j.polymer.2011.06.018)
- [42] Mack C., Sathyanarayana S., Weiss P., Mikonsaari I., Hübner C., Henning F., Elsner P.: Twin-screw extrusion of multi walled carbon nanotubes reinforced polycarbonate composites: Investigation of electrical and mechanical properties. *IOP Conference Series: Materials Science and Engineering*, **40**, 012020/1–012020/10 (2012).
DOI: [10.1088/1757-899X/40/1/012020](https://doi.org/10.1088/1757-899X/40/1/012020)
- [43] Sathyanarayana S., Wegrzyn M., Weiss P., Giminéz E., Hübner C., Henning F.: Influence of short glass fiber addition on the morphology and properties of PC/MWCNT composites. in ‘Proceedings of the 28th Annual Meeting of Polymer Processing Society (PPS28), Pattaya, Thailand’, Paper ID: P12012–348 (2012).
- [44] Ci L., Bai J.: The reinforcement role of carbon nanotubes in epoxy composites with different matrix stiffness. *Composites Science and Technology*, **66**, 599–603 (2006).
DOI: [10.1016/j.compscitech.2005.05.020](https://doi.org/10.1016/j.compscitech.2005.05.020)
- [45] Mičušík M., Omastová M., Krupa I., Prokeš J., Pissis P., Logakis E., Pandis C., Pötschke P., Pionteck J.: A comparative study on the electrical and mechanical behaviour of multi-walled carbon nanotube composites prepared by diluting a masterbatch with various types of polypropylenes. *Journal of Applied Polymer Science*, **113**, 2536–2551 (2009).
DOI: [10.1002/app.30418](https://doi.org/10.1002/app.30418)

- [46] Kanagaraj S., Varanda F. R., Zhil'tsova T. V., Oliveira M. S. A., Simões J. A. O.: Mechanical properties of high density polyethylene/carbon nanotube composites. *Composites Science and Technology*, **67**, 3071–3077 (2007).
DOI: [10.1016/j.compscitech.2007.04.024](https://doi.org/10.1016/j.compscitech.2007.04.024)
- [47] Breton Y., Désarmot G., Salvétat J. P., Delpeux S., Sinturel C., Beguin F., Bonnamy S.: Mechanical properties of multiwall carbon nanotubes/epoxy composites: Influence of network morphology. *Carbon*, **42**, 1027–1030 (2004).
DOI: [10.1016/j.carbon.2003.12.026](https://doi.org/10.1016/j.carbon.2003.12.026)
- [48] Bauhofer W., Kovacs J. S.: A review and analysis of electrical percolation in carbon nanotube polymer composites. *Composites Science and Technology*, **69**, 1486–1498 (2009).
DOI: [10.1016/j.compscitech.2008.06.018](https://doi.org/10.1016/j.compscitech.2008.06.018)

Thermally reversible cross-linked poly(ether-urethane)s

C. Gaina, O. Ursache, V. Gaina*, C. D. Varganici

'Petru Poni' Institute of Macromolecular Chemistry, 41 A Gr.Ghica Voda Alley, RO-700487 Iasi, Romania

Received 6 February 2013; accepted in revised form 14 April 2013

Abstract. Cross-linked poly(ether-urethane)s were prepared by Diels-Alder (DA) reaction of the furan-containing poly(ether-urethane) to bismaleimides and showed thermal reversibility evidenced by differential scanning calorimetry and attenuated total reflectance in conjunction with Fourier transform infrared spectroscopy (ATR-FTIR). The furan-containing poly(ether-urethane)s were synthesized by the polyaddition reaction of 1,6-hexamethylene diisocyanate (HMDI) or 4,4'-dibenzyl diisocyanate (DBDI) to poly(tetramethylene ether) glycol (PTMEG having $M_n = 250, 650, 1000, 1500$ and 2000) and 2-[*N,N*-bis(2-methyl-2-hydroxyethyl)amino]furfuryl as chain extender by the solution prepolymer method. The molar ratio of isocyanate: PTMEG:chain extender varied from 2:1:1 to 4:1:3, which produces a molar concentration of furyl group ranging between $3.65 \cdot 10^{-4}$ and $1.25 \cdot 10^{-3}$ mol/g.

Keywords: thermal properties, polyurethanes, Diels-Alder reaction, networks

1. Introduction

The application of reversible Diels-Alder (rDA) chemistry to the dynamic covalent assembly of organic materials has been only recently explored [1–4]. The number of DA reactions that undergo dynamically reversible adduct formation under mild conditions is, however, limited and there is an increasing interest in expanding the set of dynamic covalent DA reactions [5–8].

Over the past 10 years several groups have explored the use of reversible DA adduct formation in the design and synthesis of new organic materials, the most of such studies utilize the reactivity of electron-rich furan derivatives and electron-poor maleimide derivatives [9]. The DA cycloaddition of furan and maleimide can be accomplished at or slightly above room temperature, while the rDA reaction is performed at elevated temperatures.

Thermally rDA reactions have been used in numerous studies including polymer synthesis [10–17], dendrimers [18–21], epoxy resins [22–25], cross-linked polymer networks [26–30], organic-inor-

ganic polymer hybrids [31–33], surfactants [34], surface modification [35, 36] and remendable self-healing polymers [37]. Due to the fact that these reactions can proceed under mild conditions without a catalyst, they are attractive for designing covalently reversible bonds with furan and maleimide functional groups which are responsible for association and disassociation [35, 37, 38].

Polyurethanes are widely used in high resiliency flexible foam seating, rigid foam insulation panels, microcellular foam seals and gaskets, durable elastomeric wheels and tires, automotive suspension bushings, electrical potting components, high performance adhesives, surface coatings and sealants, Spandex fibers, seals, gaskets, carpet underlay, and hard plastic parts (such as for electronic instruments). For the manufacture of polyurethanes, two groups of at least bifunctional substances are needed as reactants: 1) isocyanate groups (diisocyanates, polyisocyanates), and 2) active hydrogen atoms (polyols, glycols, triols etc.). Two side reactions can occur during polyurethane synthesis: formation of

*Corresponding author, e-mail: vgaina@icmpp.ro

both allophanate and biuret linkages from isocyanate functionality and an already existing urethane link. Both reactions not only affect stoichiometry, but also introduce branching, yielding cross-linked species. Polyurethanes can thus be formed through the branching and cross-linking. Due to these types of cross-links that are typically present in polyurethane, the polyurethane materials become difficult to melt process and difficult to remove once it is potted.

Taking advantage of experimental conditions, we report the formation of poly(ether urethane) networks with reversibly removable properties. Our approach to removable polymer networks is the introduction of chemically labile linkages within cross-linked polymeric networks. We have explored the DA cycloaddition reactions between bis-maleimide and furyl monomers or polymers [39–42]. The mechanical measurements showed a greater elongation at break for obtained polyurethane networks, elongation which can be even nine times higher than that of previously obtained polyurethane networks by Diels-Alder reaction [41].

2. Experimental part

2.1. Measurements

The FTIR spectra were recorded on a Bruker Vertex 70 Instruments (Austria) equipped with a Golden Gate single reflection ATR accessory, spectrum range 600–4000 cm^{-1} .

The proton nuclear magnetic resonance ($^1\text{H-NMR}$) spectra were recorded on a Bruker NMR spectrometer, Avance DRX 400 MHz, using CDCl_3 and DMSO-d_6 as solvent and tetramethylsilane as an internal standard.

Differential scanning calorimetry (DSC) measurements were conducted on a DSC 200 F3 Maia (Netzsch, Germany). About 9 mg of sample were heated in pressed and punched aluminum crucibles at a heating rate of $10^\circ\text{C}/\text{minute}$. Nitrogen was used as inert atmosphere at a flow rate of 100 mL/minute.

Thermogravimetric analysis (TGA) was conducted on a STA 449 F1 Jupiter device (Netzsch, Germany). Around 10 mg of each sample was heated in alumina crucibles at a heating rate of $10^\circ\text{C}/\text{min}$. Nitrogen was used as inert atmosphere at a flow rate of 50 mL/min.

The reduced viscosity of polyurethane was measured ($c = 0.5 \text{ g/dL}$, $25 \pm 0.2^\circ\text{C}$) in DMF using an Ubbelohde viscometer.

Gel permeation chromatographic (GPC) analyses were carried out on a PL-EMD 950 Evaporative light Detect instrument using *N,N*-dimethylformamide (DMF) as the eluant and standard polystyrene sample for calibration.

Dynamic contact angles were performed by the Wilhelmy plate technique, using a Sigma 700 precision tensiometer produced by KSV Instruments. The sample plate dimensions were $50 \times 8 \text{ mm}$ and rate of immersion-emersion was 5 mm/min in water. Immersion depth was 5 mm in standard conditions. All measurements were the average of 3 contact angle measurements of samples.

Stress-strain measurements were performed on a test apparatus, Shimadzu AGS-J, cell load 1 kN. Measurements were run at an extension rate of 10 mm/min, at room temperature 23°C . All samples were measured three times and the averages were obtained.

2.2. Reagents and materials

Dibutyltin dilaureate (Aldrich, 95%), dimethylformamide (DMF, Aldrich, 99%), poly(tetramethylene ether) glycol (PTMEG) (Terathane-250, -650, -1000, 1500 and -2000) (Aldrich), 2-furfuryl amine (Aldrich), epoxy propane (Aldrich), 1,6-hexamethylene diisocyanate (HDMI) (Aldrich) were used as received. 4,4'-Dibenzylidiiisocyanate (DBDI) (Savinesti, Romania) was purified before use by recrystallization from anhydrous cyclohexane ($mp = 89\text{--}90^\circ\text{C}$), 4,4'-bismaleimido-diphenylmethane (**A**) was synthesized from 4,4'-diaminodiphenylmethane and maleic anhydride in a two-step method described in the literature [43] and recrystallized from toluene ($mp = 158\text{--}159^\circ\text{C}$). The oligoether urethane bis-maleimide (**B**) was synthesized from Terathane-650 and 4-maleimidophenyl isocyanate by the method described in the literature [41].

Synthesis of

2-[*N,N*-bis(2-methyl-2-hydroxyethyl)amino]furfuryl

This material was prepared according to the modified method described in the literature [44]. To a solution of epoxy propane (11.6 g, 0.2 mol) in toluene (80 mL), 2-furfuryl amine (9.3 g, 0.1 mol) and acetic acid (1 mL) were added. The mixture was stirred and refluxed for 3 hours. The solvent was evaporated out using a rotary evaporator. The crude product was washed with 50 mL cyclohexane three

times. After drying under vacuum at 50°C for 36 hours, a viscous liquid product was obtained.

Analysis calculated for $C_{11}H_{19}NO_3$ (213.273): C, 61.95; H, 8.98; N, 6.56%. Found: C, 62.13; H, 9.02; N, 6.48%.

1H -NMR ($CDCl_3$), δ (ppm): 1.12 (d, 6H, CH_3), 2.38–2.62 (m, 4H, CH_2 protons), 3.58 (s, 2H, OH protons), 3.75 (s, 2H, CH_2 protons), 3.83 (m, 2H, CH–N protons), 6.18 (s, 1H, 3-furfuryl proton), 6.30 (s, 1H, CH-furfuryl), 7.37 (s, 1H, C_5 of furan).

Synthesis of poly(ether-urethane)s containing furan ring PU-(1-12)

The polyurethanes were synthesized by the conventional two-step method under an inert atmosphere of high purity nitrogen in a 100 mL three-neck round bottomed flask equipped with a stirrer and a thermometer. A 10% w/v solution of poly(tetramethylene ether) glycol (PTMEG) in *N,N'*-dimethylformamide (DMF) was mixed with the catalyst, dibutyltin dilaureate (about 0.5 wt%) at 40°C for 30 minutes to obtain a homogeneous solution. In the first step, an excess of diisocyanate was added to obtain an isocyanate-terminated prepolymer (at several NCO/OH ratio of 2, 3 and 4) and the reaction was left for 2 hours at 80°C. The prepolymer solution was cooled at 60°C and chain extension step was performed adding stoichiometric amount of 2-[*N,N'*-bis(1-methyl-2-hydroxyethyl)amino]furfuryl in 5 mL DMF under nitrogen and stirring for

2 hours at 60°C. The solution was cooled (25°C) and the polymer was precipitated in cool distilled water and washed with methanol at room temperature. The sample was then dried at 50°C for 24 hours under reduced pressure. The polyurethane films were cast from 8 wt% solution of the polymer in DMF.

IR (KBr, cm^{-1}): 3395, 2968, 2932, 2885, 1833, 1632, 1502, 1454, 1411, 1375, 1337, 1279, 1147, 1067, 1013, 949, 838, 732 and 599.

Synthesis of polyurethane networks NPU-(1-12)A,B

To a solution of polyurethane (1.2 g) in DMF (10 mL), a stoichiometric bismaleimide monomer (A or B) was added. The mixture was stirred at 60°C for 2 hours and the solution was cast on Teflon Petri dish and the solvent was evaporated at 60°C for 24 hours. The obtained polymer films were used for all characterizations. NPU, before crosslinking, were soluble in aprotic dipolar solvents at room temperature. After crosslinking, when the samples were immersed in aprotic dipolar solvents, polyurethane networks swelled. At 140°C, the networks became soluble as a result of the de-crosslinking at this temperature.

3. Results and discussion

Polyurethanes containing furan moieties PU-(1-12) were prepared by the two-step method in DMF solution, by the reaction of DBDI or HMDI with

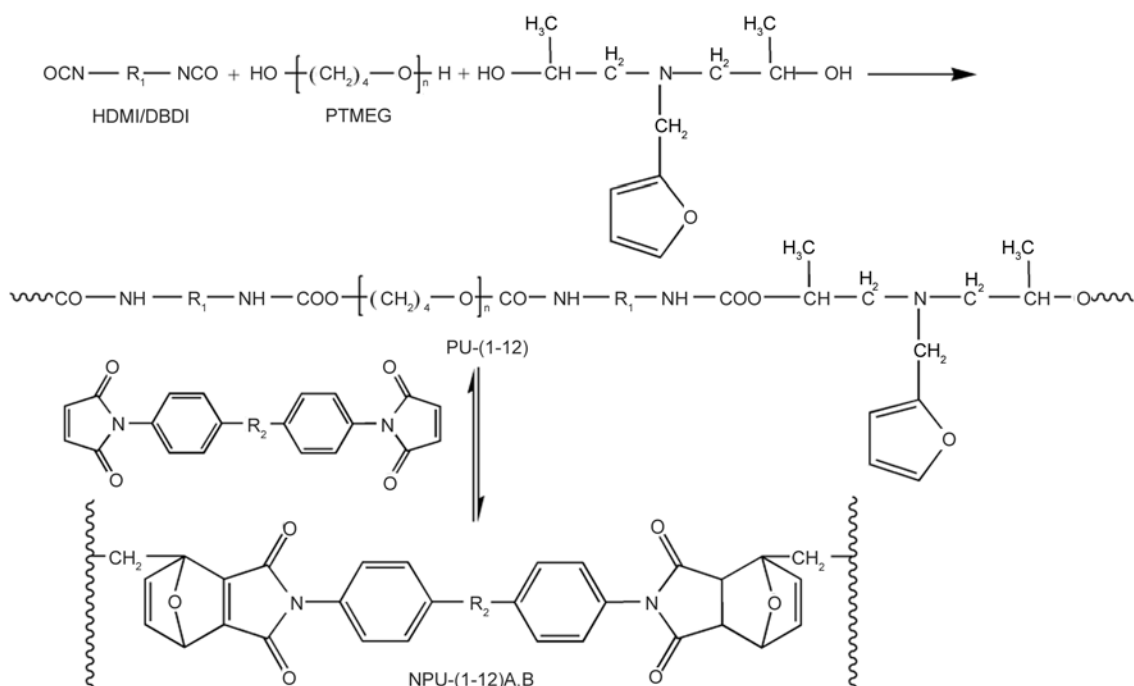
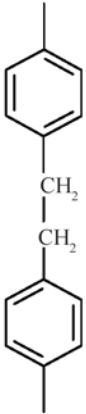
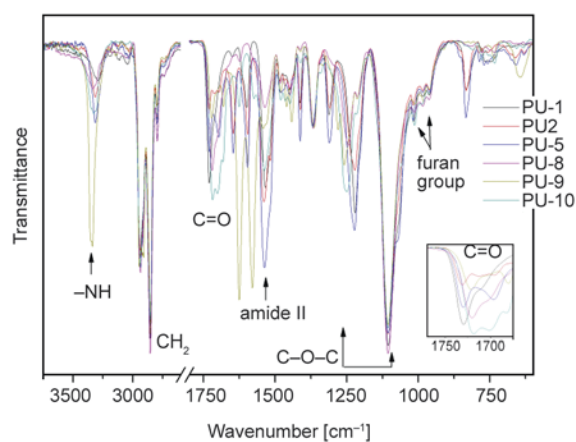


Figure 1. Synthesis of poly(ether-urethane) networks

Table 1. The composition of polyurethanes and their networks

Sample	R ₁	M _{PTMEG}	Isocyanate:PTMEG:chain extender	R ₂	
PU-0-1		2000	2:1:1	–	
NPU-1A			2:1:1	–CH ₂ –	
NPU-1B			2:1:1	–HN–OOC–PTMEG ₆₅₀ –COO–NH–	
PU-2			1500	2:1:1	–
NPU-2A				2:1:1	–CH ₂ –
NPU-2B				2:1:1	–HN–OOC–PTMEG ₆₅₀ –COO–NH–
PU-3		3:1:2		–	
NPU-3A		3:1:2		–CH ₂ –	
NPU-3B		3:1:2		–HN–OOC–PTMEG ₆₅₀ –COO–NH–	
PU-4		1000	4:1:3	–	
NPU-4A			4:1:3	–CH ₂ –	
NPU-4B			4:1:3	–HN–OOC–PTMEG ₆₅₀ –COO–NH–	
PU-5	650		2:1:1	–	
NPU-5A			2:1:1	–CH ₂ –	
NPU-5B			2:1:1	–HN–OOC–PTMEG ₆₅₀ –COO–NH–	
PU-6		250	2:1:1	–	
NPU-6A			2:1:1	–CH ₂ –	
NPU-6B			2:1:1	–HN–OOC–PTMEG ₆₅₀ –COO–NH–	
PU-7	2000		2:1:1	–	
NPU-7A			2:1:1	–CH ₂ –	
NPU-7B			2:1:1	–HN–OOC–PTMEG ₆₅₀ –COO–NH–	
PU-8		1500	2:1:1	–	
NPU-8A			2:1:1	–CH ₂ –	
NPU-8B			2:1:1	–HN–OOC–PTMEG ₆₅₀ –COO–NH–	
PU-9	1000		2:1:1	–	
NPU-9A			2:1:1	–CH ₂ –	
NPU-9B			2:1:1	–HN–OOC–PTMEG ₆₅₀ –COO–NH–	
PU-10		650	2:1:1	–	
NPU-10A			2:1:1	–CH ₂ –	
NPU-10B			2:1:1	–HN–OOC–PTMEG ₆₅₀ –COO–NH–	
PU-11	250		2:1:1	–	
NPU-11A			2:1:1	–CH ₂ –	
NPU-11B			2:1:1	–HN–OOC–PTMEG ₆₅₀ –COO–NH–	
PU-12		2000	2:1:1	–	
NPU-12A			2:1:1	–CH ₂ –	
NPU-12B			2:1:1	–HN–OOC–PTMEG ₆₅₀ –COO–NH–	

PTMEG (having number-average molecular weight of 250, 650, 1000, 1500 and 2000) and 2-[*N,N*-bis(2-methyl-2-hydroxyethyl)amino]furfuryl in molar ratio of 2:1:1, 3:1:2 or 4:1:3 as represented in Figure 1 and Table 1. The FT-IR and ¹H-NMR spectroscopy were used to investigate the formation of polyurethanes. Typical infrared spectra of synthesized polyurethanes are shown in Figure 2. They did not show the absorption band at 2270 cm⁻¹ associated with isocyanate group. The ATR-FTIR spectra of the polyurethane elastomers **PU-(1-12)** exhibited the bonds typical for the polyurethanes. As can be observed in Figure 2 the intensity of the absorption bands at 1105 cm⁻¹ corresponding to ether linkage decreased with decreasing the number-average molecular weight of PTMEG. The same behavior could be observed in the case of the

**Figure 2.** The ATR-FTIR spectra of polyurethanes

absorption band characteristic to the vibration of methylene group. These phenomena were expected

since a lower number-average molecular weight of PTMEG used in synthesis led to a decrease of the ether linkages and methylene groups ratio in the polyurethane structure.

The $^1\text{H-NMR}$ spectra of polyurethanes presented suitable signals for NH from urethane groups, CH_3 , CH_2 from polyether glycol and diisocyanate, aromatic protons from DBDI structures, furan protons from chain extender. Representative $^1\text{H-NMR}$ spectra of **PU-7** and **PU-12** were presented in Figure 3. The protons corresponding to the furyl group appeared at 6.38, 6.27 and 7.57 ppm, the protons specific to the NH from aliphatic structure from **PU-12** at 7.01 ppm and those specific to the aromatic structure from **PU-7** appeared at 6.29, 6.40, 7.57 and 9.41-9.46 ($-\text{NH}-\text{C}_6\text{H}_4-$) ppm. The ratio between integral area of furan and isocyanate protons of the obtained polymers is in agreement with the composition of the mixture used for synthesis (isocyanate:chain extender of 1:2).

The composition and inherent viscosity of **PU-(1-12)** were presented in Table 1 and Table 2. The cal-

Table 2. Properties of polyurethanes **PU-(1-12)**

Sample	$\eta_{\text{inh}}^{\text{a}}$ [dL/g]	M_w^{b}	PDI ^c	Hard segment content [%]	Furyl monomer content [mol/g]
PU-1	0.33	38 303	1.28	27.54	$3.65 \cdot 10^{-4}$
PU-2	0.63	37 877	1.34	33.63	$4.46 \cdot 10^{-4}$
PU-3	0.54	20 124	1.28	45.52	$7.35 \cdot 10^{-4}$
PU-4	0.41	21 447	1.30	53.34	$9.38 \cdot 10^{-4}$
PU-5	0.37	24 204	1.28	43.18	$5.74 \cdot 10^{-4}$
PU-6	0.43	22 306	1.28	53.90	$7.18 \cdot 10^{-4}$
PU-7	0.23	21 116	1.27	75.25	$10.08 \cdot 10^{-4}$
PU-8	0.58	26 023	1.28	21.62	$3.92 \cdot 10^{-4}$
PU-9	0.83	34 049	1.27	26.90	$4.88 \cdot 10^{-4}$
PU-10	0.51	17 519	1.29	35.56	$6.45 \cdot 10^{-4}$
PU-11	0.78	23 857	1.35	45.90	$8.33 \cdot 10^{-4}$
PU-12	0.45	22 950	1.27	68.82	$12.50 \cdot 10^{-4}$

^aInherent viscosity measured in DMF solution at 25°C

^bThe weight-average molecular weight

^cPolydispersity index

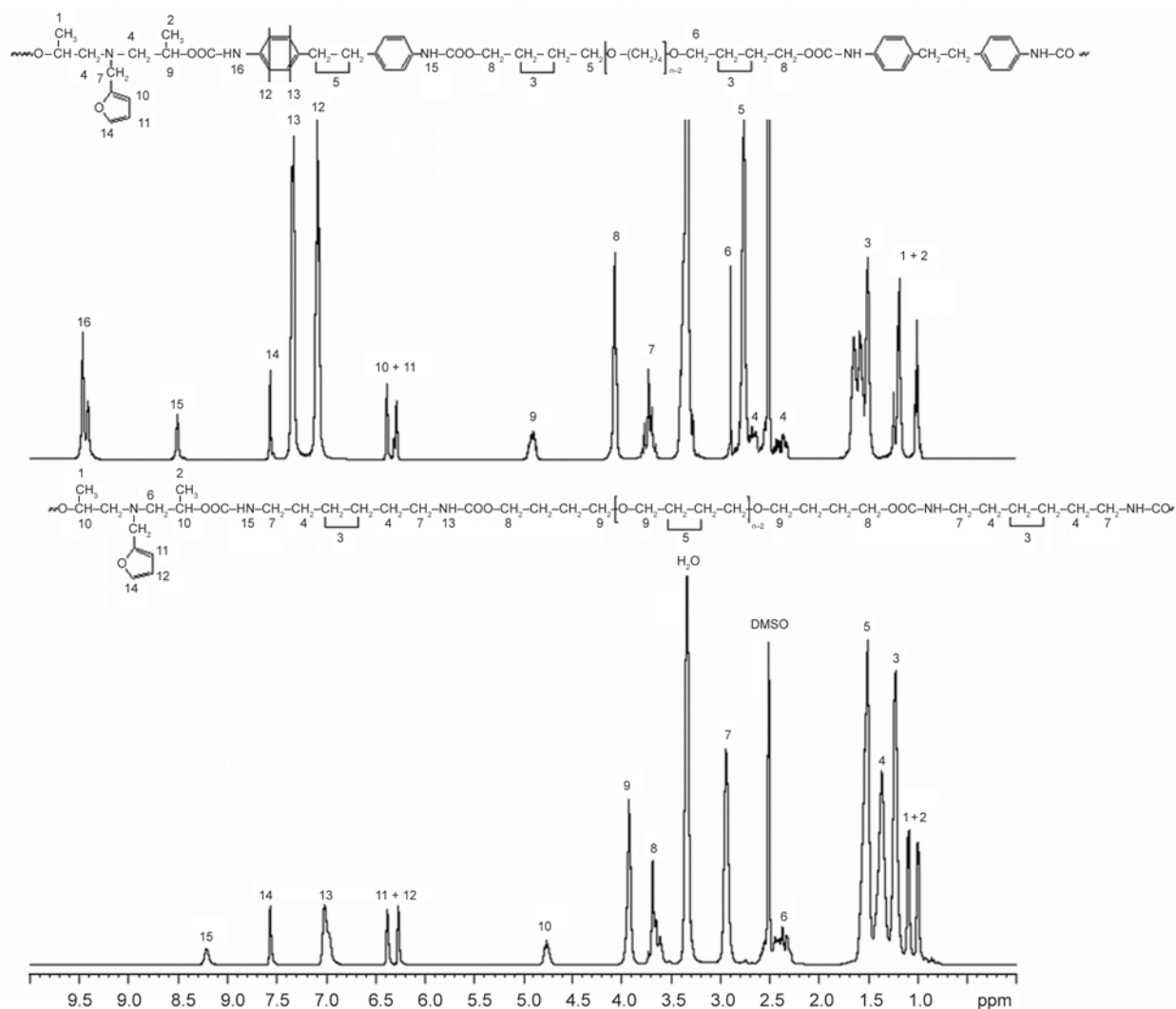


Figure 3. The $^1\text{H-NMR}$ spectra of **PU-7** and **PU-12**

culated hard segment content (as calculated from the initial composition) varied between 21.62 to 75.25% and the furfuryl monomer content varied in the range of $3.65 \cdot 10^{-4}$ – $12.50 \cdot 10^{-4}$ mol/g. The inherent viscosity measured in DMF solution at 25°C varied between 0.23 and 0.83 dL/g and decreased as the molar ratio of isocyanate:PTMEG:chain extender increases from 2:1:1 to 4:1:3. The weight-average molecular weight and polydispersity index were recorded on a PL-EMD 950 Evaporative light Detect instrument and reported in Table 2. As can be seen from Table 2, the weight-average molecular weight and polydispersity index decreased as the molar ratio of isocyanate:PTMEG:chain extender increased and the molecular weight of PTMEG decreased in the case of **PU-(1-7)**. Weight-average molecular weights and the polydispersity index of the polyurethanes were in the range of 17519–38303 and 1.27–1.35, respectively.

The polyurethane networks **NPU-(1-12)A,B** were prepared by the Diels-Alder crosslinking reaction of **PU-(1-12)** to 4,4'-bismaleimidodiphenylmethane (**A**) or oligoether urethane bismaleimide (**B**), as represented in Figure 1. The composition of polymers and networks is presented in Table 1.

The ATR-FTIR spectra of networks (Figure 4) showed the disappearance of the furan ring breathing absorption band at 1012 cm^{-1} and the appearance of new bands at 1775 cm^{-1} (C=O cycloadduct) and 1192 cm^{-1} (C–N–C succinimide ring from cycloadduct) attributed to the furan-maleimide cycloadduct [45]. The shifting absorption band characteristic to the carbonyl group to lower wavenumbers represents another confirmation of the formation of

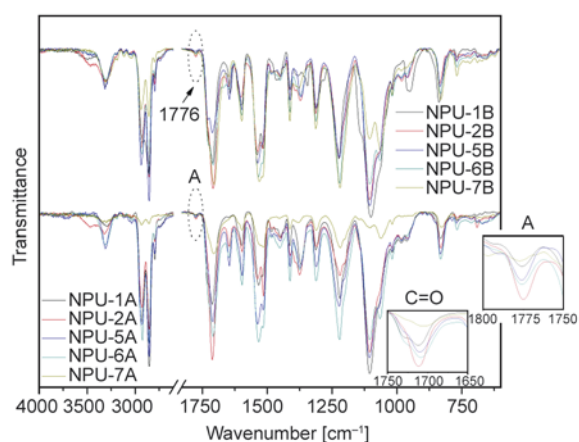


Figure 4. The ATR-FTIR spectra of networks

the Diels-Alder cycloadduct. Also, it was observed a change in the absorption bands characteristic to the non-bonded and bonded urethane C=O at 1680 – 1720 cm^{-1} .

3.1. Thermal properties

Urethanes are known to be relatively thermally unstable materials and the decomposition temperature of the urethane bond depends on the polyurethane structure. Thus, the polyurethanes and their corresponding networks based on alkyl structure (**PU-** and **NPU-(8-12)**) presented a better thermal stability than the ones based on aryl structure (**PU-** and **NPU-(1-7)**). There have been proposed three mechanisms for the decomposition of urethane bonds: dissociation to isocyanate and alcohol, formation of primary amine and olefin, and formation of secondary amine and carbon dioxide. These reactions may proceed simultaneously or separately. Figure 5 presents the thermal degradation curves of polyurethane networks **NPU-(1-2,5-7)A**. As can be seen the decomposition of the urethane bonds proceeded in two stages, meaning that two of the reactions mentioned above were overlapping. These two stages ranged between 202 – 398°C (Table 3). At higher temperatures, the decomposition stage was due to the degradation of PTMEG chain and to the other units from the polyurethane network, and ranged between 381 – 517°C . As expected, the weight loss corresponding to the first two stages increased with decreasing the number-average molecular weight of PTMEG since the urethane linkages ratio in network was higher. On the other hand the weight loss of the third stage decreased due to the fact that

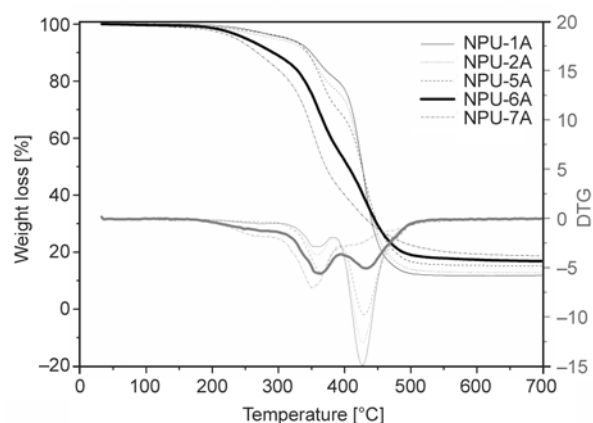


Figure 5. The TGA curves of **NPU-(1-7)A** with a isocyanate:PTMEG:chain extender molar ratio of 2:1:1

Table 3. The thermogravimetric data of PU and NPU

Sample	Weight loss/decomposition temperature [%/°C]			Y _c ^a [°C]
	Step I	Step II	Step III	
NPU-1A	4.20/216–286	13.08/332–370	70.12/402–466	11.88
PU-2	16.00/220–340	52.00/390–465	18.40/470–550	6.00
NPU-2A	4.90/160–279	17.30/329–371	64.78/398–475	12.80
NPU-2B	5.20/208–281	22.40/312–379	34.40/396–460	8.00
NPU-5A	3.76/209–285	24.40/313–376	55.54/398–494	15.25
NPU-6A	13.00/189–290	33.22/320–378	36.00/409–482	16.90
PU-7	14.00/200–278	42.80/312–392	30.80/409–492	11.30
NPU-7A	13.50/215–287	35.16/308–370	31.00/398–455	18.70
NPU-7B	8.70/213–274	36.50/318–371	38.10/410–483	15.60
PU-10	23.20/245–367	45.60/360–446	10.00/455–600	6.00
NPU-10A	26.80/240–350	43.60/383–455	92.00/460–580	11.20
NPU-10B	30.00/260–380	46.40/385–460	16.00/465–600	5.00

^aChar yield at 600°C

this decomposition step was due mainly due to the degradation of PTMEG chains.

Figure 6 shows the thermal behavior of the weight loss curves of PU-7, NPU-7A and NPU-7B. The shape of the weight loss curves of all samples was almost identical. The increase of the weight loss in the degradation second step of NPU-7B was due to the presence of the soft segment from bis-maleimide.

DSC analysis provided the information on the glass transition, crystallization, melting endotherms and also the rDA reaction of networks (Figure 7 and Figure 8). The DSC data are compiled in Table 4. Figure 7 present DSC curves of networks based on polyurethanes PU-(1-7) and bismaleimide A (Figure 7a) or B (Figure 7b). DSC curves of NPU-(2-7)A (Figure 7a) exhibited the glass transition temperature corresponding to the soft segment, the glass

Table 4. Thermal behavior of polyurethane networks

Sample	T _{g ss} ^a [°C]	T _{cryst ss} ^b [°C]	T _{melt ss} ^c [°C]	T _{g network} ^d [°C]	T _{rDA} ^e [°C]	ΔH _{rDA} ^f [J/g]
NPU-2A	-64.47	–	-2.58	–	120.14	-12.96
NPU-3A	-62.86	–	–	54.80	109.55	-44.38
NPU-4A	-66.18	–	–	53.32	112.44	-38.84
NPU-5A	-59.36	–	–	–	116.21	-3.44
NPU-6A	-36.06	–	–	53.11	109.12	-18.79
NPU-7A	–	–	–	52.06	104.25	-22.29
NPU-8A	-72.25	-34.54	22.72	–	117.46	-16.74
NPU-9A	-68.31	–	2.59	–	150.49	–
NPU-10A	-57.76	–	–	–	116.17	–
NPU-11A	-45.32	–	–	–	117.71	-30.65
NPU-12A	12.32	–	–	–	112.35	-91.16
NPU-1B	-69.25	-23.05	16.34	50.98	106.21	-2.40
NPU-5B	-56.08	–	–	46.20	121.17	-3.06
NPU-6B	-32.29	–	–	41.93	108.89	-13.76
NPU-7B	–	–	–	20.51	109.18	-46.73
NPU-8B	-72.34	-36.00	17.65	–	115.46	-6.95
NPU-9B	-69.93	–	8.20	–	109.82	-63.92
NPU-10B	-60.73	–	–	46.08	113.18	-13.02
NPU-11B	-48.69	–	–	48.05	113.05	-14.62
NPU-12B	8.34	–	–	–	113.44	-44.91

^aGlass transition temperature of soft segment polyurethanes^bCrystallization temperature of soft segment polyurethanes^cMelting temperature of soft segment polyurethanes^dGlass transition temperature of networks^eTemperature corresponding to retro Diels-Alder reaction^fHeat of the retro Diels-Alder reaction

transition temperature corresponding to networks and endothermic transition temperature corresponding to the rDA process, and varied in the range of -36.06 and -66.18°C , 50 – 55°C and 104 – 120°C , respectively. The networks based on PTMEG hav-

ing number-average molecular weight of 250 , **NPU-7A**, did not show T_g for soft segment. The rDA process energy ranged between -3.44 and -44.38 J/g depending on the number-average molecular weight of PTMEG and the isocyanate: PTMEG:chain extender molar ratio. DSC curves for networks **NPU-(1-7)B** showed the same transitions and endothermic process whose maximum temperature ranged between 106 – 121°C . On the DSC curves of polyurethane networks **NPU-(1-7)A,B** there can be observed that when decreasing the number-average molecular weight of PTMEG the T_g of network and T_g of the soft segment increased due to the fact that as the PTMEG chain's length decreases, it's mobility decreases too, leading this way to a higher glass transition temperature. The decrease of the T_g of soft segment when increasing the number-average molecular weight of PTMEG indicates that longer soft segments present a better phase separation in the corresponding poly-

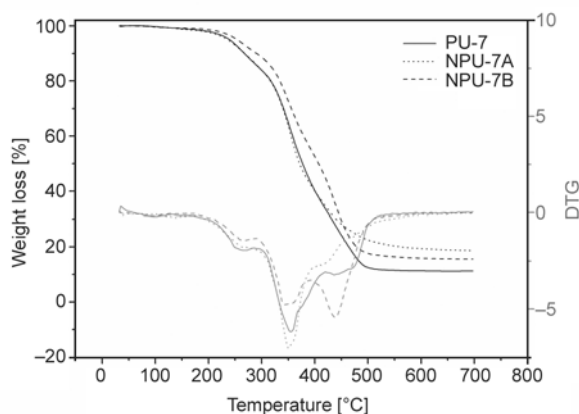


Figure 6. The TGA curves of **PU-7** and its corresponding networks

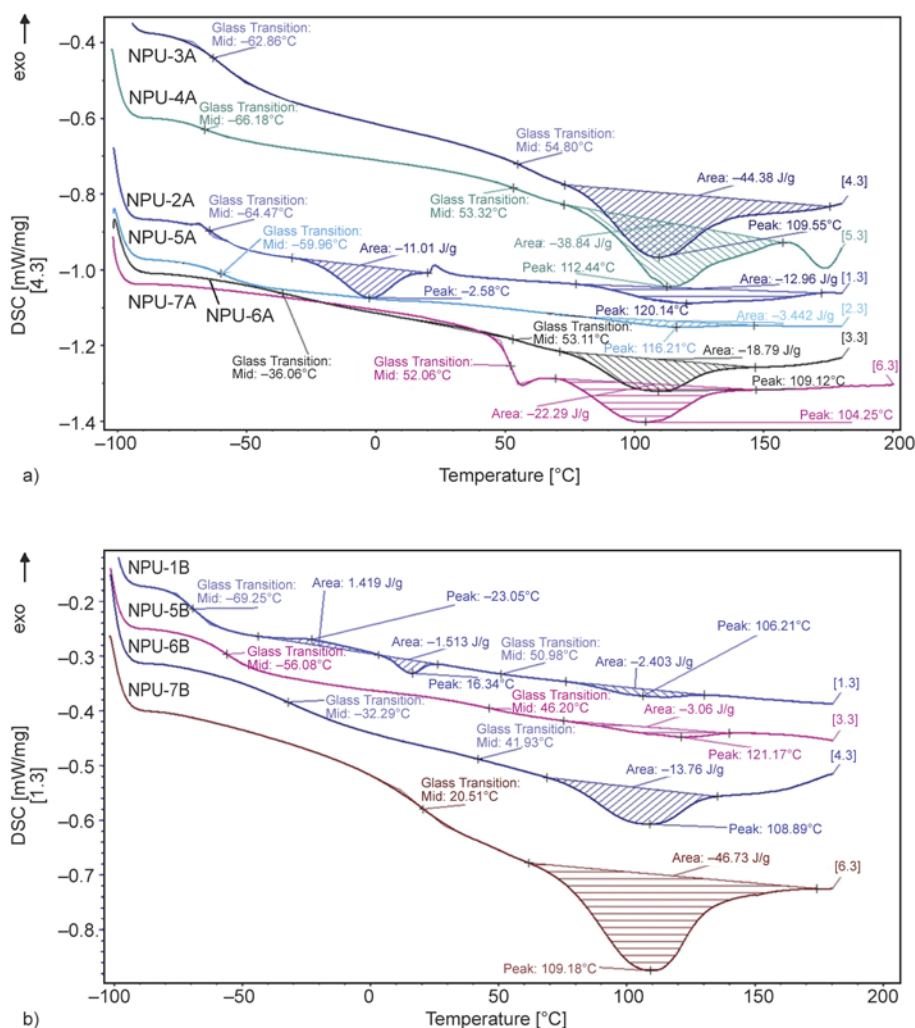


Figure 7. The DSC curves of networks based on DBDI; (a) with bismaleimide **A**; (b) with bismaleimide **B**

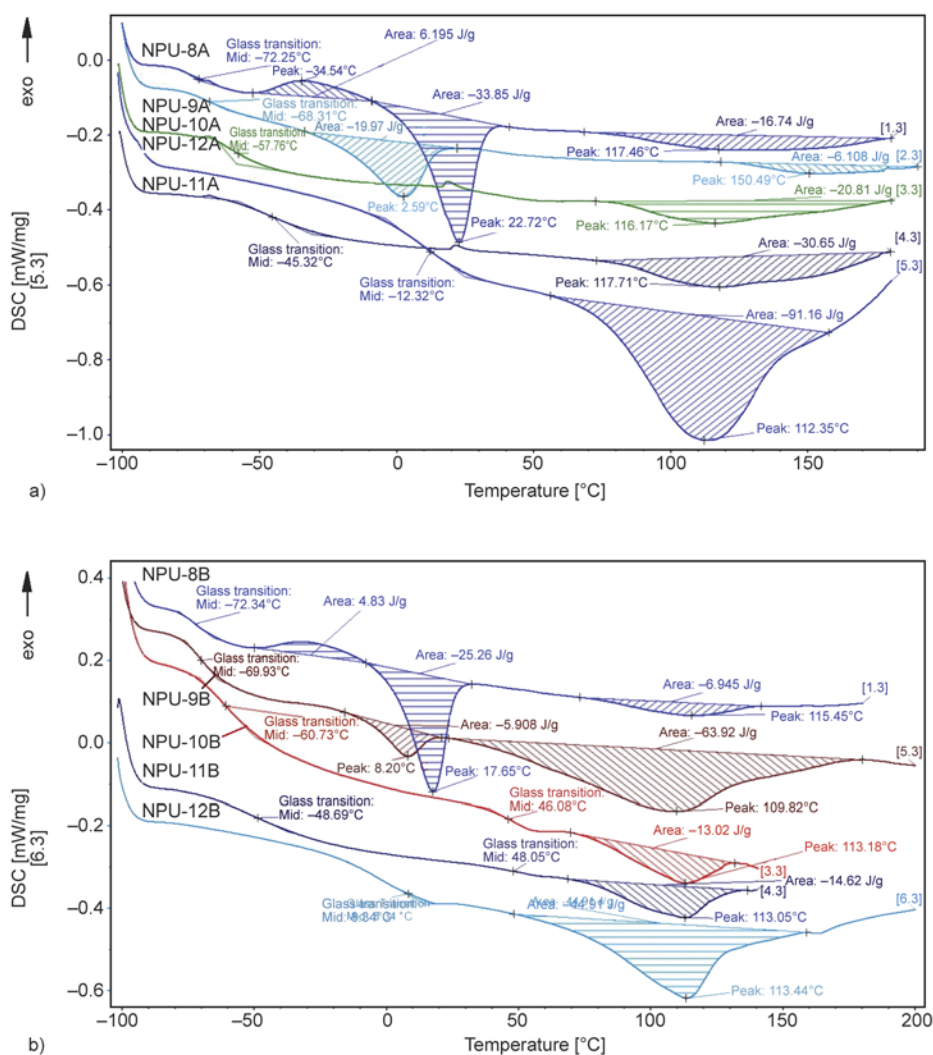


Figure 8. The DSC curves of networks based on HMDI; (a) with bismaleimide **A**; (b) with bismaleimide **B**

urethane network [46]. Also, by increasing the molar ratio (amount of chain extender) the crosslinking density increases (this was evidenced by the disappearance of melting endotherm of the soft segment) and the glass transition temperature of network slightly decreases, probably due to the longer segment lengths between network points.

The DSC curves of polyurethane networks **NPU-(8-12)A,B** are represented in Figure 8a and 8b. There can be observed that the curves presented the same characteristics as the ones of **NPU-(1-7)A,B**. Also, there can be noticed that using DBDI instead of HMDI in the synthesis of polyurethanes leads to a higher glass transition temperature of the soft segment.

Regarding the crystallization and melting processes from both Figures 7 and Figure 8 one can see that only the DSC curves of **NPU-(1,8)A,B** which contain PTMEG having the number-average molecular

weight of 2000 presented the crystallization exotherm, while the melting endotherm was present on the DSC curves of polyurethane networks which had PTMEG with the number-average molecular weight of 2000 and 1500. In the case of the networks with lower number-average molecular weight of PTMEG none of these processes could be observed, their molecular weight being too low to evidence a crystallization process [47].

3.2. Thermoreversibility of the networks

The DSC and ATR-FTIR methods were applied to evaluate the thermoreversibility of the networks. The thermoreversibility of the network (**NPU-11A**) was evidenced by applying multiple heating-cooling cycles in a differential scanning calorimeter. Thus, there can be observed that the endothermic peak characteristic to the retrodiene process appeared on all three heating curves, the maximum

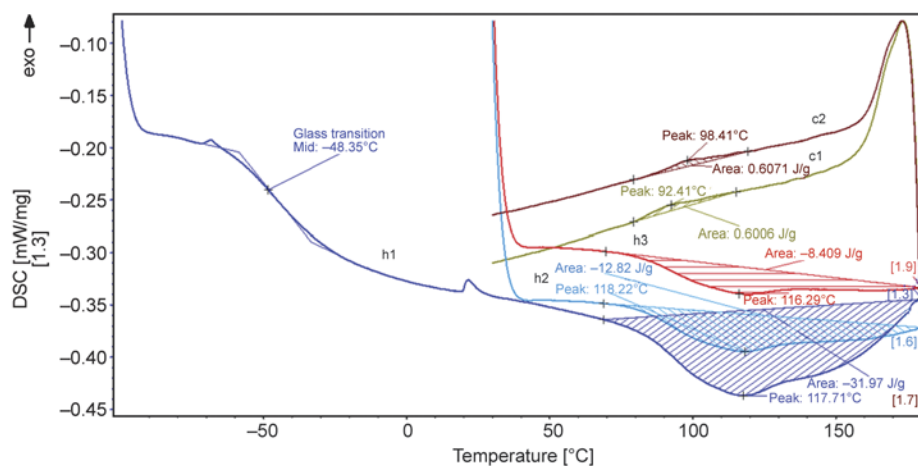


Figure 9. The DSC scans of **NPU-11A**: h1 – the first heating run; h2 – the second heating run and h3 – the third heating run; c1 – the first cooling run; c2 – the second cooling run

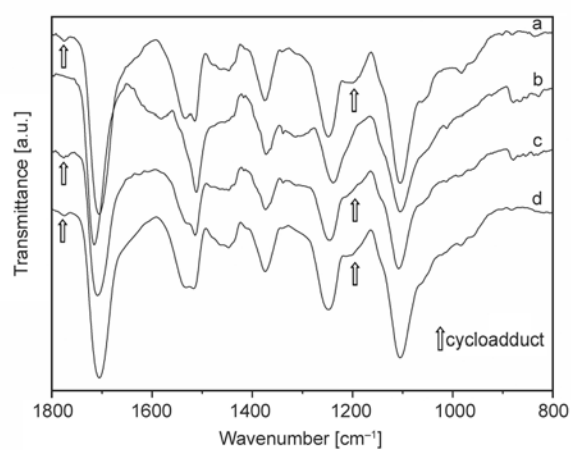


Figure 10. The ATR-FTIR spectra of **NPU-11A**: a – initial; b – at 150°C; c – after cooling; d – recovery (after heat treatment at 80°C for 6 hours)

of the endothermic peak having almost the same value around 116–118°C (Figure 9). The cooling curves presented an exothermic peak with a maximum around 92–96°C, exotherm which is specific to the dienic process of regeneration of the furan-maleimide cycloadduct.

The thermoreversibility of **NPU-11A** was also confirmed by ATR-FTIR spectroscopy (Figure 10). So, recording the spectrum for this compound at 130°C (Figure 10 curve b) we can observe that it was not present anymore the characteristic band of cycloadduct at 1775 cm^{-1} and also that the band attributed to the carbonyl stretching vibration shifted to higher values (1714 cm^{-1}). The $-\text{C}-\text{N}-\text{C}-$ absorption band from succinimide at 1197 cm^{-1} disappeared too due to the debonding of the cycloadduct in maleimide and furyl groups. After cooling the sample and recording again the spectrum, we could see that the carbonyl band shifted back to lower val-

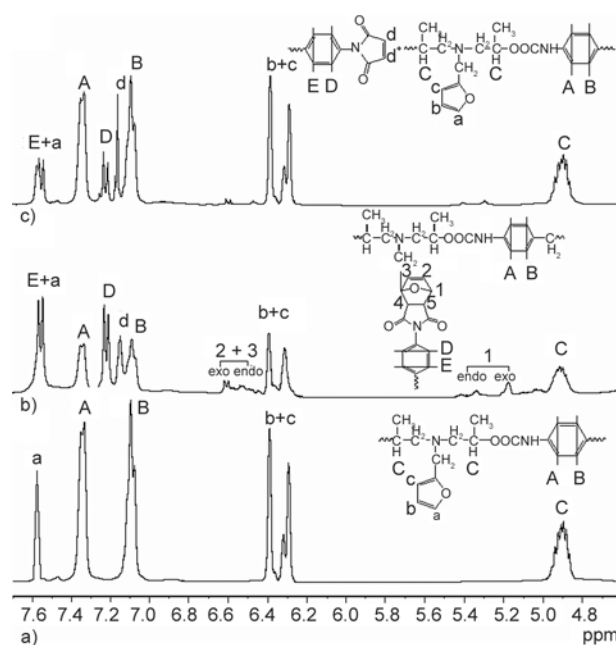


Figure 11. The ^1H -NMR spectra of Diels-Alder cycloaddition after different time periods: (a) **PU-7B**; (b) after 10 h at 60°C (**NPU-7B**); (c) retro-DA (**PU-7B** + bismaleimide **B**)

ues (1711 cm^{-1}) and the appearance of the band at 1775 cm^{-1} corresponding to the cycloadduct and the one at 1197 cm^{-1} attributed to $-\text{C}-\text{N}-\text{C}-$ from succinimide (Figure 10 curve c). After heating the sample at 80°C for 6 hours in an oven the carbonyl band shifts back to its initial value (1708 cm^{-1}) due to the complete recovery of the cycloadduct when an appropriate time was accorded to the dienic reaction took place (Figure 10 curve d).

The reaction between furyl and maleimide groups was carried out at different temperatures (60 and 140°C) in $\text{DMSO}-d_6$ (NMR tube under nitrogen atmosphere) allowing real-time ^1H -NMR character-

ization. The evolution of $^1\text{H-NMR}$ spectra were shown in Figure 11. Figure 11a represents the $^1\text{H-NMR}$ spectrum of **PU-7B**. After reacting **PU-7B** with bismaleimide **B** at 60°C for 10 h, part of formed network becomes insoluble; the $^1\text{H-NMR}$ spectrum exhibits new signals at 6.65–6.43, and 5.45–5.17 ppm assigned to exo/endo protons 2, 3, and 1 of DA adduct, respectively, along with the existing peaks at 7.57 ppm attributed to protons a from furyl unit, and at 6.42–6.25 ppm ascribed to protons b and c of furyl group (Figure 11 (b)). After complete Diels-Alder reaction, the sample became a gel and the $^1\text{H-NMR}$ spectrum could not be recorded. After the sample was heated at 140°C , the corresponding

$^1\text{H-NMR}$ spectrum exhibited the signals characteristic to the bismaleimide **B** (7.14 ppm assigned to the proton d) and **PU-7B** (Figure 11c).

3.3. Surface characterization of the networks

The dynamic contact angles of the polyurethanes and polyurethane networks were measured using Wilhelmy plate technique. The advancing contact angle values measured in water and ethylene glycol and the hysteresis values are given in Table 5. The free surface energies were calculated according to Owens and Wendt equation (Equation (1)):

$$(1 + \cos\theta)\gamma_L = 2(\gamma_S^d\gamma_L^d)^{1/2} + 2(\gamma_S^p + \gamma_L^p)^{1/2} \quad (1)$$

Table 5. Contact angle in water and ethylene glycol and dispersive and polar components of free energy of PU and NPU films

Sample	$\theta_{\text{adv water}}^{\text{a/hysteresis}}$	$\theta_{\text{adv EG}}^{\text{b/hysteresis}}$	ΔG_h^{c}		Free surface energy ^d		
			Water	EG	γ^{d}	γ^{p}	$\gamma = \gamma^{\text{d}} + \gamma^{\text{p}}$
PU-1	91.85/32.26	81.56/50.76	0.365	1.631	5.642	11.420	17.062
PU-2	87.26/22.60	75.78/22.60	0.248	1.235	6.801	13.217	20.018
PU-3	93.35/34.09	78.90/34.09	0.371	1.100	9.227	7.923	17.409
PU-4	85.66/36.77	76.68/38.21	0.669	1.110	4.932	16.246	21.178
PU-5	92.89/26.14	82.51/36.34	0.207	0.788	5.659	10.789	16.448
PU-6	96.98/43.48	73.98/34.38	0.522	1.023	19.188	2.603	21.791
PU-8	87.00/29.07	84.73/26.80	0.406	1.148	1.240	21.487	22.727
PU-9	84.10/29.96	76.43/37.31	0.420	1.071	4.094	18.473	22.567
PU-10	70.57/18.30	64.30/18.30	0.435	1.250	3.583	30.856	34.439
PU-11	76.97/23.64	64.01/30.25	0.481	1.192	8.269	19.063	27.332
PU-12	89.19/34.81	76.82/46.08	0.543	–	7.494	11.419	18.913
NPU-1A	87.41/20.76	84.14/58.37	0.209	2.051	1.622	20.202	21.824
NPU-2A	77.20/29.55	75.78/29.25	0.687	1.010	1.181	30.421	31.602
NPU-3A	86.88/31.65	75.00/43.21	0.492	1.501	7.162	13.138	20.300
NPU-4A	73.42/16.91	63.81/27.77	0.356	1.050	9.666	24.951	30.617
NPU-5A	83.29/28.38	73.50/34.88	0.480	1.064	5.606	17.177	22.783
NPU-6A	84.16/28.78	70.81/15.43	0.470	0.862	8.544	13.723	22.267
NPU-8A	89.87/31.53	77.84/38.71	0.399	1.084	7.167	11.277	18.444
NPU-9A	91.59/45.35	82.24/20.53	0.805	0.292	4.948	12.258	17.206
NPU-10A	92.30/30.34	82.58/52.81	0.307	1.713	5.185	11.584	16.769
NPU-11A	82.28/25.43	71.74/35.50	0.418	0.954	6.210	17.242	23.452
NPU-12A	86.03/29.71	74.03/37.15	0.449	1.167	7.249	13.572	20.866
NPU-1B	88.84/31.47	81.31/31.49	0.425	2.368	3.825	15.377	19.202
NPU-2B	75.05/19.93	56.84/19.93	0.405	1.642	13.106	16.362	29.468
NPU-4B	90.60/36.63	91.62/71.54	0.526	2.650	0.278	22.079	22.357
NPU-5B	85.88/29.50	70.60/35.61	0.447	1.233	10.354	11.285	21.630
NPU-6B	82.47/31.56	76.61/43.25	0.606	1.413	3.051	21.370	24.420
NPU-7B	86.19/31.20	74.95/35.47	0.489	1.035	6.650	14.060	20.710
NPU-9B	81.79/27.11	74.24/39.62	0.479	1.256	3.472	21.220	24.692
NPU-10B	88.80/36.70	82.59/36.70	0.574	–	3.261	16.184	19.445
NPU-11B	88.39/45.53	67.65/53.08	0.954	–	16.544	6.698	23.153
NPU-12B	83.37/27.71	78.16/36.63	0.459	1.045	3.812	19.438	23.250

^aAdvanced contact angle measured in water

^bAdvanced contact angle measured in ethylene glycol

^cMolar free energy of hysteresis

^dCalculated from the dispersive (γ^{d}) and polar (γ^{p}) components

where θ represents the advancing contact angle value, γ_L is the free surface energy of the liquid, γ_L^d and γ_L^p are the dispersive and polar components of the free surface energy of the liquid, and γ_S^d and γ_S^p are the dispersive and polar components of the free surface energy of the polyurethane/polyurethane network films.

The molar free energies of hysteresis, quantitatively correlation to surface interaction of the hysteresis, were also calculated using Equation (2):

$$\Delta G_h = -RT \ln \left(\frac{\sin \theta_{\text{rec}}}{\sin \theta_{\text{adv}}} \right) \quad (2)$$

where ΔG_h is the molar free energy of hysteresis and θ_{adv} and θ_{rec} represent the advancing and receding dynamic contact angle values [48].

As can be observed, in the case of polyurethanes, the contact angle value depended on the nature of the isocyanate used in synthesis. Thus, **PU-(8-12)** had lower dynamic contact angle values than the corresponding **PU-(1-7)**, due to the hydrophilic behavior of the aliphatic diisocyanate [49]. The contact angle value decreased when crosslinking **PU-(1-7)** with bismaleimides, while the free surface energy increased. On the score of crosslinking, the majority of the carbonyl and NH groups are not implied in hydrogen bonds anymore, thus being able to contribute to the increase of the hydrophilicity of the surface of polyurethane networks comparing with the ones of the polyurethanes. In the case of **NPU-(8-12)** the contact angle value increased comparing with the corresponding polyurethane (in most of the cases), even when the free surface energy increased. This fact can be due to the roughness of the surface, which is known to reduce the effective area of the contact angle, leading this way to higher values of it. As can be seen in Table 5 in the case of **PU-(8-12)** the surface roughness (given by the hysteresis value) increased when crosslinking with bismaleimides [50].

In most of the cases the polar component's value was higher than the dispersive one's indicating that the dipolar forces and the hydrogen bonds played an important role in the structure of the polyurethanes and polyurethane networks. The value of the molar free energy of hysteresis was higher in ethylene glycol than that in water, in most of the cases, suggesting that the contribution of dipolar forces and hydrogen bonds in water was more pregnant in ethylene glycol [48].

3.4. Mechanical properties

The investigated mechanical properties of the polyurethanes and polyurethane networks were: breaking strength and elongation and Young's modulus. By crosslinking the polyurethanes with bismaleimides there could be observed an increasing of the breaking elongation, elongation which can be even forth times higher (Figure 12a). The results of physico-mechanical measurements of poly(etherurethane)s evidenced a slight increase of the tensile strength from 5.51 to 6.30 MPa, and a decrease of the elongation at break (from 243.10 to 128.46%), for a rate of reagents from 2:1:1 to 3:1:2. The breaking strength increased when crosslinking with bismaleimides increased, which was more pronounced

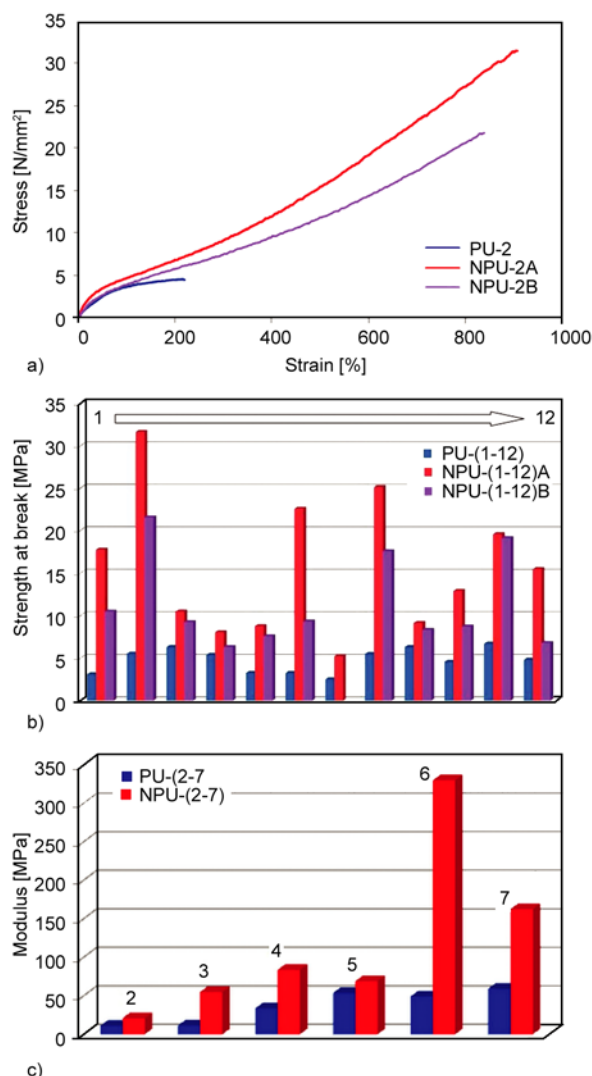


Figure 12. The mechanical properties of polyurethanes and their networks: (a) stress-strain diagram for **PU-2** and its corresponding networks; (b) strength at break of polyurethanes and their networks; (c) modulus of **PU-(2-7)** and **NPU-(2-7)A**

when using the aromatic bismaleimide (Figure 12b). The isocyanate:PTMEG:chain extender molar ratio used in this reaction also influenced the breaking strength. As can be seen in Figure 12b, an increase of the isocyanate and chain extender amount led to a decrease of the breaking strength. The Young's modulus of polyurethanes and polyurethane networks had the same behavior as breaking strength and elongation, meaning that it increased after crosslinking with bismaleimides (Figure 12c). Instead, unlike breaking strain, the modulus of the polyurethane networks increased when increasing the used isocyanate amount in synthesis, from 20.69 to 83.54 MPa for **NPU-A** and 8.28 to 57.60 MPa for **NPU-B**.

4. Conclusions

Thermally reversible cross-linked poly(ether-urethane)s were prepared by the Diels-Alder crosslinking reaction of the furan-containing poly(ether-urethane) to bismaleimides. The glass transition temperature of the soft segment of DBDI-networks was higher than that of HDMI-networks and for both types of networks it decreased with increasing the molecular weight of PTMEG.

The thermal stability of networks was given by the both bismaleimide and isocyanate structure. The thermoreversibility of the networks was evidenced by both DSC and ATR-FTIR spectroscopy. The contact angle values of networks increased or decreased compared to that of polyurethanes depending on the isocyanate structure used in the synthesis. The bismaleimide structure and the used isocyanate:PTMEG:chain extender molar ratio influenced the mechanical properties of networks. By crosslinking the polyurethanes with bismaleimides there could be observed an increasing of the breaking elongation, elongation which can be even forth times higher than that of the initial polyurethane (900%).

References

[1] Bergman S. D., Wudl F.: Mendable polymers. *Journal of Materials Chemistry*, **18**, 41–62 (2008).
DOI: [10.1039/b713953p](https://doi.org/10.1039/b713953p)

[2] Murphy E. B., Wudl F.: The world of smart healable materials. *Progress in Polymer Science*, **35**, 223–251 (2010).
DOI: [10.1016/j.progpolymsci.2009.10.006](https://doi.org/10.1016/j.progpolymsci.2009.10.006)

[3] Sanyal A.: Diels-Alder cycloaddition-cycloreversion: A powerful combo in materials design. *Macromolecular Chemistry and Physics*, **211**, 1417–1425 (2010).
DOI: [10.1002/macp.201000108](https://doi.org/10.1002/macp.201000108)

[4] Hizal G., Tunca U., Sanyal A.: Discrete macromolecular constructs via the Diels-Alder 'click' reaction. *Journal of Polymer Science Part A: Polymer Chemistry*, **49**, 4103–4120 (2011).
DOI: [10.1002/pola.24835](https://doi.org/10.1002/pola.24835)

[5] Boul P. J., Reutenauer P., Lehn J.-M.: Reversible Diels-Alder reactions for the generation of dynamic combinatorial libraries. *Organic Letters*, **7**, 15–18 (2005).
DOI: [10.1021/ol048065k](https://doi.org/10.1021/ol048065k)

[6] Kotha S., Banerjee S., Patil M. P., Sunoj R. B.: Retro Diels-Alder reaction under mild conditions: experimental and theoretical studies. *Organic and Biomolecular Chemistry*, **4**, 1854–1856 (2006).
DOI: [10.1039/B604063B](https://doi.org/10.1039/B604063B)

[7] Jones G. O., Houk K. N.: Predictions of substituent effects in thermal azide 1,3-dipolar cycloadditions: Implications for dynamic combinatorial (reversible) and click (irreversible) chemistry. *The Journal of Organic Chemistry*, **73**, 1333–1342 (2008).
DOI: [10.1021/jo702295d](https://doi.org/10.1021/jo702295d)

[8] Reutenauer P., Boul P. J., Lehn J.-M.: Dynamic Diels-Alder reactions of 9,10-dimethylantracene: reversible adduct formation, dynamic exchange processes and thermal fluorescence modulation. *European Journal of Organic Chemistry*, **2009**, 1691–1697 (2009).
DOI: [10.1002/ejoc.200801269](https://doi.org/10.1002/ejoc.200801269)

[9] Boutelle R. C., Northrop B. H.: Substituent effects on the reversibility of furan–maleimide cycloadditions. *The Journal of Organic Chemistry*, **76**, 7994–8002 (2011).
DOI: [10.1021/jo201606z](https://doi.org/10.1021/jo201606z)

[10] Pearson R. J., Kassianidis E., Philp D.: A completely selective and strongly accelerated Diels-Alder reaction mediated by hydrogen bonding. *Tetrahedron Letters*, **45**, 4777–4780 (2004).
DOI: [10.1016/j.tetlet.2004.04.079](https://doi.org/10.1016/j.tetlet.2004.04.079)

[11] Goiti E., Heatley F., Huglin M. B., Rego J. M.: Kinetic aspects of the Diels-Alder reaction between poly(styrene-co-furfuryl methacrylate) and bismaleimide. *European Polymer Journal*, **40**, 1451–1460 (2004).
DOI: [10.1016/j.eurpolymj.2004.01.036](https://doi.org/10.1016/j.eurpolymj.2004.01.036)

[12] Conley N. R., Hung R. J., Willson C. G.: A new synthetic route to authentic *N*-substituted aminomaleimides. *The Journal of Organic Chemistry*, **70**, 4553–4555 (2005).
DOI: [10.1021/jo048031q](https://doi.org/10.1021/jo048031q)

[13] Teramoto N., Arai Y., Shibata M.: Thermo-reversible Diels-Alder polymerization of difurfurylidene trehalose and bismaleimides. *Carbohydrate Polymers*, **64**, 78–84 (2006).
DOI: [10.1016/j.carbpol.2005.10.029](https://doi.org/10.1016/j.carbpol.2005.10.029)

- [14] Dag A., Durmaz H., Hizal G., Tunca U.: Preparation of 3-arm star polymers (A_3) via Diels-Alder click reaction. *Journal of Polymer Science Part A: Polymer Chemistry*, **46**, 302–313 (2008). DOI: [10.1002/pola.22381](https://doi.org/10.1002/pola.22381)
- [15] Laita H., Boufi S., Gandini A.: The application of the Diels-Alder reaction to polymers bearing furan moieties. 1. Reactions with maleimides. *European Polymer Journal*, **33**, 1203–1211 (1997). DOI: [10.1016/S0014-3057\(97\)00009-8](https://doi.org/10.1016/S0014-3057(97)00009-8)
- [16] Loy D. A., Wheeler D. R., McElhanon J. R., Saunders R. S., Durbin-Voss M. L.: Method of making thermally removable polyurethanes. U.S. Patent 6403753, USA (2002).
- [17] Bibiao J., Jianjun H., Wenyun W., Luxia J., Xinxian C.: Synthesis and properties of novel polybismaleimide oligomers. *European Polymer Journal*, **37**, 463–470 (2001). DOI: [10.1016/S0014-3057\(00\)00147-6](https://doi.org/10.1016/S0014-3057(00)00147-6)
- [18] Szalai M. L., McGrath D. V., Wheeler D. R., Zifer T., McElhanon J. R.: Dendrimers based on thermally reversible furan–maleimide Diels-Alder adducts. *Macromolecules*, **40**, 818–823 (2007). DOI: [10.1021/ma062093w](https://doi.org/10.1021/ma062093w)
- [19] Merve Kose M., Yesilbag G., Sanyal A.: Segment block dendrimers via Diels-Alder cycloaddition. *Organic Letters*, **10**, 2353–2356 (2008). DOI: [10.1021/ol800553t](https://doi.org/10.1021/ol800553t)
- [20] Vieyres A., Lam T., Gillet R., Franc G., Castonguay A., Kakkar A.: Combined Cu^I -catalysed alkyne–azide cycloaddition and furan–maleimide Diels-Alder ‘click’ chemistry approach to thermoresponsive dendrimers. *Chemical Communications*, **46**, 1875–1877 (2010). DOI: [10.1039/B924888A](https://doi.org/10.1039/B924888A)
- [21] Polaske N. W., McGrath D. V., McElhanon J. R.: Thermally reversible dendronized linear AB step-polymers via ‘click’ chemistry. *Macromolecules*, **44**, 3203–3210 (2011). DOI: [10.1021/ma200296t](https://doi.org/10.1021/ma200296t)
- [22] McElhanon J. R., Russick E. M., Wheeler D. R., Loy D. A., Aubert J. H.: Removable foams based on an epoxy resin incorporating reversible Diels-Alder adducts. *Journal of Applied Polymer Science*, **85**, 1496–1502 (2002). DOI: [10.1002/app.10753](https://doi.org/10.1002/app.10753)
- [23] Hobbs M. L.: Modeling epoxy foams exposed to fire-like heat fluxes. *Polymer Degradation and Stability*, **89**, 353–372 (2005). DOI: [10.1016/j.polymdegradstab.2005.01.021](https://doi.org/10.1016/j.polymdegradstab.2005.01.021)
- [24] Tian Q., Rong M. Z., Zhang M. Q., Yuan Y. C.: Synthesis and characterization of epoxy with improved thermal remendability based on Diels-Alder reaction. *Polymer International*, **59**, 1339–1345 (2010). DOI: [10.1002/pi.2872](https://doi.org/10.1002/pi.2872)
- [25] Tian Q., Rong M. Z., Zhang M. Q., Yuan Y. C.: Optimization of thermal remendability of epoxy via blending. *Polymer*, **51**, 1779–1785 (2010). DOI: [10.1016/j.polymer.2010.02.004](https://doi.org/10.1016/j.polymer.2010.02.004)
- [26] Goiti E., Huglin M. B., Rego J. M.: Some properties of networks produced by the Diels-Alder reaction between poly(styrene-co-furfuryl methacrylate) and bis-maleimide. *European Polymer Journal*, **40**, 219–226 (2004). DOI: [10.1016/j.eurpolymj.2003.09.017](https://doi.org/10.1016/j.eurpolymj.2003.09.017)
- [27] Adzima B. J., Aguirre H. A., Kloxin C. J., Scott T. F., Bowman C. N.: Rheological and chemical analysis of reverse gelation in a covalently cross-linked Diels-Alder polymer network. *Macromolecules*, **41**, 9112–9117 (2008). DOI: [10.1021/ma801863d](https://doi.org/10.1021/ma801863d)
- [28] Zhang Y., Broekhuis A. A., Picchioni F.: Thermally self-healing polymeric materials: The next step to recycling thermoset polymers? *Macromolecules*, **42**, 1906–1912 (2009). DOI: [10.1021/ma802767z](https://doi.org/10.1021/ma802767z)
- [29] Kavitha A. A., Singha N. K.: ‘Click chemistry’ in tailor-made polymethacrylates bearing reactive furfuryl functionality: A new class of self-healing polymeric material. *Applied Materials and Interface*, **1**, 1427–1436 (2009). DOI: [10.1021/am900124c](https://doi.org/10.1021/am900124c)
- [30] Magana S., Zerroukhi A., Jegat C., Mignard N.: Thermally reversible crosslinked polyethylene using Diels-Alder reaction in molten state. *Reactive and Functional Polymers*, **70**, 442–448 (2010). DOI: [10.1016/j.reactfunctpolym.2010.04.007](https://doi.org/10.1016/j.reactfunctpolym.2010.04.007)
- [31] Imai Y., Itoh H., Naka K., Chujo Y.: Thermally reversible IPN organic–inorganic polymer hybrids utilizing the Diels-Alder reaction. *Macromolecules*, **33**, 4343–4346 (2000). DOI: [10.1021/ma991899b](https://doi.org/10.1021/ma991899b)
- [32] Adachi K., Achimuthu A. K., Chujo Y.: Synthesis of organic–inorganic polymer hybrids controlled by Diels-Alder reaction. *Macromolecules*, **37**, 9793–9797 (2004). DOI: [10.1021/ma0400618](https://doi.org/10.1021/ma0400618)
- [33] Costanzo P. J., Beyer F. L.: Thermoresponsive, optically active films based on Diels-Alder chemistry. *Chemistry of Materials*, **19**, 6168–6173 (2007). DOI: [10.1021/cm701864r](https://doi.org/10.1021/cm701864r)
- [34] McElhanon J. R., Zifer T., Kline S. R., Wheeler D. R., Loy D. A., Jamison G. M., Long T. M., Rahimian K., Simmons B. A.: Thermally cleavable surfactants based on furan–maleimide Diels-Alder adducts. *Langmuir*, **21**, 3259–3266 (2005). DOI: [10.1021/la047074z](https://doi.org/10.1021/la047074z)
- [35] Zhu J., Kell A. J., Workentin M. S.: A retro-Diels-Alder reaction to uncover maleimide-modified surfaces on monolayer-protected nanoparticles for reversible covalent assembly. *Organic Letters*, **8**, 4993–4996 (2006). DOI: [10.1021/ol0615937](https://doi.org/10.1021/ol0615937)

- [36] Gevrek T. N., Ozdeslik R. N., Sahin G. S., Yesilbag G., Mutlu S., Sanyal A.: Functionalization of reactive polymeric coatings via Diels-Alder reaction using microcontact printing. *Macromolecular Chemistry and Physics*, **213**, 166–172 (2012).
DOI: [10.1002/macp.201100406](https://doi.org/10.1002/macp.201100406)
- [37] Liu Y-L., Hsieh C-Y.: Crosslinked epoxy materials exhibiting thermal remendability and removability from multifunctional maleimide and furan compounds. *Journal of Polymer Science Part A: Polymer Chemistry*, **44**, 905–913 (2006).
DOI: [10.1002/pola.21184](https://doi.org/10.1002/pola.21184)
- [38] McElhanon J. R., Wheeler D. R.: Thermally responsive dendrons and dendrimers based on reversible furan-maleimide Diels-Alder adducts. *Organic Letters*, **3**, 2681–2683 (2001).
DOI: [10.1021/ol0101281](https://doi.org/10.1021/ol0101281)
- [39] Gaina C., Ursache O., Gaina V.: Re-mendable polyurethanes. *Polymer-Plastics Technology and Engineering*, **50**, 712–718 (2011).
DOI: [10.1080/03602559.2010.551392](https://doi.org/10.1080/03602559.2010.551392)
- [40] Gaina C., Ursache O., Gaina V., Buruiana E., Ionita D.: Investigation on the thermal properties of new thermo-reversible networks based on poly(vinyl furfural) and multifunctional maleimide compounds. *Express Polymer Letters*, **6**, 129–141 (2012).
DOI: [10.3144/expresspolymlett.2012.14](https://doi.org/10.3144/expresspolymlett.2012.14)
- [41] Gaina V., Ursache O., Gaina C., Buruiana E.: Novel thermally-reversible epoxy-urethane networks. *Designed Monomers and Polymers*, **15**, 63–73 (2012).
DOI: [10.1163/156855511X606155](https://doi.org/10.1163/156855511X606155)
- [42] Gaina V., Gaina C.: AB-monomers. I. Synthesis and polymerization of furyl-maleimide monomers. *Revue Roumaine de Chimie*, **48**, 881–890 (2003).
- [43] Cristea M., Gaina C., Gheorghiu Ionita D., Gaina V.: Dynamic mechanical analysis on modified bis-maleimide resins. *Journal of Thermal Analysis and Calorimetry*, **93**, 69–76 (2008).
DOI: [10.1007/s10973-007-8802-4](https://doi.org/10.1007/s10973-007-8802-4)
- [44] Jingwu S., Jitao H., Shixiang S.: The synthesis of polyurethane with (alkylamino)pyridine functions. *Journal of Macromolecular Science Part A Pure and Applied Chemistry*, **32**, 319–322 (1995).
DOI: [10.1080/10601329508019177](https://doi.org/10.1080/10601329508019177)
- [45] Goussé C., Gandini A., Hodge P.: Application of the diels-alder reaction to polymers bearing furan moieties. 2. Diels-Alder and retro-Diels-Alder reactions involving furan rings in some styrene copolymers. *Macromolecules*, **31**, 314–321 (1998).
DOI: [10.1021/ma9710141](https://doi.org/10.1021/ma9710141)
- [46] Zhang J., Goodman I., Fort R. J., Sheldon R. P.: Properties of polyurethane elastomers prepared from 1,1'-iso-propylidene bis-(p-phenylene-oxy)di-propanol-2, a polyether (or polyester), and 4,4'-diphenylmethane diisocyanate (MDI) by one-step reaction method. *Polymer Communications*, **1**, 1–10 (1985).
- [47] Versteegen R. M., Kleppinger R., Sijbesma R. P., Meijer E. W.: Properties and morphology of segmented copoly(ether urea)s with uniform hard segments. *Macromolecules*, **39**, 772–783 (2006).
DOI: [10.1021/ma051874e](https://doi.org/10.1021/ma051874e)
- [48] Turri S., Levi M.: Wettability of polyhedral oligomeric silsesquioxane nanostructured polymer surfaces. *Macromolecular Rapid Communications*, **26**, 1233–1236 (2005).
DOI: [10.1002/marc.200500274](https://doi.org/10.1002/marc.200500274)
- [49] Vlad S., Spiridon I., Grigoraş C. V., Drobotă M., Nistor A.: Thermal, mechanical and wettability properties of some branched polyetherurethane elastomers. *e-Polymers*, no.004 (2009).
- [50] Joshi R. G., Goel A., Mannari V. M., Finlay J. A., Callow M. E., Callow J. A.: Evaluating fouling-resistance and fouling-release performance of smart polyurethane surfaces: An outlook for efficient and environmentally benign marine coatings. *Journal of Applied Polymer Science*, **114**, 3693–3703 (2009).
DOI: [10.1002/app.30899](https://doi.org/10.1002/app.30899)